# BULLE-EFFECT AND ITS IMPLICATIONS FOR MORPHODYNAMICS OF RIVER DIVERSIONS

BY

SOM DUTTA

DISSERTATION

Submitted in partial fulfillment of the requirements
for the degree of Doctor of Philosophy in Civil Engineering
in the Graduate College of the
University of Illinois at Urbana-Champaign, 2017

Urbana, Illinois

Doctoral Committee:

Professor Marcelo H. Garcia, Chair
Professor Paul F. Fischer
Professor Gary Parker
Professor James L. Best
Dr. Pablo Tassi, LNHE and LHSV, EDF R&D

# ABSTRACT

Bifurcations are one of the fundamental elements of a fluvial (river) system, and diversions are a special type of asymmetrical bifurcation where one of the channels after bifurcation continues along the original channel. Diversions can be found in nature, though many of them are built to divert water and sediment from the river for various purposes. Historically, diversions were built to divert water for irrigational and navigational purposes. Recently the importance of diversions has increased, as building diversions to divert sediment (and water) have been put forth as a method to rebuild deltas that have been losing land due to rapid rise in sea-level, subsidence etc. One of the prime examples is the plan under consideration by United States Army Corps of Engineers (USACE) to rebuild the Mississippi river delta through diverting water and sediment from the lower Mississippi river. Design of aforementioned diversions would be immensely benefited by a better understanding of the sediment distribution at diversions, and the hydrodynamics that drive it. One of the first and most extensive experimental studies to understand the dynamics at a diversion was conducted by Bulle in 1926, at Karlsruhe, Germany. Bulle found that a disproportionate percentage of bedload went into the lateral-channel, compared to the percentage of water entering the lateral-channel. This non-linear distribution of near-bed sediment between the two channels at a diversion is known as the Bulle-Effect; and since the seminal work of Bulle, multiple experimental studies have corroborated the phenomenon. Despite the importance of this phenomenon, till date the exact mechanism behind the Bulle-Effect is not clear. This thesis first unravels the mechanism behind the phenomenon, and then explores how Bulle-Effect might impact the morphodynamics of a diversion.

This thesis can be divided into two major parts:

1) First the mechanism behind the Bulle-Effect phenomenon is explored using high-resolution numerical simulation (Direct Numerical Simulations, Large Eddy Simulations) of flow and sediment transport for a configuration and at the scale similar to Bulle's experiment. The simulations were conducted using the highly-scalable spectral-element based incompressible Navier-Stokes solver Nek5000, on which a Lagrangian point particle submodel was developed and implemented to model the transport of sediment. The simulations were computationally very expensive ($\sim$ 240 million computational points), thus they

required the use of the peta-scale supercomputer Blue Waters for conducting them. The simulation results showed that the phenomenon is caused by the mechanism, where most of the flow near the bottom entered the lateral-channel, even when the percentage of the total water discharge entering lateral-channel is relatively smaller. The phenomenon was found to be at play not only for sediment transported as bedload, but also for suspended sediment that travels in the lower 25-35 percent of the water-column. These findings were found to hold across a range of Reynolds number $(10 - 25000)$ of the flow, and for different diversion angles.

2) In the second part of the thesis, a Reynolds Averaged Navier-Stokes (RANS) based 3D hydrodynamics and sediment transport model was developed for Bulles experiments using the open-source solver Telemac-Mascaret. This model was found to capture the phenomenon satisfactorily but at a relatively lower computational cost. The substantial reduction in computational cost is important, because at this point it impossible to conduct accurate Large Eddy Simulations (LES) of flows at the scale of real rivers. Thus it becomes important to evaluate if RANS based models can capture a complex phenomenon, and if this is the case to what extent ? The RANS model was then used to study the impact of Bulle-Effect on morphodynamics of the diversion. The separation of the flow from the left-bank of the lateral-channel was found to result in formation of a scour-hole under the high-flow zone and subsequent deposition sediment under the flow-recirculation. The impact of the change in morphology of the channel on Bulle-Effect was also analyzed.

The findings of this dissertation not only add to the fundamental understanding of an important phenomenon in nature, these also provide insights that will help in optimal design of engineered diversions and other facilities where vorticity and secondary-flow driven sediment/particle transport occurs. Based on disproportionately high sediment transported into the diversions of the Yellow River, China, Canal del Dique on the Magdalena River, Columbia etc., it can be conjectured that the Bulle-Effect plays a major role at the aforementioned diversions. Thus, in the future numerical simulations of real-world diversions should be conducted ( in conjunction with field measurements) in order to study the flow-structure and sediment distribution pattern at diversions, and to understand the extent to which the Bulle-Effect impacts real-world diversions.

*To Ankita for all her love and patience, and My Father for encouraging my questions about nature and mathematics*

# ACKNOWLEDGMENTS

First and foremost I would like to thank Prof. Marcelo H. Garcia, who has been an inspiration and continuous source of support. Over the years I have learned quite a few things from him, some directly through his classes on Sediment Transport, Open Channel Hydraulics, and discussions on various research topics; and others through all the ideas and stories he regales us with. Working with Prof. Garcia, I have been fortunate to work on different types of projects, which I think has broadened my scientific outlook and knowledge. I am indebted to him for suggesting a very interesting topic for my PhD, and then allowing me the freedom to tackle it the way I wanted. I hope to have a visionary like him as a mentor throughout my life.

In Spring 2014, I was looking for an open-source higher-order computational fluid dynamics solver to conduct the high-resolution numerical simulations I was planning for my dissertation. All the solvers I came across either could not handle complex boundary conditions, or were not higher-order. Fortunately, Prof. Paul Fischer started at UIUC that fall, and I was introduced to him and Nek5000. Since then, he has been a patient teacher and a supportive mentor to me. Discussing research and talking about new ideas with him is always very invigorating, primarily due to his infectious enthusiasm towards solving problems. Prof. Fischer's knowledge traverses multiple fields, thus I look forward to keep learning from him throughout my life.

Over the last 2.5 years, I have been interacting and collaborating with Dr. Pablo Tassi about different aspects of numerical simulation of free-surface hydrodynamics and morphodynamics using the open-source Telemac-Mascaret. Even though I have never met him in person, his inputs as a collaborator and committee member have helped improve my work immensely. And not just not just a mentor, he has also been a great friend. I hope our interactions and collaborations continue, and I also get to meet him soon.

Along with Prof. Garcia and Prof. Sivapalan (Siva), one of the first classes I took at UIUC was with Prof. Gary Parker, and he instantly left an indelible impression on me. Despite being extremely busy, the amount of time he spent with students from the Environmental Fluid Mechanics course taught me an important lesson, that great researchers are also great teachers. Since then he has been a great source of ideas, and his inputs on research topics are always

incisive. His ability to take a geomorphological phenomenon and shredding the unnecessary complexities, in order to come up with a *toy* model that captures the essence of the phenomenon is inspiring. I look forward to be inspired by his childlike enthusiasm for solving complex geomorphological puzzles.

I would also like to thank my committee member, Prof. James L. Best for his detailed inputs on my dissertation. His suggested corrections have helped improve my dissertation. During the whole process, I have also enjoyed multiple discussions with him about research and possible future avenues of collaboration. In the future, I look forward to borrow from his wealth of knowledge about large rivers and field measurements to expand the work done in the current dissertation.

I would also like to thank all the professors at UIUC, with whom I have taken classes over the years. They have all contributed towards my development as a scientist. In particular I would like to mention Prof. Siva, whose fundamental take on Surface Hydrology showed to me how a relatively complex subject could be taught starting from fundamental principles (and without a text-book); and Prof. Andreas Kloeckner, who made integral equations more accessible and introduced me to world of fast-solvers.

I would like to thank the department of Civil and Environmental Engineering for the Ravi K. Kinra and Kavita Kinra fellowship, which allowed me the time to focus on my dissertation research. I would also like to thank the Blue Waters supercomputing program at UIUC, which accorded me the time on the peta-scale HPC platform; without it the simulations in the dissertation would not have been possible.

I would like to thank all the awesome researchers I have collaborated and interacted with over the years at UIUC. They have all contributed to my evolution as a scientist. The list I will mention next is not definitive, and if I have missed someone please accept my apologies. Some of the people whom I have enjoyed working with are, Dr. Mariano Cantero, Dr. Ryan Jackon, Dr. Xiaofeng Liu, Dr. Tzu-Hao Yeh, Dr. Sumit Sinha, Dr. Talia Tokyay, Dr. Yovanni Catano-Lopera and Dr. Blake Landry.

When coming to a new country, your friends are your family, and some of the friends I have made throughout the years have made me feel at home. My former office mates and class-mates, Viviana and Zhenduo are amazing friends and great human-beings. Three of us started together, and have seen each other evolve in every way. On top of that, they are exceptional scientists with who have helped broaden my knowledge. An amazing friend who made me feel welcome right from the first weekend in US is Tatiana, her enthusiasm for everything in life is infectious, and it also shows up in her scientific work. I would like to thank Michelle and Kia for being friends who have always supported me, and made me feel welcome in US. A person who helped me understand US and enjoy its pop-culture is my friend and former room-mate Nolan. In all my years at the Hydro Lab, I not only came across people with exceptional scientific

abilities, but also people with immense intellectual capabilities, people who could hold an informed discussion about any and every thing from politics to auteur cinema; Charles, Davide, Dimitrios and Juan are a few of that ilk. Others who have positively impacted my life, through their friendship and scientific ideas are Ketan, Santiago, Dongchen, Matt, Li, Zhi, Phong, Nam Jeong, Amir to name a few.

In a new country, we all crave for some familiarity, as it brings us back to our roots. Over the years at UIUC, I have had a few Indian friends, who made me miss India a little less. Anustup da and Manisha di have always looked out for me, providing me with a sense of security, knowing that I can always rely on them if needed. Sudipto, Sayantan, Kapil, Debsunder, Debojoy, Lopa, and Shubhodeep have been my partners in culinary escapades, movies and random *adda*, without which my graduate school experience would have been incomplete.

I would like thank my mother and sister for their continuous support and enthusiasm and love. I would also like to thank my grand mother, grand father and relatives, for their blessings. I would also like to thank my research mentors from India. Prof. Sen (from IIT Kgp), trusted in my abilities when I was a sophomore, and was the first one to guide me to do research. He is also the one who advised me to study fundamental environmental fluid mechanics using CFD for my graduate studies, and I am really thankful to him for it.

Finally, the two people I have dedicated my dissertation to. Ankita, for being the person who understands me the best, for being there through the thick and thin, for being exceptionally efficient and trying to instill some discipline in my life, for all the delicious things you conjure, and off-course those deep soulful eyes I wake up to everyday. My father, for all the sacrifices he made to give me a privileged life, for encouraging my questions about nature, for making me fascinated about mathematics at an early age, for supporting my decision to go to graduate school, for instilling in me a value system that has been with me throughout my life, and last but not the least for teaching me not to give up on life despite struggles and failures.

In this long winded acknowledgement, I am sure to have missed a few people who have made positive impact on my life and research during my graduate school at UIUC. I thank all of you for making my stay at UIUC a memorable one.

# TABLE OF CONTENTS

# CHAPTER 1

# BULLE-EFFECT AND OBJECTIVES OF THIS THESIS

## 1.1 Introduction

A fundamental morphological element present in most fluvial systems is a bifurcation; where a river divides into two different channels, each carrying part of the flow and sediment. Bifurcations are mostly formed naturally, like the dendritic networks in deltas, the in stream bifurcations (followed by confluences) in braided rivers, or the splitting of a large river into two separate streams. Over the years, bifurcations have also been built for various engineering purposes, like river connectivity, flood protection and river diversion. These engineered bifurcations are more commonly referred to as diversions. One characteristic that is typical for a diversion is one of the channels after the bifurcation, continues along the direction of the original channel. The layout of diversions is also similar to asymmetric bifurcations. The lower course of the Rhine River has several examples of both man-made and natural bifurcations. At Pannerdensch Kop, near the border of Germany and the Netherlands, the Rhine River divides into two rivers (see Figure 1.1), the Waal River and the Nederrijn. This is a typical example of a bifurcation. Further downstream the rivers are again connected by artificial channels, in order to improve the transportation and connectivity of the area.

It is the desire to understand the division of flow and sediment between the main and diverted channel in the aforementioned channel network, that led H. Bulle to conduct the first systematic study about the division of bed-load sediment between bifurcating channels at the Technical University of Karlsruhe, Germany [1]. Bulle through his laboratory experiments showed that the sediment discharge distribution tends to favor the lateral channel, even in cases where the opposite trend is exhibited by the water discharge distribution (see Figure 1.2); this phenomenon is also known as the *Bulle-Effect*, as Bulle was the first person to systematically study the phenomena.

Bulle's study initiated a spate of research on alluvial diversions in Europe ([2, 3, 4]) and the United States ([5, 6]) for the next few decades. After the second world-war extensive river-engineering works were orchestrated all over the world, and this propelled the second wave of research on sediment distribution at fluvial diversions [7, 8, 9, 10, 11]. Over the next few decades, there were some

Figure 1.1: Rhine River bifurcates into Wall River and Nederrijn at Pannerdensch Kop, in Netherlands. The arrows show the direction of the flow. The lower Rhine is an example, where both natural and man-made bifurcations exist. (image courtesy: https://beeldbank.rws.nl/).

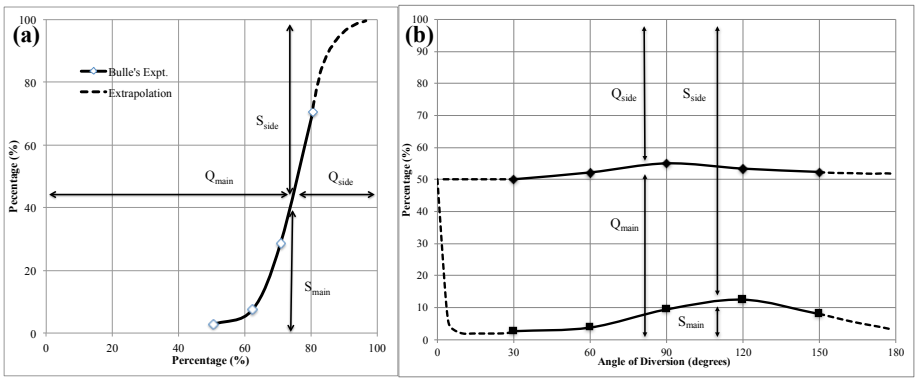


Figure 1.2: Percentage of solid ($S$) and liquid ($Q$) discharges in the main ($Q_{main}$, $S_{main}$) and diverted ($Q_{side}$, $S_{side}$) channels for $Q_{total} = 0.005\ m^3 s^{-1}$ (where $Q_{total} = Q_{main} + Q_{side}$). (a) The data is for a 30-degree diversion, where percentage of the total flow ($Q$) passing through each channel after the diversion is plotted on the x-axis, and the corresponding percentage of bedload has been plotted on the y-axis (b) This data corresponds to experiments with different angles of diversion. Angle of diversion represents the angle between the center-lines of the main and the diverted channel. It is evident from the above plot that sediment discharge ($S_{side}$) entering the diverted channel is disproportionately higher than that remaining in the main channel ($S_{main}$), even in cases where $Q_{main} > Q_{side}$. The solid line represents data from conducted experiments, and dashed line represents expected trends. Data reproduced from Bulle's Experiments [1].

work on fluvial diversions [12, 13, 14]; but the focus of the scientific community primarily shifted towards studying the flow-dynamics and sediment distribution at natural bifurcations [15, 16, 17]. The latest study that explored the phenomenon under movable bed condition was conducted by Herrero in 2013, and the study concluded that observations of Bulle held true even under movable bed condition [18]. This showed that the phenomenon of Bulle-Effect is valid under different conditions.

Interest in fluvial diversions has increased the last decade. Clogging up of diverted channels in different parts of the world (e.g. Canal del Dique on the Magdalena River in Colombia [19]) have rekindled the question of sediment distribution at fluvial diversions. In the context of Unites States, in the last few years there have been concerted efforts to study the viability of diverting flow (and sediment) from the lower Mississippi River to mitigate potential loss of coastal land in Louisiana [20, 21]. Various possible designs and locations of flow diversion structures along the Mississippi River are being evaluated [22, 23] to ascertain the optimal case that would allow maximum amount of sediment to be diverted for a particular water discharge. Studies based on field observations [24], and field-scale numerical simulations [25] have been conducted, in order to figure out the possible quantity and makeup of sediment discharge at different possible diversion locations. And not just in US, channelization, that is creating artificial diversions, has been put forward as a possible solution to the global problem of maintenance of large deltas in light of sea-level rise due to climate-change [26]. The Indian government's plan to interconnect rivers by diverting the flow [27], provides enough real-world motivation to study Bulle-Effect and its implications on river morphodynamics.

The aforementioned real world applications would require buillding diversions, and finding the optimal location and layout for a diversion will be easier if the fundamental mechanism that causes *Bulle-Effect* is well understood. Despite the importance of the phenomenon, to this day a clear mechanistic explanation for *Bulle-Effect* is missing. Better understanding of the mechanism behind Bulle-Effect will not only assist optimal design of diversions, it will also help in the fundamental understanding of the dynamics at asymmetric fluvial bifurcations. This thesis fills the gap in fundamental understanding of the Bulle-Effect and related phenomena, such as secondary flows and vorticity-driven sediment transport. And scope of the thesis goes beyond fluvial diversions, as secondary flows and vorticity-driven sediment/particle transport are not only present in nature, but also systems like grit chambers at water reclamation plants [28, 29] and sediment transport at run of the river dams [30]. In the next section the objectives of this dissertation are elucidated. In summary, this dissertation first unravels the mechanism behind the phenomenon called the Bulle-Effect, and then explores how it impacts the morphodynamics at a diversion.

## 1.2 Objectives of the Dissertation

The aim of this dissertation, is to study in detail the mechanism behind the phenomena called the Bulle-Effect, and then fathom its implications on morphology of a river, especially on the bathymetry of the river bed at a fluvial diversion. The dissertation has three major components:

1) The phenomenon of the Bulle-Effect was studied and analyzed systematically for the first time by Bulle in 1926 [1]. Since then there have been a number of studies, exploring different aspects of the phenomenon. These studies not only span across time, but also across different languages. For example, Bulle's report was in German, Cristani's experiments were published by Benini in Italian [3]. This might have contributed to the lack of a study, despite the importance and novelty of the phenomenon, that brings together the publicly available experimental data from disparate sources to analyze it. As part of this dissertation, a thorough literature review was performed, and available experimental data on *Bulle-Effect* was analyzed. The findings from the literature review and analysis of the data are discussed in Chapter 2 of the thesis.

2) The next objective of the thesis is to unravel the mechanism behind the Bulle-Effect. For this, high-resolution numerical simulations were conducted to simulate the hydrodynamics and sediment transport at idealized diversions, with configuration similar to Bulle's experiments. Simulations were conducted for different Reynolds numebrs, ranging from bulk Reynolds ($Re_b$) number of 10 to 25,000. The $Re_b = 25,000$ cases have a Reynolds number the same as that of Bulle's experiments. The simulations at Reynolds number 7000 or less were fully resolved, thus can be referred to as Direct Numerical Simulations (DNS). Simulations with $Re_b \geq 20,000$ have resolution good enough to be high-resolution Large Eddy Simulations (LES). The simulations have been conducted using the open-source Spectral Element based highier-order incompressible Navier-Stokes solver Nek5000 [31]. The sediment was modeled as Lagrangian Point Particles, and a novel semi-implicit Lagrangian particle tracking algorithm was developed and implemented in Nek5000. Details of the developed algorithm are discussed in Chapter 3. In order to get an initial insight into the mechanism of the phenomenon, LES of a 90-degree diversion was conducted at $Re_b = 20,000$ with particles big enough that they traveled as bed-load. The results from the aforementioned LES simulation provide the first hint towards the primary mechanism behind Bulle-Effect, which can be attributed to the proclivity of the flow near the bottom of the channel to move into the lateral-channel, compared to the flow near the top, majority of which continues in the main-channel. The findings from the aforementioned simulation are discussed in Chapter 4. In the next two chapters the phenomenon is further examined under laminar and turbulent flow conditions, for a range of $Re_b$ and particle sizes. The major finding from

these simulations was that the phenomenon of Bulle-Effect is not only valid for sediment traveling as bedload, but even for suspended sediment traveling within 20-30 percent of the depth from the bottom.

Simulations conducted in this portion of the study were at an unprecedented scale, and required up to ∼240 million computational points. These simulations were computationally very expensive, thus they were run on the peta-scale supercomputer Blue Waters at National Center for Supercomputing Applications. To our knowledge, there are no published studies that have tackled the problem of fluvial diversions using high-resolution LES for the flow and Lagrangian particles for modeling sediment. This portion of the dissertation has not only helped in unraveling the fundamental mechanism of the Bulle-Effect, but it has also pushed the limits at which high-resolution LES is used for studying probelms in river mechanics. This part of the dissertation also provide insights that will help improve Reynolds Averaged Navier-Stokes (RANS) based numerical models of diversions/bifurcations.

3) In the next part of the dissertation, the phenomenon for Bulle-Effect was studied using RANS based hydrodynamics model. For this, the complete set of Bulle's experiments were simulated using the free-surface hydrodynamic solver Telemac-3d, along with SISYSPHE for sediment transport [32]. The major motivation to conduct this study was to ascertain that to what extent can a RANS based 3D model can predict the complex phenomenon of Bulle-Effect. This is important in light of the fact that at this point of time, conducting LES of field-scale diversions is impossible. The RANS based simulations were found to capture the phenomenon satisfactorily (within 10 percent error), but at substantially less computational cost. The details of the findings have been discussed in Chapter . Next this model was used to run simulations with an erodible bed. Using an erodible bed in the model allowed evolution of the bottom, thus providing an insight on how Bulle-Effect might impact the morphodynamics at a diversion. This in turn also provided an insight into how the phenomenon is itself impacted by change in morphology at the diversion. The details of the analysis has been discussed in the next Chapter. Even though the above analysis were done at the scale of an experimental diversion, it provides insights which will be valid for actual field cases.

# CHAPTER 2

# *BULLE-EFFECT*: THE NON-LINEAR DISTRIBUTION OF NEAR-BED SEDIMENT AT FLUVIAL DIVERSIONS


## Authors

Som Dutta and Marcelo H. Garcia


## 2.1 Introduction

A morphological element present in most fluvial systems is a bifurcation; where a river divides into two different channels, each carrying part of the flow and sediment. Diversions are a special class of asymmetric bifurcations in which one of the channels after bifurcation continues along the original channel (see Figure 2.1). Diversions are often engineered for various purposes, ranging from irrigation to navigation. A problem many of the these diversion canals have is clogging up with sediment, a prime example being Canal del Dique on the Magdalena River in Colombia, which has had to be dredged numerous times in its 500 year history [19]. Due to the problem of clogging of diversions, flow dynamics and sediment transport at a diversion have been an area of interest for river-engineers. The question of sediment distribution at a diversion has also been studied by researchers interested in morphodynamic evolution of bifurcations (especially asymmetric bifurcations) [17]. Thus a better understanding of the process of sediment distribution at a diversion, not only has engineering applications but has the potential to improve our fundamental understanding of fluvial bifurcation dynamics.

In the last few years there has been a renewed interest in the area of hydrodynamics and sediment transport at diversions. This interest has been propelled both from the application perspective, and fundamental geomorphological questions. On the engineering application side, diversions have gained importance after they have been put forth as a solution to reclaim deltas that are at risk of getting submerged due to rising sea-level rise, deltaic subsidence and other processes [33, 26]. One of the prime example of the above, already on the drawing board is the planned diversions on the lower Mississippi River, which is expected to help reclaim at least upto 25 percent of the delta [34, 20]. On

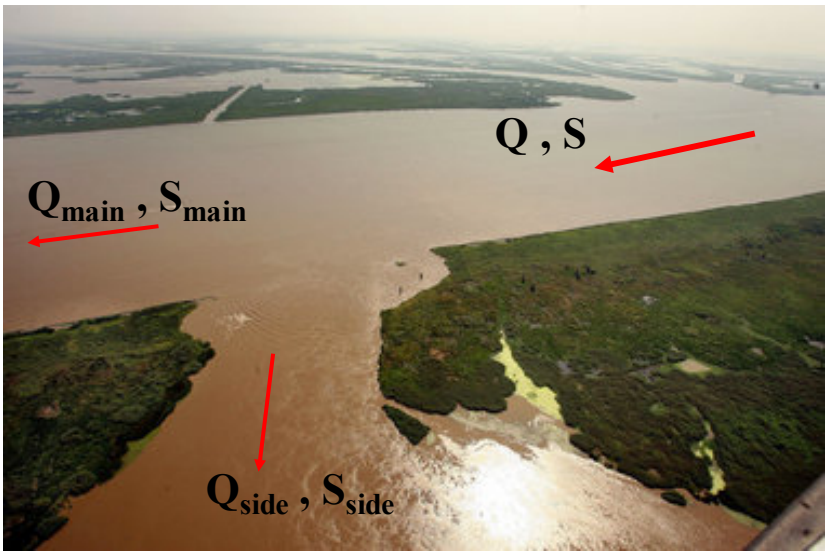


Figure 2.1: The photograph of Mississippi River and its West Bay diversion, this illustrates a diversion and its specific characteristics. The main channel has water and sediment discharge of $Q$ and $S$, which then gets divided into $Q_{main}, S_{main}$ and $Q_{side}, S_{side}$. (image courtesy: https://media.nola.com/).

that cue, concerted studies are being conducted to find the optimal location and layout of the diversions, that would allow efficient diversion of sediment while maintaining navigability of the Mississippi River [23]. A better understanding of the hydrodynamics and sediment transport at diversions, will definitely help in better design of the diversions. One of the first studies that systematically explored the dynamics of sediment-transport (specifically bed load) at a diversion was conducted by Bulle in 1926, at the Technical University of Karlsruhe, Germany [1].

Bulle studied the effect of water discharge ratio, and diversion angle on the distribution of bedload between the main and lateral channel. Even though Rehbock in 1926 [35], and Thoma in 1923 [36] through their experiments in Germany were the first ones to observe the phenomenon where the bedload entering the lateral-channel ($S_{side}$) is disproportionately higher than the discharge of water ($Q_{side}$); Bulle was the first to conduct an extensive set of experiments that showed that the phenomenon was valid for different diversion angles and across a wide-range of flow split (see fig. 2.2). This non-linear phenomenon is often referred to as the *Bulle-Effect*.

Since the seminal work of Bulle, over the next few decades experimental studies on fluvial diversions corroborated Bulle's findings and analyzed other parameters that might effect the phenomenon, e.g. particle size, Froude and Reynolds number of the flow, etc. Some of the notable studies were by Cristani (published by Benini) in Italy [3], Vogel [5], Linder [6] and Dancy [37] in United States, Riad in the Netherlands [9], Eicke in Germany [38], and more recently Herrera in Spain [39] among others. Even though all the studies after Bulle

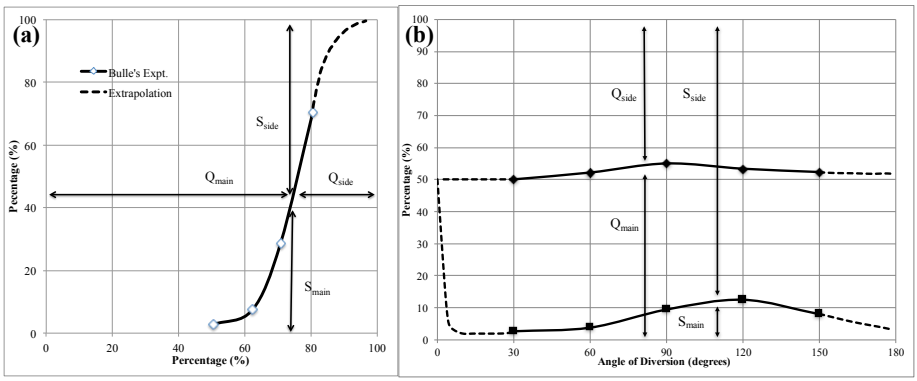


Figure 2.2: Percentage of solid ($S$) and liquid ($Q$) discharges in the main ($Q_{main}$, $S_{main}$) and diverted ($Q_{side}$, $S_{side}$) channels for $Q_{total} = 0.005\ m^3 s^{-1}$ (where $Q_{total} = Q_{main} + Q_{side}$). (a) The data is for a 30-degree diversion, where percentage of the total flow ($Q$) passing through each channel after the diversion is plotted on the x-axis, and the corresponding percentage of bedload has been plotted on the y-axis (b) This data corresponds to experiments with different angles of diversion. Angle of diversion represents the angle between the center-lines of the main and the diverted channel. It is evident from the above plot that sediment discharge ($S_{side}$) entering the diverted channel is disproportionately higher than that remaining in the main channel ($S_{main}$), even in cases where $Q_{main} > Q_{side}$. The solid line represents data from conducted experiments, and dashed line represents expected trends. Data reproduced from Bulle's Experiments [1].

provided further evidence about the phenomenon, none until the work of Dutta et al. [40] provided a clear hint about the mechanism behind the phenomenon.

Due to the fundamental nature of the phenomenon of Bulle-Effect, it also has implications on morphological evolution of fluvial bifurcations. Especially, bifurcations that have a layout similar to that of a diversion. Some cases where the above is applicable are chute cutoffs at meander-bends [41] and asymmetric bifurcations in deltas [17]. Some recent studies on bifurcations that have explored different aspects of flow dynamics at bifurcations under different conditions are; experimental studies on symmetric bifurcations to understand the secondary flow structure [42, 43], and numerical studies to understand the effect of backwater on bifurcation stability [44]. Even though the general flow structure at a diversion differs from a symmetric bifurcations, in both the cases secondary flow circulations play a major role in the transport of sediment. Thus, the current study will also contribute towards further insight into sediment transport dynamics at all kinds of bifurcations. This will further the understanding about stability of distributary networks and the accompanying bifurcations, like the ones found in deltas [45].

Despite the wide ranging implications of the phenomenon and renewed interest in diversion dynamics, there has not been an analysis that brings together the experimental findings spread across almost a century. It is necessary to take a holistic looks at the available literature, as it can provide information

about the gaps in our knowledge about the phenomenon, and hints towards the avenues that need to be explored. The current study tries to fulfill that requirement, by reviewing and analyzing the major experimental studies on Bulle-Effect. In the next section, Bulle's seminal work has been discussed in some details. Next, then the major findings of the subsequent experimental studies have been summarized, along with an analysis of all the publicly available data on the phenomenon. The study closes with a discussion about the possible mechanism behind the phenomenon, and its implications.

## 2.2 The seminal work of Bulle, 1926

As mentioned before, the first systematic and extensive study of sediment discharge at fluvial diversions was done by Bulle in 1926 [1], that is why the phenomenon of disproportionate distribution of bed-load sediment between the lateral-channel and the main channel, at a fluvial diversion is often referred to at as the Bulle-Effect. Bulle's study was built upon initial work on fluvial diversions done by Thoma in 1923 [36], at the laboratory for Hydraulics at Munich, and by Rehbock in 1926 at the River Engineering Laboratory of Karlsruhe [35]. The studies were motivated by hydraulics and water intake structure being built on at the Middle Isar River in Oberfohring, Germany. Both Thoma and Rehbock found that that even when the water entering the the lateral channel was about 50 percent of the total-flow, the percentage of sediment entering the lateral was disproportionately higher. Specifically, Thoma conducted experiments on a 30 degree and 90 degree diversion, using wet sawdust, sand and coal to model sediment; and found 85. 2 percent and 92.1 percent sediment going into the lateral channels. Rehbock also suggested that the phenomenon was caused due to the flow near the bed preferentially entering the lateral-channel, and attributed it to the formation of *helicoidal* currents in the flow.

Bulle used a 20 cm wide rectangular flume for his experiments, with a bottom slope of 0.003 for the main and lateral channel. The length of the lateral-channel and main-channel after diversion was kept equal. Bulle used adjustable weirs as tail-gates at the downstream end of both canals, this allowed him to get different flow splits between the two canals. The experiments Bulle performed can be divided into two broad categories, first in which he varied the diversion angle (between 30 to 150 degrees) and kept crest height at the weirs equal. This provided similar hydraulics forcing (pressure difference) across the two channels, with variance in flow entering the lateral-channel occurring due to differences in diversion angle. The other set in which the diversion angle was kept constant at 30-degree, the flow split between the two channels was controlled by the weir at the end of the main-channel. Bulle conducted experiments with both rigid (non-erodible) bead and erodible sand bed, but quantified measurement of bedload distribution was only reported for the rigid bed experiments. For

all the experiments Bulle reported, the total flow in the main-channel ($Q$) was kept constant at 0.005 $m^3 s^{-1}$.

Bulle first conducted experiments without any sediment, and varying the diversion angle from 30-degrees to 150-degrees. In all the cases he observed that the flow separated from the left-wall of the lateral-channel (see fig. 2.3), and the size of the separation zone depended on the angle of diversion. He also observed the flow in the separation zone to be recirculating, and additionally he found that the size (width) of the flow-separation was smaller near the bottom of the channel, when compared to the surface. For diversion angle of 30-degree and $Q = 0.005 m^3 s^{-1}$, he found that the flow split equally between the two-channel ($Q_{main} : Q_{side} = 1$). For diversion angles greater than 30-degree, this ratio found to be slightly greater than 1.

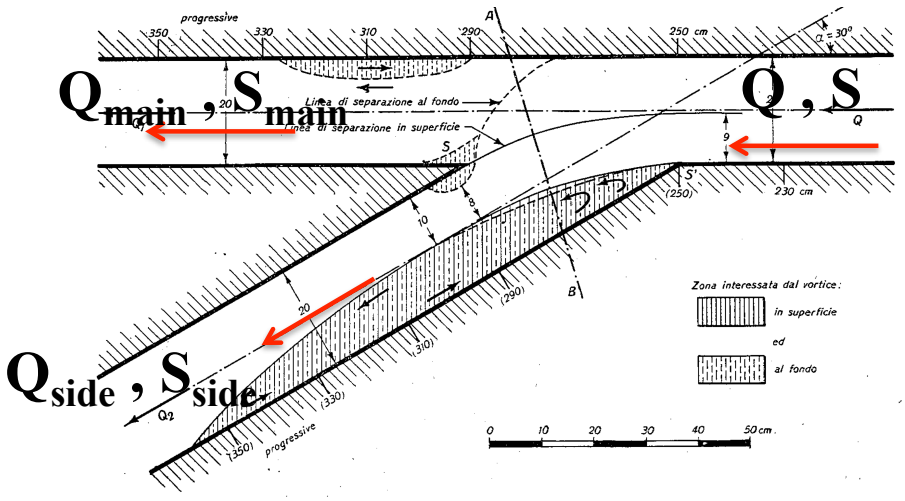


Figure 2.3: The figure shows a diversion with an angle of 30 degree. The figure has been reproduced from [1], and it shows the two recirculation zones observed by Bulle in his experiment. The arrows indicates the flow direction.

Like Rehbock, Bulle also observed that majority of the flow near the channel bottom entered the lateral-channel, which then resulted in relatively smaller flow re-circulation/separation zone in the main-channel, jsut after the diversion. Unlike the separation-zone in the lateral-channel, the width of the one in the main-channel decreased near the surface. The width of the separation-zone in the lateral-channel was found to increase with increase in diversion-angle, sometimes taking upto half of the channel width. An interesting aspect of the flow-split at the diversion is the fact that the case when the smallest percentage of total flow enters the lateral-channel is the 90-degree diversion. One might expect that compared to 90-degree, the cases 120-degree or 150-degree might have even less amount of flow entering the lateral-channel, due the pressure gradient that the flow needs overcome in-order to move into the lateral-channel. Though another factor tilts the balance, and that is width of the entrance of the lateral-channel. Two experiments were also conducted with rounded corners of

the lateral-channel. The rounding of the edge was found to decrease the size (width) of the eddy in the lateral-channel, and slight increase in water entering the lateral-channel (for diversion-angle > 30-degree).

Next the experiments were conducted with sediment, which were of the size smaller than 0.0012 $m$, and density equal to 1500 $kgm^{-3}$. For the prevailing experimental conditions, the sediment was found to move only as bedload. First the effect of diversion angle ($\alpha$) on the bed load distribution at the diversion, for a constant $Q_{total} = 0.005\ m^3s^{-1}$ was studied (Figure 2.2b). The experiments clearly showed the proclivity of the bed load to enter the lateral channel, and the observations agreed with the conclusions drawn by Thoma and Rehbock [36, 35]. Bulle attributed the aforementioned phenomenon to his observation that majority of the flow near the bottom of the channel, entered the lateral channel. Next, Bulle extended the analysis to ascertain the effect of different ratios of flow discharge $Q_{main}/Q_{side}$ on the bedload distribution at a 30-degree fluvial diversion, for a constant $Q_{total} = 0.005m^3s^{-1}$ (see fig. 2.2a). It can be observed that increase in flow discharge in the main channel, results in increase in bedload continuing into the main-channel. But this increase is not linear, hence the phenomenon of *Bulle-Effect* may be called a non-linear phenomenon.

The extent of non-linearity of the phenomenon can be ascertained through a small exercise. The relationship between the ratio of bedload discharge moving into the two channels $S_{side}/S_{main}$, and the ratio of the corresponding water discharge $Q_{side}/Q_{main}$ can be defined using the equation. The relationship is similar to the one often used for bifurcations [15]:

$$\frac{S_{side}}{S_{main}} = a\left(\frac{Q_{side}}{Q_{main}}\right)^b \tag{2.1}$$

where $a$ and $b$ are constants. If the distribution of bedload sediment between the two channels were linear, then $b = 1$. Bulle's experimental data for diversion angle of 30-degree and different $\frac{Q_{side}}{Q_{main}}$ is plotted in fig. 2.4. Two different fits were tried on the data, first a liner fit that gives the relationship $\frac{S_{side}}{S_{main}} = 28.582\left(\frac{Q_{side}}{Q_{main}}\right)$ with a $R^2 = 0.75$. Next a non-linear (power-law) fit was tried, and it gave the relationship $\frac{S_{side}}{S_{main}} = 45.104\left(\frac{Q_{side}}{Q_{main}}\right)^{3.193}$, with $R^2 = 0.985$. This clearly shows that the phenomenon is highly non-linear.

Bulle also conducted a few experiments to ascertain the effect of decrease in width of the lateral-channel and lateral-channel corner rounding. For the experiments with lateral-channel of width 0.1 $m$ (compared to 0.2 $m$ of the main-channel). Two experiments were conducted, one with $Q_{main}/Q_{side} = 2.23$ and the other with $Q_{main}/Q_{side} = 1$. The case where only 31 percent of the flow enters the lateral-channel, about three times more sediment was found to enter the lateral-channel ($S_{side} \sim 76\%$). When the flow was equally split between the two channels, the reduction in lateral-channel width was not found to affect $S_{side}/S_{main}$ too much, as 89 percent of the total bedload went into the

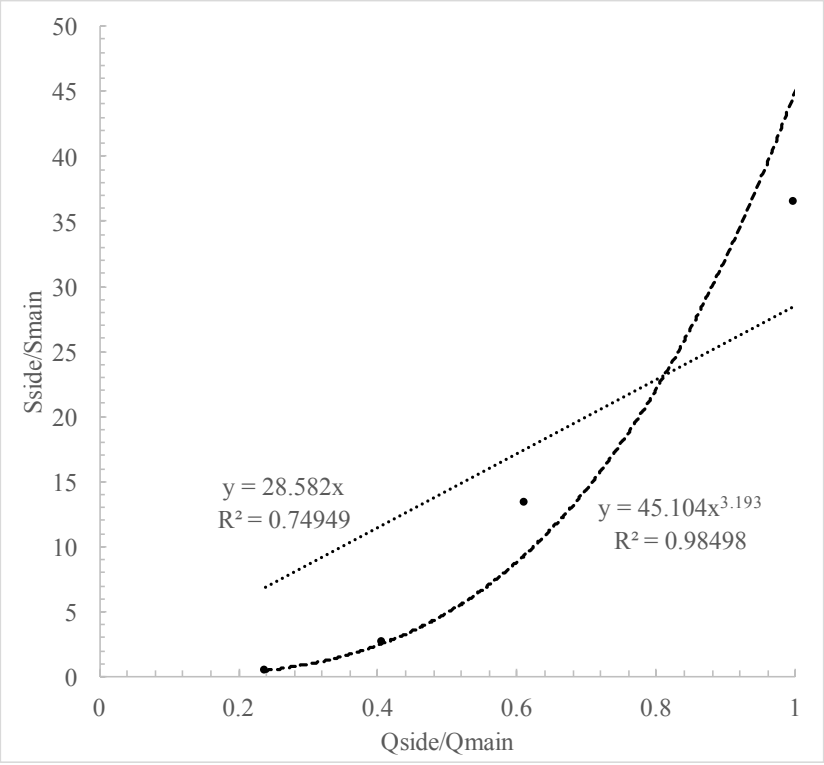


Figure 2.4: Effect of different ratios of $Q_{side}/Q_{main}$ on the bed load distribution ($S_{side}/S_{main}$) at a 30 degree fluvial diversion, for a constant $Q_{total} = 0.005m^3s^{-1}$. Two curves were fitted to the data, one linear and the other a power-law (non-linear). The $R^2$ values for the two fits clearly shows that the phenomenon is highly non-linear.

lateral-channel. For the 90-degree cases with equal channel width $S_{side} \sim 90\%$. Bulle also conducted experiments for diversion angles of 30, 60 and 90 degrees, with the corner at the upstream entrance edge being rounded. The amount of bedload entering the lateral-channel was found to decrease slightly, but the relative change from the sharp-corner was not significant, especially for 30-degree and 90-degree. For the 60-degree case the reduction in bedload entering the lateral-channel was slightly more significant. So it can be concluded based on Bulle's experiments that rounding of the corners does not have a significant effect on the phenomenon of Bulle-Effect.

## 2.3 Subsequent Experiments by other researchers

After the seminal work of Bulle in 1926, interest in sediment distribution at diversions picked up significantly, with major studies being conducted in United States of America (USA) and Europe. Some of the major ones have been discussed below.

### 2.3.1 Colonel Vogel and the US Waterways Experimentation Station

Colonel H.D. Vogel, the then director of the US Waterways Experimentation Station (USWES) at Vicksburg, Mississippi, reported the results of the experiments done on a forked channel [5]. One of the first set of experiments were conducted on a 61 cm wide flume, with a branch at a diversion angle of 30 degree. In the experiments $Q_{total}$ was held constant, while varying the percentage diverted to the lateral channel. In the experiments two kinds of sediment were used. Very fine sediment called loess that was primarily carried in suspension, and Red River sand, which was primarily transported as bed load. Vogel's results showed the same trend as that of Bulle's. Vogel performed a second set of experiments with a semicircular flume, which had the main channel radius of 61 cm and diverted channel radius of 30.5 cm. The diversion angle was 30 degrees, and two different sizes of sand was used. The results showed the proclivity of the bedload to move into the lateral branch, though the percentage of bedload entering the lateral channel was less than that observed by Bulle in his experiments. Vogel's experiments showed that depending on the size of the sediment, sediment that traveled as bedload tended to move into the lateral-channel, whereas sediment moving in suspension divided between the main and lateral-channel according to the ratio of water entering the two channels.

Around the same time as Vogel, Sokolow came up with a relationship between the diversion angle, the depth of the flow in the main channel prior to the diversion and ratio of the specific discharges in the main and diverted channel [2]. The main limitation of the study was that he did not consider sediment in

the flow, which is an important factor while deciding the diversion angle of a lateral channel. Linder in his paper reported experiments on fluvial diversions that were being conducted at USWES, Vicksburg [6]. The experiments used a model of a Mississippi bend for the main channel, and diversions with three different diversion angles were placed at different locations on the bend (see Figure 2.5). The percentage of bed load diverted during the experiments was similar to the values found by Bulle. The results were surprising because the flow in the main channel was relatively much larger than the flow in the lateral channel, so according to the findings of Bulle the amount of bed load in the diversion channel must have been smaller. Linder attributed the slight anomaly to the location of the diverted channels; the diverted channels were placed on the convex bank of the bend, which placed them in the most favorable position to receive maximum amount of bed load. He further suggested that if the diversion was placed on the concave bank, the bed load being diverted would have been much lower. To our knowledge the reported experiments were the first one in which, a model of an actual river was used to study fluvial diversions. On the same topic, Brink [46] conducted an experimental and numerical study to find the optimal location for a lateral intake on the outer bank of a river bend. He found a relationship between the optimal location of the intake, and the total bend angle and the ratio between the radius of curvature and the channel width. Though the analysis was only based on the velocity field at the bend, and not the possible sediment discharge.

Researchers like Thoma, Bulle, and Linder, had attributed the Bulle-Effect to the tendency of the near bed currents to enter the lateral channel, while the near surface currents followed the main channel. Tison's experiments verified this claim [7]. Tison also conducted experiments on a curved main channel, and he noticed that the maximum deviation of sediment towards the convex side occurred at a short distance downstream of the apex of the bend. Confirming the conclusions made by Linder, when an experiment was carried out with the lateral channel at the concave side, no bed load was found to divert into the lateral channel. It needs to be pointed out that even-though the mechanism that was causing this phenomenon was known, but the exact reason why the flow near the bottom tended to enter the lateral-channel was not clear.

### 2.3.2 Dancy 1947

Dancy [37] explored the effect of sediment particle size on the sediment distribution at a 30 degree fluvial diversion (fig. 2.6). The experiments revealed that as size of the sediment particle reduces, the percentage of sediment entering the lateral channel also reduced. For large particle sizes ($D_{50} > 1.43mm$), Dancy found that disproportionate amount of sediment entered the lateral-channel. This was because most of the sediment in that sediment size range traveled as bed-load or near the bed. For $D_{50} = 0.34 \sim 0.17mm$, the amount of sediment

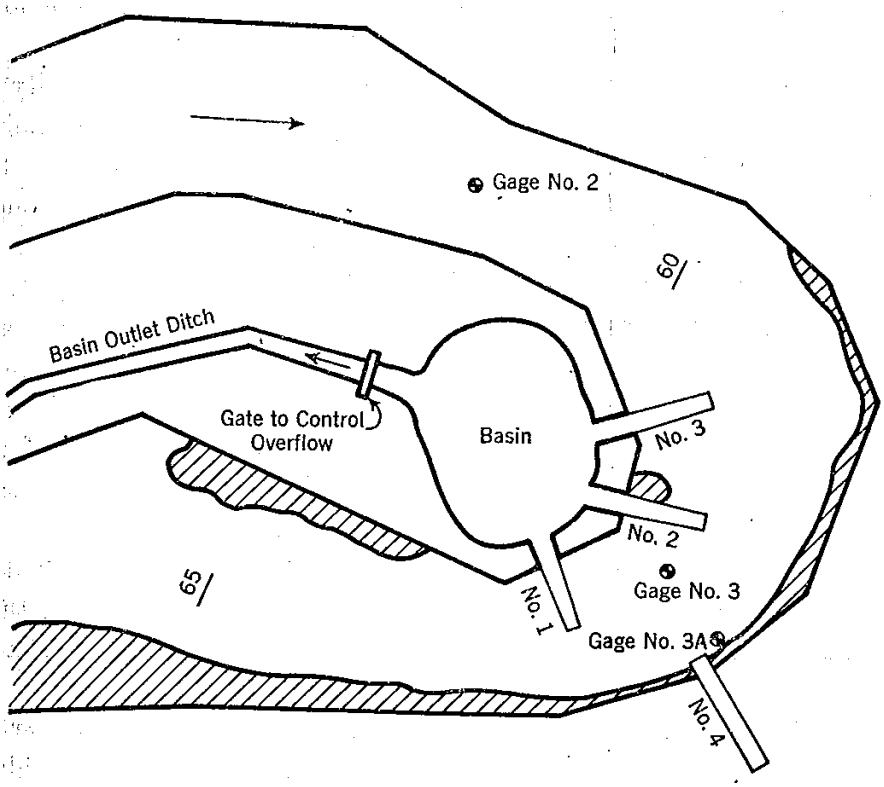


Figure 2.5: The experiments used a model of a Mississippi bend for the main channel, and diversions with three different diversion angle were placed at different locations on the bend. Figure reproduced from Linder [6].

entering the lateral-channel varies linearly with amount of water entering the lateral-channel. This can be attributed to the fact that sediment in that particular range of sizes, is primarily transported as suspended load. Interestingly, sediment size $D_{50} = 0.11mm$ can be seen to have a slight tendency to move into the main-channel. This may be due to the sediment's tendency to stay in the upper portion of the water-column.

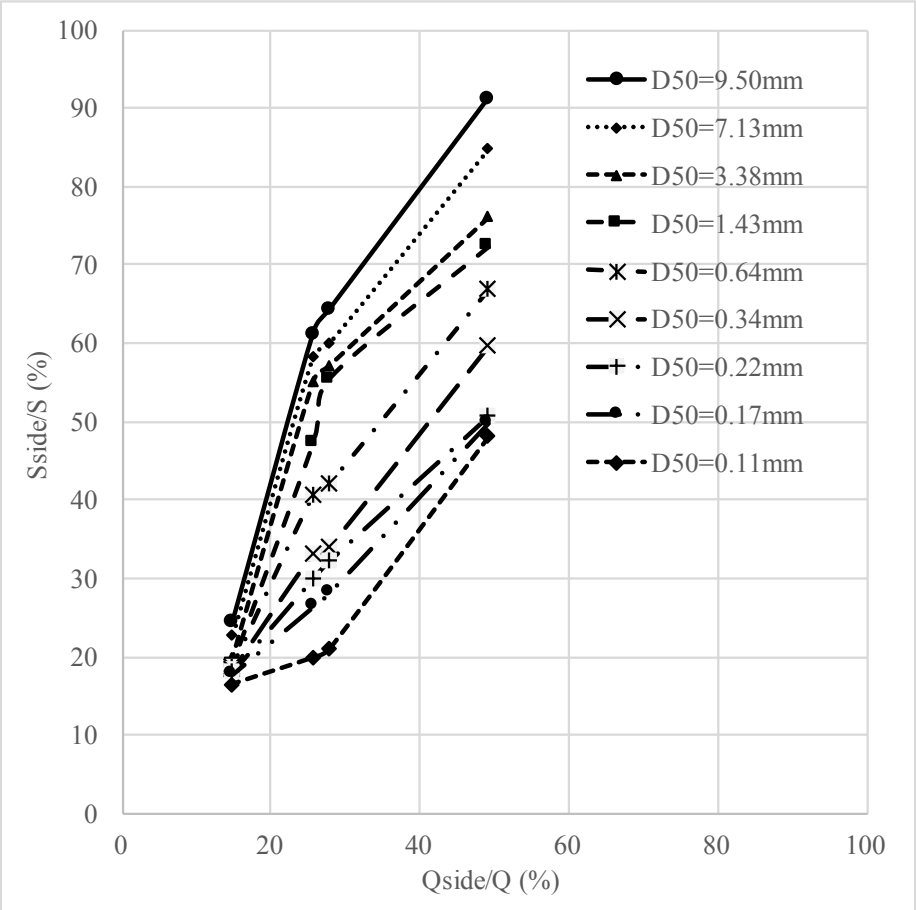


Figure 2.6: Effect of different sediment sizes on ratio of sediment entering the lateral-channel $S_{side}/S$. Sediment with $D_{50} > 0.64mm$ primarily moves into the lateral-channel, whereas sediment with $D_{50} < 0.34mm$ was distributed between the two-channels according to the split in water discharge. Data reproduced from Dancy's Experiments [37].

### 2.3.3 Cristani-Benini 1952

Benini in 1952 published an article summarizing the finding in the subject in the last 25 years, along with results from experiments done by Cristani at the Hydraulics laboratory of Padua in 1944 [3]. Through his experiments, he studied the effect of $Q_{total}$, flow partitioning, lateral channel width, main channel water depth and sediment size, on a $26^o45^{'}$ fluvial diversion. The experimental results

(see Figure 2.7) confirmed the trend shown by Bulle's experiment in Figure 2.2, though for cases with higher value of main channel flow depth were found to have a linear relationship between percentage of flow and bed load entering the lateral diversion. Apart from matching with Bulle's findings, Cristani's experiments also confirmed the trend that was just suggested based on extrapolation in Figure 2.2. It is interesting that Cristan's experiment showed almost exact trends to that of Bulle's, despite the diversion angle being slightly different, and the cross-section of the experimental channels trapezoidal for Cristani and rectangular for Bulle. This points towards a mechanism that is independent of small differences in diversion-angles and cross-section area, and will be explored in this proposed thesis.

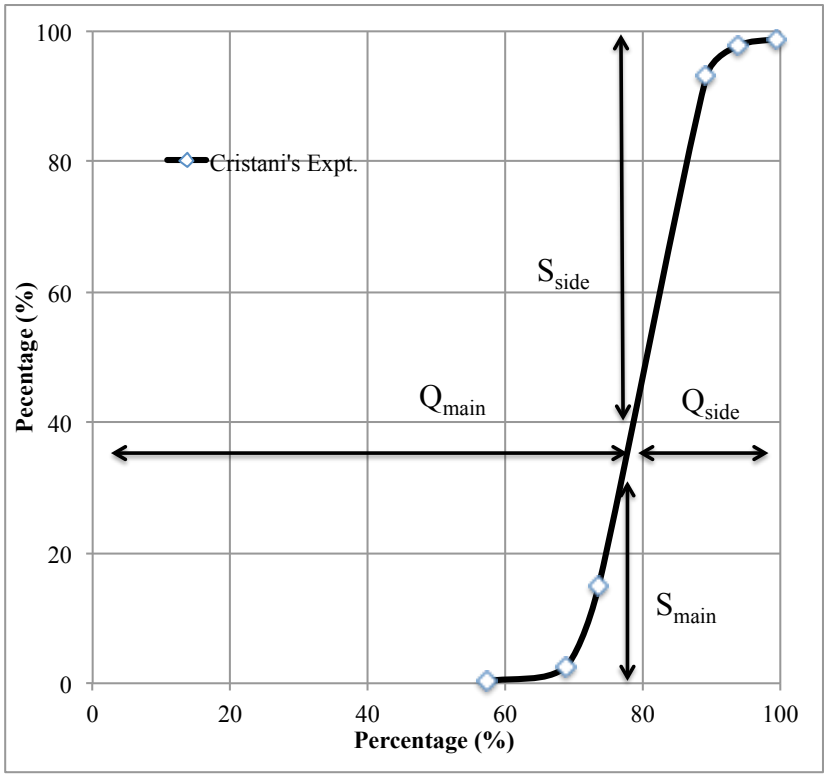


Figure 2.7: Effect of different ratios of $Q_{main}/Q_{side}$ on the bed load distribution at a $26^o45^{'}$ fluvial diversion, for a constant $Q_{total} = 0.0234m^3s^{-1}$. It can be observed that by increasing the discharge in the main channel while decreasing it in the lateral branch, more material could be made to move down the straight channel. Data reproduced from Cristani's Experiments [3].

### 2.3.4 Eicke 1958

Eicke conducted experiments on a 31-degree diversion, with the experimental model of length 17-18 m, and bottom slope of 1:600 [38]. Unlike previous ex-

periment, Eicke used a layer of sand to line up the bottom of the flume. This led to formation of a scour hole below the high-flow zone in the lateral-channel. The movable bed layer had a grain size of 0.1 to 3 $mm$, with a median of 0.7 $mm$. Eicke observed that once the bed-layer had stabilized, 25-30 percent of the total flow and only 15 percent of the bedload entered the lateral-channel. These percentage rose to 40-50 when the width of the main-channel was decreased. The Eicke compared his experimental results with those of Bulle and Cristani-Benini (fig. 2.8).

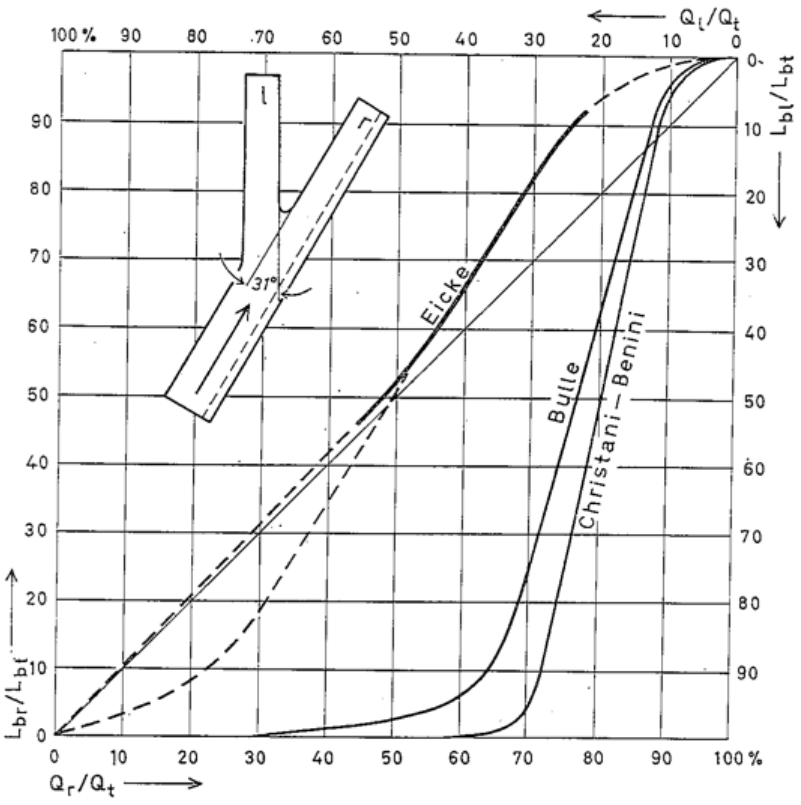


Figure 2.8: The figure compares the experimental results of Eicke with that of Bulle's [1] and Cristani-Bennini [3]. $L_{br}$ represents the sediment load entering the main-channel, and $L_{bl}$ the load entering the lateral-channel, where $L_{bt} = L_{bl} + L_{br}$. Figure reproduced from Eicke [38].

It is clear from the above figure that Eicke's observations differed from that of previous researchers like Bulle, Cristan-Benini and Dancy. This may be attributed to the fact that the unlike the previous experiments, in Eicke's experiments the lateral-channel was longer than the main-channel. This may decrease the transport capacity of the channel, thus reducing its ability to pass sediment. The other contributing factor might be the size of the sediment. Bulle and Cristani-Benini used particles in the size range $0.66 - 1.2mm$, which made the particles travel as bed-load. Whereas, Eicke used sediment with median size of 0.7 $mm$, with a relatively higher discharge. This in all probability made

some of the sediment move as suspended load in Eicke's experiemts. As the Bulle-Effect is stronger for sediment that move as bedload, sediment traveling primarily in suspension tend to continue into the main-channel.

### 2.3.5 Theoretical Analysis by Ismail, Riad and Rocha

Ismail approached the problem of fluvial diversions from a very mechanistic perspective, thus he divided the parameters into 3 groups of non-dimensional parameters [8]. First group was those related to shape of the channels; straightness or curvature of both the channels were represented using curvature to width ratio (i.e $\frac{r}{W}$), relative width ratio of the branches ($\frac{W_{side}}{W_{main}}$) and the diversion angle ($\alpha$). Second group were those related to the flow of water; Reynolds number ($Re$), Froude's number ($Fr$) and ratio of the mean flow velocity in the main and diverted channel ($\frac{V_{side}}{V_{main}}$). Third group consists of parameters which represent the sediment transport properties; sediment concentration at the bed ($C_o$), relative roughness due to the sediment $\frac{d}{D}$ (where $d$ is the sediment grain size and $D$ is the depth of the flow), ratio of mean flow velocity and the mean sediment fall velocity ($\frac{V}{V_s}$), the geometric standard deviation of sediment fall velocity from its mean ($V_s\sigma$), and $\frac{V_sT}{a}$, where $T$ represents the duration of the test and $a$ is a certain length representing the field of the test. The total amount of sediment going in the lateral channel was then defined as a function of all the above mentioned parameters

$$S_{side} = \left( \frac{r}{W}, \frac{W_{side}}{W_{main}}, \alpha, Re, Fr, \frac{V_{side}}{V_{main}}, C_o, \frac{d}{D}, \frac{V}{V_s}, V_s\sigma, \frac{V_sT}{a} \right) \tag{2.2}$$

By conducting laboratory experiments, Ismail checked the sensitivity of different parameters in the above equation. He concluded that $\frac{V_{side}}{V_{main}}$ was the most important parameter which governed the quantity of bed load sediment entering the lateral channel. This finding was akin to that of Bulle's and Cristani's (see figures 2.2 and 2.7), as higher lateral channel to main channel water discharge ratio was found to transfer disproportionately higher bed load into the lateral channel. Ismail attributed the dependence of Bulle-Effect on $\frac{V_{side}}{V_{main}}$, by directly correlating strength of the spiral motion that sweeps bed load into the lateral channel, to $\frac{V_{side}}{V_{main}}$. In the proposed dissertation research, one of the primary goals is to conclusively unravel the mechanism which correlates the ratio of strength of the flows in the two channels, with diverted bed load.

In line with the mechanistic approach shown by Ismail, Riad [9] used dimensional analysis to come up with the most generic list of dimensionless parameters that might effect the bed load distribution at a fluvial diversion:

$$\frac{s_{side}}{s_{main}} = \left( \frac{q_{side}}{q_{main}}, \frac{W_{side}}{W}, \frac{W_{main}}{W}, \alpha, Re, Fr, \frac{r_i}{W_{side}}, \frac{r_o}{W_{side}}, \frac{\Delta D}{D}, \frac{d}{D}, \frac{\sigma}{D}, R \right) \tag{2.3}$$

In the above relation $s_{side}$ and $s_{main}$ are volumetric rate of sediment entry per unit width for the lateral channel and the main channel after the diversion. $R = \frac{\rho_s - \rho_w}{\rho_w}$, $Re$ and $Fr$ is the Reynolds number of the flow in any of the channels. $q_{side}$ and $q_{main}$ is the specific discharge of water in the lateral channel and the main channel. $W$, $W_{side}$, and $W_{main}$ is the width of original, lateral and the main channel; for many of the laboratory experiments on fluvial diversions (like [1]), all the three are equal. $D$ is the depth of the flow in the original channel before the diversion and $\Delta D$ is the difference in the bottom level between the original and the lateral channel. $d$ is the mean sediment diameter and $\sigma$ is the standard deviation of the sediment distribution. $r_i$ and $r_o$ are the inside and the outside radius of curvature of the main channel, for the case when the original/main channel is curved. Riad in his dissertation also comes up with a simple relationship between $\frac{s_{side}}{s_{main}}$ and $\frac{q_{side}}{q_{main}}$

$$\frac{s_{side}}{s_{main}} = \left(\frac{q_{side}}{q_{main}}\right)^{2\beta} \tag{2.4}$$

The above relationship is the same as the one Wang etal. [15] mention in their work on river bifurcations. If equations 2.3 and 2.4 are compared, the parameter $\beta$ in equation 2.4 is expected to take into account all the parameters except $\frac{q_{side}}{q_{main}}$. Riad then conducted experiments on a 45 degree diversion with rectangular channels, and used the data to do sensitivity study on a simplified version of equation 2.3

$$\frac{s_{side}}{s_{main}} = \left(\frac{q_{side}}{q_{main}}, Re, Fr, \frac{d}{D}\right) \tag{2.5}$$

For the conducted experiments, the ratio of sediment diverted into the lateral channel was found to depend primarily on $\frac{q_{side}}{q_{main}}$, with higher $\frac{q_{side}}{q_{main}}$ resulting in higher $\frac{s_{side}}{s_{main}}$. This agrees with observations made by Bulle [1], Benini [3] and Ismail [8]. Definite conclusions about relationship between $\frac{s_{side}}{s_{main}}$ and, $Re$ and $Fr$ of the flow could not be made, due to limited range of $Re$ and $Fr$ in the experiments. Though $\frac{s_{side}}{s_{main}}$ was found to depend on the bed roughness ($\frac{d}{D}$).

Similar analysis was done by Rocha [10]. Rocha put forward the relationship

$$\frac{s_{side}}{s} = \left(\frac{q_{side}}{q}, \alpha, \frac{V_s}{V}, \frac{q}{Vd}\right) \tag{2.6}$$

Where $V$ and $q$ are the mean velocity and specific discharge in the original channel. Rocha used data from his own experiments (conducted on a 30 degree diversion) and data from Dancy's experiments [37], to demonstrate the dependence of amount of sediment entering the lateral channel on the Rouse number ($\frac{V_s}{u_*}$, where $u_*$ is the shear velocity of the flow) and roughness of the bed. Amount of sediment entering the diversion channel was found to increase with increase in $\frac{V_s}{u_*}$ and bed roughness. This is along the expected lines, because for the same $q$ higher Rouse number and bed roughness correspond to

higher sediment particle size, which means higher percentage of sediment will be transported as bed load, thus more sediment will find its way into the lateral channel due to Bulle-Effect.

## 2.4 Impact of Bulle-Effect on Diversion design

A primary area of motivation for studying the Bulle-Effect is to understand its implications on real world diversions built to divert water and sediment. A recent study that used numerical simulations to explore in detail the effect of different parameters on the sediment capture efficiency of a real world diversion was conducted by Gawesh and Meselhe [23]. The study is timely because throughout the world the long-term future of large-deltas is under threat due to climate-change and other anthropogenic factors [33]. And one of the proposed solutions are engineered sediment diversions, that would divert water and sediment from rivers in order to mitigate land-loss at deltas. In the context of United States, the plan to build land in Louisiana through diverting sediment (and water) from the Lower Mississippi River (LMR) is a prime example [47]; and the discussed study is a positive step in that direction.The authors used a coupled three-dimensional hydrodynamic and sediment transport model, to evaluate possible design specifications of a Sediment Diversion to be built on the LMR. The validated model was used to evaluate the effect of different attributes of the planned sediment diversion, on its sediment capturing efficiency. The attributes assessed were, the angle of diversion, ratio of the elevation of the bottom of the diversion with that of the main river, and width of the diversion that directly correlates with the discharge of water going through the diversion. Central to all the analysis done by the authors was the parameter Sediment Water Ratio (SWR) and Cumulative Sediment Water Ratio (CSWR), which was used to quantify the sediment capture efficiency of the diversion. This section primarily focuses on the comprehensive definition of $SWR$, why it is important, and the fact that $SWR$, as defined by Gaweesh and Meselhe, might not estimate the right percentage of sediment diverted from a river.

### 2.4.1 A Comprehensive Definition of Sediment Water Ratio (SWR)

The definition of sediment water ratio (SWR) used by Gaweesh and Meselhe (eqn. 1 in [23]) is expressed as

$$SWR = \frac{S_D}{S_R} \times \frac{Q_R}{Q_D} = \frac{C_D}{C_R} \tag{2.7}$$

where $Q_R$ and $Q_D$ are the water discharge in the river before the diversion and water discharge going into the diversion; $S_R$ and $S_D$ are the sediment

discharge in the river and sediment discharge diverted; and $C_R$ and $C_D$ are the concentration of sediment in the river and diverted, respectively. The primary issue with the above definition is that it does not specify the location at which the concentration is measured, and if the concentration is depth and width averaged. Without the above stated information, the definition is valid only for the case where sediment is uniformly distributed throughout the depth and width of the river and the diversion channel, which is rarely the case in most river systems. In the following subsections, we will put forth a comprehensive definition of SWR and explain why it is important to use such definition to assess the amount of sediment diverted from a given river or canal.

Derivation of Sediment Water Ratio (SWR)

A definition of SWR that takes into account spatial variability of the sediment in both the vertical and transverse flow directions, in the river and associated diversion is given by

$$SWR = \frac{\left[\int\int u_D c_D dzdw / \int\int u_D dzdw\right]}{\left[\int\int u_R c_R dzdw / \int\int u_R dzdw\right]} \tag{2.8}$$

$$= \frac{\left[\int\int u_D c_D dzdw\right]}{\left[\int\int u_R c_R dzdw\right]} \frac{\left[\int\int u_R dzdw\right]}{\left[\int\int u_D dzdw\right]} \tag{2.9}$$

where $\int\int udzdw$ corresponds to the water discharge ($Q$) passing through a specific cross-section, with $u$ being the mean point velocity of water that is integrated across the depth and width of the cross-section. Similarly, $\int\int ucdzdw$ corresponds to the sediment discharge ($S$) at a cross-section, where $c$ is the mean, point volumetric sediment concentration. The circumstance under which eqn. 3, reduces to the definition of SWR used by the authors (eqn. 2.7) is when the sediment concentrations $c_D$ and $c_R$ do not vary in depth ($z$) or along the width ($w$) [48]. In that case eqn. 3 can be reduced to

$$SWR = \frac{\left[\int\int u_D c_D dzdw\right]}{\left[\int\int u_R c_R dzdw\right]} \frac{\left[\int\int u_R dzdw\right]}{\left[\int\int u_D dzdw\right]} \tag{2.10}$$

$$= \frac{\left[C_D \int\int u_D dzdw\right]}{\left[C_R \int\int u_R dzdw\right]} \frac{\left[\int\int u_R dzdw\right]}{\left[\int\int u_D dzdw\right]} \tag{2.11}$$

$$= \frac{C_D}{C_R} \tag{2.12}$$

resulting in eqn. 2.7 submitted by the authors. Next, we discuss the appropriateness of defining $SWR$ in the context of flow and sediment transport at river diversions.

SWR in context of river diversions

A simple equation that relates the ratio of sediment discharge going into the diversion and the sediment discharge remaining in the river ($S_D/S_M$), and the ratio of water discharge going into the diversion and the discharge remaining in the river ($Q_D/Q_M$) is given by

$$\frac{S_D}{S_M} = \alpha \left( \frac{Q_D}{Q_M} \right)^{\beta} \tag{2.13}$$

where $\alpha$ and $\beta$ are dimensionless. And for a particular diversion geometry, $\beta$ and $\alpha$ depends on the sediment properties and flow parameters. Similar nodal relation have been previously used in the context of river bifurcations [49, **?**] and diversions [50]. The above equation can be written in terms of $Q_D$ and $Q_R$, and $S_D$ and $S_R$. Where $Q_R = Q_D + Q_M$ and $S_R = S_D + S_M$. The transformed relation is given by

$$\frac{S_D}{S_R} = \frac{\alpha \left( Q_D/Q_R \right)^{\beta}}{\left( 1 - Q_D/Q_R \right)^{\beta} + \alpha \left( Q_D/Q_R \right)^{\beta}} \tag{2.14}$$

For sediment fine enough to be uniformly distributed throughout the depth, like sediment moving as washload, $\beta \approx 1$ and $\alpha \approx 1$. For relatively coarser sediments that are transported near the bed, $\beta > 1$ and $\alpha > 1$. This non-linear behavior can be observerved in the data from experiments done on physical models of diversions [1, 50, 51]. Recently, Ordoñez published data compiled from different studies on diversions made over the years, along with data from a physical model of the Canal del Dique diversion on the Magdalena River.], Colombia [52]. The experimental data compiled by Ordoñez cover cases with diversion angle varying between 30-150 degrees, and different sediment sizes (see fig. 2.9). For this data, which was compiled across multiple studies, $\beta \approx 1.54$ and $\alpha \approx 9.2$.

Further hint of $\beta > 1$ and $\alpha > 1$ at river diversions is evident from the data of sediment diverted at different diversions for irrigation from the Lower Yellow River [53]. Observations of percentage of the total sediment load diverted ($S_D/S_R$) at different points along the Lower Yellow River (LYR) have been reproduced (see fig. 2.10). At all the four diversions the percentage of sediment diverted is substantially higher than the percentage of flow diverted, and this non-linear sediment distribution is only possible if $\beta > 1$. Among the four diversions the People's Victory Canal gate the most upstream, followed by Heigangkou, Shanyizhai and Dayuzhang gates. It is evident from fig. **??** that the degree of non-linearity of the sediment division at the diversion decreases as one moves downstream. This may be attributed to a decrease in $\beta$ and $\alpha$ due to downstream fining of the sediment [54]. For the diversions at LYR, $\beta$ is in the range $1.78 - 2.4$, and $\alpha$ is in the range $3.16 - 35.6$.

The dependence of $\beta$ and $\alpha$ on $V_s/u_*$ is also evident from the experiments of

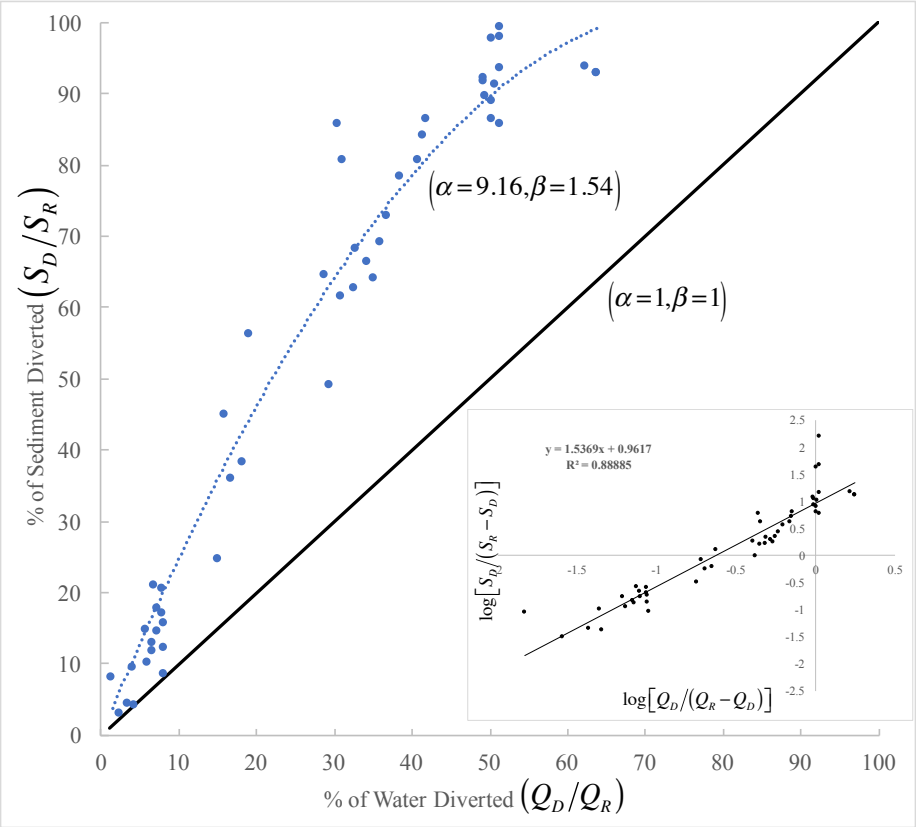


Figure 2.9: y-axis shows the percentage of the total initial sediment captured by the diversion, and x-axis shows the corresponding percentage of water entering the diversion. The data has been reproduced from Ordoñez (2013), and the plot corroborates the assertion of $\beta > 1$ and $\alpha > 1$ for sediment traveling near the bed. (Inset) $\alpha$ and $\beta$ was ascertained from the plot between $log\,[S_D/(S_R - S_D)]$ and $log\,[Q_D/(Q_R - Q_D)]$.

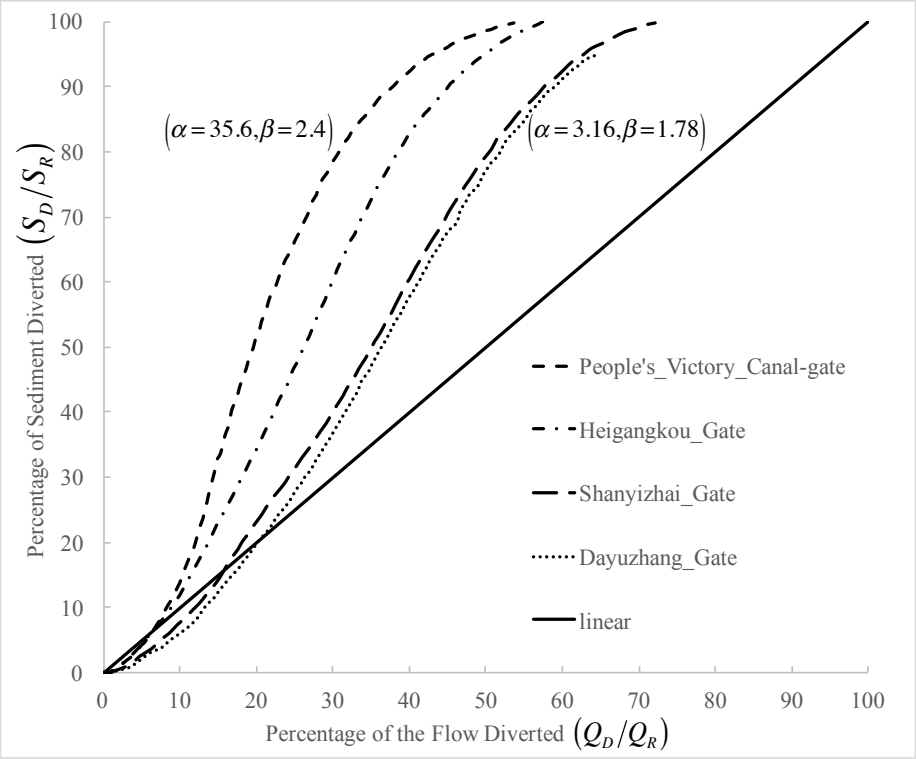


Figure 2.10: y-axis shows the percentage of the total sediment captured by the diversion, and x-axis shows the corresponding percentage of water entering the diversion. The data is from 4 diversions/gates along the Lower Yellow River, with the People's Victory Canal gate at the upstream end of the reach and Dayuzhang gate at the downstream end of the reach (Erxun 1989).

Dancy [55] (see fig 2.6), which is one of the only experimental studies conducted using sediment of different sizes. For sediment varying between the size $0.075 - 9.5$ mm, $\alpha$ and $\beta$ is in the range $0.8 - 11.8$ and $1 - 2$, respectively. In the experiments relatively larger percentage of coarser sediment was found to enter the 30-degree diversion. This happens because relatively coarser sediment that tends to move near the bottom of the channel, will be diverted by the secondary flow induced by the flow rotation while turning into the diversion. This is known as the Bulle-Effect in the literature [40], since Bulle was the first to observe such non-linear behavior in the laboratory [56] [p. 330].

In case there is no data available to estimate $\alpha$ and $\beta$, an approximate way to estimate $\beta$ could be to use an expression obtained by integrating the Rousean equilibrium profile [57]. The expression is $\beta = 1 + 31.5\,(V_s/u_*)^{1.46}$, where $u_*$ is the fluid shear velocity and $V_s$ is sediment fall velocity. Reiterating the point made earlier, for a particular diversion, $\alpha$ and $\beta$ depends on property of the sediment ($V_s$) and the flow ($u_*$). Though in general, $\alpha$ may also varies with other properties of the diversion, i.e. diversion-angle, diversion width and depth etc.

Getting back to the definition of SWR

$$SWR = \frac{S_D}{Q_D}\frac{Q_R}{S_R} \tag{2.15}$$

$$= \left(\frac{S_D}{S_R}\right)\frac{Q_R}{Q_D} \tag{2.16}$$

Now replacing $S_D/S_R$ in the above relationship using eqn. 2.14, yields the following

$$SWR = \frac{\alpha\,(Q_D/Q_R)^{\beta}}{(1 - Q_D/Q_R)^{\beta} + \alpha\,(Q_D/Q_R)^{\beta}}\frac{Q_R}{Q_D} \tag{2.17}$$

$$= \frac{\alpha\,(Q_D/Q_R)^{\beta-1}}{(1 - Q_D/Q_R)^{\beta} + \alpha\,(Q_D/Q_R)^{\beta}} \tag{2.18}$$

For a particular diversion, $\alpha$ and $\beta$ will depend on the ratio of sediment fall velocity and shear velocity ($V_s/u_*$), thus SWR would also vary with size of the sediment. This was also observed by the authors, when they evaluated capture efficiency for different sand sizes. To reduce eqn. 10 to the relationship for SWR used by the authors (eqn. 2.7), it has to be assumed that the relationship between sediment discharge and water discharge is linear, that is $S = CQ$, which is akin to assuming $\beta = 1$. Introducing $\beta = 1$ into eqn. 12, $SWR$ reduces to

$$SWR = \frac{\alpha}{1 + (\alpha - 1)\,Q_D/Q_R} \tag{2.19}$$

A case with $\beta = 1$ is usually accompanied by $\alpha \approx 1$. Though in some cases $\alpha > 1$. The range of $\alpha$ encountered by Gaweesh and Meselhe in their study under discussion is $0.05 - 2.2$. The values were calculated using eqn. 2.19 and

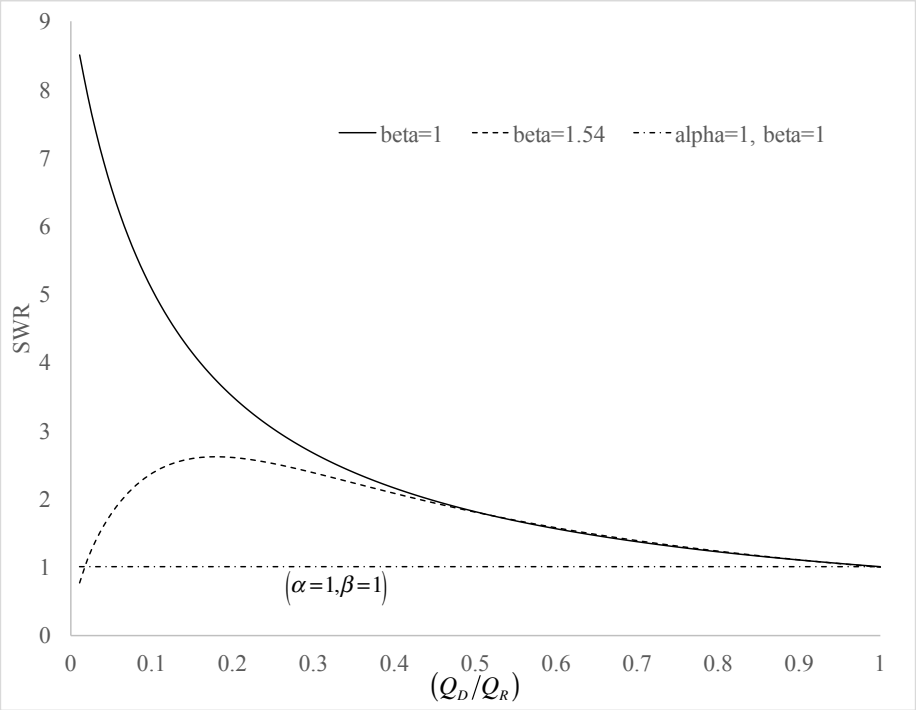


Figure 2.11: y-axis shows $SWR$, and x-axis shows the ratio of water entering the diversion with respect to the total water in the river. Two scenarios have been plotted, with $\beta = 1$ and $\beta = 1.54$. For both cases, $\alpha = 9.16$. Eqn. 12 was used to calculate $SWR$.

the observed values of SWR in the study. On the basis of the studies cited earlier, it can be concluded that for relatively coarser sediment ($\beta > 1$) $\alpha$ is usually greater than 3.

In order to compare the effect of $\beta$ on the calculation of $SWR$, two cases with the same $\alpha = 9.16$ have been plotted in fig. 2.11. The value of $\alpha$ used is from the data compiled by Ordoñez [52]. The comparison is done in order to ascertain the difference in computed value of $SWR$ for relatively coarser sediments, that is if $\beta$ is assumed to be 1 (as done by Gaweesh and Meselhe) instead of $\beta > 1$. The values of $\beta$ used are 1 and 1.54, which was empirically evaluated from the data of Ordoñez. The above mentioned set of data was used for empirical values of $\alpha$ and $\beta$ because the data covers a gamut of different cases, with different diversion geometries and sediment sizes.

From fig. 2.11 it can be concluded that for relatively coarser sediment and $Q_D/Q_R$ relatively low ($Q_D/Q_R < 0.3$), $SWR$ predicted with the assumption of $\beta = 1$ would overestimate $SWR$. The magnitude of overestimation decreases with increase in $Q_D/Q_R$, and once $Q_D/Q_R > 0.45$, $SWR$ calculated assuming $\beta = 1$ are practically the same as in the case $\beta > 1$. From fig. 2.11 it can be concluded that the behavior of $SWR$ when $\beta = 1$ is not physically correct. First, at $Q_D/Q_R = 0$, $SWR$ should be equal to zero, instead $SWR = \alpha$. On the other hand the case $\beta > 1$ converges to 0 at $Q_D/Q_R = 0$. Secondly, when the

sediment is relatively coarse and travels near the bed, at relatively low $Q_D/Q_R$ (say $< 0.1$), $SWR$ should be less than 1, as a certain percentage of the flow needs to be moving into the diversion for Bulle-Effect to kick in. This is also portrayed in the data from LYR (see fig. 2.10). The case $\beta > 1$ captures this behavior, but the case $\beta = 1$ is unable to capture this non-linear phenomenon.

From the analysis done herein, it may be concluded that due to not accounting for $\beta > 1$ for relatively coarse sediment at a diversion, sediment capture efficiency ($SWR$) calculated using the definition used by Gaweesh and Meselhe (eqn. 2.7) may over estimate the amount of sediment being diverted, especially at relatively lower values of $Q_D/Q_R$. Thus instead of using the ratios of sediment concentration ($C_D/C_R$), it would be better to use the more comprehensive definition of $SWR$ (see eqn. 3) that takes into account the fact that $\beta > 1$ for relatively coarser sediment.

### 2.4.2 Concluding Remarks

The thought-provoking study by Gawesh and Meselhe evaluates numerically the impact of different design characteristics of a sediment diversion on its sediment capture efficiency. Central to the evaluation of different design characteristics is the parameter used for quantifying the efficiency of sediment capturing capability of a diversion. The authors use a definition for $SWR$ (see eqn. 2.7), which may not be the most comprehensive way of calculating it, and may lead to over or under estimation of $SWR$ for relatively coarser sediments that tend to travel along the bottom third of the water column in a river. The definition of $SWR$ that would work under all the circumstances, irrespective of the parameter $V_s/u_*$, is given by eqn. 3. As evidence for the point being made above, this discussion is based on data from laboratory scale and real-world diversions, which show the proclivity of relatively coarser sediment for entering the diversion. The discussion also included a short analysis about $SWR$ calculated based on the assumption of the sediment being uniformly distributed ($\beta = 1$), and sediment being relatively coarser and not uniformly distributed in the vertical ($\beta > 1$). The analysis clearly shows that for coarse sediment, $SWR$ approximated at relatively lower values of $Q_D/Q_R$ will be overestimated if $\beta = 1$. Even though the analysis is based on certain assumptions, the general conclusion drawn about calculation of $SWR$ should hold true irrespective of the assumptions.

In the current study it was conclusively shown that a robust definition of $SWR$ is required for accurate calculation of the sediment capture efficiency. Though it is also amply clear that further experimental and numerical studies are required to further the general understanding of the dynamics at diversions, especially the effect different parameters like $V_s/u_*$ and different aspects of diversion geometry. Finally, one of the implications of building diversions on the Lower Mississippi River, is the deposition of sediment just downstream of

the diversion due to loss of stream-power. It should be pointed out that the aim of the diversion is to divert sediment with $SWR > 1$, that means a larger percentage of the total sediment would be diverted than water. In this scenario, some analysis should also be done about the fate of the sediment once it enters the diversion. A question that might be important is, how far will the sediment travel after being diverted ? And, will the flow be strong enough to take it to its desired destination, or will most of it be deposited in and around the diversion channel ?

# CHAPTER 3

# A SEMI-IMPLICIT LAGRANGIAN PARTICLE TRACKING MODEL FOR SPECTRAL-ELEMENT BASED INCOMPRESSIBLE NAVIER-STOKES SOLVERS

## Authors

Som Dutta, Paul Fischer, Marcelo H. Garcia

prepared for Journal of Scientific Computing, Springer.

## Abstract

Particle-laden flows are prevalent in nature, as well as in the industrial setting. The modeling methodology that has been popular for modeling these particle-laden flows is the Eulerian-Lagrangian approach, where the fluid phase is modeled under the Eulerian framework, and the particles are modeled under the Lagrangian framework. Currently almost all the Lagrangian particle tracking method use explicit time integration schemes for time-stepping, e.g. Rung-Kutta, Adam Bashforth etc. A need for a semi-implicit method for Lagrangian particle tracking arises due to the stability constraint on the size of the time-step in explicit time-steppers. The strictness of the constraint increases with decreases in Stokes number of particle. Thus, the proposed method is best suited for problems with poly-disperse particles, that is a set of particles covering a wide-range of Stokes number, where the particles with the smallest Stokes number significantly reduces the maximum time-step size for the particle time-stepper. In this paper a fast semi-implicit time-stepping algorithm has been put forth, first for the case where Stokes drag is the only force acting on the particles. Then the formulation has been extended to include other forces that act on the particle, e.g gravity, lift, added mass etc. An algorithm has been provided for implementation on any existing computational fluid dynamics (CFD) solver. Finally, the implementation of the algorithm on the higher-order spectral-element based incompressible Navier-Stokes solver Nek5000 was tested for various fundamental flows.

## 3.1 Introduction

Particle-laden flows are one of the most common variant of multiphase flows, and a short list of examples includes cases under natural settings like dispersal of aerosols, dust and volcanic ash, sediment in rivers and marine environments etc. [58, 40]; and cases under engineered settings like fuel sprays, carbon soot in engines, fluidized bed reactors etc [59, 60]. Among the computation methodologies used for modeling particle-laden flows, Lagrangian point-particle approach (also referred to as Lagrangian particle tracking) has the longest history [61, 62], and is suited to handle handle relatively large particles [63]. Methods that resolve the flow around the particle is certainly more accurate for large particles, but due to currently these methods are restricted to limited number of particles. For smaller particles, the Lagrangian particle-tracking approach works perfectly, though Eulerian approaches might be more efficient. Though under appropriate conditions, Lagrangian particle-tracking's performance is comparable to Eulerian approaches. So, the Lagrangian particle-tracking method is the only approach that works efficiently across different space and time scales, for large number of particles, and for particles with different sizes (polydisperse particles).

The Lagrangian particle-tracking approach retains the Lagrangian description of the particles, and the complexity of the model depicting the motion of the particles depends on the size, relative density, and concentration of the particles. At the simplest level, the motion of particles can be modeled as Lagrangian tracers, where the velocity of a particle is directly interpolated from the fluid around it. This version of the model works well for very small particles that has density close to that of the ambient fluid. In this model the particles are expected to follow the flow, thus success of the model depends on accuracy of the interpolation scheme used for interpolating the fluid velocity to the position of the particle [64]. In the model, evolution of particle position is usually predicted through integrating the particle velocity using an higher-order explicit time-stepping scheme like Adam-Bashforth, Runge-Katta. Details of the Lagrangian tracer model is discussed in section 3.2.

For particles that cannot be modeled as Lagrangian tracers, the model solves the equations of motion to track the position, and momentum ( mass and energy if required) of the particles. Levels of complexity of this model can vary from one-way coupled model to the four-way coupled model [65]. In the one-way coupled model, the flow affects the motion of the particle and there is no feed-back of the particles back to the flow. This methodology of modeling works best for particles that are not big enough to appreciably disturb the ambient fluid, and the particle concentration is low enough that they rarely collide with each other or modulate turbulence [66]. The two-way coupled models involve feedback from the particles to the fluid momentum equations (the Navier-Stokes equation) [67], and the four-way coupled models additionally takes into account the

interaction between the particles [68]. Irrespective of the levels of coupling used in the model, the equations defining the motion of the particles are integrated in time using a higher-order time-stepping scheme, and traditionally the models have used explicit time-steppers like Adams-Bashforth (AB), Runge-Kutta (RK) or some variation of RK [69, 70, 71]. Though, stability of the explicit time-stepping schemes becomes an issue for cases where particle response time is becomes smaller than the simulation time-step, this usually happens due to relatively small particles or highly viscous ambient fluid. This leads to reduction of time-step size, thus making the simulation computationally expensive [60].

The current study briefly explores the root of instability in explicit time-stepping schemes for Lagrangian-particles, and then puts forth a semi-implicit time-stepping algorithm for the Lagrangian particle tracking method. The algorithm has been implemented and tested for a one-way coupled model, but can be extended to two-way and four-way coupling. The implementation and testing of the model was done on the higher-order spectral-element based incompressible Navier-Stokes solver Nek5000 [31]. Sengupta et al. summarize some previous studies on higher-order spectral-based simulations of turbulent particle-laden flows [72]. Recently, a Lagrangian point-particle model was implemented on Nek5000. Amongst the forces acting on the particle, the model only takes into account the Stokes drag, and it uses the explicit time-stepper Adams-Bashforth for integrating the governing equations of the particles [73]. To the authors knowledge, the model proposed in this paper is the firs semi-implicit Lagrangian particle-tracking model in the literature.

Henceforth, the paper has been divided into sections. The second section briefly discusses the particle tracking using an explicit time-stepper, initially elucidating the Lagrangian-tracer model and then the more generic case where the velocity of the particle is a function of the relative velocity between the particle and the ambient fluid. This section has been provided as context for the upcoming sections about the semi-implicit time-stepper. The third section elucidates the reason behind the requirement for an semi-implicit time-stepper, and then proposes a time-stepper that is the combination of the Extrapolation scheme and the Backward Difference scheme. In the aforementioned section, the analysis is done for a model where Stokes drag is the only force acting on the particle. In the next section (section 4) the method has been extended to a model where there are additional forces, e.g. lift, added mass, gravity etc., acting on the particle. These additional terms in the particle momentum balance equation is required for accurate modeling of the dynamics of the particle under complex flow conditions. This section also elucidates the step-wise algorithm of the model, this information can be used for implementing the model into an existing computational fluid dynamics (CFD) solver. In section five, various components of the full particle model have been tested under specific flow conditions, in order to test the model's veracity. Finally, in section six, the efficiency of the model has been tested for real application flows.

## 3.2 Explicit time stepping for Lagrangian particle tacking

To begin, we consider particle tracking model based on Lagrangian transport, often referred to as Lagrangian-tracer. The particle position $\mathbf{x} := (x, y, z)$ is governed by the first order ordinary differential equation (ODE)

$$\dot{\mathbf{x}} = \mathbf{v} = \mathbf{u}(\mathbf{x}, t), \qquad \mathbf{x}(t = 0) = \mathbf{x}_0, \tag{3.1}$$

where $\mathbf{v}$ is the particle velocity, $\cdot$ denotes the time derivative, and $\mathbf{u}(\mathbf{x}, t)$ is the fluid velocity at position $\mathbf{x}$ and time $t$.

Equation (3.1) can be advanced with any standard integrator having the desired cost/accuracy trade-offs. For engineering geometries, there is a high cost associated with interpolating the flow field at arbitrary points and explicit schemes are generally preferred. A convenient choice is third-order Adams-Bashforth (AB3),

$$\mathbf{x}^n \quad = \quad \mathbf{x}^{n-1} + \Delta t \left( \frac{23}{12} f^{n-1} - \frac{16}{12} f^{n-2} + \frac{5}{12} f^{n-3} \right), \tag{3.2}$$

where $f^{n-q} := \mathbf{u}^{n-q}(\mathbf{x}^{n-q})$ and $\mathbf{u}^{n-q}$ is the velocity field at time level $t^n$. AB3 requires only one nonlinear function evaluation per timestep. For Lagrangian tracer like models, the non-linear function evaluation is interpolation of the Eulerian fluid velocity field onto the position of the particle. For the model problem $\dot{x} = \lambda x$, the method has a well-known stability region in the complex $\lambda \dot{t}$-plane that encompasses a segment of the imaginary axis spanning -.7236$i$ to +.7236$i$. In general, stability for (3.2) is not an issue but accuracy is. In effect, there is only one timescale in the kinematic description (3.1) and the particle must simply be advanced with steps sufficiently small to accurately resolve the path that it traces. If it deviates from that path it will pick up the wrong velocity, but there will be no amplification associated with numerical instability.

The above model can be slightly modified to include the case in which the particles being tracked behave like a Lagrangian tracer, but has gravity acting on them. The way gravity manifests in the model is through a constant particle fall velocity ($V_s$) in direction of the gravitational acceleration. So, the equation representing the modified model is

$$\dot{\mathbf{x}} = \mathbf{v} = \mathbf{u}(\mathbf{x}, t) + V_s \hat{e_g}, \qquad \mathbf{x}(t = 0) = \mathbf{x}_0, \tag{3.3}$$

where $e_g$ is unit vector in direction of gravitational acceleration. The aforementioned models have be to be coupled with appropriate problem specific boundary

and initial conditions.

Now, expanding the Lagrangian particle tracking model to the more general case where velocity of the particle not only depends on the velocity of the ambient fluid, but also the velocity of the particle itself. This happens because, for particles bigger than a certain size [we might need to define this limit], there is disparity between the velocity of the particle and velocity of the fluid around the particle. Thus, velocity of the particle at any point of time is a non-linear function of the relative velocity of the particle. The ODEs defining the motion of the particle is

$$\begin{aligned} \dot{\mathbf{x}} &= \mathbf{v}, & \mathbf{x}(0) &= \mathbf{x}_0, \\ \dot{\mathbf{v}} &= f\left(\mathbf{u}-\mathbf{v}\right), & \mathbf{v}(0) &= \mathbf{v}_0, \end{aligned} \tag{3.4}$$

Similar to the case of the Lagrangian tracer, an explicit time-stepper can be used to integrate the above equations in time. If AB-3 is used, the equivalent of the relationship 3.2 is.

$$\mathbf{x}^n = \mathbf{x}^{n-1} + \Delta t \left( \frac{23}{12}\mathbf{v}^n - \frac{16}{12}\mathbf{v}^{n-1} + \frac{5}{12}\mathbf{v}^{n-2} \right), \tag{3.5}$$

$$\mathbf{v}^n = \mathbf{v}^{n-1} + \Delta t \left( \frac{23}{12}f^{n-1} - \frac{16}{12}f^{n-2} + \frac{5}{12}f^{n-3} \right), \tag{3.6}$$

But unlike the case of Lagrangian tracers, the stability of the time integrator is an issue, even for the simplest case, where Stokes drag is the only force acting on the particle. In the next section the reason behind the stability constraint has been discussed; and then a semi-implicit time-stepping scheme has been proposed to address the problem, without increasing the computational cost.

## 3.3 Fast Semi-Implicit particle tracking

We next consider a *dynamic* model in which the particle is accelerated by fluid drag forces. We use Stokes drag as an example but the basic concepts can be extend to more complicated models that has been be discussed in the next few sections. The Stokes drag formulation used here assumes the stokes number of the particle to be constant, which is plausible if the drag coefficient $C_D$ is constant. Then the system of ODEs governing the motion of the particles is,

$$\begin{aligned} \dot{\mathbf{x}} &= \mathbf{v}, & \mathbf{x}(0) &= \mathbf{x}_0, \\ \dot{\mathbf{v}} &= \alpha\left(\mathbf{u}-\mathbf{v}\right), & \mathbf{v}(0) &= \mathbf{v}_0, \end{aligned} \tag{3.7}$$

where $\mathbf{u} = \mathbf{u}(\mathbf{x}, t)$. Here, $\alpha = \frac{1}{\tau}$, where $\tau$ (the Stokes number) represents the relaxation time between the particle and fluid velocities. Small $\tau$ implies that the particle rapidly assumes the velocity of the neighboring fluid, which is the case for sufficiently small particles or sufficiently viscous fluids. Unfortunately, a small value of $\tau$ also implies that (3.7) is *stiff*, in the sense that there are disparate timescales. There is the slow scale associated with the motion of the particle, which we wish to resolve, and the fast scale associated with the rate at which $\mathbf{v} \longrightarrow \mathbf{u}$. We can see the potential for trouble in a couple of different ways.

First, equation (3.7) can be rewritten as a second-order ODE, which nominally needs two initial conditions,

$$\tau\ddot{\mathbf{x}} + \dot{\mathbf{x}} = \mathbf{u}, \qquad \mathbf{x}(0) = \mathbf{x}_0, \qquad \dot{\mathbf{x}}(0) = \dot{\mathbf{x}}_0. \tag{3.8}$$

In the limit $\tau \longrightarrow 0$, the nature of (3.8) is changed. It becomes a first-order ODE and the second initial condition is dropped in favor of $\dot{\mathbf{x}} \equiv \mathbf{u}$. Because the highest-order derivative is multiplied by a small value, (3.8) is singularly perturbed and one of the eigenvalues of the characteristic polynomial goes to infinity as $\tau \longrightarrow 0$. The irony is that, in this limit, the system should become easier to solve rather than harder because the physics is more straightforward.

Another way to see the stiffness induced by small particle sizes is to look at the eigen-structure of (3.7), which can be rewritten as

$$\begin{pmatrix} \dot{\mathbf{x}} \\ \dot{\mathbf{v}} \end{pmatrix} = \begin{bmatrix} 0 & I \\ 0 & -\alpha I \end{bmatrix} \begin{pmatrix} \mathbf{x} \\ \mathbf{v} \end{pmatrix} + \alpha \begin{pmatrix} 0 \\ \mathbf{u} \end{pmatrix}. \tag{3.9}$$

This system has the structure

$$\dot{\underline{q}} = A\underline{q} + \underline{f}(\underline{q}, t) \tag{3.10}$$

with eigenvalues of $A$ being 0 and $-\alpha$ and the vector $\underline{q}$ the vector containing position and velocity. We illustrate the stiffness by considering a simple uniform flow with $\mathbf{u} \equiv (1, 0, 0)$ and initial conditions $\mathbf{x} = \mathbf{v} = (0, 0, 0)$. This reduces to a $2 \times 2$ system governing the particle motion along the $x$ axis,

$$\begin{pmatrix} \dot{x} \\ \dot{v} \end{pmatrix} = \begin{bmatrix} 0 & 1 \\ 0 & -\alpha \end{bmatrix} \begin{pmatrix} x \\ v \end{pmatrix} + \alpha \begin{pmatrix} 0 \\ 1 \end{pmatrix}. \tag{3.11}$$

The solution to (3.11) is $v = 1 - e^{-\alpha t}$. Thus, the stability constraints for explicit timesteppers will dictate a stepsize $\Delta t \approx 1/\alpha = \tau$ *for all time*, even when $v \longrightarrow 1$. The essential difficulty here is that $\tau$ is controlled by the particle size, which is part of the problem specification. One would like to have a method that will be stable for a broad range of particle sizes.

For large values of $\alpha$ it is clear that some type of implicit time-stepping is

required. One option would be a fully implicit scheme such as a $k$th-order backward difference formula (BDF$k$). For $k$=2, equation 3.10 can be written as

$$\frac{d\underline{q}}{dt} \approx \frac{3\underline{q}^n - 4\underline{q}^{n-1} + \underline{q}^{n-2}}{2\Delta t} = A\underline{q}^n + \underline{f}^n. \tag{3.12}$$

The difficulty is that $\underline{f}$ is nonlinear, so solving the above equation would require relatively expensive iterative equation solver, like Netwon-Raphosn.

However, as we have shown, the stiffness of this system is associated with the matrix $A$ and not with $\underline{f}$. The system (3.10) is a classic example of a stiff system in which the fast (and relatively uninteresting) part of the system is linear and can be easily treated implicitly while the resolved (i.e., slow and interesting) physics involves an expensive non-linearity that is readily treated through explicit updates. So, a semi-implicit scheme, such as BDF$k$ plus $k$th-order extrapolation (EXT$k$), is ideally suited to this situation. The basic idea is to evaluate each term in the original system implicitly if it contributes to stiffness and explicitly otherwise. For $k$=2, the scheme is

$$\frac{3\underline{q}^n - 4\underline{q}^{n-1} + \underline{q}^{n-2}}{2\Delta t} = A\underline{q}^n + (2\underline{f}^{n-1} - \underline{f}^{n-2}). \tag{3.13}$$

Rearranging, the update step is of the form

$$\left(\frac{3}{2}I - \Delta t A\right)\underline{q}^n = \frac{4}{2}\underline{q}^{n-1} - \frac{1}{2}\underline{q}^{n-2} + \Delta t(2\underline{f}^{n-1} - \underline{f}^{n-2}), \tag{3.14}$$

which requires solution of $d$ upper-triangular $2\times2$ systems in $d$ space dimensions. We remark that the work required for BDF3/EXT3 is essentially the same as for (3.14) and that both schemes readability generalize to variable step size. The general formula for each velocity component, $i = 1, \cdots, d$ is

$$v_i^n = \frac{1}{\beta_0 + \Delta t\alpha}\left(\sum_{j=1}^{k}\beta_k v_i^{n-j} + \alpha\Delta t\sum_{j=1}^{k}\alpha_j u_i^{n-j}\right) \quad \text{(velocity)} \tag{3.15}$$

$$x_i^n = \frac{1}{\beta_0}\left(\sum_{j=1}^{k}\beta_k x_i^{n-j} + \Delta t\, v_i^n\right) \quad \text{(position)}. \tag{3.16}$$

Table 1 lists the BDF$k$ and EXT$k$ coefficients for the case of uniform $\Delta t$. For variable $\Delta t$, one simply needs the polynomial interpolation and derivative constants associated with the time points $t^{n-j}$ [74].

It should be noted that, in most simulations of turbulent flow the timestep $\Delta t_f$ is governed by the Courant condition, which requires that the Courant number be bounded by an order unity constant,

$$C := \max_i \Delta t_f\left(\left|\frac{u_i}{\Delta x_i}\right| + \left|\frac{v_i}{\Delta y_i}\right| + \left|\frac{w_i}{\Delta z_i}\right|\right) < C^* \tag{3.17}$$

Table 3.1: BDF$k$ and EXT$k$ Coefficients for Uniform $\Delta t$

| $k$ | $\beta_0$ | $\beta_1$ | $\beta_2$ | $\beta_3$ | $\alpha_1$ | $\alpha_2$ | $\alpha_3$ |
|---|---|---|---|---|---|---|---|
| 1 | 1 | 1 | 0 | 0 | 1 | 0 | 0 |
| 2 | $\frac{3}{2}$ | $\frac{4}{2}$ | $-\frac{1}{2}$ | 0 | 2 | -1 | 0 |
| 3 | $\frac{11}{6}$ | $\frac{18}{6}$ | $-\frac{9}{6}$ | $\frac{2}{6}$ | 3 | -3 | 1 |

Here, the maximum is taken over all gridpoints (or cells) $i$ with local gridspacing $(\Delta x_i, \Delta y_i, \Delta z_i)$. There is generally no reason to expect that $\Delta t$ required for accurate particle tracking should be equal to $\Delta t_f$. It can often be much larger, particularly in regions of slow flow or where pathlines are relatively straight.

## 3.4 Lagrangian particle tracking model with additional force terms

In this section, we will discuss a more generalized Lagrangian particle model that takes into account additional physics: the lift force acting on the particle, the fluid stresses acting on the particle (both shear and normal stress), gravitational acceleration and added mass. The version of the model used in the current study is similar to the one derived by Auton et al. [75], which considered the inviscid limit for the continuous-phase. The other commonly used model is the Maxey-Riley equations [76], which considered the viscous limit for the continuous-phase. The version of the model we have used in this study does not have any bearing on the semi-implicit time-stepping scheme that has been discussed here and any conclusions for one version of the model, can be extended to the other. The reason we chose the model similar to Auton et al., was our motivation to use the model to simulate near-bed sediment transport in turbulent flows, similar to the study by Escauriaza and Sotiropoulos [77]. Additionally, the feedback of the particles on to the fluid, which becomes important for cases with high particle concentration, has not been considered. Other assumptions made are, the particles only translate that is they do not rotate while moving, and the particles also do not collide with each other. The aforementioned assumptions are valid for cases where the particle concentration is relatively low and the particle diameters are small enough that particle rotation can be neglected while moving through the fluid. The motion of the particles are defined by the equations

$$m\frac{dv_i}{dt} = f_i \qquad \text{(velocity equation)} \tag{3.18}$$

$$\frac{dx_i}{dt} = v_i \qquad \text{(position equation).} \tag{3.19}$$

where $m$ is the mass of the particles, $x_i$ and $v_i$ are the position and velocity of the particles. $f_i$ represents all the forces acting on the particles. Velocity of the fluid at the particle (that is interpolated to the position of the particle) have been represented using $u_i$. And the relative velocity between the particle and the fluid has been represented using $v_{ri} = (u_i - v_i)$. Equation 16 is has been rewritten as

$$m\frac{dv_i}{dt} = \frac{1}{2}\rho C_D \frac{\pi d^2}{4}|v_{ri}|v_{ri} + \left(1 - \frac{\rho}{\rho_s}\right) m g_i + \rho C_L \frac{\pi d^3}{6}\left(\epsilon_{ijk} v_{rj} \omega_k\right) + \rho C_m \frac{\pi d^3}{6}\left(\frac{Du_i}{Dt} - \frac{dv_i}{dt}\right) + \rho \frac{\pi d^3}{6}\left(-\frac{1}{\rho}\frac{\partial p}{\partial x_i} + \nu \frac{\partial^2 u_i}{\partial x_j x_j}\right) \quad (3.20)$$

where the first term corresponds to fluid drag acting on the particle, in which $\rho$ is the density of the ambient fluid, $d$ is the diameter of the particle and $C_D$ is the drag coefficient. $C_D$ is usually a function of the particle Reynolds number $Re_p$, which is defined as $Re_p = \frac{|v_r|d}{\nu}$, where $\nu$ is the kinematic viscosity of the fluid. There are different relationships for $C_D$, a commonly used for modeling spheres for relatively low $Re_p$ is $C_D = \frac{24}{Re_p}$, and more complex relationships are avaialble for higher $Re_p$ and different shapes of the particle [48]. The commonly used relationship for sand and gravel for $Re_p \leq 10^4$ is [78]

$$C_D = \frac{24}{Re_p} + 1.5 \quad (3.21)$$

The next term in equation 5.17 corresponds to the net gravitational force acting on particle. The acceleration due to gravity always acts along the negative z-direction (if z is chosen as the vertical-axis), thus $g_i = -g\delta_{i3}$ where $g$ is the gravitational acceleration and $\delta_{ij}$ is the Kronecker-delta. $\rho_s$ in the gravitational force term is material density of the particle.

The third force term corresponds to the lift force acting on the particle, where $C_L$ is the lift coefficient, $\omega$ is the vorticity of the fluid around the particle and $\epsilon_{ijk}$ is the alternating unit tensor. The lift force depends on the gradient of velocity around a particle that is moving in a non-uniform rotational flow. The lift coefficient has been shown to be constant for inviscid flows [75]. For relatively smaller Reynolds number the lift coefficient relationship suggested by Mei [79] can be used, which is a modified version of the relationship proposed in the seminal work of Saffman [80].

The next term corresponds to force on the particle due to added mass. This is force is important for cases in which the particle is large enough to pull in additional fluid along with it, and the added mass coefficient is generally considered a constant, equal to the inviscid approximation $C_m = 0.5$ [59]. In this force term, $\frac{Du_i}{Dt}$ correspond to the material derivative of the fluid. The last term in the momentum balance equation of the particle corresponds to the force induced by fluid stresses on the particle, and have been calculated by

interpolating the flow-field variables to the position of the particle. Loth [81] has argued that a simple addition of forces, as done in equation 5.17 may not be perfectly correct, due to non-linear interactions between the fluid forces, but in general these effects are assumed to be small and the simple addition is expected to hold for most practical purposes. Equation 5.17 can be further simplified by dividing through out by mass of the particle $m = \rho_s \frac{\pi d^3}{6}$ and then multiplying by $\frac{\rho_s}{\rho}$. Thus equation 5.17 reduces to

$$\left(\frac{\rho_s}{\rho} + C_m\right)\frac{dv_i}{dt} = \frac{3}{4}\frac{C_D}{d}|v_{ri}|v_{ri} + \left(\frac{\rho_s}{\rho} - 1\right)g_i + C_L\left(\epsilon_{ijk}v_{rj}\omega_k\right) + C_m\frac{Du_i}{Dt} + \left(-\frac{1}{\rho}\frac{\partial p}{\partial x_i} + \nu\frac{\partial^2 u_i}{\partial x_j x_j}\right) \quad (3.22)$$

Also if $\frac{\rho_s}{\rho} - 1$ is represented as $R$, whose value for quartz based sand is about 1.65; and $C_m\frac{Du_i}{Dt}$ is added and subtracted to the right hand side of equation 5.19, it can be further simplified to

$$\frac{dv_i}{dt} = \frac{1}{C_m^R}\left[\frac{3}{4}\frac{C_D}{d}|v_{ri}|v_{ri} + Rg_i + C_L\left(\epsilon_{ijk}v_{rj}\omega_k\right) + \left(C_m + 1\right)\frac{Du_i}{Dt}\right] \quad (3.23)$$

where $C_m^R = 1 + R + C_m$. As most high-resolution simulations are conducted in non-dimensional space, the above equations should be non-dimensionalized using the appropriate velocity and length scales. e.g. In the case we are simulating flow in an open-channel, we can use the mean streamwise velocity of the flow in the channel $U_m$ as the velocity scale and the depth of the channel $H$ as the length scale. Then equation 5.20 can be normalized by multiplying it by $\frac{H}{U_m^2}$. Thus the non-dimensional form of equation 5.20 is

$$\frac{d\tilde{v}_i}{d\tilde{t}} = \frac{1}{C_m^R}\left[\frac{1}{St}\tilde{v}_{ri} - \frac{\delta_{i3}}{Fr^2} + C_L\left(\epsilon_{ijk}\tilde{v}_{rj}\tilde{\omega}_k\right) + \left(C_m + 1\right)\frac{D\tilde{u}_i}{D\tilde{t}}\right] \quad (3.24)$$

In the above equation $Fr^2$ is the square of the densimetric Froude number of the flow, and $St$ is the Stokes number of the flow. Ther are defined as

$$Fr^2 = \frac{U_m^2}{RgH} \quad (3.25)$$

$$St = \frac{4}{3C_D}\frac{\tilde{d}}{|\tilde{v}_{ri}|} \quad (3.26)$$

### 3.4.1 Integration of the additional force terms

The semi-implicit time stepper discussed in section 2 have been used with some modifications. $1+R+C_m$ for almost all cases would be a constant, so henceforth

it will be referred to as $C_m^R$. For purpose of implementation of equation 5.21 using the aforementioned semi-implicit time-stepper, it can be rewritten as

$$\frac{d\tilde{v}_i}{d\tilde{t}} = \frac{1}{StC_m^R}\left(\tilde{u}_i - \tilde{v}_i\right) - \frac{\delta_{i3}}{Fr^2 C_m^R} + \frac{C_L}{C_m^R}\epsilon_{ijk}\left(\tilde{u}_j - \tilde{v}_j\right)\tilde{\omega}_k + \frac{(C_m+1)}{C_m^R}\frac{D\tilde{u}_i}{D\tilde{t}} \tag{3.27}$$

In the above equation clubbing all the terms on the right-hand side that depend on the particle velocity ($v_i$), we get

$$\frac{d\tilde{v}_i}{d\tilde{t}} = \left(-\frac{1}{StC_m^R}\tilde{v}_i + \frac{C_L}{C_m^R}\epsilon_{ijk}\tilde{\omega}_j\tilde{v}_k\right) + \frac{1}{StC_m^R}\tilde{u}_i - \frac{\delta_{i3}}{Fr^2 C_m^R} + \frac{C_L}{C_m^R}\epsilon_{ijk}\tilde{u}_j\tilde{\omega}_k + \frac{(C_m+1)}{C_m^R}\frac{D\tilde{u}_i}{D\tilde{t}} \tag{3.28}$$

In Nek5000, the term $\frac{D\tilde{u}_i}{D\tilde{t}}$ can be evaluated in the eulerian grid (mesh for the fluid simulation) and then interpolated to the location of the particles for updating particle velocity, and henceforth $\frac{D\tilde{u}_i}{D\tilde{t}}$ would be referred to as $\tilde{w}_i$. Also, for purpose of analysis different coefficients and constants in force terms have been represented by different symbols

$$\alpha = \frac{1}{StC_m^R}, \quad \beta = \frac{C_L}{C_m^R}, \quad \gamma = \frac{1}{Fr^2 C_m^R} \quad \text{and} \quad \eta = \frac{1+C_m}{C_m^R} \tag{3.29}$$

so equation 3.28 can be rewritten as

$$\frac{d\tilde{v}_i}{d\tilde{t}} = \left(-\alpha\tilde{v}_i + \beta\epsilon_{ijk}\tilde{\omega}_j\tilde{v}_k\right) + \alpha\tilde{u}_i - \delta_{i3}\gamma + \beta\epsilon_{ijk}\tilde{u}_j\tilde{\omega}_k + \eta\tilde{w}_i \tag{3.30}$$

The system of ODE that has to be solved in order to update the velocity and position of a particle has been rewritten using equation 16 and 3.30. Also, as the equations have already been non-dimensionalized, henceforth all the variables (like $\tilde{u}$, $\tilde{v}$ etc.) have been used without the $\tilde{}$

$$\begin{pmatrix} \dot{x}_i \\ \dot{v}_i \end{pmatrix} = \begin{bmatrix} 0 & I \\ 0 & \left(-\alpha\delta_{ik} + \beta\epsilon_{ijk}\omega_j\right) \end{bmatrix} \underline{q} + \begin{pmatrix} 0 \\ \alpha u_i - \delta_{i3}\gamma - \beta\epsilon_{ijk}\omega_j u_k + \eta w_i \end{pmatrix} \tag{3.31}$$

this is similar to the analysis done in section 2, and the above ODE system has the structure

$$\dot{\underline{q}} = A\underline{q} + \underline{f}(\underline{q}, t) \tag{3.32}$$

In the above system $A$ is the primary source of stiffness, though unlike section , it also has a non-linear component. Also, $A$ in the current system is not a constant, and has to be evaluated before every update of $q$. So like section 2, an implicit method (like BDF-k) would be used to update $\underline{q}$ and an explicit method (like EXT-k) would be used to update $\underline{f}$. Using the notation for BDF-k and

EXT-k (k can be 1, 2 or 3 depending on the order of accuracy required) used in section 2, equation 3.32 can be written as

$$(\beta_0 I - \Delta t A^n)\,\underline{q}^n \quad = \quad \sum_{j=1}^{k} \left(\beta_j \underline{q}^{n-j} + \Delta t \alpha_j \underline{f}^{n-j}\right) \tag{3.33}$$

From the above equation it is obvious that the relationship for updating the position of the particle is exactly similar to the one elucidated in section 2. The new particle velocity update relationship is

$$B^n_{3\times 3} \begin{pmatrix} v_1 \\ v_2 \\ v_3 \end{pmatrix}^n \quad = \quad \sum_{j=1}^{k} \left(\beta_j v_i^{n-j} + \Delta t \alpha_j C_i^{n-j}\right) \tag{3.34}$$

In the above equation the index $i$ corresponds to the space-dimensions. $B$ is a $3 \times 3$ matrix (for a 3D case) and when expanded

$$B^n_{3\times 3} \quad = \quad \begin{bmatrix} \beta_0 + \Delta t\alpha & \beta\Delta t\omega_3^n & -\beta\Delta t\omega_2^n \\ -\beta\Delta t\omega_3^n & \beta_0 + \Delta t\alpha & \beta\Delta t\omega_1^n \\ \beta\Delta t\omega_2^n & -\beta\Delta t\omega_1^n & \beta_0 + \Delta t\alpha \end{bmatrix} \tag{3.35}$$

And $C_i$ is defined by

$$C_i = \alpha u_i - \delta_{i3}\gamma + \beta\epsilon_{ijk}u_j\omega_k + \eta w_i \tag{3.36}$$

In order to get an explicit relationship for $v_i$ from equation 3.34, $B$ needs to be inverted. So solution of equation 3.34 is

$$\begin{pmatrix} v_1 \\ v_2 \\ v_3 \end{pmatrix}^n \quad = \quad B^{-1} \left[\sum_{j=1}^{k} \left(\beta_j v_i^{n-j} + \Delta t \alpha_j C_i^{n-j}\right)\right] \tag{3.37}$$

$B^{-1}$ can be evaluated using the Cramer's rule for a $3 \times 3$ matrix, that is

$$B^{-1} \quad = \quad \frac{1}{|B|} \begin{bmatrix} b_{22}b_{33} - b_{32}b_{23} & b_{13}b_{32} - b_{33}b_{12} & b_{12}b_{23} - b_{22}b_{13} \\ b_{23}b_{31} - b_{33}b_{21} & b_{11}b_{33} - b_{31}b_{13} & b_{13}b_{21} - b_{23}b_{11} \\ b_{21}b_{32} - b_{31}b_{22} & b_{12}b_{31} - b_{32}b_{11} & b_{11}b_{22} - b_{21}b_{12} \end{bmatrix} \tag{3.38}$$

where $|B|$ is equal to
$(b_{11}(b_{22}b_{33} - b_{32}b_{23}) - b_{12}(b_{21}b_{33} - b_{23}b_{31}) + b_{13}(b_{21}b_{32} - b_{22}b_{31}))$.

Now equation 3.37 can be written as

$$\begin{pmatrix} v_1 \\ v_2 \\ v_3 \end{pmatrix}^n = B^{-1} \begin{pmatrix} \sum_{j=1}^{k} \left( \beta_j v_1^{n-j} + \Delta t \alpha_j C_1^{n-j} \right) \\ \sum_{j=1}^{k} \left( \beta_j v_2^{n-j} + \Delta t \alpha_j C_2^{n-j} \right) \\ \sum_{j=1}^{k} \left( \beta_j v_3^{n-j} + \Delta t \alpha_j C_3^{n-j} \right) \end{pmatrix} \tag{3.39}$$

Using the relationship 3.38 and representing the three components of the right-hand side matrix as $R_1$, $R_2$ and $R_3$, equation 3.39 can be simplified to

$$v_1 = \frac{1}{|B|} \left[ R_1(b_{22}b_{33} - b_{32}b_{23}) + R_2(b_{13}b_{32} - b_{33}b_{12}) + R_3(b_{12}b_{23} - b_{22}b_{13}) \right] \tag{3.40}$$

$$v_2 = \frac{1}{|B|} \left[ R_1(b_{23}b_{31} - b_{33}b_{21}) + R_2(b_{11}b_{33} - b_{31}b_{13}) + R_3(b_{13}b_{21} - b_{23}b_{11}) \right] \tag{3.41}$$

$$v_3 = \frac{1}{|B|} \left[ R_1(b_{21}b_{32} - b_{31}b_{22}) + R_2(b_{12}b_{31} - b_{32}b_{11}) + R_3(b_{11}b_{22} - b_{21}b_{12}) \right] \tag{3.42}$$

A point to note is that all the components of matrix $B$ should be calculated at time $t^n$ and for particle position $x_i^n$. This is tricky because $\omega_i^n$ is required to be interpolated to particle position $x_i^n$ before calculation of $x_i^n$. In order to get around this quandary, $\omega_i^n$ would be approximated using $EXT - k$ from the previously saved values of $\omega_i$, along with $v_i$ and $u_i$. In the next subsection, the algorithm for the model has be described step by step. The algorithm can be used to implement the semi-implicit Lagrangian particle tracking model on an existing CFD code.

### 3.4.2 Algorithm for implementation into a CFD code

In this section we elucidate the important portions of the algorithm for implementing the Lagrangian particle method discussed in the previous two sections. For purpose of describing the algorithm, position of particle in 3D is represented using $x^n, y^n, z^n$, where the superscript $n$ describes the time step or iterations since the simulation started. Velocity of a particle in 3D is represented using $vx_n^n, vy_n^n, vz_n^n$, the superscript $n$ describes the time step and the subscript $n$ describes the position of the particle. So, $vx_{n+1}^n$ represents velocity of the particle in x-direction at time $n$ and at position $x^{n+1}, y^{n+1}, z^{n+1}$. $ux^n, uy^n, uz^n$ correspond to the velocity field of the fluid at time $n$, and $ux_n^n, uy_n^n, uz_n^n$ correspond to the velocity of the fluid at time $n$ and at the position corresponding to time $n$. Similar notation have been used for fluid vorticity $\omega x^n, \omega y^n, \omega z^n$, and the material derivative of the fluid velocity $wx^n, wy^n, wz^n$. Rest of the notations used are same as the ones used in the previous sections.

1. Initialize particles with their positions $(x^0, y^0, z^0)$, velocities $(vx_0^0, vy_0^0, vz_0^0)$, diameter, relative density, lift coefficient, etc.

2. At this time the Eulerian fields, like fluid velocity $(ux^0, uy^0, uz^0)$ has been

initialized using the initial condition of the flow or previous computation result.

3. Calculate vorticity $(\omega x^0, \omega y^0, \omega z^0)$ using the Eulerian fluid velocity.

4. Calculate the material derivative $(wx^0, wy^0, wz^0)$ using the Eulerian velocity field. The material derivative has two parts, the $\frac{du}{dt}$ term that has been calculated using the BDF$k$, and the non-linear part that has been evaluated for the whole Eulerian field. A small issue in using BDF is that at this point of time in the simulation there is no record of $ux^{-1}$ .. etc., thus for BDF-1 $ux^{-1}$ has been assumed to be equal to $ux^0$. This results in $\frac{du}{dt}$ being equal to zero. Even though the approximation of $ux^{-1} = ux^0$ is erroneous, it is acceptable because $ux^{-1}$ is used in BDF$k$ for only the first three time iterations.

5. Interpolate the Eulerian fields to the current particle locations to get, the fluid velocity at the particle location $ux_0^0, uy_0^0, uz_0^0$, the fluid vorticity at the particle location $\omega x_0^0, \omega y_0^0, \omega z_0^0$, and the material derivative of the fluid velocity at the particle location $wx_0^0, wy_0^0, wz_0^0$.

6. Extrapolate particle velocity $(vx_0^0, vy_0^0, vz_0^0)$, and fluid velocity interpolated to the particle positions $(ux_0^0, uy_0^0, uz_0^0)$, using EXT$k$ (k=1, for first time-step). The extrapolated velocities $vx_0^1$.. and $ux_0^1$.. are an initial approximation for $vx_1^1$.. and $ux_1^1$.., which will be required for calculation of $\alpha$ in the matrix $B$ (see equations 29 and 3.35).

7. Similarly extrapolate fluid vorticity at current particle location $\omega x_0^0, \omega y_0^0, \omega z_0^0$ to approximate the vorticity at the updated particle location $x^1, y^1, z^1$ (which have not been calculated yet). In general $\omega x_0^1, \omega y_0^1, \omega z_0^1$ is calculated using EXT-$k$, e.g. EXT1 $\omega x_0^1 = \omega x_0^0$.

8. Calculate right-hand side ($R_1, R_2$ and $R_3$) of equation 34, using the required parameters ($ux_0^0, ..., \omega x_0^0$... etc.) calculated in the previous steps.

9. Compute components of matrix $B$, $b_{11}, b_{12}, ...$ using equation 3.35.

10. Update the particle velocity $(vx_1^1, vy_1^1, vz_1^1)$ using $R_1, R_2$ and $R_3$, components of matrix $B$, and equations 40 to 42.

11. Calculate the new particle position $x^1, y^1, z^1$ using $x_0, y^0, z^0$ and $vx_1^1, vy_1^1, vz_1^1$ calculated in the previous step.

12. Impose the applicable boundary conditions for the particles, thus correcting the position and velocity of the particles if it goes out of the computational domain after the previous step.

13. Repeat steps 3 to 12, the only difference being the order for BDF and EXT would be 2 for the next step and then 3 for rest of the computation. Also

the previously computed and saved (from the previous three iterations) values of particle positions ($x^n, ..$), particle velocity ($vx_n^n, ..$), interpolated fluid velocity ($ux_n^n, ..$) at the particle location, interpolated fluid vorticity ($\omega x_n^n, ..$) at the particle location, interpolated material derivative of the fluid velocity ($wx_n^n, ..$) at the particle location, and the Eulerian fluid velocity field ($ux^n, ..$) have to used for the calculations.

## 3.5 Testing the model

The model described in the previous sections was implemented on the massively-parallel open-source incompressible Navier-Stokes solver Nek5000 [31]. Nek5000 uses spectral-element method for spatial discretization [82], with higher-order orthogonal Legendre polynomial basis on Gauss-Lobatto-Legendre (GLL) nodes. The temporal discretization in Nek5000, uses a semi-implicit scheme that is a mix of third-order Backward difference (BDF3) and Extrapolation (EXT3) schemes. In this section, different components of the particle model would be tested to check the veracity of the model.

### 3.5.1 Particle under a Plane-Couette flow

This test was designed to check the portion of the model simulating the lift force acting on the particle. In the particle momentum balance equation (see eqn. 5.21), the lift force acting on the particle is a cross-product of the relative velocity of the particle (with respect to the flow) and vorticity of the fluid at the particle. In order to test the implementation of the model, the best option is to test it under the condition of constant vorticity. Thus, for this test a laminar Plane-Couette flow was used. The flow is induced by the top plate, which moves with a constant velocity 1 in the positive x-direction (see figure 1a). The bottom plate is kept stationary, thus the velocity profile between the plates is defined by $u = \frac{1+y}{2}\hat{i}$, where $u$ is the flow velocity in the x-direction. The vorticity due to the flow is constant throughout the domain, and is equal to $-0.5\hat{k}$. In this flow, a particle was placed at the center of channel ($y = 0$). In the particle model, all the components of momentum balance equation (eqn. 5.21), except the lift force, were turned off. So, in the system the only force acting on the particle was due to the lift induced by the constant vorticity field $\overrightarrow{\omega} = -0.5\hat{k}$. A constant lift coefficient of $C_L = 6.0$ was used to simplify the analysis, along with the relative density $(1+R)$ of the particle equal to 1.5. The result from the simulation was compared with the relationship for motion of the particle under the aforementioned conditions, the relationships were derived from the ODEs

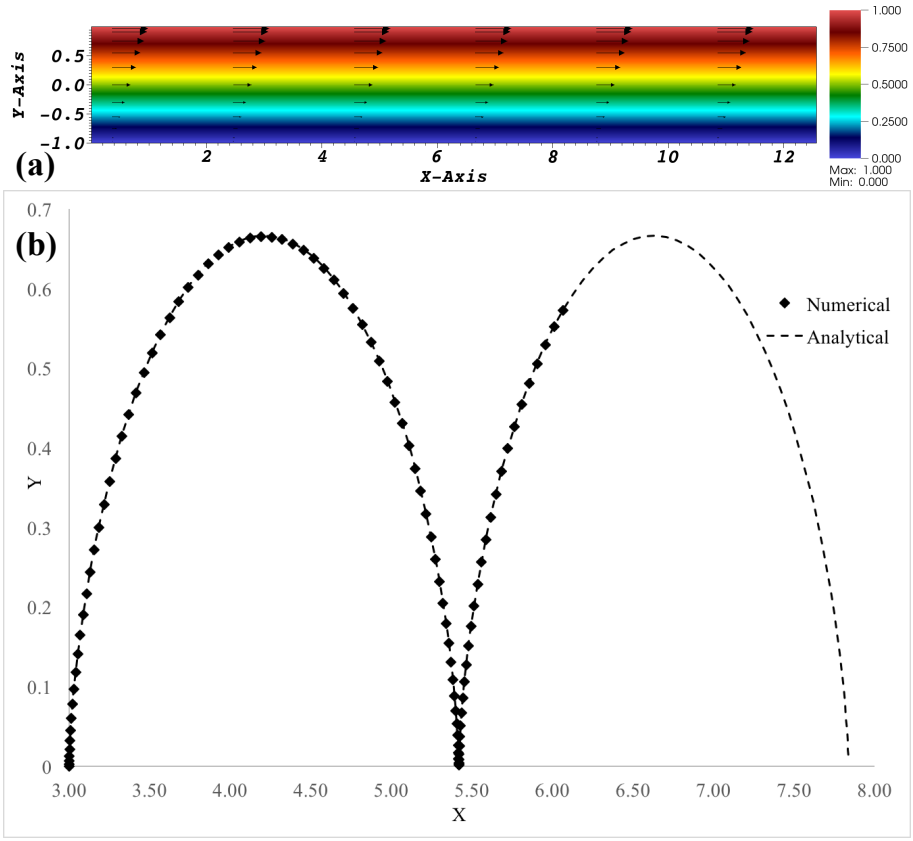


Figure 3.1: Results from test to check the accuracy of the model for lift force. (a) Velocity magnitude between the two plates of the laminar Plane-Couette flow. (b) Comparison between the analytical relationship and the numerical simulation.

representing the motion of the particle:

$$y = y_0 + \frac{1}{k - 0.5}\sin^2(\frac{\theta t}{2}) \tag{3.43}$$

$$x = x_0 + \frac{k}{2\,(k - 0.5)}\left(t - \frac{\sin(\theta t)}{\theta}\right) \tag{3.44}$$

where $k = \frac{0.5C_L}{1+R}$, and $\theta^2 = k(k - 0.5)$. $t$ is time, $(x, y)$ are the x and y coordinates of the particle, and $(x_0, y_0)$ is the coordinate of the particle before it starts moving. Figure 3.1 compares the particle position predicted by the above relationships, with the particle trajectory predicted by the numerical simulation. For all practical purposes, the two match perfectly, thus confirming the accuracy of the semi-implicit model in modeling the lift force acting on the particle.

### 3.5.2 Particle moving in a circular flow

The next test was designed to test the working of the part of the momentum balance equation, that models the force induced by the fluid stresses on a particle.

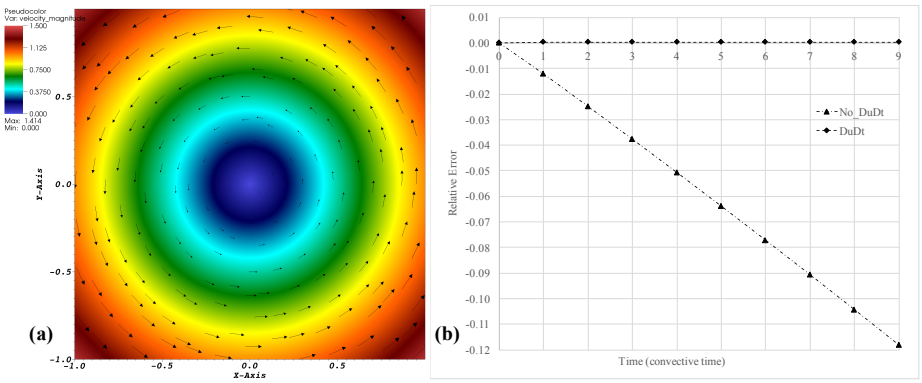


Figure 3.2: Results from test to check the accuracy of the model for the force induced by fluid stresses on the particle. (a) Velocity magnitude for the laminar circular flow. (b) Relative error of the model in predicting the path of the particle in the circular flow, with and without the $Du/Dt$ term.

The fluid stress terms are modeled using the $\frac{Du}{Dt}$ term in equation 24, without the $C_m$ in front, which comes from the "added mass" term. For the test, a particle of fluid ($R = 0$) was placed in a constant circular flow (see figure. 3.2a), defined by $\overrightarrow{u} = (-y\hat{i}, x\hat{j}, 0\hat{k})$. In a physical experiment, the particle of fluid will continue to rotate with rest of the fluid in a circle, without any deviation. This happens because the stress from the surrounding fluid keeps the particle moving along the circular path. So, if the fluid stresses are not considered in the momentum balance equation that defines the motion of the particle, the particle is expected to have a deviate from the circular path. Thus, First a case was simulated with only Stokes drag acting on the particle. In this case the particle was found to have both a tangential and a outward radial velocity. The radial velocity deviates the particle away from the circular path it is expected to move in. In the next case, the part of the model that captures the fluid induced stress terms was switched on. The particle was found to behave according to expectation, and move along a circular path. Relative error of the model in predicting the path of the particle in the circular flow, with and without the fluid stress term ($Du/Dt$) have been plotted in figure 3.2b. This provides evidence that the model is able to capture the fluid stress terms accurately.

### 3.5.3 Free falling particles in a quiescent fluid

One of the most fundamental force that acts on a particle is due to gravity. A particle falling freely through quiescent fluid, accelerates due to gravity. But once the particle velocity is high enough that the force due to gravity is balanced by the drag on the particle induced by the ambient fluid, the particle stops accelerating. The velocity at which this occurs, is called the terminal velocity of the particle, and it depends on the size of the particle, viscosity of the ambient fluid, and relative density of the particle. A Lagrangian point-particle model

should be able to model this dynamic correctly, with the particle converging to terminal velocity. The test in this section has been designed to check the aforementioned aspect of the model. So, a particle with $R = 1.65$ was placed in a periodic domain containing quiescent fluid. The viscosity of the fluid was set equal to $10^{-6}$, diameter of the particle was set at $D = 0.015$, and the constant force acting on the particle (like gravity) was set equal to $10^3$. All the above stated parameters are in the non-dimensional space, and the values were chosen to setup a case that would result in a relatively high terminal-velocity, thus taking the model longer to converge to the terminal-velocity. During the test, the only force terms included in the particle momentum balance equation were the Stokes drag and body force (gravity).

First the tests were performed for $C_D = \frac{24}{Re_p}$. Based on the assumed values of the parameter, the terminal velocity to which the particle velocity is expected to converge is 12500. Velocity of the particle at each time-step has been plotted for different time-step sizes in fig. 3.3a. As expected, the particle velocity converges in about 550 iterations, when the time-step size is 1.0 time units. As the method put forth in this paper is a semi-implicit method, one expects to take larger time-steps and reach convergence in relatively fewer iterations, without problems with stability of the method. Simulations with time-step size ranging between 100 to 1000 time units have been plotted in fig. 3.3a, and the particle velocity can be seen to converge in about 10-15 iterations. Next, the test was performed with $C_D = \frac{24}{Re_p} + 1.5$. For time-step size of 0.01 time units, the particle velocity converges to approximately 3.651 in about 50 iterations (see fig. 3.3b). For time-step greater than 0.01, the particle velocity can be seen to oscillate around the value it is expected to converge to. Interestingly, the amplitude of the oscillations slightly decreases with increase in iterations. So, the instability does not grow over time (rather damps very slowly). The convergence issues, for complex functions of $C_D$, at relatively large time-steps can be addressed by conducting a few Newton-Raphson iterations during the particle-velocity update step in the algorithm. In the current algorithm the aforementioned step has not been implemented, because for most practical cases the ambient flow does not impose the strict constraints assumed for this test case. Additionally, the time-step used for most practical flows is small enough that convergence of the algorithm under constant body force (like gravity) is not expected be an issue.

## 3.6 Conclusion

Lagrangian particle tracking is one of the most popular modes of modeling particle-laden multiphase flows, both in natural and engineered settings. Almost all the Lagrangian point-particle models use an explicit time-stepper, like Adam-Bashforth, Runge-Kutta etc., to integrate the particle momentum bal-

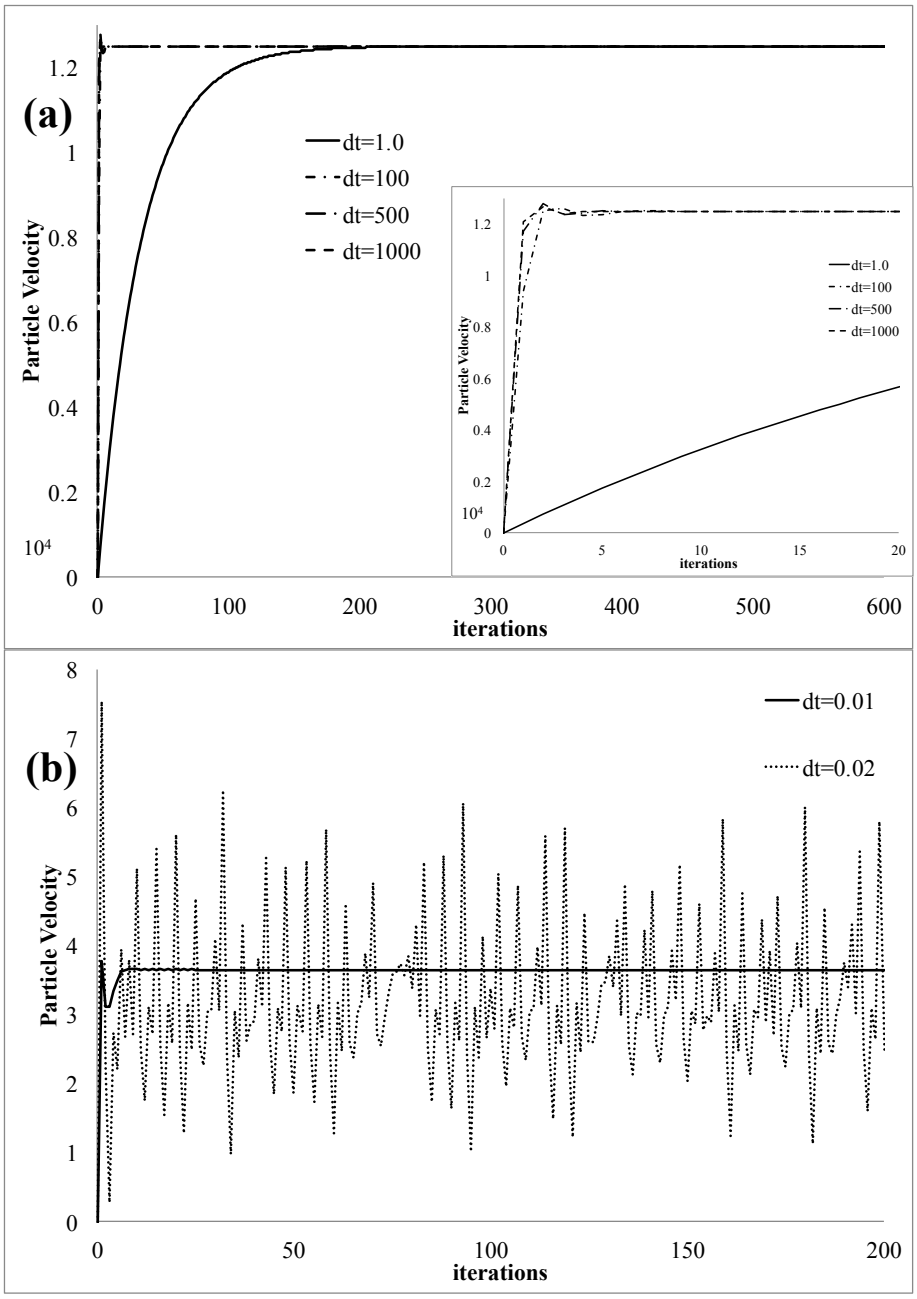


Figure 3.3: Results from test to check the accuracy of the model for a constant body-force like gravity. (a) Number of iterations required for the particle to converge to terminal-velocity, for different size of time-step. In this case where the drag coefficient for the particle is defined by $C_D = \frac{24}{Re_p}$. (b) Number of iterations required for the particle to converge to terminal-velocity, for different size of time-step, where the drag coefficient for the particle is defined by $C_D = \frac{24}{Re_p} + 1.5$.

ance equations. Though, an explicit time-stepper was shown to impose a strict time-step size constraint, especially in cases with small particle size or high fluid viscosity. The current paper puts forth a semi-implicit method, that treats the fast but linear part of the physics implicitly and the slow but non-linear part of the physics explicitly. The implicit part is dealt using Backward difference (BDF-k), and the explicit part is dealt using an extrapolation scheme (EXT-k). The method was first derived for the case where Stokes drag is the only force acting on the particle, and then it was extended to a more complex force-balance equation for the particle. The more complex force-balance equation for the particle included the lift force, fluid stresses at the particle, added mass and gravity. An algorithm that can be used for implementing the proposed method on an existing CFD solver was also elucidated. The derived method was implemented on the high-order spectral element based incompressible Navier-Stokes solver Nek5000. Implementation of the algorithm was tested under different flow conditions, and the algorithm was found to work along the expected lines. Finally, the performance of the method was tested for different complex flows, thus providing further evidence of applicability of the proposed semi-implicit method. The proposed method is one of the first semi-implicit time-stepper devised for Lagrangian particle tracking. Unlike explicit time-steppers, the time-step size in the proposed method is not constrained by the size of the particle, thus underlying its applicability in problems that have a disparate range of particle sizes, like sediment transport, bubble transport and dynamics, dust and particulate flows to name a few.

# CHAPTER 4

# LARGE EDDY SIMULATION (LES) OF FLOW AND BEDLOAD TRANSPORT AT AN IDEALIZED 90-DEGREE DIVERSION: INSIGHT INTO BULLE-EFFECT

## Authors

Som Dutta, Paul Fischer, Marcelo H. Garcia, Published: River Flow 2016, pages:101–109, CRC Press, 2016.

## Abstract

Bifurcations are an integral part of river systems, thus better understanding of the dynamics flow and sediment transport is important for accurate prediction of the long-term geomorphological evolution of these systems. A class of bifurcations in which one of the bifurcating channels continues along the direction of the main channel, and the other comes out laterally, is also referred to as diversion. In 1926, Bulle conducted one of the first studies that quantified the hydrodynamics and bedload transport at a diversion, and to this day his study remains one of the most extensive studies on the topic. Bulle put forth the phenomena of preferential movement of near-bed sediment at a diversion towards the lateral channel, thus this phenomenon is often referred to as the Bulle-Effect. In the current study, the governing mechanism of Bulle-Effect has been explored by conducting LES of the flow and bedload transport at an idealized 90-degree diversion. The scale of the simulated diversion and the bulk Reynolds number are similar to the experiments conducted by Bulle. The simulation was conducted using the open-source spectral element based Navier-Stokes solver Nek5000. Bed load transport was modeled using the Lagrangian particle tracking method. The simulation results clearly portray the tendency of the near bed currents at the bifurcation to move into the side-channel, consequently taking most of the near-bed sediment along with it. The results also affirm the presence of vortices in both the channels after the diversion. The Dynamics of bedload transport at the bifurcation was captured successfully, with the percentage of total sediment entering the side-channel matching Bulles experimental observation. Apart from taking a detailed look at the mechanism behind Bulle-Effect, the current study is also one of the first to use high-resolution LES and Lagrangian particle dynamics to study the hydrodynamics and bed-load transport

dynamics at an experimental scale bifurcation.

## 4.1 Introduction

Bifurcations are an integral part of natural and engineered river systems, thus better understanding of dynamics of the flow and sediment transport at the bifurcations is important for accurate prediction of the long-term geomorphological evolution of these systems. Historically, laboratory experiments on idealized bifurcations have been used to understand the flow and sediment transport at bifurcations; consequently that knowledge has been successfully extrapolated to improve our understanding of field-scale bifurcations. A class of bifurcations in which one of the bifurcating channels continues along the direction of the main channel, and the other comes out laterally, is also referred to as a diversion. Most engineered bifurcations are usually of the diversion variety, and typically they are built to divert water for navigational and irrigational purposes. Recently, diverting water and sediment from rivers has been proposed as a method to rebuild deltas (e.g. the Mississippi river delta in Louisiana, USA [23], which are in danger of being lost due to sea-level rise and other factors. Few natural bifurcations also have layout similar to a diversion, thus studying flow and sediment transport at fluvial diversions have both scientific and engineering implications.

Bulle [1] conducted the first study that quantified the hydrodynamics and bedload transport at a diversion, and to this day it remains one of the most extensive studies on that topic. Bulles work for the first time put forth the phenomena of preferential movement of near-bed sediment discharge at a diversion towards the lateral channel, thus this phenomenon is often referred to as the Bulle-Effect. Over the years there have been studies corroborating the findings of Bulle [9, 39], and it is known that the phenomenon is due to spiraling flow near the bed primarily going into the lateral channel, but the definitive mechanism governing the phenomena is still elusive. In the current study, the governing mechanism has been explored through conducting Large Eddy Simulation (LES) of the flow and bedload transport at an idealized 90 degree diversion, whose scale matches the experiments conducted by Bulle.

Previous studies that have used high-resolution numerical simulations to study the hydrodynamics at 90-degree diversions were either in the laminar regime [83], or used Reynolds Averaged Navier Stokes (RANS) equations for simulating the flow [84]. RANS based models may capture the mean hydrodynamics of the flow, but fail to capture coherent structures, accurate flow separation length, and other details that would provide the full picture of the mechanism behind a highly non-linear phenomena like the Bulle-Effect. Ideally, one would like to conduct Direct Numerical Simulations (DNS) to capture all the turbulent eddies, but it becomes exorbitantly costly for high Reynolds numbers. Thus the current study conducts LES, which resolve the energy producing (and transport-

ing) scales and models the energy dissipating scales of turbulence [85, 86]. Also, bedload transport has been modeled using the Lagrangian particle formulation for bedload transport [87].

## 4.2 Numerical Model

The simulation was conducted using Nek5000, an open-source spectral element based incompressible Navier-Stokes solver [31]. The full 3D Navier-Stokes equation is solved using the Spectral Element Method (SEM), which combines the accuracy of spectral methods with the flexibility of numerical methods based on local approaches (like FEM) [88]. Nek5000 uses Legendre polynomials as the basis function, along with a Gauss-Lobatto-Legendre grid. Time stepping is based on the 3rd order backward difference for the time derivative, and 3rd order extrapolation for the nonlinear convective terms. All the other terms are evaluated implicitly at time level $t^n$. As part of the LES, turbulent energy from the unresolved scales has to be dissipated; this process is modeled using a local element based explicit cutoff filter (a spectral filter) in the wave number space to remove energy from the highest wave-numbers [89].

### 4.2.1 Details of the Flow Model

Layout of the simulated domain has been reproduced in fig. 4.1. The dimensions are similar to the experiment conducted by Bulle for the 90-degree diversion. The dimensions have been non-dimensionalised using depth of the channel. Reynolds number of the simulated flow is 20,000, which is comparable to Bulles experiment, and is calculated using the mean flow velocity in the main-channel and depth of the channel. As part of the inflow boundary condition, the flow in the main-channel had been re-circulated in order to have a fully developed turbulence before the flow reaches the area of interest at the diversion. Turbulent outflow boundary condition was imposed at the outlets; and a 50-50 flow-split was imposed at the bifurcation, using a fast implicit enforcement of the flow division, for accurate yet faster convergence of the simulation. A similar algorithm has been previously used to study flow at a vascular bifurcation [90]. A no-slip condition was imposed at the bottom, and sidewalls whereas slip (or symmetry) condition was imposed at the top wall to replicate open-channel flow.

The simulation was conducted for at least 180 convective time units, before data was collected for Reynolds averaging and analysis of the flow results. 180 convective time units was found to be long enough for the flow in the inlet channel to become fully turbulent. Transition of the flow to fully turbulent was relatively fast due to the use of wall-bounded vorticity coupled with random fluctuations as the initial condition. All the simulations were conducted on the

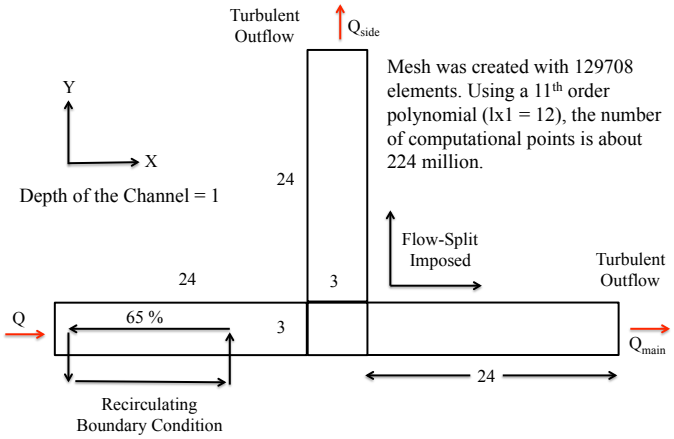


Figure 4.1: Layout of the simulated domain, with the imposed boundary conditions and other imposed conditions like flow-splitting and recirculating inflow.

peta-scale supercomputer BlueWaters, housed at NCSA, University of Illinois at Urbana-Champaign. The simulations were run using up to 32768 processors.

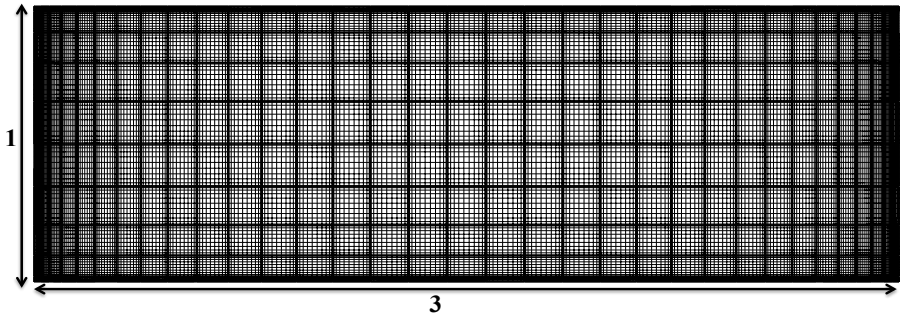


Figure 4.2: Cross-section of the channel shows part of the mesh, illustrating the distribution of the elements along with the collocation points. The first grid point in the z-direction is placed approximately at $z^+ = 0.058$, and in the y-direction at $y^+ = 0.65$.

### 4.2.2 Sediment Transport Model

Sediment phase, especially suspended load can be modeled relatively accurately using an Eulerian approach [66]; though recent studies have shown that eddy-resolved flow simulation combined with Lagrangian particle model for sediment tend to provide a more realistic representation of bedload sediment transport [91]. As the Bulle-Effect is relatively more pronounced for near-bed sediment, the current study models bedload using Lagrangian particle formulation. The sediment has been assumed to be spherical non-rotating particles. The coupling between sediment and water is assumed to be one-way, that is the moving

water imparts force on the sediment, but the size and concentration of sediment is assumed to be small enough that there is no significant force acting on the water due to the sediment. Also, the concentration of sediment is assumed to be small enough that the interaction between the sediments can be ignored.

The motion of the particle is defined using the equations

$$\frac{d\tilde{x}_i}{d\tilde{t}} = \tilde{v}_i \tag{4.1}$$

$$\frac{d\tilde{v}_i}{d\tilde{t}} = \frac{1}{1+R+C_m}\left[\frac{1}{St}\tilde{v}_{ri} - \frac{\delta_{i3}}{Fr^2} + C_L\left(\varepsilon_{ijk}\tilde{v}_{rj}\tilde{\omega}_k\right) + \left(C_m+1\right)\frac{D\tilde{u}_i}{D\tilde{t}}\right] \tag{4.2}$$

The above equations are in the non-dimensional form, and they have been non-dimensionalized using the mean fluid velocity and depth of the channel. The first equation is used to define the position of the particle ($x_i$) according to its velocity ($v_i$). The second equation is the momentum balance equation for the particle, where the term outside the bracket on the right-hand side consists of $R$, which is referred to as submerged specific gravity. For the combination of sand and water, $R$ is usually taken as 1.65. $C_m$ is the coefficient of added mass, and is associated with the force on the particle due to the added mass of fluid it pulls with itself while moving. For the current study we ignore the force due to added mass, thus $C_m$ is zero. The first term inside the bracket corresponds to the drag force on the particle, and is related to the particles Stokes number ($St$) that depends on the diameter of the particle and the relative velocity between the particle and the fluid ($v_{ri}$). The next term corresponds to the force of gravity on the particle, and in the non-dimensional form acceleration due to gravity has been parameterized using the Froude number ($Fr$). The next terms corresponds to lift force on the particle due to the fluid. The lift force is important to model the saltation path of a sand particle accurately [87], and it can also act as a surrogate for the extra wall-normal force on the particle due to turbulent bursts. In the current model the resolution is high enough to capture the turbulent bursts, thus a surrogate is not required to represent this aspect of the physics. In the current study we do not take into account the lift force on the particle due to vorticity of the fluid around the particle. So, the version of the model used in the current study is a simplified version of the full model, represented by the aforementioned equation, that takes into account the drag force and gravitational acceleration. The governing equations of the particles have been integrated in time using a stable semi-implicit scheme that is stable even in the limit $St$ goes to 0. The particles were introduced in the computational domain only after the turbulent flow had reached a statistically steady state. A set of 11,250 particles was placed upstream from the diversion, upstream enough that the influence of the diversion on the flow is not felt by the particles when they initially start moving. Interaction of the particles with the walls was defined as a partially elastic collision; momentum in the wall-normal direction (both bottom and side-walls) was factored by the coefficient

of restitution of 0.2, and tangential momentum was factored in by coefficient of restitution 0.89 [87].

## 4.3 Results

The result section has been divided into two parts. In the first part, all the flow results would be discussed, and then in the second the results related to the particle dynamics would be discussed.

### 4.3.1 Hydrodynamics at the Diversion

The instantaneous velocity magnitudes at different depths in the channel have been plotted in fig. 4.3. At the height of 1 percent and 5 percent from the bottom, the flow in the main-channel primarily moves into the lateral channel. At height of 50 percent from the bottom the flow is more equitably distributed between the two channels, and at 75 percent more flow goes into the main-channel. The aforementioned observation can be attributed to be the reason behind preferential movement of near-bed sediment towards the lateral channel. In the figure, akin to Bulles observation one can also observe the flow getting separated from the left wall of the lateral channel and the right wall of the main channel.

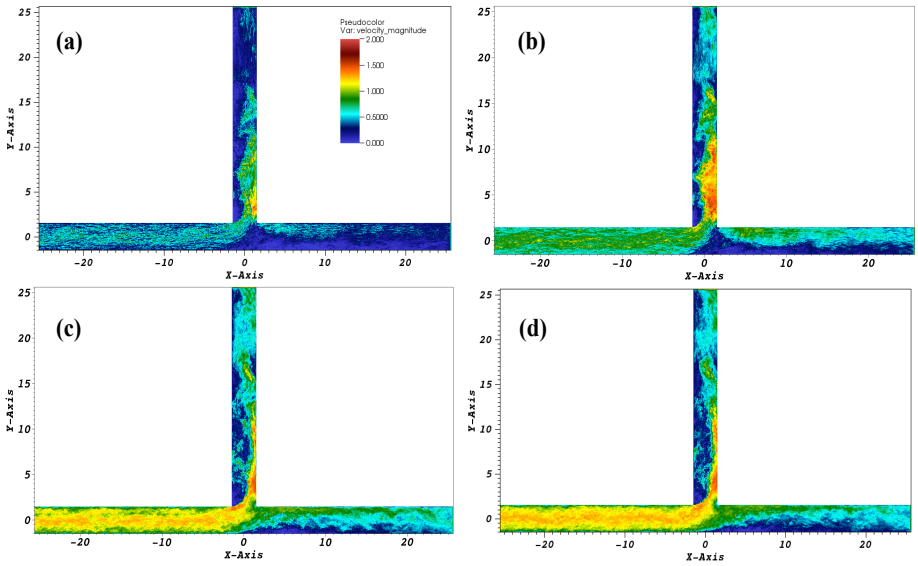


Figure 4.3: Instantaneous velocity magnitude in the channel at: (a) 1 percent height from the bottom (b) 5 percent height (c) 50 percent height (d) 75 percent height from the bottom.

Also, the flow separation in the lateral channel is relatively wider at heights 50 percent and above, and relatively narrower near the bed. The opposite is

observed for the flow separation in the main channel, and this perfectly matches observations made by Bulle. We can also observe the turbulent streaks at the bottom of the main-channel, especially for the profile at a height 1 percent from the bottom (Fig. 4.3a). In order to get a holistic picture of the flow the time-averaged velocity magnitude has been plotted below (see Fig. 4.4). The time averaging was done over 4 convective time unit.

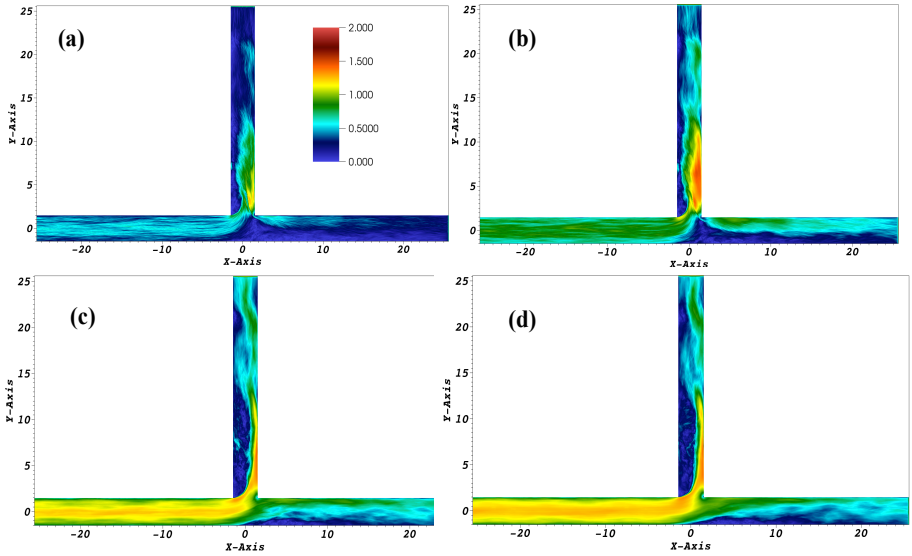


Figure 4.4: Time-averaged velocity magnitude in the channel at: (a) 1 percent height from the bottom (b) 5 percent height (c) 50 percent height (d) 75 percent height from the bottom.

The time-averaged velocity magnitudes at different depths are in general similar to the instantaneous velocity magnitude profiles, though with the fluctuations smoothed out thus providing a more complete view of the preferential flow path. The average flow near the bottom primarily moves into the side-channel, and the portion that continues into the main-channel primarily sticks to the left bank. For the flow entering the side-channel, the flow near the bottom (at a depth of 1 to 10 percent from the bottom) covers almost the whole width of channel, whereas in the upper half of the channel the flow separates appreciably from the left wall and stays confined near the right wall. On the other hand for the flow continuing in the main-channel, in the upper half of the channel the flow almost covers the whole width. Finally, the flow in both the channels becomes uniform after about 10 channel lengths, but this process is impeded in the side-channel due to presence of the vortexes that are shed at regular interval.

The instantaneous velocity magnitude at different cross-sections has been plotted in Fig 4.5. Cross-sections (a) and (b) are in the main channel before the bifurcation, (c) is in the main-channel just after the bifurcation, and (d) is in the lateral channel just after the bifurcation. At x = -10 (see Fig. 4.5a) the flow has not been influenced by the diversion, thus the high velocity core

is located at the center of the channel. At x = -2 (see Fig. 4.5b) the high velocity core has shifted towards the diversion (right side in the plot as the flow is coming out of the plane). In the instantaneous velocity magnitude plots, ejections and turbulent bursts from bottom and the sidewalls can be seen, thus showing further evidence of a well-resolved boundary-layers at the walls.

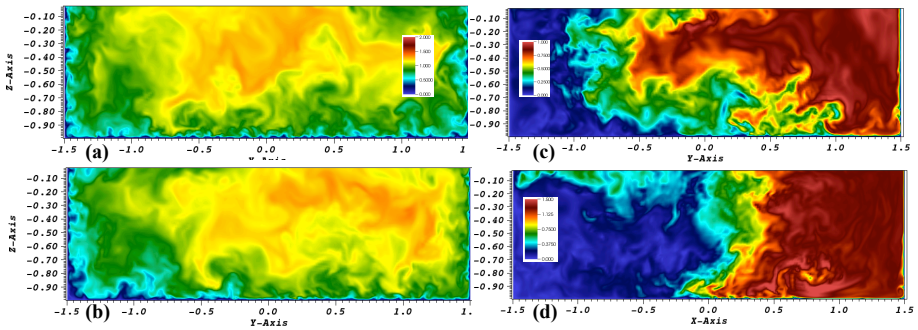


Figure 4.5: Instantaneous velocity magnitude in the channel at different cross-sections: (a) at x = -10 (b) at x = -2 (c) at x = 3 (d) at y = 3. For (a), (b) and (c), the flow is coming out of the plane, for (d) the flow is going into the plane. Also, (a-b), (c) and (d) have been plotted using different scales.

The panels (c) and (d) correspond to cross-sections at x =3 and y = 3, that is just after the bifurcation in both the channels. The flow can be seen to have separated from one of the sidewalls, with the width of separation zones increasing with increase in depth for (c), and vice-versa for (d). These observations are consistent with those of Bulle.

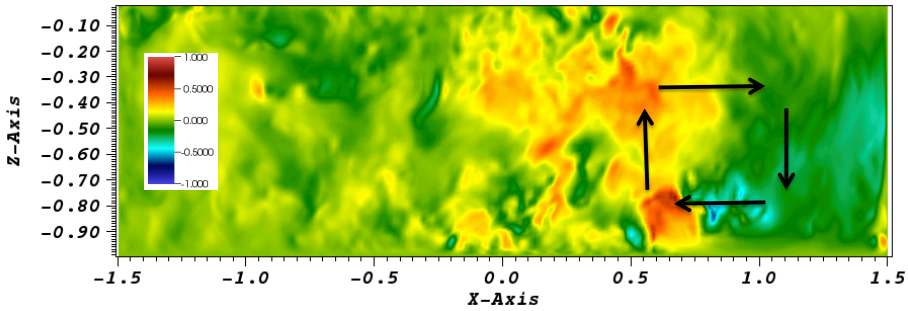


Figure 4.6: Instantaneous vertical velocity at the cross-section y = 3, this is a cross-section in the lateral channel just after the bifurcation. Direction of the flow is into the plane, and the rotating arrows show the clock-wise rotating vortex that is formed in the lateral channel.

Instantaneous vertical velocity (z) has been plotted in Fig. 4.6, for a cross-section in the lateral channel just after the bifurcation (same as Fig. 4.4d). Pronounced positive and negative z-velocity next to each other can be observed in Fig 4.6, indicating presence of clock-wise rotating vortex in the high-flow core of the cross-section, with the flow going into the plane. The instantaneous velocity field may not show all the important features of a flow, due to presence

of strong fluctuations; thus the time-averaged velocity at different cross-sections has also been analyzed later.

Flow in the main-channel before the bifurcation is uniformly distributed, but the bifurcation influences the flow by pulling the high velocity core towards the direction of the side-channel. This was obvious from the plot of the velocity magnitude (Fig. 5 a, b). What also happens is part of the momentum of the flow in the x-direction is transformed into momentum in the y-direction. And this becomes obvious from the plot of the time-averaged velocity in the y-direction at different distances from the diversion (see Fig. 7 below).

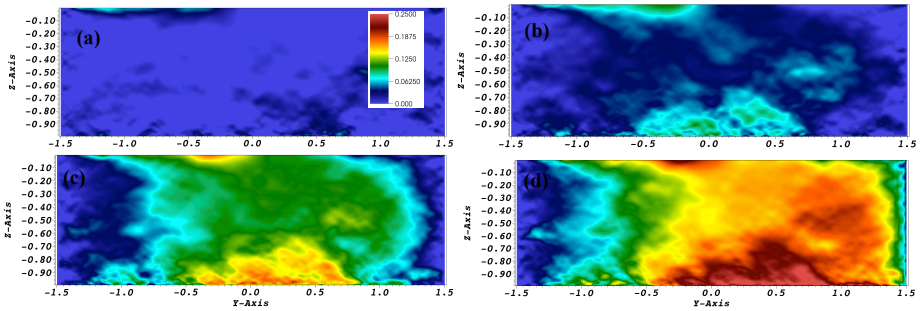


Figure 4.7: Velocity in the y-direction in the main-channel at different cross-sections: (a) at x = -10 (b) at x = -3 (c) at x = -2 (d) at y = -1.5. The mean flow is out of the plane, and the maximum of the velocity scale is 0.250.

At x = -10, no influence of bifurcation is felt by the flow, as the velocity in the positive y-direction is zero (see Fig. 4.7a). But as one moves closer to bifurcation, at x = -3 the flow near the bottom of the channel shows the first significant sign of changing direction with relatively higher value of y-velocity than rest of the cross-section. And this transfer of momentum gets stronger as one moves closer to the bifurcation. The flow in the main-channel was also analyzed, by visualizing the flow at different cross-sections after the bifurcation (see Fig. 4.8 and 4.9).

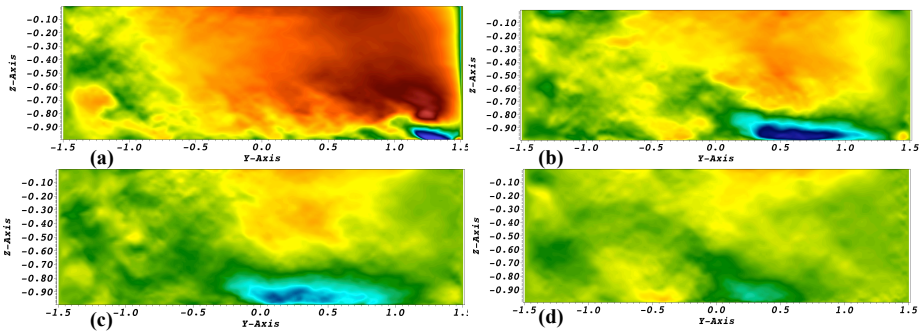


Figure 4.8: Velocity in the y-direction in the main-channel at different cross-sections: (a) at x = 1.5 (b) at x = 3 (c) at x = 5 (d) at x = 10. The flow in general is coming out of the plane, and the maximum of the velocity scale is 0.500.

In Fig. 4.8 velocities in the y-direction have been visualized, and Fig. 9 velocities in z-direction has been visualized. They together portray the presence of secondary flow structures.

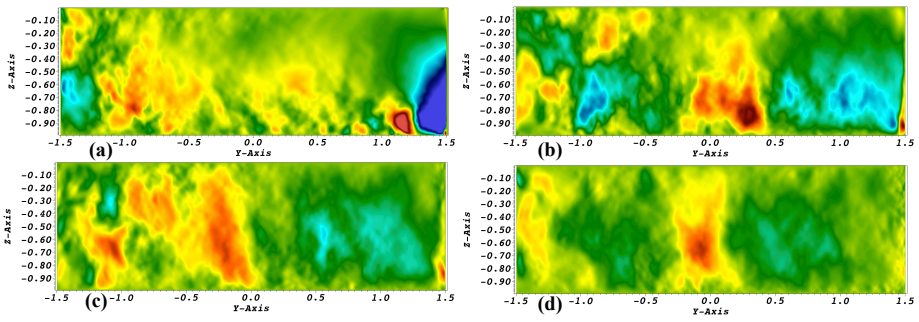


Figure 4.9: Velocity in the z-direction in the main-channel at different cross-sections: (a) at x = 1.5 (b) at x = 3 (c) at x = 5 (d) at x = 10. The flow in general is coming out of the plane, and the maximum of the velocity scale is 0.250.

At start of the main-channel after the bifurcation, a counter-clockwise rotating (with the flow going downstream from the bifurcation) secondary flow vortex can bee seen to be form at the corner of left side of the channel (see Fig. 4.8, 4.9a). In Fig. 4.8 and 4.9, it is on the right bottom corner because the flow is coming out of the plane in the panels. Along with the strong vortex in the high velocity core of the flow, a weak vortex is formed in the region where the flow gets separated (more obvious in z-velocity plots in Fig. 4.9). The weaker vortex have been formed due to the shear created by a stronger vortex, and this can be interpreted from the fact that right next to the region of positive z-velocity lies the region of negative z-velocity. Both the vortices get weak by the time they reach a distance of 10 from the center of the bifurcation. Next the structure of the flow going into the side-channel was analyzed. Similar to the case of the flow in the main-channel, time-averaged x-velocities (see Fig. 4.10) and z-velocities (see Fig. 4.11) at different cross-sections have been visualized. Similar to the vortex in the main-channel, a vortex is initiated at the bottom corner of the high-velocity core of the flow, at the start of the side-channel (see Fig 4.10-4.11 a). Though by the time the flow reaches the other end of the section (x = 1.5), the magnitude of x-velocity reduces. A similar but opposite trend, that is relatively smaller to bigger magnitude, is portrayed by velocity in the y-direction at this section.

At the section y = 3, the clock-wise rotating vortex can be seen to have become stronger (Fig. 4.10-4.11 b). And like in the case of the main-channel, the strong vortex also induces a weak clock-wise rotating vortex in the low-flow region of the cross-section. Though in contrast to the main-channel, instead of maintaining two vortices (one strong and one weak) the flow coalesces into a single vortex that remains strong till y = 10 (see Fig. 4.10-4.11 c, d). In order

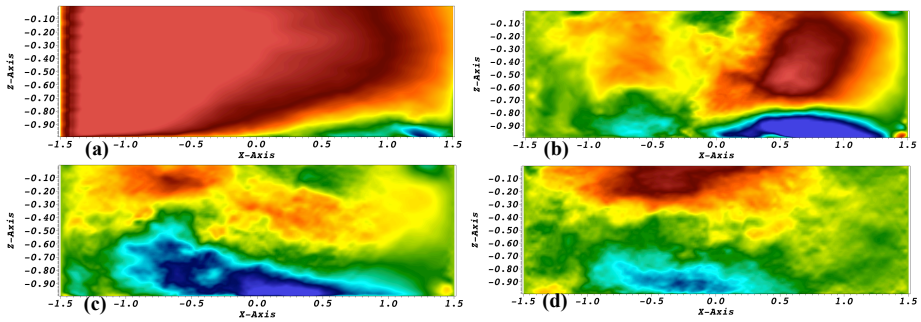


Figure 4.10: Velocity in the x-direction in the side-channel at different cross-sections: (a) at y = 1.5 (b) at y = 3 (c) at y = 5 (d) at y = 10. The flow in general is going into the plane, and the maximum of the velocity scale is 1.0 for (a), 0.5 for the rest.

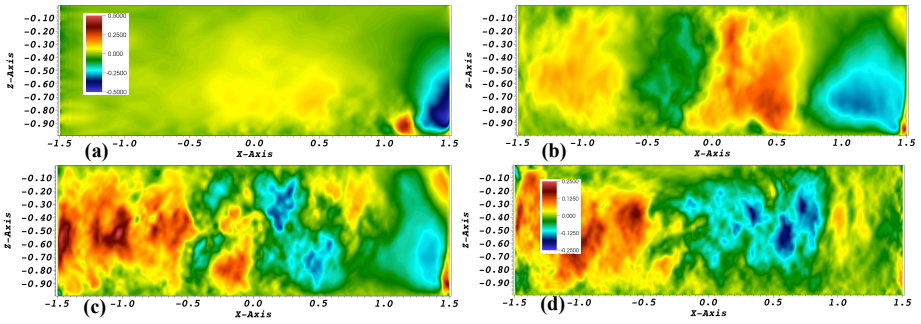


Figure 4.11: Velocity in the z-direction in the side-channel at different cross-sections: (a) at y = 1.5 (b) at y = 3 (c) at y = 5 (d) at y = 10. The flow is coming out of the plane, and the maximum of the velocity scale is 0.5 (a-b) and 0.25 (c-d).

to find regions of the flow where the vorticity is relatively higher, magnitude of total instantaneous vorticity at three sections before and after the diversion were analyzed (see Fig. 4.12).

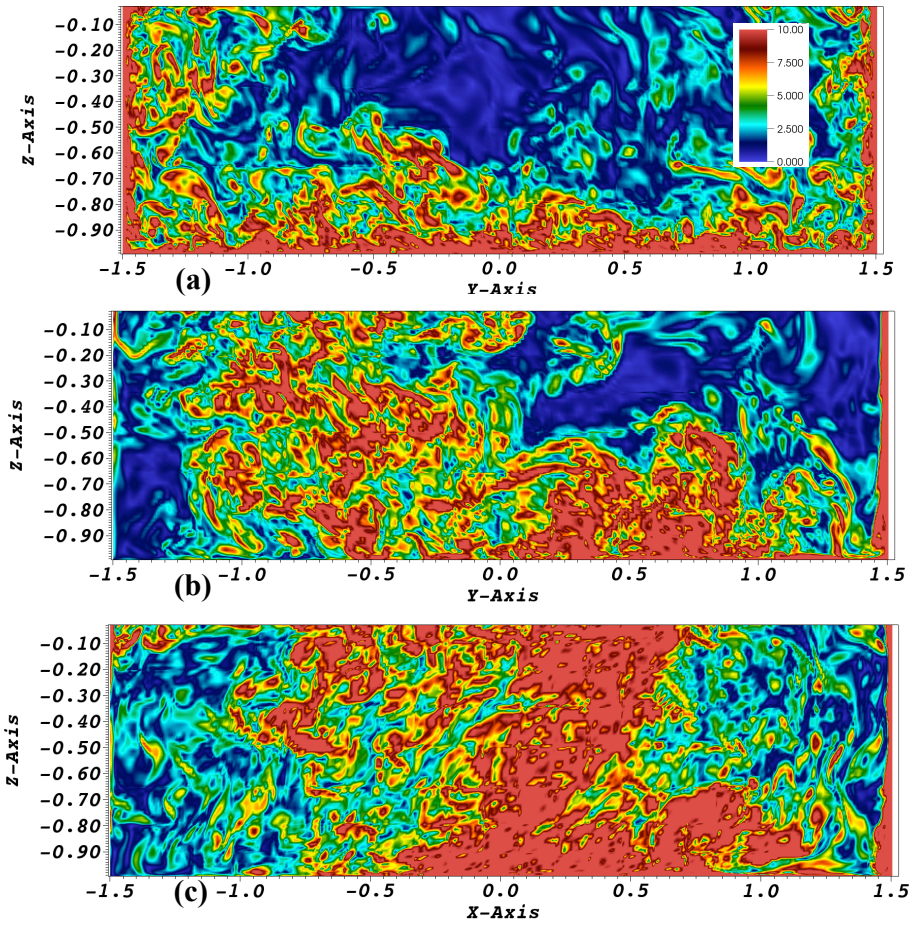


Figure 4.12: Magnitude of instantaneous vorticity at three different cross-sections, (a) x = -5, (b) x = 3 and (c) y =3. Direction of the flow is coming out of the plane for (a) and (b), and into the plane for (c).

In Fig. 4.12, the first panel (a) shows magnitude of instantaneous vorticity at a section in the channel before the diversion. Flow in this section is not biased towards any of the sidewalls. Thus vortices can be seen to shed from all the three walls almost evenly. The next panel (b) represents the vorticity at a cross-section in the main-channel but just after the diversion. Signature of the strong counter-clockwise rotating vortex can be seen on the right hand side of the cross-section (near the bottom). One can also observe vortex shedding at the interface of the high-velocity region, and the region where the flow has separated from the wall. This may be caused due to the shear between portions of the flow having diametrically opposite characteristics. Similar phenomena can be also observed in the cross-section taken in the side channel (c). The

strong signature of the clockwise rotating vortex is on the right hand side of the section, whereas the vortex shedding due to shear between the two regions of the flow is at the center of the channel. In the current section, the characteristics of the flow have been studied in some details. In the next subsection, the transport of bedload sediment at the diversion is discussed.

### 4.3.2 Bedload Transport at the Diversion

A set of 11250 particles representing sand grains was released near the bottom of the channel, upstream from the diversion. The particles were uniformly distributed in three layers (in z) between x = -5 to -2, y = -1 to 1, and z = 0.02 to 0.11. The diameter of the particle used was 0.015 (dimensionless), which was based on the reported size of particle used by Bulle in his experiments. Starting from top of the channel, the time required by a particle to reach the bottom of channel under quiescent condition is 0.42 convective time units. This means irrespective of the initial position of the particles in the vertical, they have been placed far enough upstream that they all travel near the bed by the time they reach the diversion.

In physical units, the equivalent diameter of the particles is 1.05 mm, and density 2.65 $kgm^{-3}$. The position and velocity of each particle was tracked over time, thus the time-evolution of the horizontal positions of the particles have been reproduced below (see Fig. 4.13 and 4.14). After being released the sediment in general moves in a straight line, discounting small deviations due to turbulent fluctuations of velocity, till the last position portrayed in panel (a) of Fig. 4.13, where for the first time the particles show proclivity to move into the side-channel. In the final position portrayed in panel (b), the left side of the sediment set has already moved into the side-channel. This is obviously caused by the flow near the bottom, which flows preferentially into the side-channel. In panel (c) it is clear that major portion of bedload will enter into the side-channel. Also, the sediment that have moved into the side-channel with the fast moving flow, can be seen to be moving away from the right wall of the channel. The movement of the sediment away from the right wall, towards the left hand side of the diverted channel becomes obvious in panel (d). This can be completely attributed to the clock-wise rotating vortex discussed in the previous subsection. Even though the sediment is taken into the side-channel by the fast bottom-hugging currents that is primarily confined to the right hand side of the diverted-channel; the clock-wise rotating vortex sweeps the sediment towards the left hand side of the channel. The sediment swept to the left hand side then gets trapped into the recirculation zone formed in the region where the flow has separated. This becomes apparent by the final evolution state of the sediment in panel (d) of Fig. 4.13.

In order to analyze the percentage of total sediment that enters the side-channel, the simulation with the particles was further continued. Results from

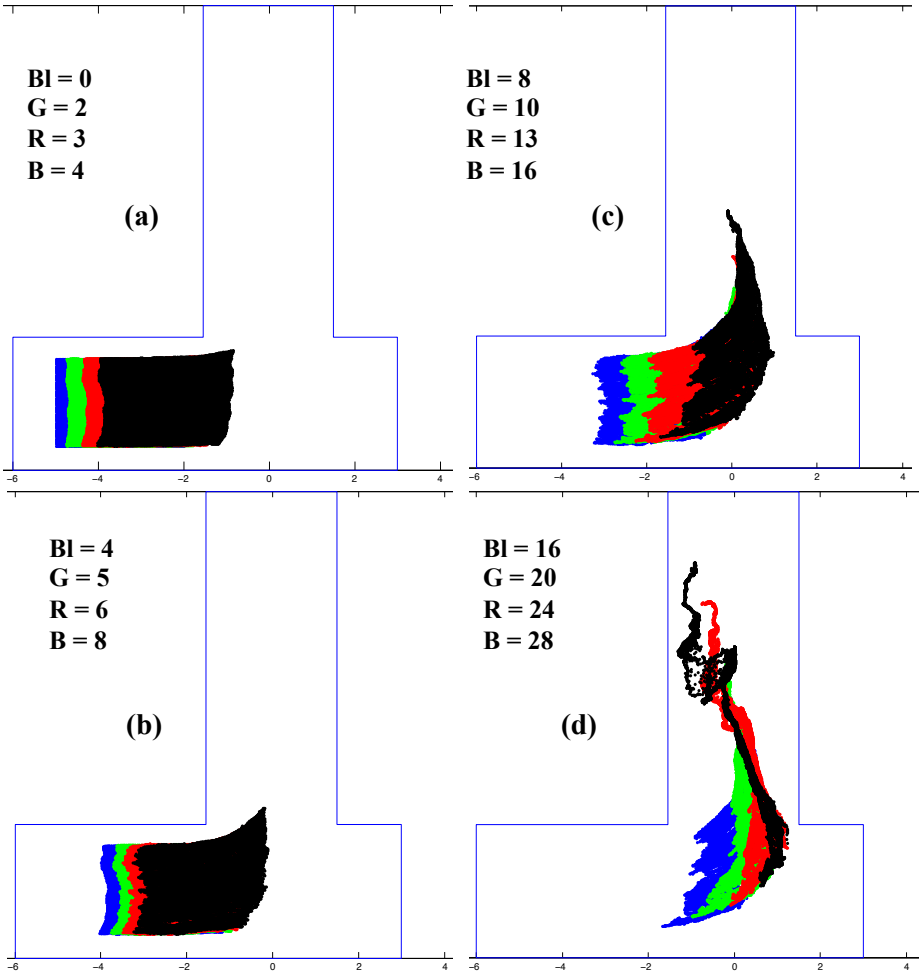


Figure 4.13: The plot shows the time evolution of horizontal positions of sediment particles moving in the channel. In every panel, the initial position is represented using blue, followed by green, red and black respectively. Also, the final position in a panel is the initial position in the next panel. That means black in (a) is blue in (b). The labels correspond to time of simulation in convective time unit. Bl is blue, and B is black.

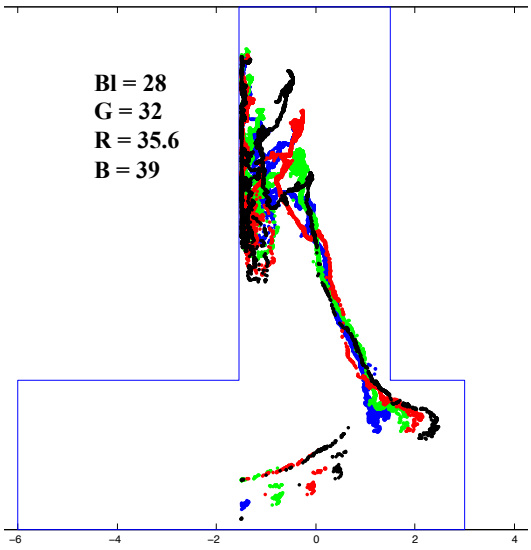


Figure 4.14: Evolution of horizontal position of the sediment particles. The sequence of colors representing the earliest to latest position of sediment in the figure are, blue, green, red and black. After the rapid evolution shown in panels 13 c and d, the evolution portrayed in the current panel is relatively slow. The labels correspond to time of simulation in convective time unit. Bl is blue, G is green, R red, and B is black.

the last few evolution state have been plotted in Fig. 4.14. From the positions of the particles portrayed in Fig. 4.14, two conclusions can be drawn. First, the process of preferential entry of the near bed sediment into diverted-channel is relatively quick, but once the sediment has entered the channel it has a tendency to get trapped in the recirculation zone near the left-wall. Second, once the sediment enters the recirculation-zone, it gets slowly spread throughout the recirculation zone. It is also obvious that very small amount of the total sediment finally entered the main-channel. This percentage was found to be around 4.29 percent. Bulle in his experiment on the 90-degree diversion observed that 9.45 percent sand entered the main-channel, but in his experiments only 45.2 percent of the total flow entered the side-channel, whereas we used a 50-50 split for our simulations. Thus Bulles experiment with which we should compare our numbers is the 30-degree case, where 50 percent of the flow enters the side-channel. For that case, Bulle observed that depending on how long the experiment was run, 2.67 to 4.47 percent of sediment entered the main-channel. Our number 4.29 percent is close to the range observed by Bulle. On the other hand, expecting that only 2.67 percent of the sediment enters the main-channel for our case is erroneous, because the side-channel for the 30-degree case has higher entrance width than the 90-degree case, thus allowing more near-bed sediment to enter the side-channel. And 4.47 might be erring on the higher side, because that experiment is influenced by the deposition of sediment near the entrance. So, the case that might be comparable is the 60-degree diversion case,

as percentage of water entering side-channel is closer to 50 percent (it is 48.2 percent); and the width of the side-channel entrance is closer to the 90-degree case. For the aforementioned experiment, Bulle observed that 3.8 percent of the sediment entered the main-channel. An interesting observation that can be made from fig. 4.14, is that some sediment at the center of the main-channel have been aligned with the separation-curve between the flow going in to the lateral channel, and the flow remaining in the main channel. From the plot, it can also be inferred that the flow on the right hand side of the separation-curve is relatively slower than that on the left hand side of the curve.

## 4.4 Conclusions

The current study used LES to numerically model the flow at a 90-degree diversion. Additionally, a Lagrangian particle-tracking model was used for modeling the bedload transport at the diversion. The numerical simulations were conducted using the open source spectral element based incompressible Navier-Stokes solver Nek5000. The simulation was found to successfully capture the expected hydrodynamics like, preferential movement of the near-bed flow into the side-channel, presence of a clockwise vortex in the side-channel and anti clockwise in the main-channel. It was also able to capture the flow separation zones in the two channels, with the one in the side-channel decreasing in width with depth, whereas the one in the main-channel increased in width with increase in depth. Some surprising elements of the flow were also unearthed, like the presence of a weak vortex in conjugation with the stronger vortices in each channel.

Bedload transport at the diversion was also modeled successfully. 11250 particles were released from upstream of the diversion. Most of them entered the side-channel, with only 3.85 percent moving into the main-channel. The percentage of sediment entering the main-channel agrees with the observations made by Bulle. Sediment was found to enter the side-channel with the fast-moving bottom-hugging currents confined to right hand side of the channel. Once inside the side-channel, sediment was swept to the left hand side of the channel by the vortex. Thus, most of the sediment entering the diverted-channel was eventually trapped in the recirculation zone formed due to separation of the flow from the left wall of the side-channel. This phenomenon may cause formation of sandbars under the recirculation zone.

The current study is one of the first to successfully conduct LES of flow at an experimental scale diversion, along with modeling bedload transport. All the previous studies had used RANS based hydrodynamic models, or simulated the flow in the laminar regime. The current study is a step towards conducting LES coupled with large-scale Lagrangian particle tracking (to model sediment transport), for other configurations of the diversion. This would not only provide

further insight into the inherent mechanism of Bulle-Effect, but also enhance the understanding of flow and sediment transport at bifurcations. This knowledge should prove useful to quantify the amount of sediment that could be diverted at different locations to rebuild the Mississippi Delta.

# CHAPTER 5

# INSIGHT INTO BULLE-EFFECT USING HIGH-RESOLUTION NUMERICAL SIMULATIONS: ANALYZING THE SENSITIVITY OF THE PHENOMENON

## 5.1 Introduction

In the previous chapter results from Large Eddy Simulation (LES) of flow and sediment transport at an idealized 90-degree diversion was discussed. The simulation was conducted for the case of $Re_{bulk} = 20000$, thus the flow was fully turbulent. The layout of the simulation is similar to the geometry used by Bulle [1] in his experiments, though in the case of Bulle only 45 percent of the total flow moves into the lateral channel and the bulk Reynolds number is around 25000. From the simulation results, it is clear that under the simulated conditions most of the flow near the bed enters the lateral channel, even though only 50 percent of the total flow enters the lateral-channel. This provides glimpse of the mechanism that causes disproportionate amount of bedload sediment to enter the lateral-channel. The evidence for the mechanism is further corraborated by the behavior of the bedload sediment modeled as Lagrangian particles. The simulation was also able to capture strong secondary flow circulation in the lateral and the main channel after the diversion, and similar observation have been previously made by Neary et al. in context of 90-degree lateral intake [84].

In the current chapter the phenomena of Bulle-Effect is further analyzed by performing Direct Numerical Simulation (DNS) and Large Eddy Simulation (LES) of flow and sediment transport through different configurations of the idealized diversion similar to Bulle's experiments. By virtue of theoretical analysis by Riad [9] had zeroed onto a set of parameters that might influence the distribution of sediment between the two channels at a simplified diversion:

$$\frac{s_{side}}{s_{main}} = \left( \frac{q_{side}}{q_{main}}, Re, Fr, \frac{d}{D} \right) \tag{5.1}$$

where $s_{side}$ and $s_{main}$ is the sediment entering the side and the main channels, $q_{side}/q_{main}$ is the ratio of the flow entering the two channels, $Re$ is the Reynolds number of the flow, $Fr$ is the Froude number or the flow, $d$ is the size of sediment and $D$ is the depth of the flow at the diversion. In order to explore the effect of the above parameters on the phenomenon of Bulle-Effect, DNS and LES simulations were conducted for the 90-degree diversion for different bulk Reynolds number ($Re_{bulk}$), different sediment sizes ($d/D$), and different flow-

splits ($q_{side}/q_{main}$). in the next section the numerical model has been described in some details, especially the algorithm used for imposing the flow-split. After that the Results have been discussed, and finally the chapter has been concluded by summarizing the major findings.

## 5.2 Numerical Model

The computational fluid dynamics (CFD) solver used for all the simulations is the open-source spectral-element based higher-order incompressible Navier-Stokes solver Nek5000 [31]. Depending on the $Re_{bulk}$, the simulations required anywhere between 37.5 million to 240 million computational grid points. Thus the simulations were conducted on the peta-secale High Performance Computing (HPC) system Blue Waters, NCSA, UIUC. Sediment transport in the simulations were modeled as Lagrangian particles. A Semi-implicit Lagrangian particle tracking algorithm was implemented in Nek5000, and some details of the model have been discussed in this section, and more have been elaborated in Chapter 3.

### 5.2.1 The Navier-Stokes Solver

The Navier-Stokes equation (shown below) is solved without any modeling in the domain, subjected to appropriate boundary and initial conditions.

$$\frac{\partial \mathbf{u}}{\partial t} + \mathbf{u} \cdot \nabla \mathbf{u} = -\nabla p + \frac{1}{Re} \nabla^2 \mathbf{u} \tag{5.2}$$

and

$$\nabla \cdot \mathbf{u} = 0 \tag{5.3}$$

where $\mathbf{u}$ is the velocity vector/field, $p$ is the hydrodynamic pressure normalized by the density, and $Re$ is the Reynolds number of the flow. $Re = UD/\nu$, where $U$ is the characteristic velocity of the flow, which in the current simulations was assumed to be the mean streamwise velocity $U_{mean}$. $D$ is the characteristic length scale, and in the current study the depth of the flow was assumed to be the characteristic length-scale. $\nu$ is kinematic viscosity. Thus for the current simulations, $Re = Re_{bulk}$.

The above equations are spatially discretized using the spectral element method (SEM) [88, 92]. The SEM is a high-order method that uses the weighted residual approach similar to finite element method (FEM). SEM combines the flexibility of FEM with the high-order accuracy and fast convergence of Spectral methods. Higher-order polynomial based methods are especially suited and necessary for turbulent flow simulations because, high-order polynomial eliminates dispersion errors, which is very important for large-scale and long-term turbulence calculations [93].

For temporal discretization, a semi-implicit time-stepping scheme is used, in which the nonlinear terms of the Navier-Stokes equation are treated explicitly; and the linear part that is the Stokes problem is treated implicitly. The time derivative in eqn. 5.2 is calculated by using a kth-order backwards difference formula (BDF-k, where k=2 or 3). The formula for $k = 2$ is:

$$\frac{3\mathbf{u}^n - 4\mathbf{u}^{n-1} + \mathbf{u}^{n-2}}{2\Delta t} = S\left(\mathbf{u}^n\right) + NL^n \tag{5.4}$$

where $\mathbf{u}^{n-q}$ is the velocity at time $t^{n-q}$ (q = 0,1,2), $S(\mathbf{u}^n)$ is the linear symmetric Stokes operator. This operator implicitly contains the divergence-free constraint (eqn. 5.3). $NL^n$ corresponds to the nonlinear terms at time $t^n$, and is calculated through extrapolation by using the formula

$$NL^n = -\sum\nolimits_j \alpha_j \mathbf{u}^{n-j} \cdot \nabla \mathbf{u}^{n-j} \tag{5.5}$$

For 2nd order scheme ($k = 2$), the values of $\alpha_1$ and $\alpha_2$ used are 2 and -1, respectively. Though primarily a 3rd order scheme is used ($k = 3$), where $\alpha_1 = 8/3$, $\alpha_2 = -7/3$ and $\alpha_3 = 2/3$. The 3rd order extrapolation scheme is similar to 3rd order Adam-Bashforth, as it has a stability region that encompasses a part of the imaginary axis. This leads to the unsteady Stokes problem. which will be solved implicitly:

$$H\mathbf{u}^n - \nabla p^n = \mathbf{f}^n \tag{5.6}$$

$$\nabla \cdot \mathbf{u}^n = 0 \tag{5.7}$$

For $k = 2$, the Helmholtz operator $H = \left(\frac{3}{2\Delta t} - \frac{1}{Re}\nabla^2\right)$. Using the form of an operator the above equation can also be referred to as $S_{us}\left(\mathbf{u}^n = \mathbf{f}^n\right)$.

Coming back to the spatial discretization, the type of SEM used for the current simulations is $\mathbf{P}_N - \mathbf{P}_N$. In SEM functions are estimated as tensor products of Lagrange polynomials. These polynomials are of degree $N$, and are used for each all the $E$ elements of the domain/mesh. So the number of unknown basis for each component of velocity is $n \approx EN^d$, where $d = 1$ or $d = 2$. N usually takes the values between 4 and 16. The high polynomial degree used in SEM is enabled by using tensor product bases of the form (in 2D):

$$\mathbf{u}\left(\mathbf{x}^e\left(r,s\right)\right)|_{\Omega^e} = \sum_{i=0}^{N}\sum_{j=0}^{N} \mathbf{u}_{ij}^e h_i^N\left(r\right) h_j^N\left(s\right) \tag{5.8}$$

where the nodal basis coefficients are represented using $\mathbf{u}_{ij}^e$, and the Lagrange polynomial based on the Gauss-Lobatto quadrature points is represented by $h_i^N$. The Gauss-Lobatto quadrature points are the zeros of the expression $\left(1-\xi^2\right)L_N^{'}\left(\xi\right)$, where $L_N$ is the Legendre polynomial of degree N. The coordinate mapping between $\hat{\Omega} = [-1,1]^d$ and $\Omega^e$ is represented using $\mathbf{x}^e\left(r,s\right)$. A characteristic of SEM that allows substantial reduction of memory and opera-

tions count is that all the operator evaluations and iterative solutions of the implicit steps are computed in matrix-free format [94]. This leads to unstructured data access at the global level, but within each element the data is structured in the form $i - j - k$. For example, differentiation, which is one of the most used operations in operator evaluation, is implemented as a memory-efficient matrix-matrix product.

The spectral element method (SEM) basis from eqn. 5.8 is inserted in the unsteady Stokes operator defined by eqn. 5.6; and after application of numerical quadrature, the discrete form of the unsteady Stokes operator is obtained:

$$\hat{H}\underline{\mathbf{u}}^n - D^T\underline{p}^n = B\underline{\mathbf{f}}^n \tag{5.9}$$

$$D\underline{\mathbf{u}}^n = 0 \tag{5.10}$$

where $\hat{H} = \frac{3}{2\Delta t}B + \frac{1}{Re}A$, $-A$ is the discrete form of the Laplacian operator, $D$ is the discrete form of the divergence operator, the diagonal mass-matrix representing the velocity-mesh is $B$, and the non-linear terms that are treated explicitly are represented by $\underline{\mathbf{f}}^n$. As the Galerkin approach is used in SEM, consequently the eqn. 5.9 is symmetric and all the matrices involved $(\hat{H}, A, B)$ are symmetric positive definite.

The discretized Stokes system defined above, is solved using an iterative method by using a $k - th$ order operator splitting [95]. Operator splitting is applied to the discretized system, this helps avoid ad-hoc boundary conditions. For the 2nd order case ($k = 2$), the equation first computed is:

$$\hat{H}\ \hat{\underline{\mathbf{u}}} = B\underline{\mathbf{f}}^n + D^T\underline{p}^{n-1} \tag{5.11}$$

The above step is followed by the pressure correction step

$$E\delta\underline{p} = -D\ \hat{\underline{\mathbf{u}}} \tag{5.12}$$

$$\underline{\mathbf{u}}^{\ n} = \ \hat{\underline{\mathbf{u}}}\ + \Delta t B^{-1}D^T\delta\underline{u} \tag{5.13}$$

$$\underline{p}^n = \underline{p}^{n-1} + \delta\underline{p} \tag{5.14}$$

In the above system of equations $E = \frac{2}{3}\Delta t D B^{-1} D^T$ is the Schur complement of the Stokes operator that governs the pressure in the absence of the viscous term. The above computation steps are solved iteratively using preconditioned conjugate gradient (PCG). As $\hat{H}$ is strongly diagonally dominant, Jacobi preconditioning works perfectly for eqn. 5.11. On the other hand E, which is relatively less well-conditioned, is solved by multilevel overplapping Schwarz method [96], or by a Schwarz multigrid methods [97]. The step defined by eqn. 5.12 is the most computationally intensive substep of the Navier-Stokes solver.

### 5.2.2 Computational Domain and Boundary Conditions

The computation domain used for the simulations is an idealized version of Bulle's experiments. The mean depth of the flow was used as the characteristic length-scale, and was used to normalize the dimensions of the geometry of the diversion. Also, the mean inflow velocity ($U_{mean}$) was used as characteristic velocity-scale. The layout for the 90-degree case, along with the imposed boundary conditions have been illustrated in fig. 5.1 below. The number of ele-

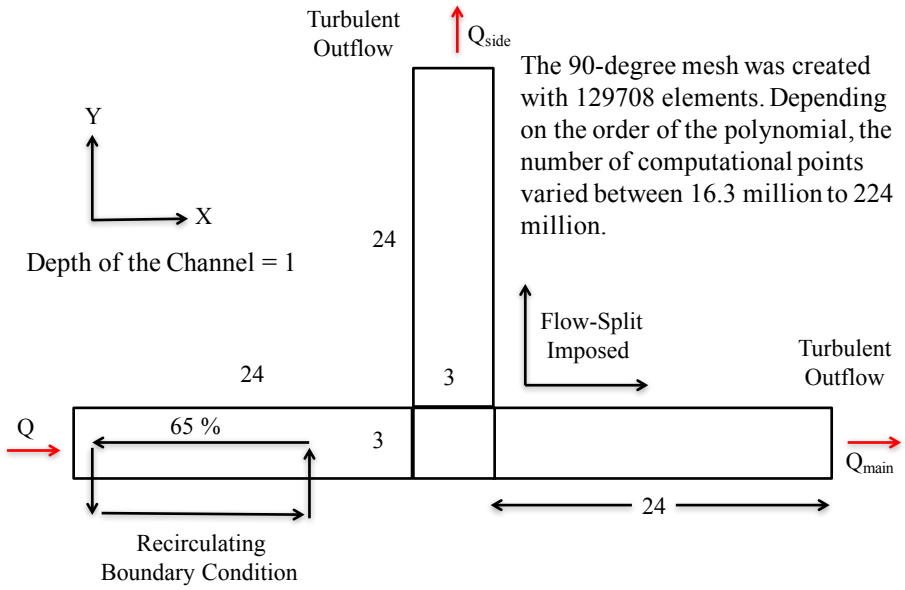


Figure 5.1: Layout of the simulated domain for the 90-degree diversion, with the boundary conditions and other imposed conditions like flow-splitting and recirculating inflow. The figure also mentions the total number of computational points, that vary between 16.3 million to 224 million depending on the Reynolds number of the flow.

ments in the 90-degree case is $\approx$ 130,000, and depending on the bulk Reynolds number of the flow being simulated, the polynomial order is chosen so that all the important turbulence scales are resolved. Thin elements boundary-hugging were placed near the walls in order to efficiently resolve the boundary-layer, and this process was done using an in-house code [98]. For cases with laminar inflow, that is $Re_{bulk} = 10 - 1000$, the polynomial order used are 4 ($lx1 = 5$) for the cases with flow after the diversion being steady and 7 ($lx1 = 8$) for the cases the flow after the diversion is unsteady. Thus the number of computation points in the above mentioned cases are $\sim$ 16.3 million and 66.4 million. For the turbulent cases, that is $Re_{bulk} = 7000 - 25000$, the polynomial order used is 11 ($lx1 = 12$). So, the number of computational points in those cases are $\sim$ 224 million. The distribution of the grid points at any rectangular cross-section for the case with $lx1 = 12$ is shown in fig. 5.2 below. For the cases with $Re_{bulk} = 7000$, the resolution is good enough for the simulations to be DNS,

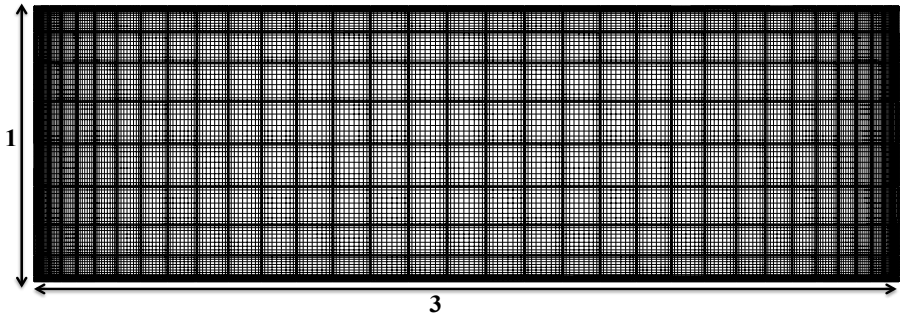


Figure 5.2: Cross-section of the channel shows part of the mesh, illustrating the distribution of the elements along with the collocation points. For the cases with $Re_{bulk} = 7000$, the first grid point in the z-direction is placed approximately at $z^+ = 0.020$, and in the y-direction at $y^+ = 0.21$. And the cases with $Re_{bulk} = 25000$, the first grid point in the z-direction is placed approximately at $z^+ = 0.072$, and in the y-direction at $y^+ = 0.81$.

that is the resolution is high enough that it resolves all the relevant turbulence scales [99]. For cases with $Re_{bulk} = 25000$, the resolution in the z-direction is good enough for DNS, and in the y-direction it is akin to a high-resolution LES. In the high-resolution Large Eddy Simulations (LES) conducted for the current study, most of the relevant turbulent scales have been resolved. For the smallest (the energy dissipating) scales, a spectral element-level high-pass filter is used to dissipate the residual turbulence energy [89]. Resolution of the computational mesh near the wall used in the current LES simulations is higher than LES simulations conducted at a similar scale in other recent studies.

For all the cases an inflow with a constant mean-velocity ($U_{mean} = 1$) was imposed. For the turbulent flow cases, transition of the flow to fully turbulent happens relatively quickly due to the use of wall-bounded vorticity coupled with random fluctuations as the initial condition. For the turbulent flow cases, the incoming flow has to be turbulent and the boundary-layer of the flow before reaching the diversion (the area of interest) should be fully developed. In experiments the latter issue is addressed by making the inflow channel long enough that the boundary layer in the flow is fully developed. In the current simulations, a recycling inflow boundary condition has been implemented, that maps the velocity field from 65 percent of the channel to the start of the channel. The flow after a few recycling in the input channel becomes fully turbulent, thus after some time the flow reaching the diversion would have a fully developed boundary-layer. At the outflow of the two channels, Turbulent Outflow boundary condition is implemented. This boundary condition takes into account instability caused due to the interaction of negative local fluxes, generated by strong turbulent vortices, and a Neumann boundary condition at the outflow. In order to address the above stated issue, the Turbulent Outflow boundary condition effectively acts like a virtual nozzle, which mildly accelerates the flow

going out, thus ensuring the characteristics of the flow going out always points outwards [90].

One of the most important component of the simulations at the diversion is the accurate splitting of the flow between the two channels after the diversion. A often used method for imposing a prescribed flow division is to impose Dirichlet velocity condition at one of the outlets and Neumann condition at the other. The branch with the Drichlet velocity condition is then usually made longer, in order to diminish any spurious effects of the imposed boundary condition on the flow at the diversion. This method also increases the time required by the flow to converge to the imposed flow-split. Alternatively, in the current study a method has been adopted that allows implementation of Neumann boundary condition at both the outlets, thus rescinding the requirement of overtly long outflow channel. Thus the alternative method, results in substantial reduction in computational requirement for a converged solution of the flow. The method used in the current-study had been successfully used for analyzing flow through vascular bifurcations [90, 100].

The flow splitting scheme uses the semi-implicit approach used in the Navier-Stokes solver. The method utilizes the fact that the Stokes operator, which is unsteady and controls the boundary conditions, is linear and is treated implicitly. Linearity of the unsteady Stokes operator allows superposition; that is if $S_{us}\left(\tilde{\mathbf{u}}^n\right) = \mathbf{f}^n$ and $S_{us}\left(\tilde{\mathbf{u}}_0\right) = 0$ for different boundary conditions, then $\mathbf{u}^n = \tilde{\mathbf{u}}_0 + \tilde{\mathbf{u}}^n$ will satisfy $S_{us}\left(\mathbf{u}^n\right) = \mathbf{f}^n$ for the boundary condition that is equivalent to the superimposition of the two original boundary conditions for $\tilde{\mathbf{u}}_0$ and $\tilde{\mathbf{u}}^n$. In order to implement it, during pre-processing first the unsteady Stokes problem is solved with all the flow going through one of the branch. Next, the same is done but with all the flow going through the other branch. With the velocity and pressure field saved from the above two steps, during time-stepping the solution of the flow is a linear combination of the two cases solved in the pre-processing step. This results in substantially fast convergence to the expected solution, under and imposed flow split. As the unsteady Stokes operator is solved implicitly, the method provides an interation-free approach to applying the flow divsion. Algorithmic details of the implementation can be obtained from Fischer et al. [90].

All the simulation was conducted for at least 180 convective time units, before data was collected for Reynolds averaging and analysis of the flow results. 180 convective time units was found to be long enough for the flow in the inlet channel to become fully turbulent. As the simulations were computationally very intensive, all of them were conducted on the peta-scale supercomputer BlueWaters, housed at NCSA, University of Illinois at Urbana-Champaign. The simulations were run using up to 32,768 processors. In case the simulations were run with 32,768 mpi ranks, the parallel efficiency was found to be below 50 percent, thus most of the simulations were run with with 4096 to 8192 mpi ranks.

### 5.2.3 The Lagrangian Particle Tracking Model for Sediment Transport

In the current study sediment has been modeled as Lagrangian particles, which has been typically modeled under the Eulerian framework [101]. In this section the main features of the Lagrangian particle model has been discussed. A more detailed description of the model can be found in Chapter 3. The model used in the current study is similar to the one derived by Auton et al. [75], which considered the inviscid limit for the continuous-phase. The other commonly used model is the Maxey-Riley equations [76], which considered the viscous limit for the continuous-phase. The model is similar to the one used in the study by Escauriaza and Sotiropoulos [77], for studying bedload transport at a junction under unidirectional turbulent flow. The feedback of the particles on to the fluid, which is important for cases with relatively high sediment concentration, has not been accounted for. Other assumptions are, the particles only translate in the flow, and the particles do not collide with each other. These assumptions are valid for cases where the particle concentration is relatively low, and the particle diameter is small enough for it to not rotate while moving in the fluid. The motion of the particles are defined by the equations:

$$m\frac{dv_i}{dt} = f_i \qquad \text{(velocity equation)} \tag{5.15}$$

$$\frac{dx_i}{dt} = v_i \qquad \text{(position equation).} \tag{5.16}$$

where $m$ is the mass of the particles, $x_i$ and $v_i$ are the position and velocity of the particles. $f_i$ represents all the forces acting on the particles. Velocity of the fluid at the position of the particle has been represented using $u_i$. The relative velocity between the particle and the fluid is represented by $v_{ri} = (u_i - v_i)$. Equation 5.15 in terms of all the different forces acting on it is given by:

$$m\frac{dv_i}{dt} = \frac{1}{2}\rho C_D \frac{\pi d^2}{4}|v_{ri}|v_{ri} + \left(1 - \frac{\rho}{\rho_s}\right) m g_i + \rho C_L \frac{\pi d^3}{6}\left(\epsilon_{ijk} v_{rj} \omega_k\right) + \rho C_m \frac{\pi d^3}{6}\left(\frac{Du_i}{Dt} - \frac{dv_i}{dt}\right) + \rho \frac{\pi d^3}{6}\left(-\frac{1}{\rho}\frac{\partial p}{\partial x_i} + \nu \frac{\partial^2 u_i}{\partial x_j x_j}\right) \tag{5.17}$$

the first term represents the fluid drag acting on the particle, $\rho$ is the density of the fluid, $d$ is the diameter of the particle and $C_D$ is the drag coefficient of the particle. $C_D$ is a function of the particle Reynolds number $Re_p$, defined as $Re_p = \frac{|v_r|d}{\nu}$, where $\nu$ is the kinematic viscosity of the fluid. A commonly used relationship of $C_D$ used for modeling spheres at relatively low $Re_p$ is $C_D = \frac{24}{Re_p}$ [48]. For the current study the relationship used is the one used for sand and

gravel at $Re_p \leq 10^4$ [78]:

$$C_D = \frac{24}{Re_p} + 1.5 \tag{5.18}$$

The second term in equation 5.17 if for the net gravitational force acting on particle. The acceleration due to gravity always acts along the negative z-direction (if z is chosen as the vertical-axis), thus $g_i = -g\delta_{i3}$ where $g$ is the gravitational acceleration and $\delta_{ij}$ is the Kronecker's delta. $\rho_s$ in the gravitational force term is material density of the particle.

The third term is the lift force acting on the particle, where $C_L$ is the lift coefficient, $\omega$ is the vorticity of the fluid around the particle and $\epsilon_{ijk}$ is the alternating unit tensor. The lift force depends on the gradient of velocity around a particle that is moving in a non-uniform rotational flow. The lift coefficient is constant for inviscid flows [75]. For relatively smaller Reynolds number, the lift coefficient relationship suggested by Mei [79] can be used, which is a modified version of the relationship proposed in the seminal work of Saffman [80]. In the current study, the relationship by Mei has been used.

The fourth term is the force on the particle due to added mass. This force is important for cases in which the particle is large enough to pull in additional fluid along with it, and the added mass coefficient is generally considered a constant, and equal to the inviscid approximation $C_m = 0.5$ [59]. In this force term, $\frac{Du_i}{Dt}$ is the material derivative of the fluid. The last term in the momentum balance equation of the particle corresponds to the force induced by fluid stresses on the particle. Equation 5.17 can be further simplified by dividing through out by mass of the particle $m = \rho_s \frac{\pi d^3}{6}$ and then multiplying by $\frac{\rho_s}{\rho}$. Thus equation 5.17 reduces to:

$$\left(\frac{\rho_s}{\rho} + C_m\right)\frac{dv_i}{dt} = \frac{3}{4}\frac{C_D}{d}|v_{ri}|v_{ri} + \left(\frac{\rho_s}{\rho} - 1\right)g_i + C_L\left(\epsilon_{ijk}v_{rj}\omega_k\right) + C_m\frac{Du_i}{Dt} + \left(-\frac{1}{\rho}\frac{\partial p}{\partial x_i} + \nu\frac{\partial^2 u_i}{\partial x_j x_j}\right) \tag{5.19}$$

$\frac{\rho_s}{\rho} - 1$ can be represented as $R$, whose value for quartz based sand is about 1.65. Also, $C_m\frac{Du_i}{Dt}$ is added and subtracted to the right hand side of equation 5.19, which is then further simplified to:

$$\frac{dv_i}{dt} = \frac{1}{C_m^R}\left[\frac{3}{4}\frac{C_D}{d}|v_{ri}|v_{ri} + Rg_i + C_L\left(\epsilon_{ijk}v_{rj}\omega_k\right) + \left(C_m + 1\right)\frac{Du_i}{Dt}\right] \tag{5.20}$$

where $C_m^R = 1 + R + C_m$. The above equations have ben non-dimensionalized using the appropriate velocity and length scales. In the current study the mean streamwise velocity of the flow in the channel $U_{mean}$ is the velocity scale, and the depth of the channel $D$ as the length scale. Then equation 5.20 can be normalized by multiplying it by $\frac{D}{U_{mean}^2}$. Thus the non-dimensional form of equation

5.20 is:

$$\frac{d\tilde{v}_i}{d\tilde{t}} = \frac{1}{C_m^R}\left[\frac{1}{St}\tilde{v}_{ri} - \frac{\delta_{i3}}{Fr^2} + C_L\left(\epsilon_{ijk}\tilde{v}_{rj}\tilde{\omega}_k\right) + \left(C_m + 1\right)\frac{D\tilde{u}_i}{D\tilde{t}}\right] \tag{5.21}$$

In the above equation $Fr^2$ is the square of the densimetric Froude number of the flow, and $St$ is the Stokes number of the flow. They are defined as:

$$Fr^2 = \frac{U_{mean}^2}{RgD} \tag{5.22}$$

$$St = \frac{4}{3C_D}\frac{\tilde{d}}{|\tilde{v}_{ri}|} \tag{5.23}$$

The equations defining the motion of the particles are integrated in time using a novel semi-implicit time-stepping scheme designed to handle particles of of disparate size and Stokes number at the same time efficiently, without the simulation going unstable. The scheme is an amalgamation of the implicit (in time) Back Differencing and explicit (in time) Extrapolation schemes. This is important for simulating sediment transport phenomena in nature, as in most of the cases there is a multiple order of difference between the coarsest and finest sediment in the system. For the current study, the range of sediment sizes simulated fall in the range of $xyz - pqr$, which clearly shows the need for the aforementioned semi-implicit time-stepping scheme. Details of the scheme have been illustrated in Chapter 3. Finally, as a boundary condition, the particles were assumed to go through an elastic collision with the walls. This means, the particles after colliding with the walls changed their direction, but the magnitude of the velocity was unhampered. This is a perfectly plausible assumption for the tangential (w.r.t to the wall) velocity of the particles, as usually the coefficient of restitution is $\sim 0.9$ [87]. The coefficient of restitution for the normal velocity of the particles is usually $\sim 0.3$, this will reduce the wall-normal particle velocity. In context of the current study, the decrease in the wall-normal velocity might have some effect on the outcome of the sediment distribution at the diversion, but difference will not be substantial, as the phenomenon of Bulle-Effect is primarily driven by the structure of the flow. Thus for the current study, the assumption of elastic collision of the particles with the wall is acceptable.

## 5.3 Results and Discussion

The results from the simulations have been discussed in this section. First the flow structure has been discussed for $Re_{bulk} = 10 - 1000$, which are the cases with Laminar inflow. Next the flow structure has been discussed for $Re_{bulk} = 7000 - 25000$, which are the cases with turbulent inflow. Next the results from the simulations with the particles have been discussed. First, the

results with very-fine and perfectly buoyant particles have been discussed. These particles essentially moved along with the flow, thus the distribution of these particles essentially shows how the flow is distributed at the diversion. Finally, results from the simulations with particles of different sizes have been discussed. Those results would illustrate the effect of size of the sediment on Bulle-Effect.

### 5.3.1 Flow Structure under Laminar Inflow

In order to explore the topic systematically, first the 90-degree diversion was simulated with the incoming flow being laminar. First the case with incoming flow Reynolds number $Re_{bulk} = 10$ is analyzed. Magnitude of velocity has been plotted at 5 percent height from the bottom (see fig. 5.3).

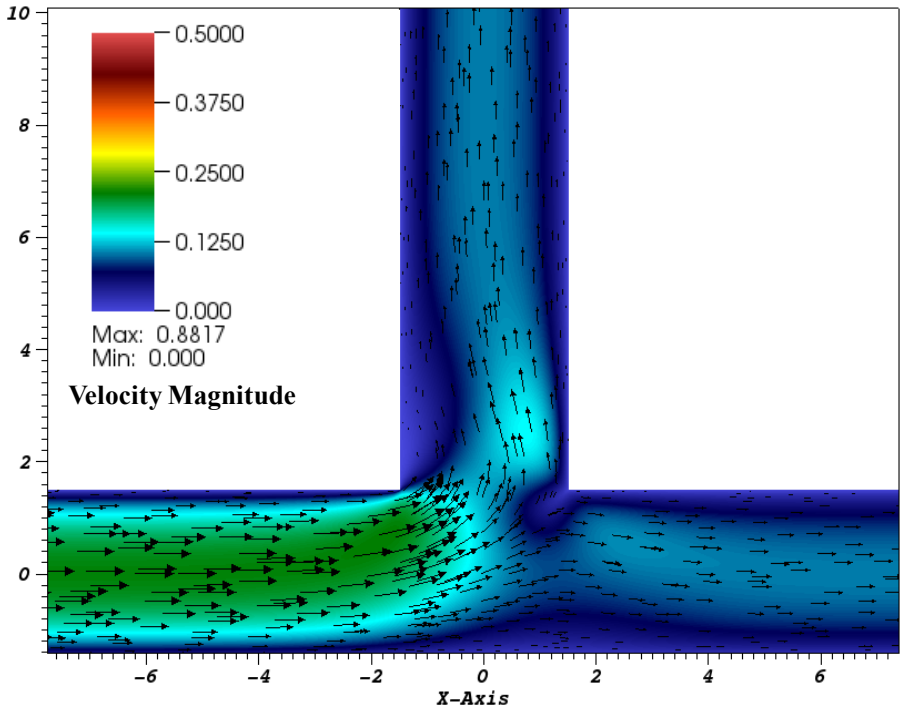


Figure 5.3: Velocity magnitude at the diversion for $Re_{bulk} = 10$ and $50 : 50$ flow division, at 5 percent height from the bottom. Most of the flow is going into the lateral-channel.

Similar to the turbulent flow case in the previous chapter, most of the flow near the bottom moves into the lateral-channel, even though the total flow is divided $50 : 50$. At an height of 50 percent from the bottom, about 50 percent of the total flow can be seen to be entering the lateral-channel (see fig. 5.4a). And at 90 percent height from the bottom, most of the flow can be seen to be continuing into the main-channel (see fig. 5.4b).

In general the flow at the diversion is steady. The Reynolds number of the case under analysis is relatively very low, to an extent that it could be deemed a plug

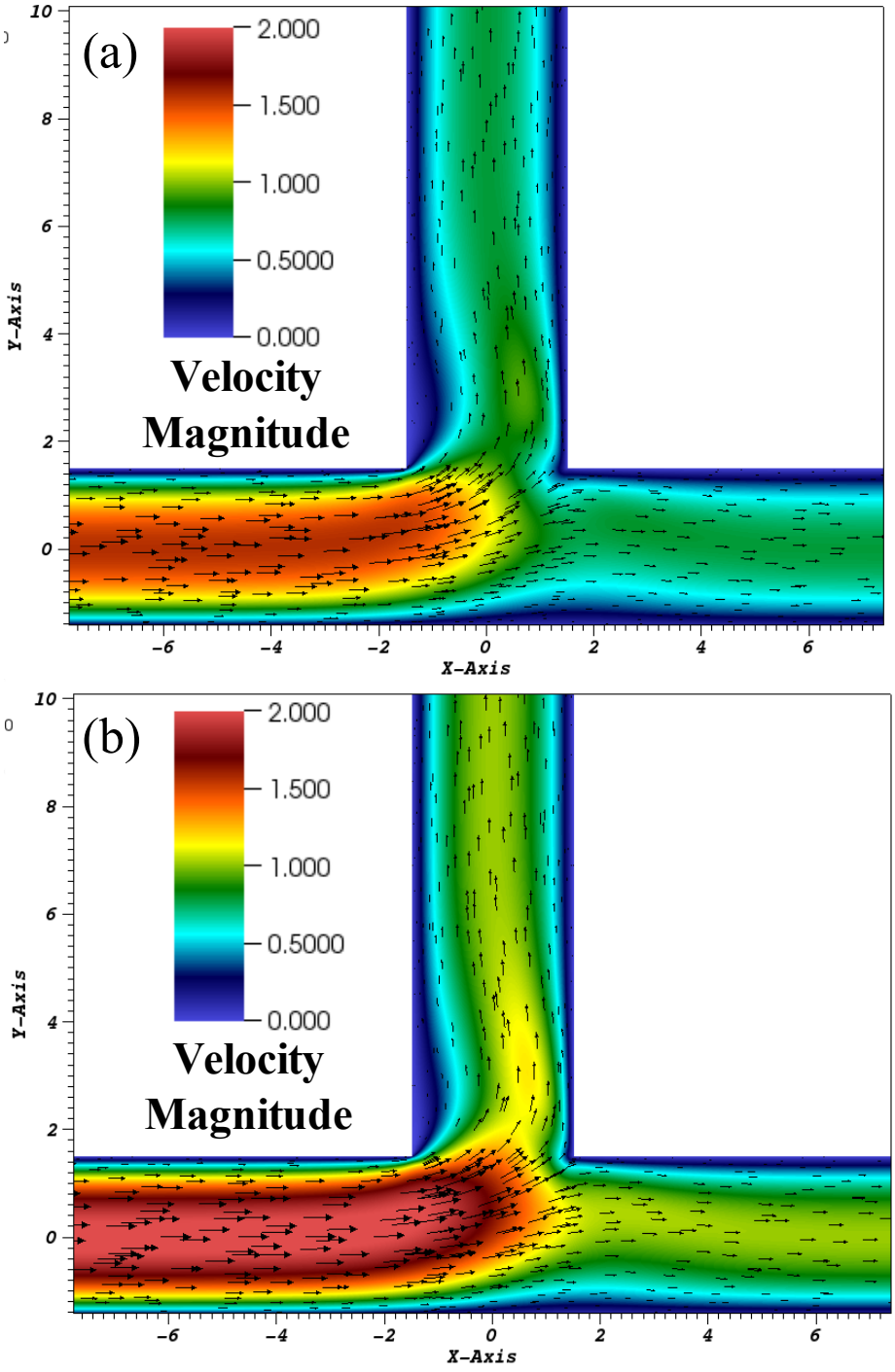


Figure 5.4: Velocity magnitude at the diversion for $Re_{bulk} = 10$ and $50:50$ flow division, at (a) 50 percent height from the bottom (b) 90 percent height form the bottom. In (a), $\sim 50$ percent of the flow is going into the lateral-channel. In (b) more than 50 percent of the flow continues into the main-channel.

flow. Even though the flow is relatively slow, in the lateral-channel the flow separates from the left-wall and in the main-channel it separates from the right-wall. Interestingly, the size of the separation-zone in the lateral-channel increases with increase in depth; which is contrary to the trend observed for the turbulent flow case in the previous chapter, where the width of the separation-zone in the lateral-channel near the bottom of the channel is lower than the width near the top. Next the flow was analyzed to check for presence of secondary flow circulations (see fig. 5.5). Vertical velocity has been plotted for two cross-sections

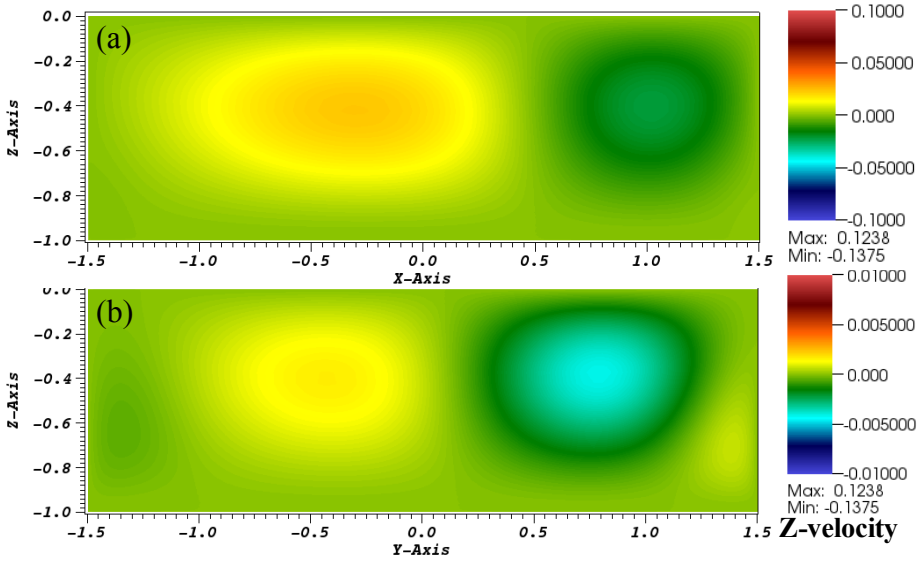


Figure 5.5: Velocity in the z-direction at two different cross-sections after the diversion. (a) at y=3 on the lateral-channel, a relatively weak clockwise rotating secondary-circulation can be seen (b) at x=3 on the main-channel, the counter clockwise rotating secondary circulation is even weaker than the one in the lateral-channel. In (a) the general flow is going into the plane, whereas for (b) it is coming out of the plane.

after the diversion. Both the clockwise rotating secondary-circulation in the lateral-channel and the counter-clockwise rotating secondary-circulation in the main-channel are weaker than the ones observed for the turbulent flow case in the previous chapter. Additionally, the secondary-circulation in the main-channel (fig. 5.5b) is weaker than the one in the lateral-channel (fig. 5.5b), and this is obvious from the velocity-scale of the two cases. From the current case, it can be concluded that the flow mechanism that propels Bulle-Effect is also present at very low Reynolds number.

Next the case with $Re_{bulk} = 100$ and $50 : 50$ flow division has been analyzed. The flow throughout the domain is laminar and steady. First the magnitude of velocity at 10 percent of the height from the bottom has been plotted (see fig. 5.6).

Like the previous cases, most of the flow near the bottom of the channel can be seen to be entering the lateral-channel. It also results in formation of a

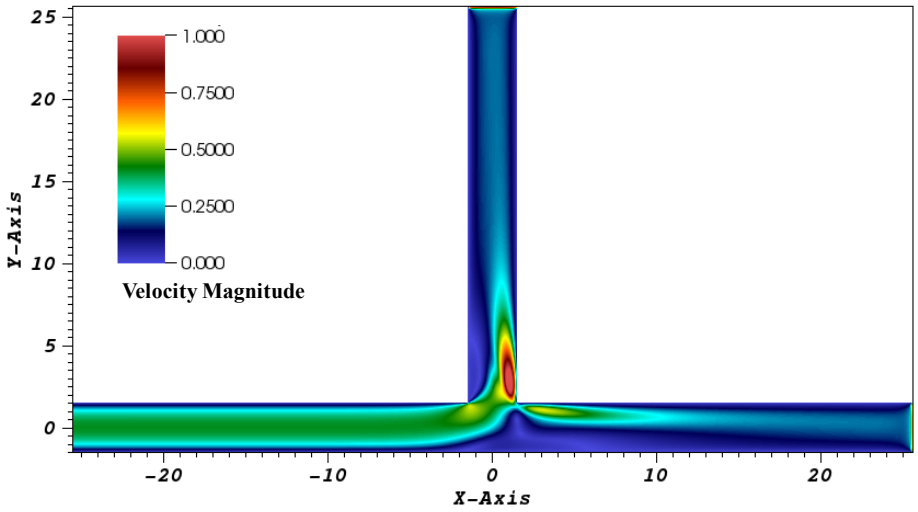


Figure 5.6: Velocity magnitude at 10 percent height from the bottom, for the case with $Re_{bulk} = 100$ and $50 : 50$ flow split. Most of the flow is entering the lateral-channel.

high-velocity zone on the right side of the lateral-channel, which will result in high-shear stress at the bed. The flow can also be seen to seen to be separating from the left-wall in the lateral-channel and right-wall of the main-channel (see fig. 5.7).

Though unlike the previous case with $Re_{bulk} = 10$, the width of the separation-zone in the lateral-channel seems to decrease with increase in depth, whereas the trend in opposite for the separation-zone in the main-channel. And not just the separation-zones, even the secondary circulations for the current case is appreciably stronger than those observed for $Re_{bulk} = 10$ (see fig. 5.8). This is to an extent expected, as the $Re_{bulk} = 10$ is more similar to a slow moving plug-flow.

Next the case with $Re_{bulk} = 300$, and $50 : 50$ flow division is analyzed. The flow at the diversion is still steady. From the velocity magnitude plots at the bottom and top of the channel (see fig. 5.9), it is clear that almost all the flow near the bottom enters the lateral-channel and most of the flow near the top continues into the main channel. Near the bottom, the strength of the current going into the lateral channel is so strong that it completely stagnates the flow on the right-side of the main-channel at the diversion.

This shows that the principle mechanism behind Bulle-Effect might be relatively stronger for cases with laminar inflow. In order to ascertain that, a cases with $Re_{bulk} = 300$ and with 15 percent of the total flow entering the lateral-channel was analyzed. For that particular case, the velocity magnitude at 5 percent height from the bottom has been plotted (see fig. 5.10).

The plot shows that even though only 15 percent of the total flow was entering the lateral-channel, most of the flow near the bottom of the channel entered

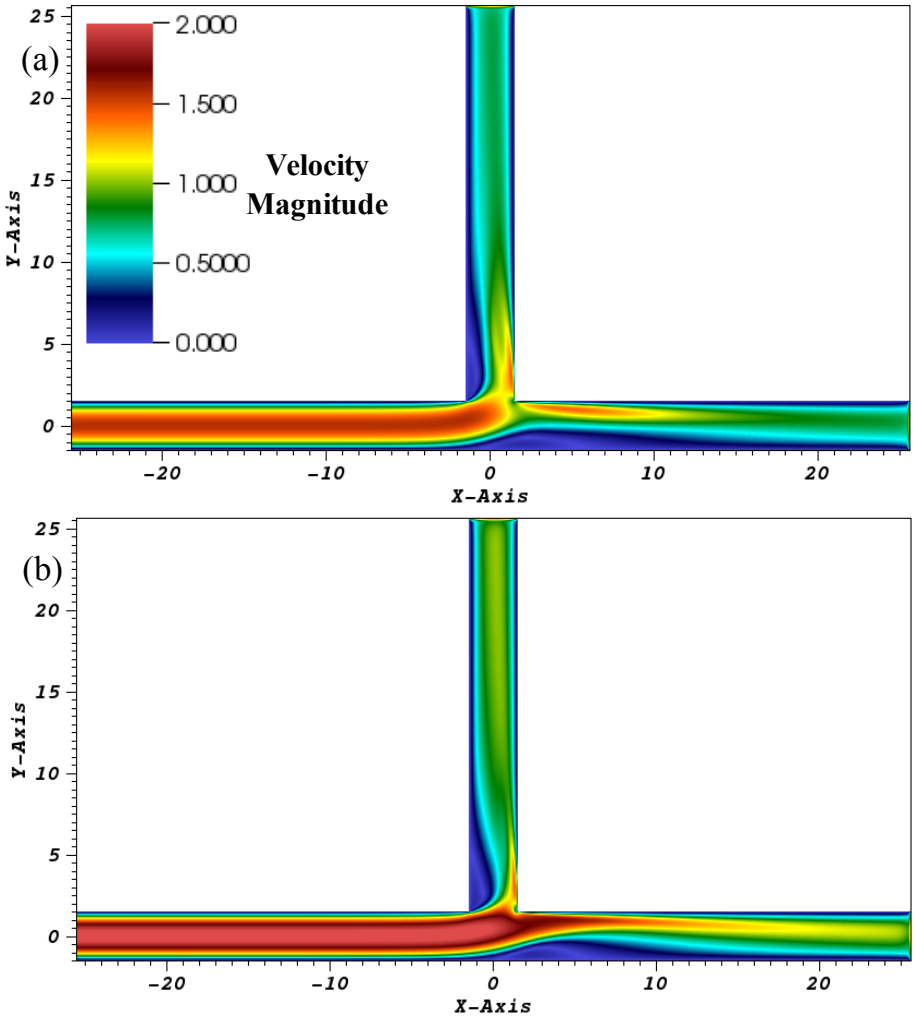


Figure 5.7: Velocity magnitude at (a) 50 percent and (b) 95 percent height from the bottom, for the case with $Re_{bulk} = 100$ and $50 : 50$ flow split. At 50 percent, the flow is almost equally divided between the two-channels, and at the surface most of it is continuing into the main-channel.

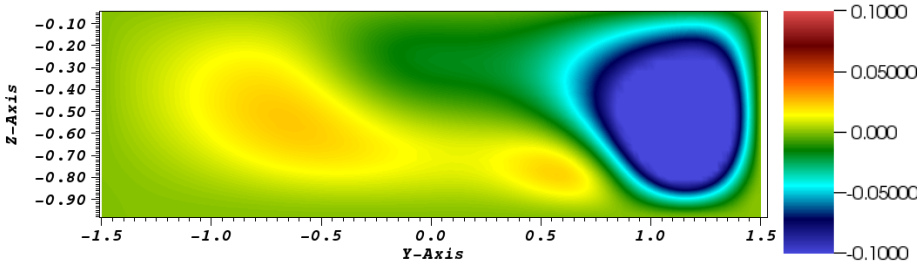


Figure 5.8: Velocity in the z-direction at at x=3 on the main-channel, the counter clockwise rotating secondary circulation is relatively stronger than the case $Re_{bulk} = 10$. The general flow is coming out of the plane.

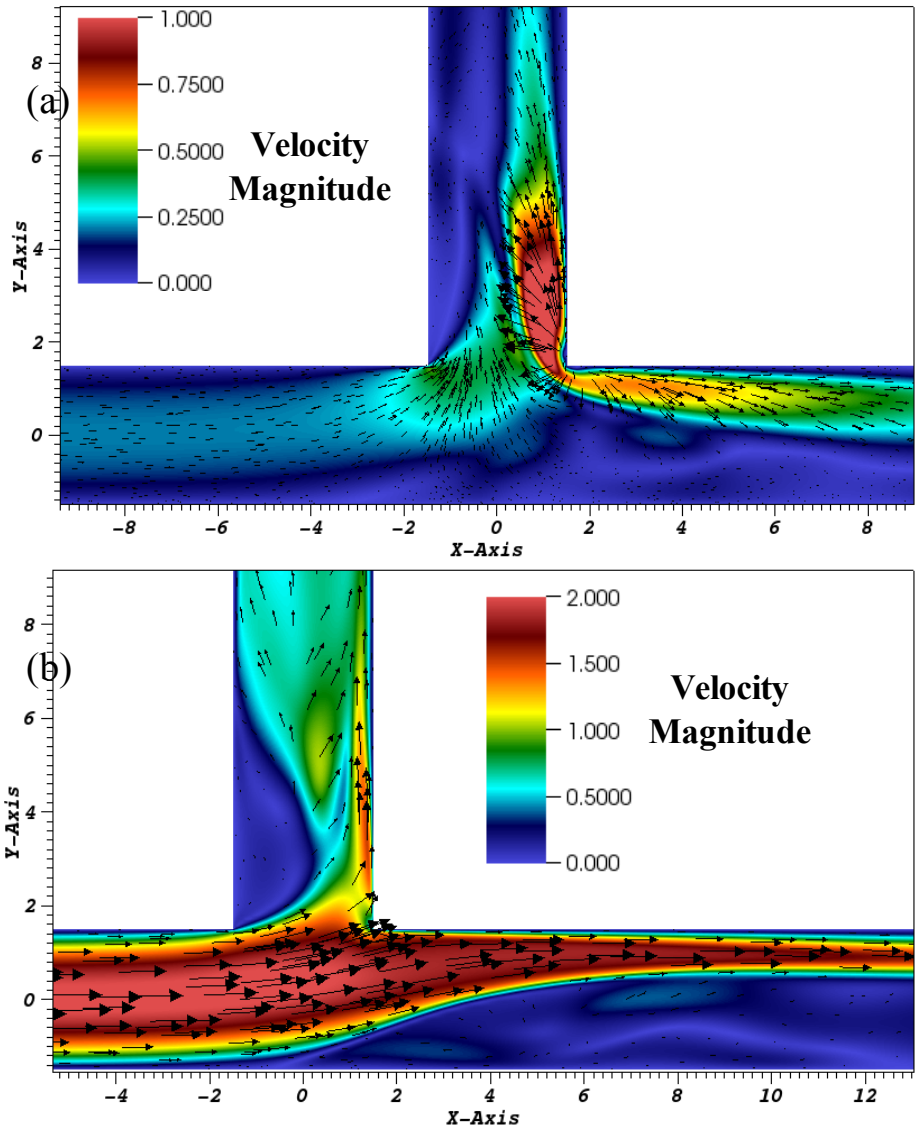


Figure 5.9: Velocity magnitude for $Re_{bulk} = 300$ and $50:50$ flow split. (a) at 5 percent height from the bottom (b) at 90 percent height from the bottom. Almost all the flow near the bottom enters the lateral-channel, and most of the flow near the top continues along the main-channel.

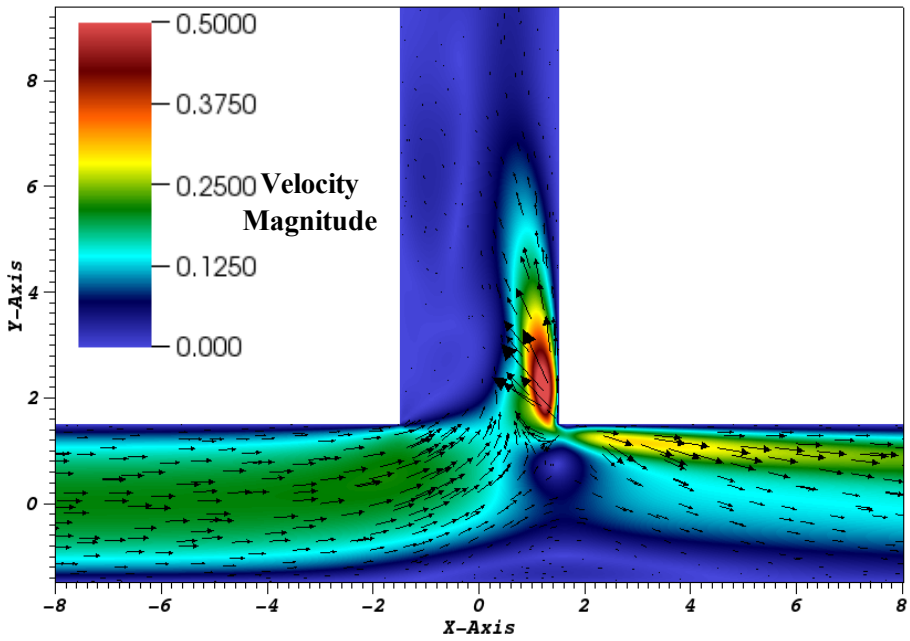


Figure 5.10: Velocity magnitude for $Re_{bulk} = 300$ and $15 : 85$ flow split, where 15 percent of the total flow is entering the lateral-channel, at a height 5 percent from the bottom.

the lateral channel. While analyzing the effect of different flow-divisions on the structure of the flow at the diversion, it was observed that for the current $Re_{bulk}$ if more than 65 percent of the flow entered the lateral-channel, then the flow at and after the diversion turns unsteady. The flow starts to have instabilities and shed votex at regular interval. In case the flow division is kept at $50 : 50$, the first instability shows up approximately around $Re_{bulk} = 350$. And by the time $Re_{bulk} = 400$, the flow starts to show sustained instability. This can be observed from the plots for velocity magnitude at 30 percent height from the bottom, for $Re_{bulk} = 400, 500 \text{and} 1000$ (see fig.5.11).

Clearly the instability in the system gets heightened with increase in $Re_{bulk}$. By $Re_{bulk} = 500$, the frequency of vortex shedding increases appreciably, and the breakdown of the vortex in the channels after the diversion causes turbulence at the local level. And by the time $Re_{bulk} = 1000$, the flow in two channels after the diversion could be called turbulent. This is interesting because the flow in the main-channel before the diversion is still laminar. As the speed of flow is two-channels after the diversion is half of original channel, one would expect that reduction in Reynolds number would further laminarize the flow in the channels after the diversion; but that is not the case at least in the domain just after the diversion. Similar type of transition of laminar flow into locally turbulent one has previously been observed at vascular bifurcations [100]. Also, the approximate $Re_{bulk} = 350$ at which the transition happens between steady to unsteady/locally-turbulent flow in the current simulations, is similar to the

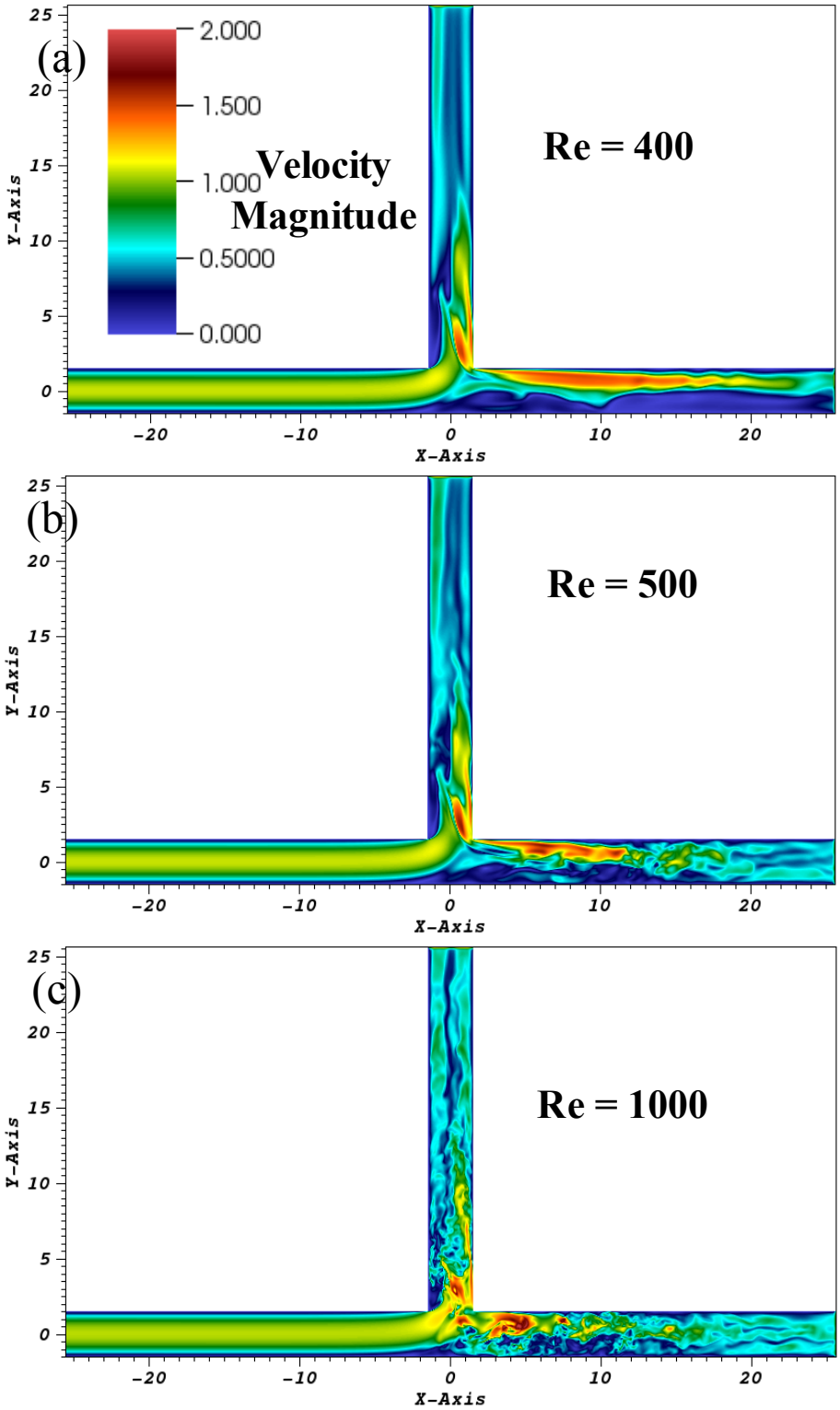


Figure 5.11: Velocity magnitude for 50 : 50 flow split at 30 percent height from the bottom, for (a) $Re_{bulk} = 400$ (b) $Re_{bulk} = 500$ (c) $Re_{bulk} = 1000$.

Reynolds number observed in other studies on laminar flow at bifurcations, e.g. at T-shaper pipe bifurcations [102] and vascular bifurcatoins [103]. Thus, there seem to be a universality of the transition mechanism, to an extent irrespective of the geometry of the bifurcation. Even though the point made above may not have major implication for Bulle-Effect, yet it is an interesting fundamental fluid-mechanics phenomenon that might have wider implications for physiological and industrial applications[104, 105].

In context of Bulle-Effect, it can be observed in fig. 5.11 that even at 30 percent height from the bottom, most of the flow enters the lateral-channel, even though the total flow is equally divided between the two-channels. So, it can be concluded that for laminar inflow cases, the flow mechanism that drives Bulle-Effect is stronger compared to turbulent flow. From the above stated figure it can also be ascertained that with increase in Reynolds number, the flow mechanism driving Bulle-Effect might get weaker. Reynolds number of the flow does effect the strength of the secondary-flow circulation. This is evident from the plot of vertical-velocity at two cross-sections after the diversion for the case $Re_{bulk} = 300$ and $50:50$ flow division (see fig. 5.12).

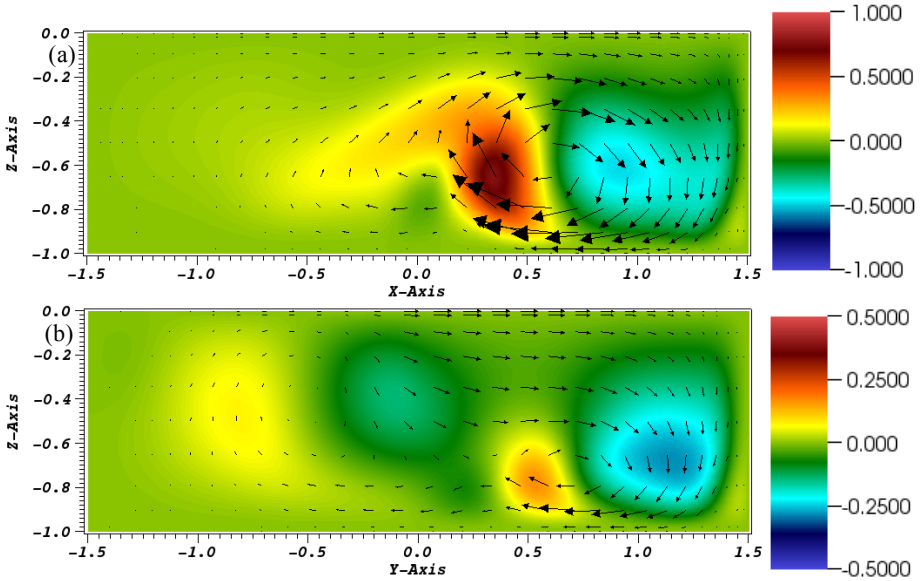


Figure 5.12: Vertical-velocity for the case $Re_{bulk} = 300$ and $50:50$ flow division, at (a) y=3 (b) x=3. In (a) the flow is going into the plane, and a strong clockwise rotating secondary-circulation is evident. In (b) the flow is coming out of the plane, and a relatively weaker counter-clockwise rotating secondary-circulation can be observed.

In general the strength of the secondary-circulation is relatively stronger than previously observed for $Re_{bulk} = 10$ and $Re_{bulk} = 100$. In the lateral-channel the secondary circulation is confined to the high-flow zone on the right-side of the channel. Whereas in the main-channel, the secondary-circulation is on the high-flow zone on the left-side of the channel, where it also induces a weak secondary-

circulation in the right-side of the channel (see fig. 5.12b). A similar analysis is done for the case $Re_{bulk} = 1000$ and $50 : 50$ flow division, but instead of vertical-velocity, the hydrodynamic pressure along with vertical-velocity vectors has been plotted (see fig. 5.13).

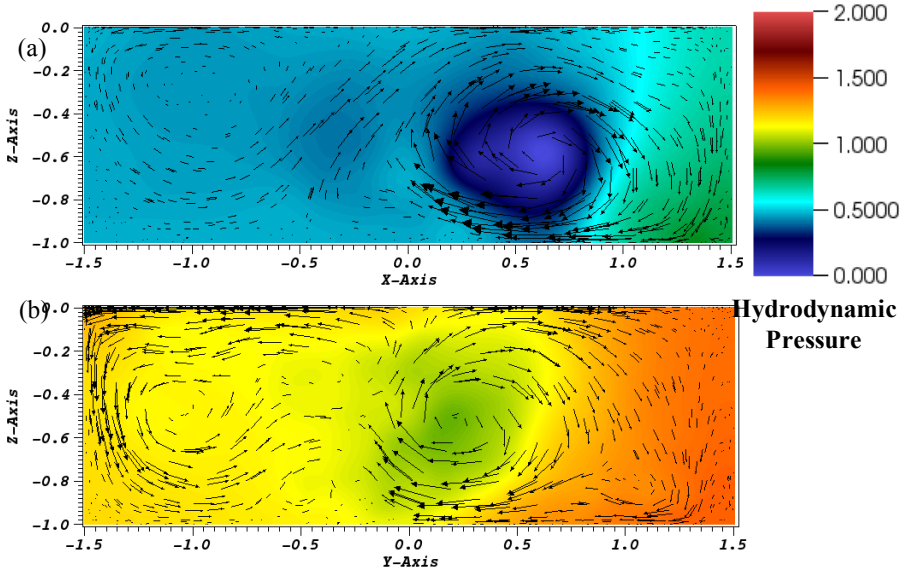


Figure 5.13: Hydrodynamic pressure and vectors representing vertical-velocity has been plotted for the case $Re_{bulk} = 1000$ and $50 : 50$ flow division, at (a) y=3 (b) x=3. In (a) the flow is going into the plane, and a strong clockwise rotating secondary-circulation is evident. In (b) the flow is coming out of the plane, and a relatively weaker counter-clockwise rotating secondary-circulation can be observed.

The exact position of the strong secondary-flow circulation is beautifully captured by the presence of the low-pressure core that is formed at the center of a rotating flow (vortex). In the lateral-channel the core of the clock-wise rotating secondary-circulation is closer to the right wall, whereas the position of the counter-clockwise rotating secondary-circulation core in the main-channel is more central. Like the case $Re_{bulk} = 300$, the primary secondary-circulation in the main-channel induces a weak vortex at the right-side of the channel.

### 5.3.2 Flow Structure under Turbulent Inflow

In the current section, the structure of the flow in the turbulent flow cases have been analyzed. One of the first cases analyzed is $Re_{bulk} = 7000$, and for different flow divisions. Velocity magnitude at 70 percent height from the bottom has been plotted for $50 : 50$ flow-division (see fig. 5.14).

The flow can be seen to be fully turbulent, both in the inflow channel and the post-diversion channels. In accordance with the expectation, most of the flow at 70 percent height from the bottom continues into the main-channel. And the opposite trend is shown at depths closer to the bottom of the channel. In order

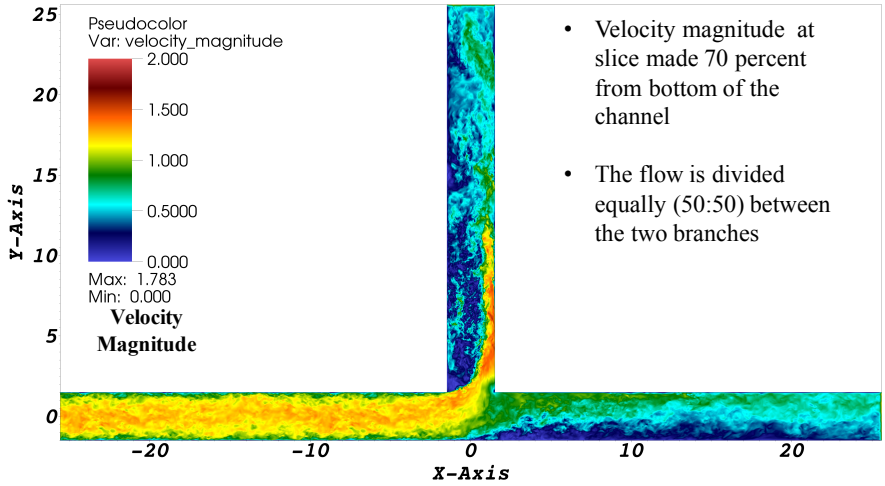


Figure 5.14: Velocity magnitude at 70 percent height from the bottom, for $Re_{bulk} = 7000$ and $50:50$ flow division. Most of the flow at this height is moving into the main-channel.

to observe the evolution of structure of the flow before the diversion, velocity magnitude at cross-sections at different distance from the diversion has been plotted (see fig. 5.15).

At $x = -5$, the flow does not seem to have been influenced by the diversion yet (see fig. 5.15a). Though, as one gets closer to the diversion, the high-velocity core shifts towards the left-side of the channel, that is towards the direction of the lateral-channel. The structure of the flow after the diversion has been analyzed by plotting the velocity-magnitude at two cross-sections, at $x = 2$ in the main-channel and $y = 2$ in the lateral-channel (see fig. 5.16).

After the diversion, in the main-channel the high-velocity core shifts towards the left-wall (fig. 5.16a), whereas in the lateral-channel is shifts towards the right-wall (fig. 5.16b). Interestingly, the high-velocity core in the main-channel seem to be confined more near the top of the channel. This matches with the observation that majority of the flow near the top of the channel continues into the main-channel. A characteristic of the flow-separation size discussed earlier is also corroborated here, that is in the lateral-channel the width of the flow-separation is relatively wider near the top and decreases with increase in depth. On the other hand, in the main-channel the above trend is reversed. Also, the interface between the high-flow zone and the low-flow zone in the lateral-channel is relatively sharper than that of the main-channel. Next for the $Re_{bulk} = 7000$ case, different flow divisions were analyzed (see fig. 5.17).

At 70 percent height from the bottom, the structure of the flow mirrors previous observations about the flow near the top of the channel. e.g. In the case $65:35$, even though majority (65 percent) of the total flow is entering the lateral-channel, still a major portion of the flow at that depth is continuing

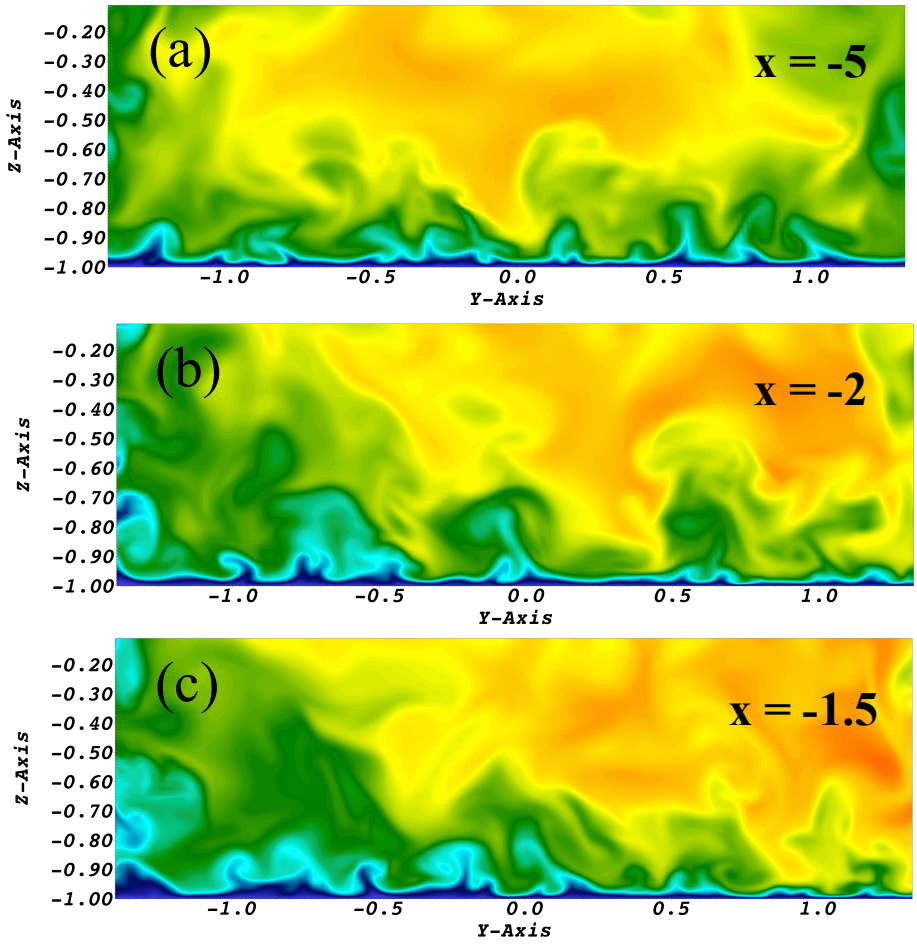


Figure 5.15: Velocity magnitude at different cross-sections before the diversion, for $Re_{bulk} = 7000$ and $50:50$ flow division. The general-direction of the flow is coming out of the plane. (a) x= -5, (b) x= -2, (c) x= -1.5. At (a) the flow is uniformly distributed in the cross-section with the high-velocity core at the center. As one gets closed to the diversion, the high-velocity core moves towards the left-side of the main-channel.

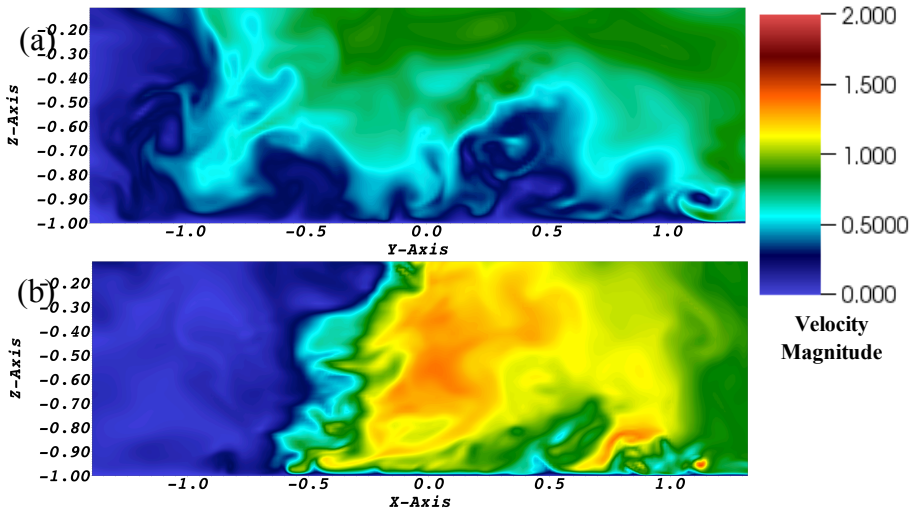


Figure 5.16: Velocity magnitude at different cross-sections after the diversion, for $Re_{bulk} = 7000$ and $50:50$ flow division. The general-direction of the flow is coming out of the plane for (a) x= 2, and into the plane for (b) y= 2.

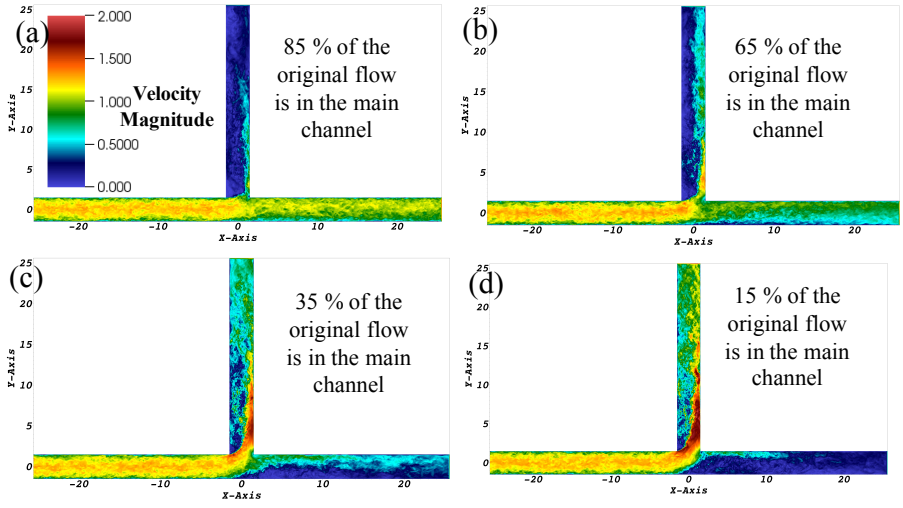


Figure 5.17: Velocity magnitude at 70 percent height from the bottom, for $Re_{bulk} = 7000$ and different flow divisions (a) $15:85$ (b) $35:65$ (c) $65:35$ (d) $85:15$.

into the main-channel. On the other hand, near the bottom of the channel the opposite trend is obvious (figure not produced here).

The above stated trend is further evident in the plot of velocity magnitude at 5 percent height from the bottom, for $Re_{bulk} = 25000$ and flow-division of $46 : 54$ (see fig. 5.18). This case is exactly similar to the 90-degree experiment of Bulle.

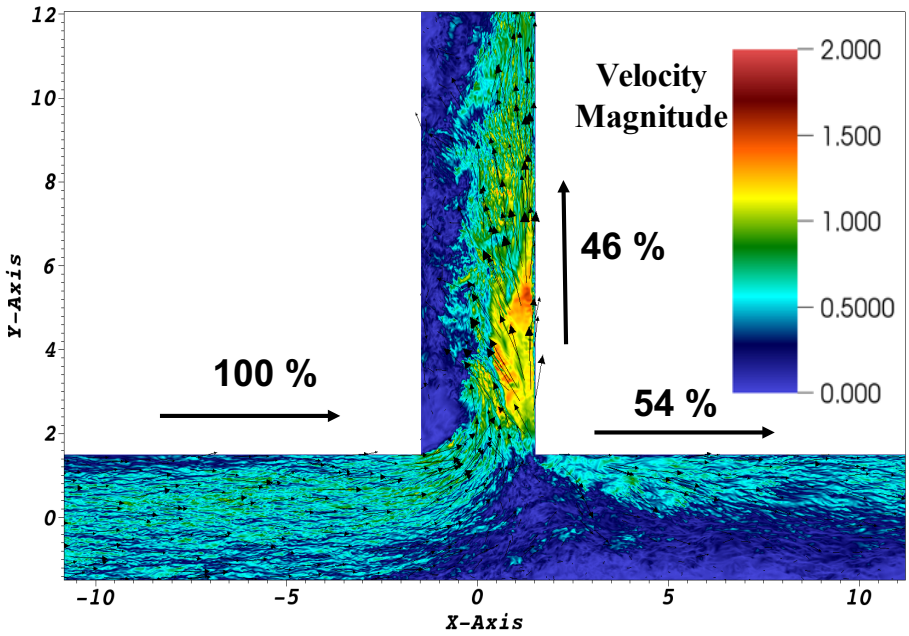


Figure 5.18: Velocity magnitude at 5 percent height from the bottom, for $Re_{bulk} = 25000$ and flow division of $46 : 54$. Even though a larger percentage of the total flow is entering the main-channel, most of the flow near the bottom enters the lateral-channel.

In this case, even though majority of the total flow enters the main-channel, most of the flow near the bed enters the lateral-channel. This will result in majority of the sediment traveling as bedload to enter the lateral channel, akin to Bulle's experimental observations. Flow in the lateral-channel can be seen to hug the right-wall, with relatively high velocity just after the diversion. This is an area that would be susceptible to scouring, and in case of a real stream/river may even result in bank failure. In the main-channel the flow near the bottom hugs the left-wall, and separates from the right-wall. Akin to Bulle's observations, the size of the separation-zone near the bottom is larger in the main-channel, compared to the lateral-channel. In order to ascertain the effect of different flow divisions on the structure of the flow near the bottom of the channel, four different flow divisions for $Re_{bulk} = 25000$ were analyzed (see fig. 5.19 and 5.20).

For the cases with flow divisions $85 : 15$ and $65 : 35$, almost all the flow at 5 percent height from the bottom is entering the lateral channel. So, it can be expected that in these cases almost all the sediment traveling as bedload should

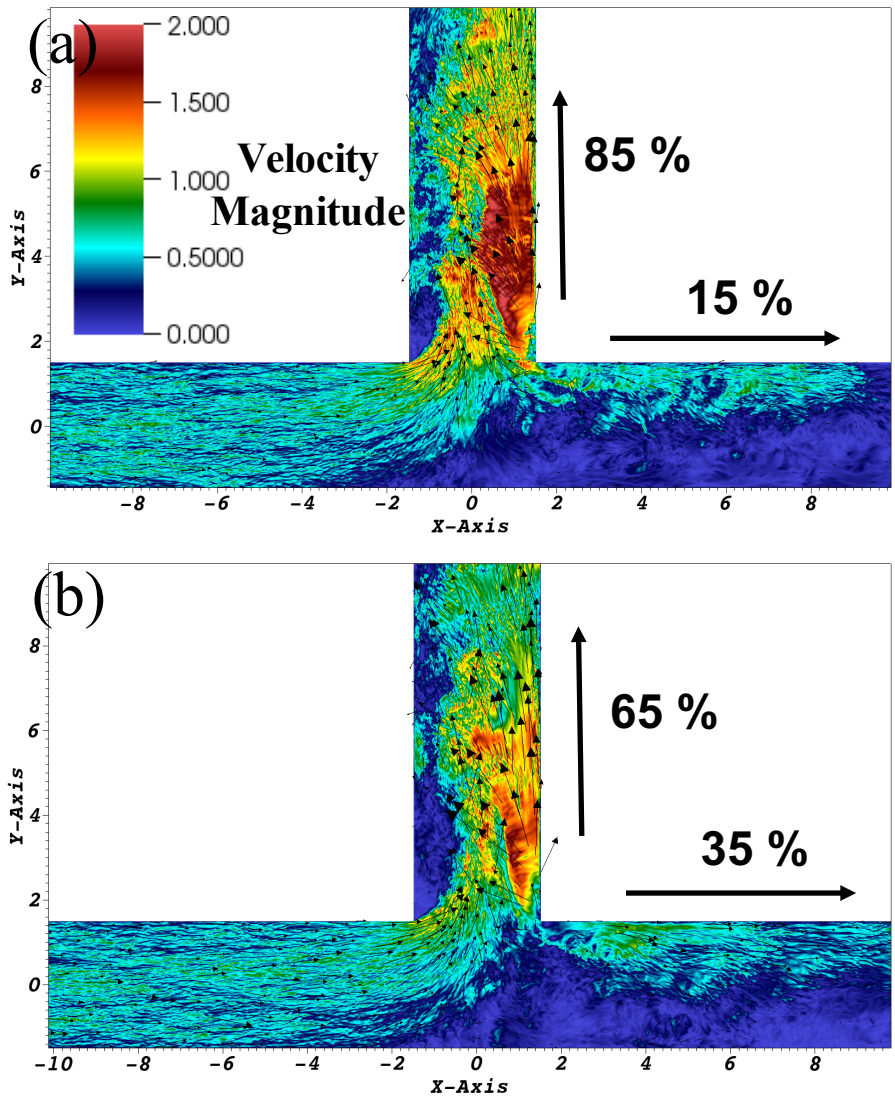


Figure 5.19: Instantaneous velocity magnitude at a 90-degree diversion at a height 5 percent from the bottom. Bulk Reynolds number of the flow is 25000, thus the incoming flow is fully turbulent. (a) In this case 85 percents the total flow enters the lateral-channel . (b) In this case 65 percent of the flow goes into the lateral-channel.

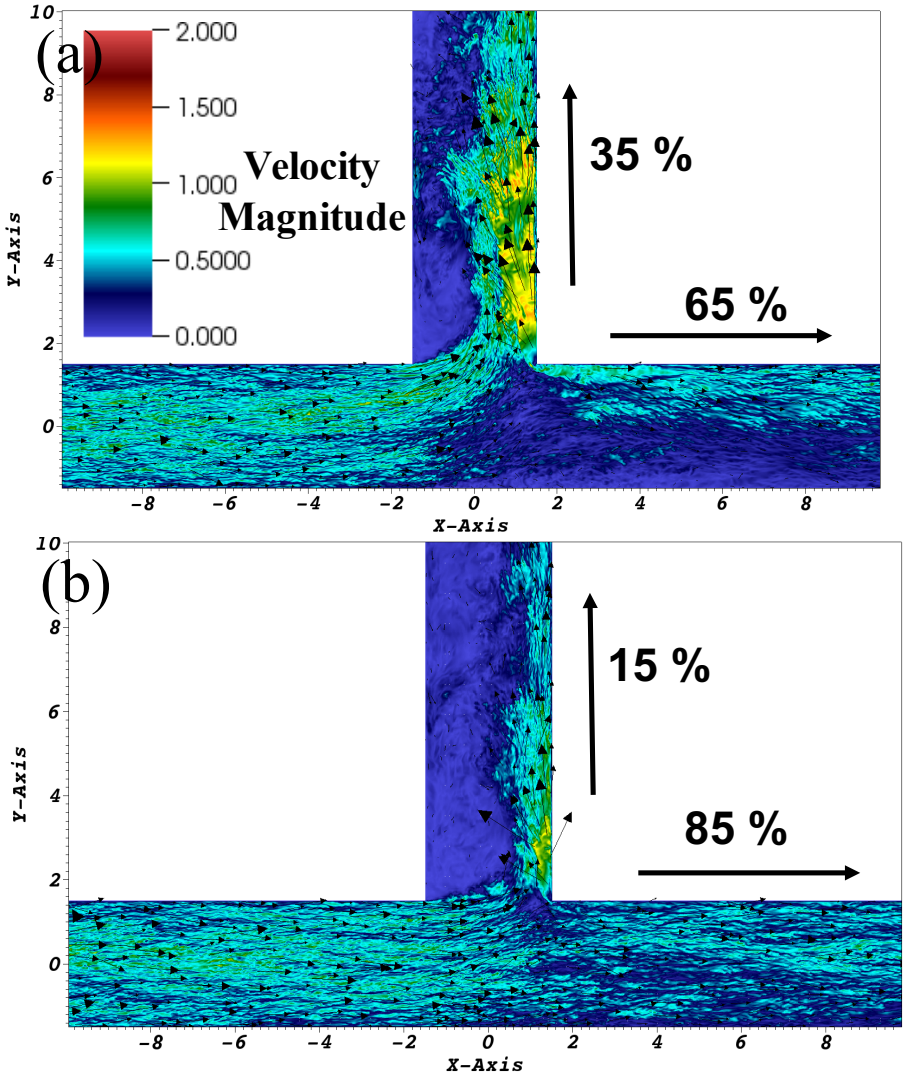


Figure 5.20: Instantaneous velocity magnitude at a 90-degree diversion at a height 5 percent from the bottom. Bulk Reynolds number of the flow is 25000, thus the incoming flow is fully turbulent. (a) In this case 35 percent of the flow enters the lateral-channel. (b) 15 percent of the flow goes into the lateral-channel. Even for the case where only 35 percent of the flow enters the lateral-channel, most of the flow near the bottom actually enters the lateral-channel.

enter the lateral-channel. The extent to which the flow near the bottom favors the lateral-channel gets obvious for the case 35 : 65, where only 35 percent of the total flow enters the lateral-channel. Despite that, majority of the flow at 5 percent height from the bottom enters the lateral-channel (see fig. 5.20a). This clearly portrays the extent of non-linearity of the phenomenon of the Bulle-Effect. Once the percentage of flow entering the lateral-channel reduces to 15 percent, there seem to be a change in *regime* of the flow (see fig. 5.20b). In this case, majority of the flow near the bed continues into the main channel. Bulle observed a similar regime shift for a flow division of $\sim 20 : 80$. In the new *regime*, the flow in the main-channel is almost uniformly distributed throughout the width, and there is no flow-separation from the walls. On the hand, in the lateral-channel, the flow is confined to less than third of the channel width.

The next set of cases that has been analyzed are cases having diversion-angle more or less than 90-degree. All the cases have $Re_{bulk} = 25000$, and are geometrically similar to Bulle's experiments. The imposed flow-division between the two channels is same as that of the corresponding Bulle's experiments. The flow division imposed at the diversions were 50 : 50, 48.2 : 51.8, 47 : 53 and 47.4 : 52.6 for the 30, 60, 120 and 150 degree cases, respectively. First the velocity magnitude at 5 percent height from the bottom has been analyzed (see fig. 5.21 and 5.22).

In the 30-degree case, despite the total flow being divided equally between the two-channels, most of the flow near the bottom enters the lateral-channel. Exactly the same can be seen happening for the 150-degree case too. Despite that similarity, the difference in structure of the flow between the 30-degree and 150-degree case is significant. In the 30-degree case the flow to an extent smoothly divides itself between the two-channels, and the virtual plane dividing parts of the flow entering the two channels intersects the junction of right-wall of the lateral-channel and the left-wall of the main-channel. This changes for the 150-degree case, with the point of intersection moving into the lateral-channel. The flow can be seen to be stagnating at that point causing a small separation zone, left of it all the flow enters the lateral-channel, and right of it all the flow enters the main-channel.

Similar stagnation zone can also be seen in the 120-degree case (see fig. 5.22b), though its position is relatively less prominent compared to the 150-degree case. The proclivity of the flow near the bottom to enter the lateral-channel is also present for the 60-degree and 120-degree cases (see fig. 5.22). If observed carefully, a trend that becomes obvious is that the maximum-velocity in the high-flow zones in both the lateral and the main-channel increases with increase in diversion angle. In all probability it is due to increase in strength of the secondary-flow circulation, with increase in diversion-angle. The evolution of the structure of the flow due to change in diversion-angle can also be seen in the velocity magnitude plots at a height of 95 percent from the bottom (see fig. 5.23).

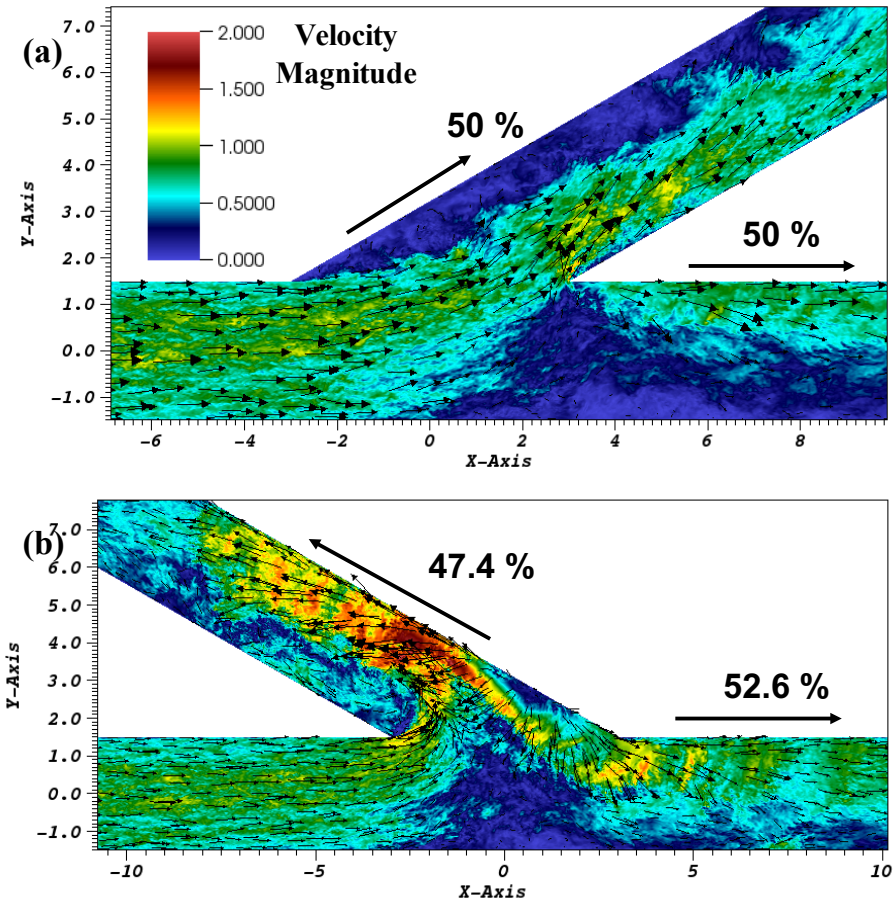


Figure 5.21: Instantaneous velocity magnitude at 5 percent height from the bottom, Reynolds no. 25000: (a) Diversion angle 30 degree, flow division 50 : 50 (b) Diversion angle 150 degree, flow division 47.4 : 52.6. Most of the flow near the bottom enters the lateral-channel. In the 150-degree case the the high-flow zone near the bottom covers more width of the main-channel than the 30-degree case.

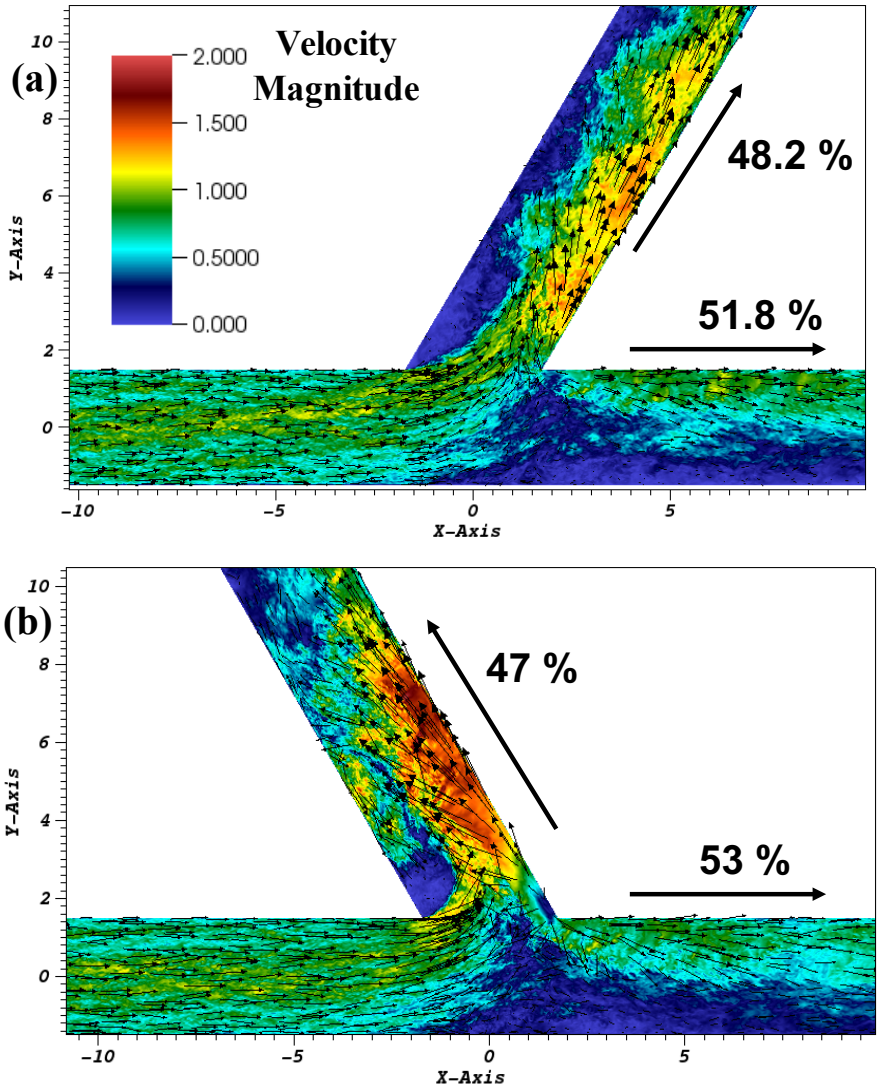


Figure 5.22: nstantaneous velocity magnitude at 5 percent height from the bottom, Reynolds no. 25000: (a) Diversion angle 60 degree, flow division 48.2 : 51.8 (b) Diversion angle 120 degree, flow division 47 : 53. Most of the flow near the bottom enters the lateral-channel.

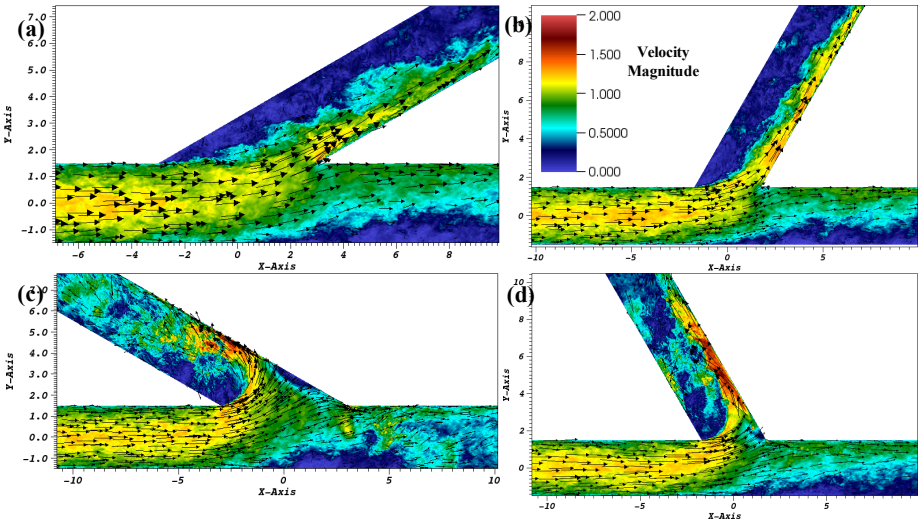


Figure 5.23: Instantaneous velocity magnitude at 95 percent height from the bottom, Reynolds no. 25000: (a) 30-degree (b) 60-degree (c) 150-degree (d) 120-degree.

Like the previous cases, most the flow near the top continues into the main-channel, even though the flow divisions for all the cases are $\sim 50:50$. Also, the size of the separation-zone in the lateral-channel, at the top of the channel is larger than at the bottom, and the trend in opposite in the main-channel. Size of the stagnation zone in the 150-degree case is also relatively larger near the top, compared to bottom of the channel (see fig. 5.23c). Compared to the 30 and 60 degree cases, the flow in the lateral-channel for 120 and 150 degree cases can be seen to be hitting the right-wall of the lateral-channel. In case the walls and the bed of the diversion are erodible, the right-wall in the 120 and 150 degree case would have failed, resulting in the lateral-channel to shift towards a less obtuse angle. The process described above might be the mechanism used by nature to avoid asymmetric bifurcations with an obtuse bifurcation-angle.

An observation was previously made about the effect of diversion-angle on the strength of the secondary-circulations, that with increase in diversion angle the strength of circulation would increase. In order to analyze that hypothesis, instantaneous vertical velocity have been analyzed for 30 and 150 degree cases at $x = 5$ in the main-channel (see fig. 5.24). It evident from the velocity plots that the counter-clockwise rotating secondary circulation for the 150-degree case is substantially stronger.

### 5.3.3 Distribution of Fine Buoyant Particles at the Diversion

A mechanism that comes across about the phenomenon of Bulle-Effect is that most of the flow near the bottom enters the lateral-channel, even when majority of the total flow continues along the main-channel. This results in two major

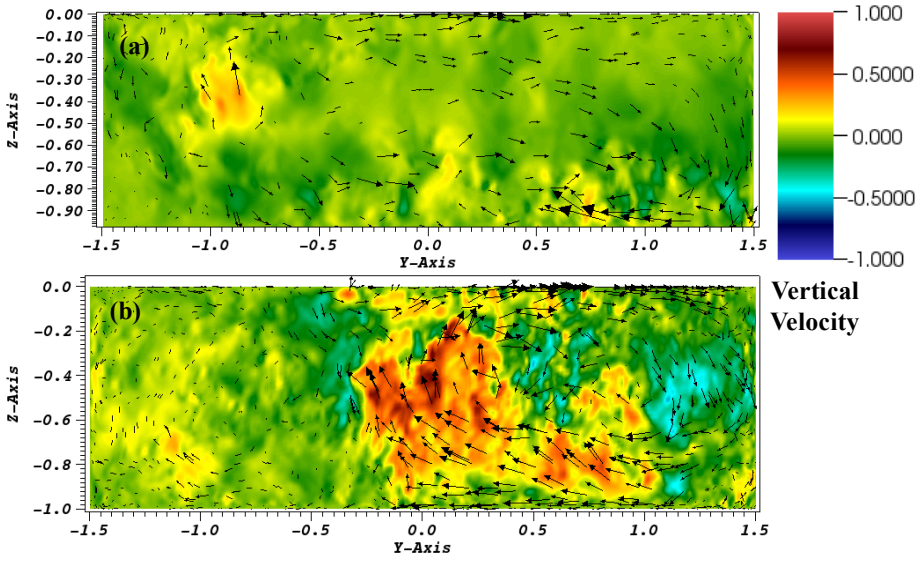


Figure 5.24: Instantaneous vertical velocity at cross-section in the main-channel after the diversion, Reynolds no. 25000: (a) 30-degree, at $x = 5$ (b) 150-degree, at $x = 5$. The general direction of the flow is out of the plane. The strength of the secondary-circulation is appreciably higher for the 150-degree case.

questions, first is how far away from the bottom does the flow preferentially enter the lateral-channel, and second is what percentage of the total flow at a particular height from the bottom enters the lateral-channel.

In order to answer the above questions, simulations were conducted for a range of $Re_{bulk}$ and 50 : 50 flow division, with a total of 100,000 lagrangian particles uniformly distributed at different layers of the flow in the main-channel (see fig. 5.25a). The particles were buoyant and the size was fine enough that they perfectly follow the flow, like wash-load in sediment transport. These simulations were conducted for a range of Reynolds number, from $Re_{bulk} = 10$ to $Re_{bulk} = 25000$. In order to count and visualize the particles, they were labeled using the height from the bottom they initially stated. Out of the six cases simulated, four with laminar inflow and two with turbulent inflow, two of them have been visualized here. First, evolution of the position of the particles for the case $Re_{bulk} = 25000$ can be seen in fig. 5.25 and 5.26.

Once the particles have been released, it travels down the main-channel and the effect of turbulence on the particle distribution int the vertical becomes evident (see fig. 5.25b). One could clearly see the colors, representing different initial height of the particles, diffusing into each other. After the particles start to move into the two channels after the diversion, it is evident that more of the particles near the bed (blue colored) has moved into the lateral-channel, and most of the particles near the surface (yellow colored) has continued into the main-channel (see fig. 5.26a). In general, the particles seems to have divided equally between the two channels, which is expected as the flow was also equally

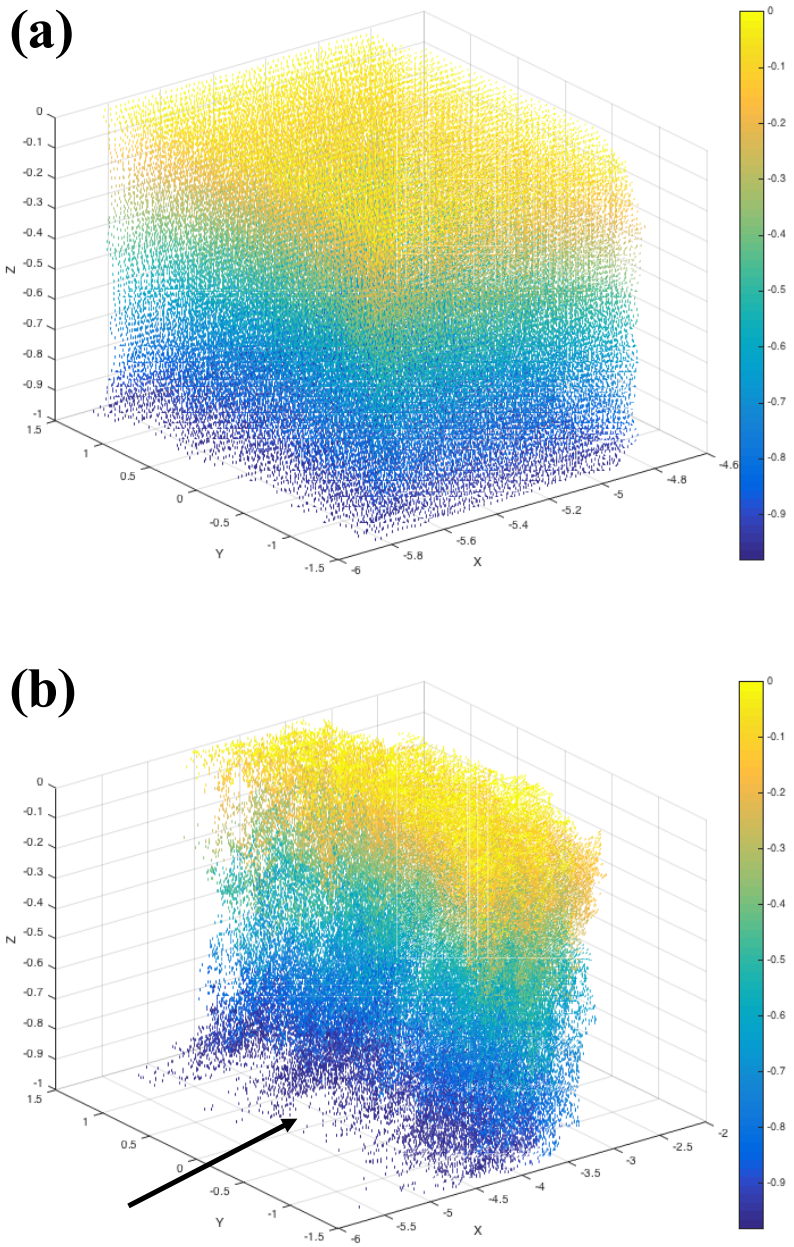


Figure 5.25: Lagrangian particle colored according to their initial height in the channel. Reynolds no. of the flow is 2500, and flow split 50:50: (a) Just after the particle have been initialized (b) After some time turbulence mixes up the particles in the vertical.

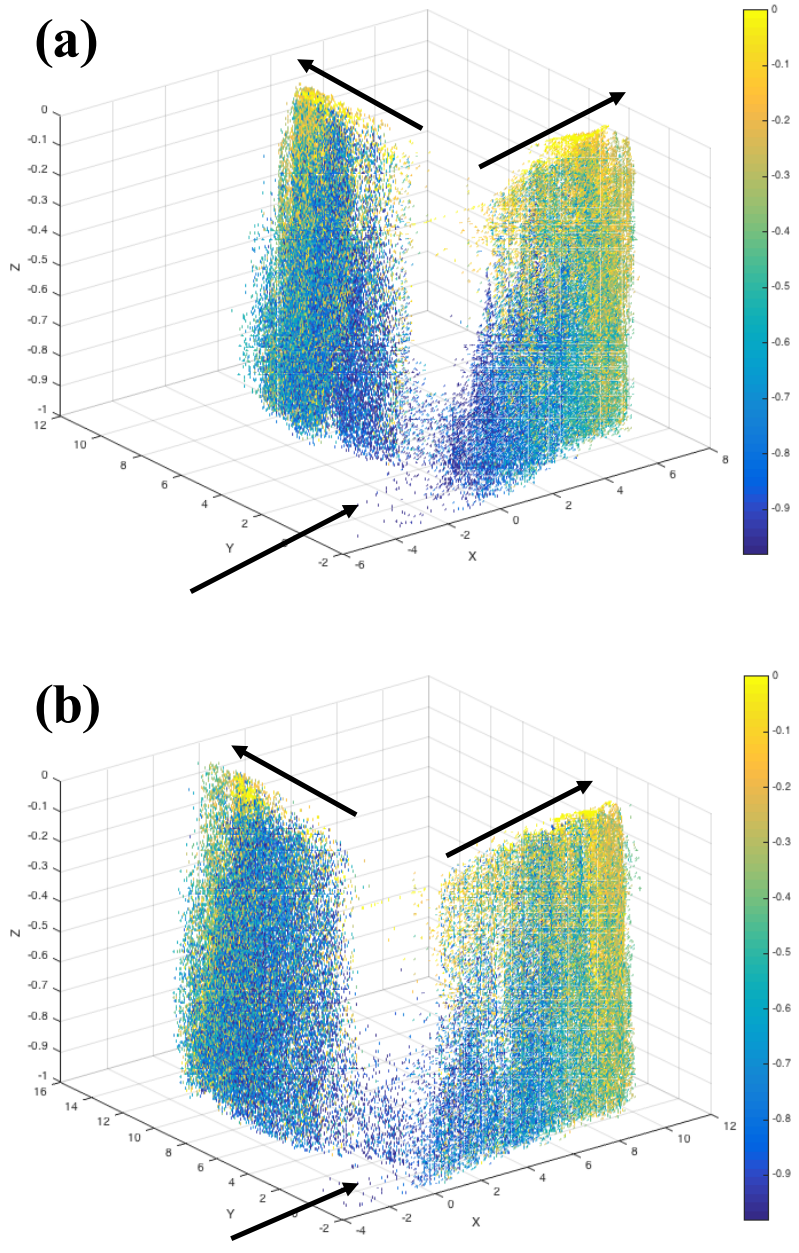


Figure 5.26: Lagrangian particle colored according to their initial height in the channel. Reynolds no. of the flow is 2500, and flow split 50:50: (a) Majority of the particles near the top (yellow) enters the main-channel, and most of them near the bottom enters the lateral-channel (b) The total number of particles gets divided almost uniformly between the two channels.

divided. Next the case with $Re_{bulk} = 300$ has also been visualized (see fig. 5.27 and 5.28).

The difference in the movement of the particles initiated near the bed, and those initiated near the top of the channel is even more evident for the laminar inflow case (see fig. 2.27b). Even though the total flow is divided 50 : 50, it is evident that almost all the particles near the bottom of the channel is enters the lateral-channel. This mirrors observations made from the velocity magnitude plots near the bed for the corresponding laminar flow cases (see fig. 2.28a). A striking difference between the the turbulent case and laminar case, is that in the laminar case an appreciably higher number of particles (of the total 100,000) enter the lateral-channel, even though the total flow is equally divided between the two channels.

In order to analyze the extent and cause of this non-linearity, the total number of particles entering each channel were counted. Depending on their initial height from the bottom, the particles were divided into 10 bins; and the total number of particles entering the two channels from each bin was also counted. This exercise was done for different $Re_{bulk}$ and 50 : 50 flow division. The findings have been plotted in fig. 5.29 below.

The results in fig. 5.29 shows a marked difference in behavior of the flow in the laminar and the turbulent regime. For the laminar flows $Re = 100to1000$, almost all the particles in the bottom 3rd of the channel enters the lateral-channel. And as the movement of the particles perfectly mirror that of the flow, thus for laminar flows it can be said that all the flow in the bottom third of the channel moves into the lateral-channel. For the turbulent flow cases, around 65-70 percent of the flow within the bottom 10 percent of the flow enters the lateral-channel, and this number only reduces to 55-60 percent within the bottom 30 percent of the flow. This is a significant finding, because it shows that Bulle-Effect is not just valid for bedload, but even for suspended load traveling within the bottom 10-30 percent of the channel. Thus, even if the flow is divided equally between the two channels, if the sediment is traveling in the bottom 30 percent of the flow, then majority of it will enter the lateral-channel. Both the turbulent cases show almost similar particle distribution trend, so does the three laminar cases with $Re_{bulk} \geq 100$. An outlier to the laminar cases is $Re_{bulk} = 10$. This case is different because at that Reynolds number the flow is somewhat similar to a Stoke's flow (creeping flow). Even though the formal definition of Stoke's flow is $Re < 1$, but at $Re_{bulk} = 10$ it is already approaching the Stokes flow regime.

An interesting finding to come out of the analysis is that out of the 100,000 particles released, for the turbulent flow cases the total number of particles are equally divided between the two channels as the flow division is also 50 : 50. Though for the laminar flow cases ($Re_{bulk} = 100 - 1000$), about 63-65 percent of the particles were found to enter the lateral-channel. This can be attributed to the parabolic nature of the laminar flow profile, which makes the velocity

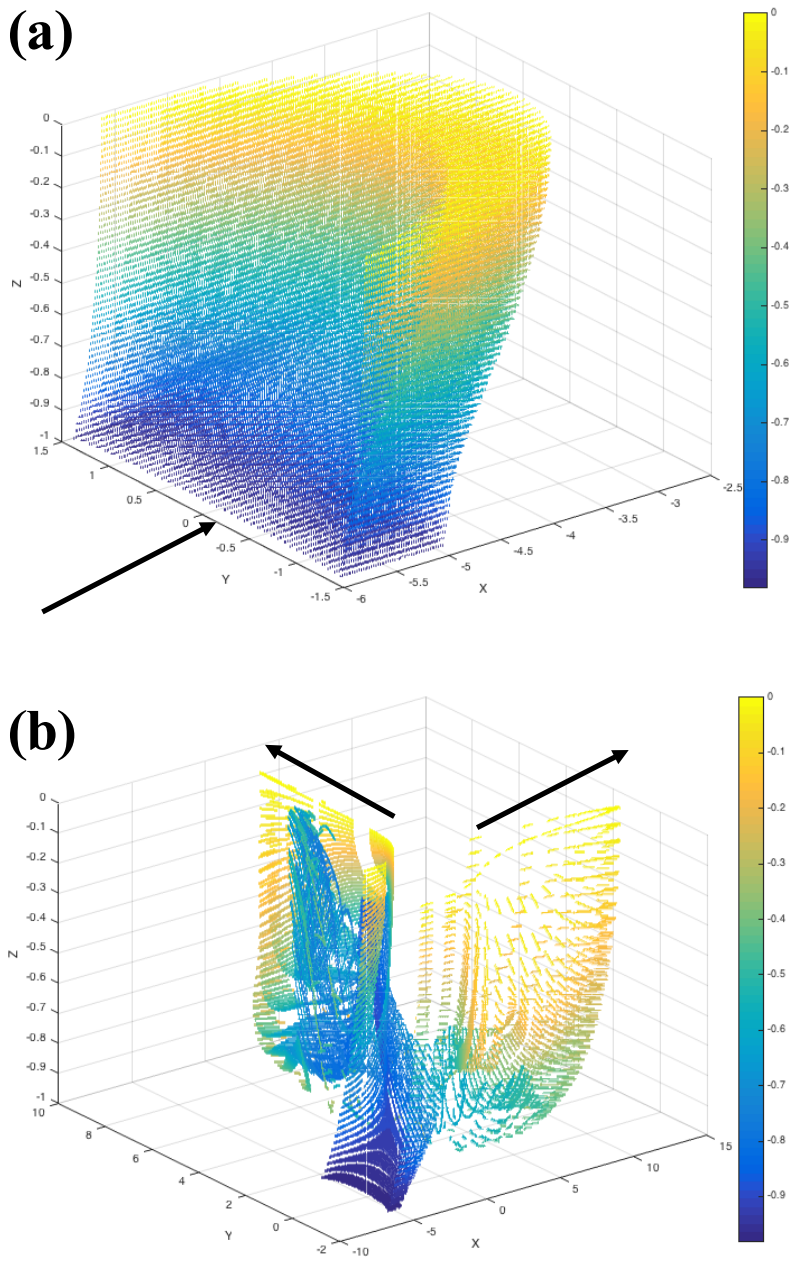


Figure 5.27: Lagrangian particle colored according to their initial height in the channel. Reynolds no. of the flow is 300, and flow split 50:50: (a) Just after the particle have been initialized (b) Majority of the particles near the top (yellow) enters the main-channel, and most of them near the bottom (blue) enters the lateral-channel.

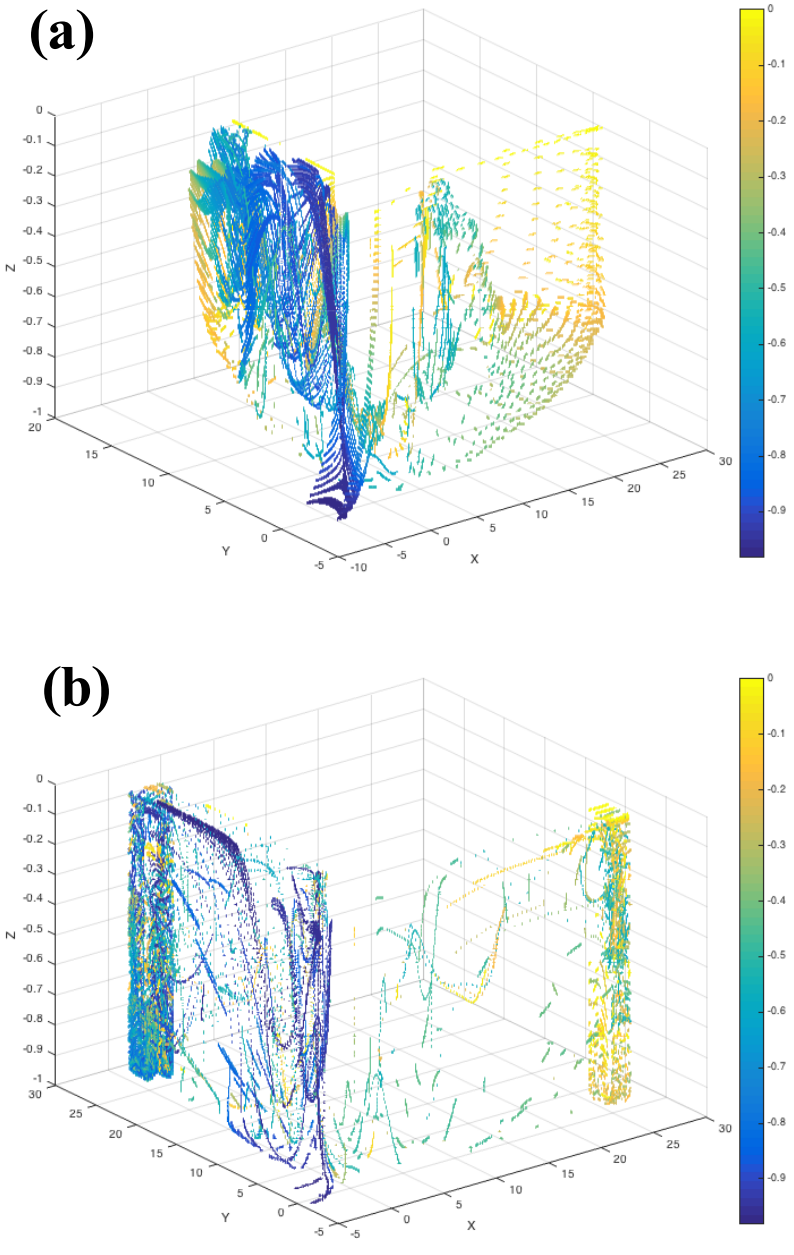


Figure 5.28: Lagrangian particle colored according to their initial height in the channel. Reynolds no. of the flow is 300, and flow split 50:50: (a) In the lateral-channel the particles can be seen to be rotating with the strong clock-wise rotating vortex (b) particles near the bottom of the main-channel not only moves into the lateral-channel, it also seem to jump up while doing so.

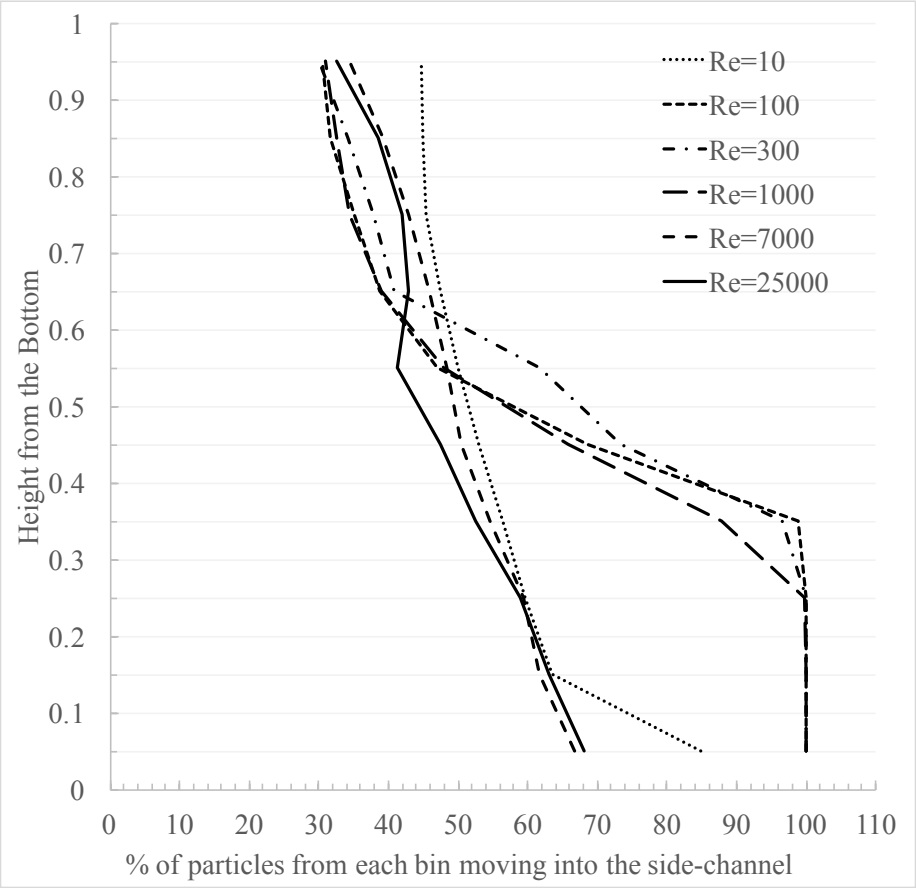


Figure 5.29: x-axis represents the percentage of the particles from each bin/layer entering the lateral-channel, for a 90-degree diversion and a 50:50 flow-split. y-axis represents the mean height of each bin/layer. Results from six different Reynolds number was plotted.

of the flow near the bottom appreciably smaller than near the top. Through a simple derivation it cane be shown that if 50 percent of the total flow is entering the lateral channel, and if all the flow comes from the lower section of the water-column, then about 65 percent of the height of the water-column from bottom would be required to provide for 50 percent of the total-flow to the lateral channel.

### 5.3.4 Distribution of Poly-Disperse Sediment

From the results discussed in the previous section it is clear that the phenomenon of Bulle-Effect is not just valid for sediment moving as bedload, but also suspended sediment that may be concentrated atthe bottom third of the water-column. It also became clear that if the flow in the channel is laminar, then almost all the sediment moving in the bottom third of the water-column will enter the lateral-channel. Based on the above finding, for a 90-degree diversion simulations were conducted for 5 different flow divisions for $Re_{bulk} = 7000$ and 6 different flow divisions for $Re_{bulk} = 25000$, with poly-disperse sediment. In the current study, poly-disperse sediment is implemented by using sediments of different diameter. The sediment used varied in the range of very coarse sand to medium-coarse silt. That apart particles corresponding to wash-load was also used. All the sediment was assumed to have specific gravity of 2.65, which is the value usually used for sand [48].

Sediment of six different diameter was put in the main-channel before the diversion. Size of five of the sediment fall in the range, 1.4 mm to 0.035 mm, and as mentioned earlier, one of the sediment is fine enough to be considered as wash-load. Bulle for his experiments used sand whose *diameter did not exceed* 1.2 mm, and had a specific gravity of 1.5. As Bulle did not mention a specific diameter, a $D_{50}$ of 0.7 mm is a plausible assumption. With those information about the sediment used by Bulle, the particle fall velocity ($V_s$) of the sediment used by Bulle is slightly higher than the 0.35 mm sand (medium sand) used in the current simulations. Of the six different sediment size used, for the $Re_{bulk} = 7000$ case two of them would primarily move in suspension, and for the $Re_{bulk} = 25000$ case three of the sediment sizes used would primarily move in suspension. For the $Re_{bulk} = 25000$ case, apart from the wash load, the two particle diameters (type) that would remain in suspension are the very fine sand (0.07 mm), and medium-coarse silt (0.035 mm). For the sediments primarily traveling as bedload, the particles were uniformly distributed along the width of the channel, and at 4 levels near the bottom of the channel. For the sediment primarily traveling in suspension, the initial height of the particles were calculated based on the Rouse-Ippen-Vannoni relationship [48]. And the sediment concentration profiles for the case of $Re_{bulk} = 25000$ has been produced in fig. 5.33, along with their corresponding sediment diameter and Rouse number. Rouse number is defined as $V_s/(u_*\kappa)$, where $V_s$ is particle settling velocity, $u_*$

is the bed shear velocity and $\kappa$ is the Von Karman constant.

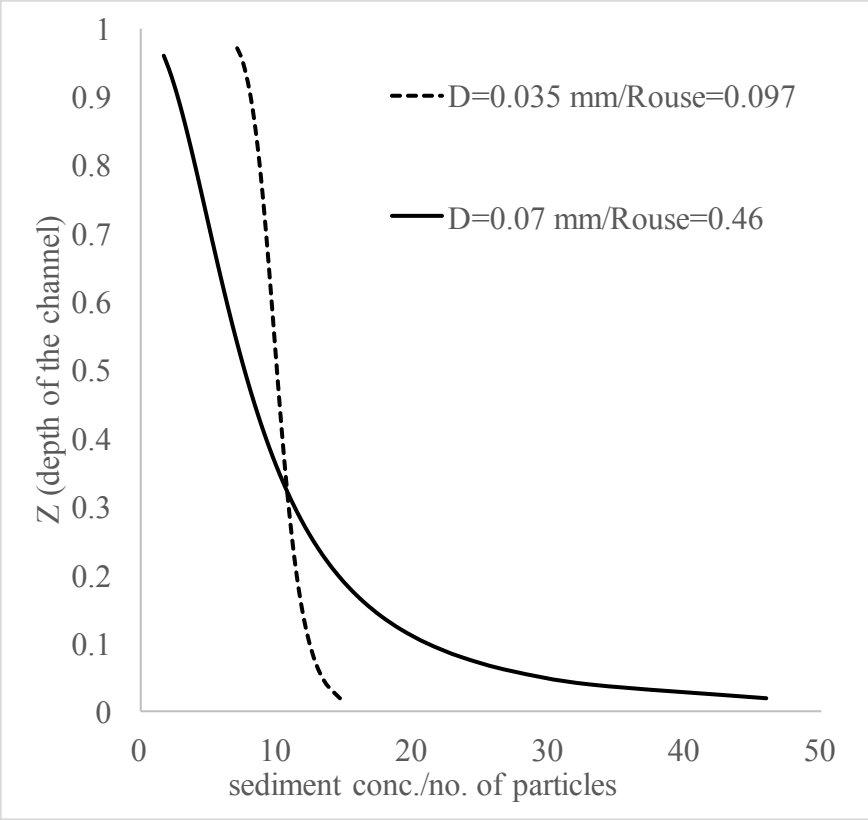


Figure 5.30: Concentration profiles used for initializing the suspended sediments for the $Re_{bulk} = 25000$ case. The profiles are based on the Rouse-Ippen-Vannoni relationship for suspended sediment [48].

Analyzing the results from the simulations, first the case $Re_{bulk} = 7000$ has been presented (see fig. 5.31). Apart from the wash-load, the Rouse number of the other sediment in suspension in this case is $\sim 0.35$, thus the initial sediment profile used for it is similar to that of the 0.07 mm case in fig. 5.30.

The wash-load can be seen to have been simulated correctly, with the distribution between the channels almost matching the flow division. It is also evident that apart from the flow-division, the size of the sediment plays a major factor in deciding the sediment distribution at the diversion. For the same flow-division, the amount of sediment entering the lateral-channel increases with increase in sediment size. Similar results were also observed experimentally by Dancy [55] and in the field by Erxun [53] (see Chapter 2). And not just sediment moving as bedload, but even suspended sediment can be seen to enter the lateral-channel, when it has higher concentration at the bottom 20 percent of channel. The way size of sediment effects sediment distribution is; larger sediment tend to get transported closer to the bottom of the channel, and the flow closer to the bottom primarily enters the lateral-channel, thus sediment that move closer to the bottom of the channel will have a higher chance to enter the

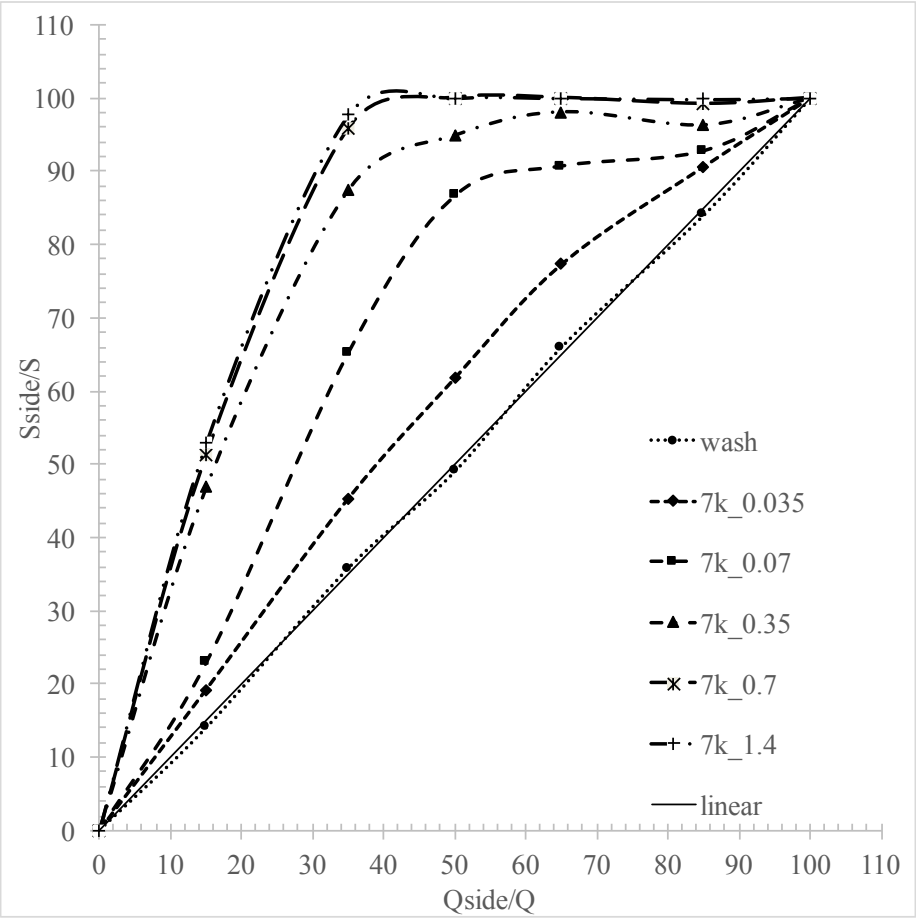


Figure 5.31: y-axis represents the percentage of total sediment entering the lateral-channel ($S_{side}/S$), and x-axis represents the percentage of water entering the lateral-channel ($Q_{side}/Q$). The case presented here is the 90-degree diversion, and $Re_{bulk} = 7000$. The plot shows the effect of flow-division and sediment-size on the distribution of sediment at the diversion.

lateral-channel.This basically confirms the hypothesis that Bulle-Effect can be also used for efficiently diverting suspended sediment.

Next the case of $Re_{bulk} = 25000$ has been analyzed (see fig. 5.32). Along with the results from the simulations, results from Bulle's experiments have also been plotted. Among Bulle's experiments, there is only case that matches the simulation configuration, that is the case with 90-degree diversion and about 45 percent of the flow entering the lateral-channel. Though there are other experiments with different flow-divisions, but with diversion angle of 30-degree. Thus, in order to check the general trend of variation of $S_{side}/S$ with respect to $Q_{side}/Q$ for a particular sediment size, the results from the 30-degree and 90-degree experiments have been plotted together.

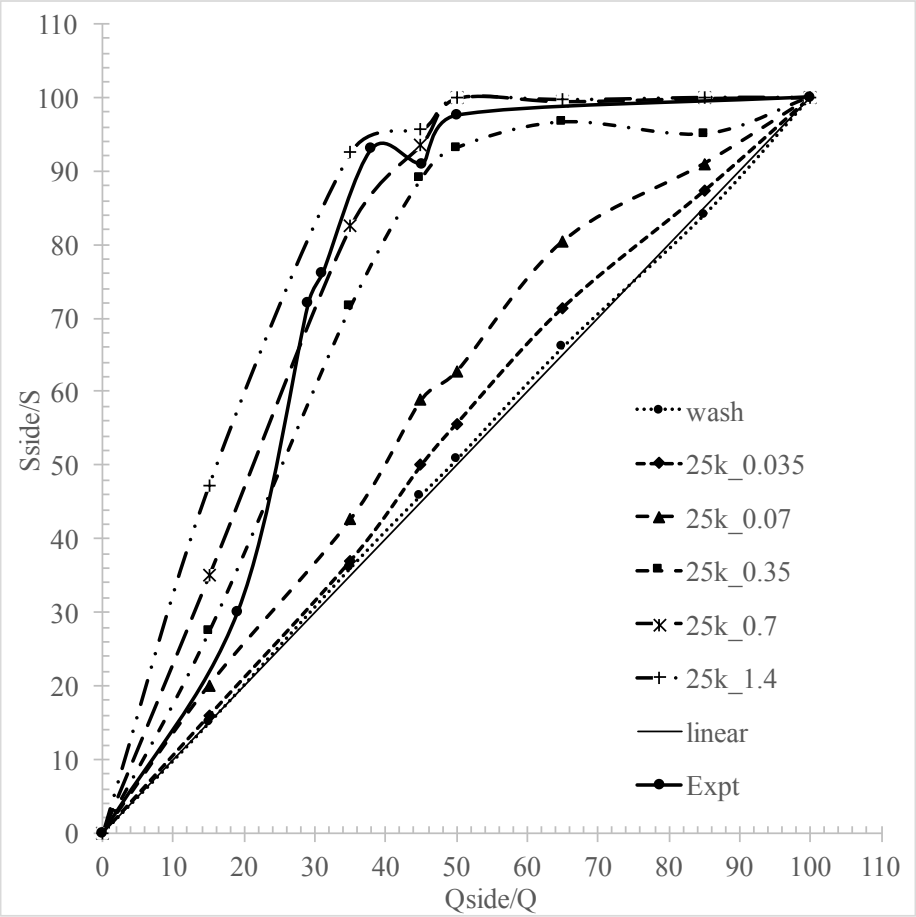


Figure 5.32: y-axis represents the percentage of total sediment entering the lateral-channel ($S_{side}/S$), and x-axis represents the percentage of water entering the lateral-channel ($Q_{side}/Q$). The case presented here is the 90-degree diversion, and $Re_{bulk} = 25000$. The plot shows the effect of flow-division and sediment-size on the distribution of sediment at the diversion. Results from Bulle's experiments have been plotted for comparison.

For this case too, the trend of increase in $S_{side}/S$ with increase in sediment size is evident. The general trend agrees with the trend shown in Bulle's ex-

periments. Also, the $S_{side}/S$ predicted by the simulation with a configuration similar to Bulle's experiments, which is $Q_{side}/Q = 45$ but slightly higher Rouse number than the 0.35 mm case from the simulations, is within 2 percent of Bulle's observations. Among the suspended sediment cases, the sediment which is relatively more uniformly distributed (0.035 mm), the non-linearity in the sediment due to Bulle-Effect distribution only kicks in once $Q_{side}/Q \geq 45$.

The trend shown by sediment distribution at the diversion with respect to sediment size shows a pattern that is also dependent on the $Re_{bulk}$ of the flow. Thus a better parameter to represent the sediment in this context is the Rouse number, as it represents the properties of the sediment through particle settling velocity ($V_s$) and the Reynolds number of the flow through bed shear velocity ($u_*$). Thus, all the simulated results along with the data from Bulle's experiments have been plotted together in fig. 5.33, with the legends showing the corresponding Rouse number. It is evident from the plots that $S_{side}/S$ increases with increase in Rouse number. With, the cases with similar Rouse numbers but with different $Re_{bulk}$ showing very similar trends, e.g. the cases $7k - Rouse = 0.35$ and $7k - Rouse = 0.45$. Among the simulations, the only part where the simulations show slight discrepancy from the trends shown by Bulle's experiments is at lower $Q_{side}/Q$, i.e. $Q_{side}/Q = 15 - 20$. Some of the cases (in particular two) that are expected to have relatively lower values of $S_{side}/S$ compared to Bulle's experiments, have higher values. This might be related to the fact that particle-particle interactions and feedback from the sediments to the flow, are not modeled in the current Lagrangian-particle model for sediment. Though we can see that, despite the assumptions made for the model, it captures the general trend well.

## 5.4 Conclusions

In this chapter first the structure of the flow was analyzed for different $Re_{bulk}$, diversion angles and flow splits. Then the distribution of sediment particles were analyzed, based on their Rouse number and where in the water-column they are initiated. Here we briefly summarize all the findings from this chapter.

First, the simulations confirmed the fact that at a diversion, majority of the flow near the bottom of the channel enters the lateral-channel, whereas majority of the flow near the top continues into the main channel. And this was found to be true, even when only 35 percent of the total flow was going into the lateral-channel.

Second, the mechanism causing Bulle-Effect was found to be stronger for laminar flows, compared to turbulent. For the laminar flow cases, it was found that for the case where 50 percent of the total flow is entering tha lateral-channel, almost all the flow in the bottom 30 percent of the channel enters the lateral-channel. Whereas for turbulent flows, this percentage is about 65-70

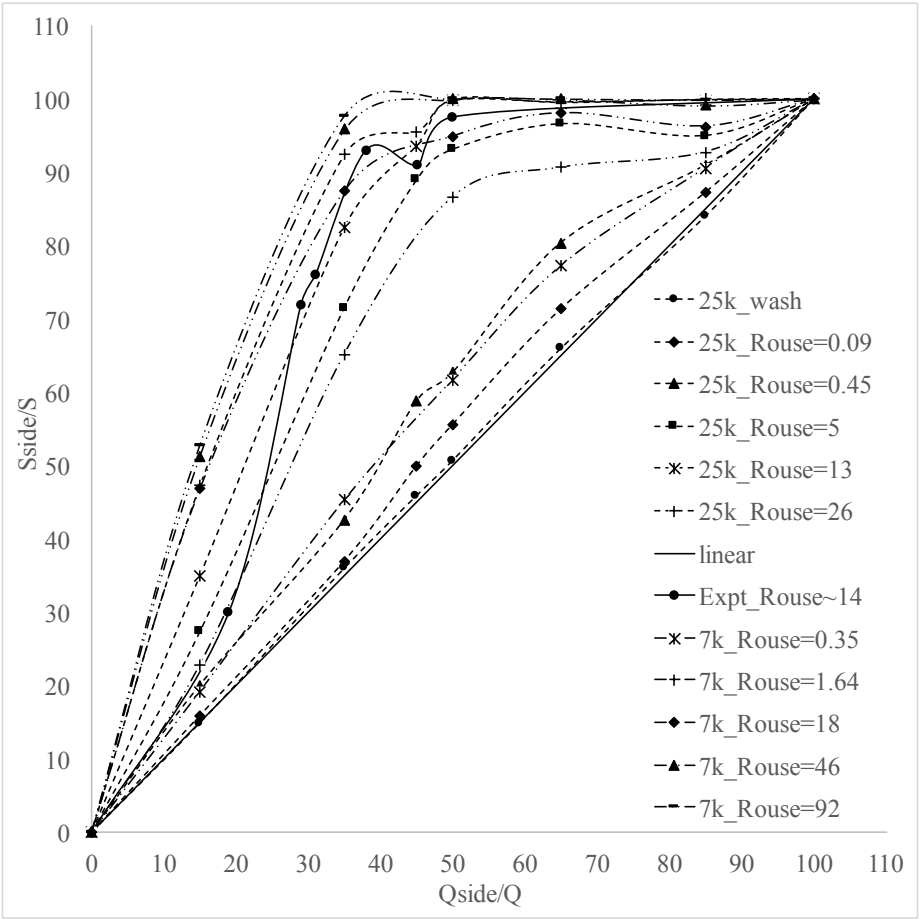


Figure 5.33: y-axis represents the percentage of total sediment entering the lateral-channel ($S_{side}/S$), and x-axis represents the percentage of water entering the lateral-channel ($Q_{side}/Q$). The cases presented here are the 90-degree diversion, and $Re_{bulk} = 7000$ and $Re_{bulk} = 25000$. The plot shows the effect of flow-division and sediment-size on the distribution of sediment at the diversion. Results from Bulle's experiments have been plotted for comparison. For comparison purposes, the approximate Rouse number for all the cases have also been provided in the legends.

percent in the bottom 20 percent of the channel. The difference is primarily due to difference in mean-velocity profile in the laminar (parabolic) and turbulent cases (log law).

The trend seen for the 90-degree diversions were found to also occur for other diversion angles like 30,60,120 and 150 degree. Though the structure of the flow at the diversion in the 120 and 150 degree cases were found to be slightly different from the 30 and 60 degree cases. The strength of secondary circulations, formed in the lateral and main channels after the diversion, were found to increase with increase in diversion angle. With appreciable difference being shown between the 30-degree and 150-degree cases (see fig. 5.24).

The simulations with small buoyant particle graphically showed that most of the flow entering the lateral-channel comes from bottom of the channel, whereas the flow near the top primarily continues into the main-channel (see fig. 5.25 to 5.28). It also showed the extent to which the mechanism causing Bulle-Effect is stronger for laminar flow cases. The particles initiated at different height from the bottom were counted to check if they entered the main or lateral channel (see fig. 5.29). It was found that for laminar flow cases, 90-100 percent of the particles starting in the bottom 40 percent of the channel entered the lateral-channel. For the turbulent flow cases, 60-70 percent of the particles initiated in the bottom 30 percent of the flow entered the lateral-channel.

Finally, simulations were conducted with poly-disperse sediment, that is sediment with different diameters. First it was found that, Bulle-Effect can non-linear sediment distribution not only for sediment moving as bedload, but also suspended sediment that move in the lower 20–30 percent of the water-column. Second, along with the parameter $Q_{side}/Q$, size of the sediment was also found to influence the percentage of sediment entering the lateral channel ($S_{side}/S$) (see fig. 5.31 and 5.32). Though, the parameter Rouse number of the sediment was later found to be more of a representative parameter than size of sediment (see fig. 5.33), as it combines the information about the sediment (through particle settling velocity $V_s$) and the flow (through shear velocity $u_*$).

At the start of this chapter, based on Riad's analysis [50] it was mentioned that the factors on which sediment distribution at a diversion depend are

$$\frac{S_{side}}{S} = \left( \frac{Q_{side}}{Q}, Re, Fr, \frac{d}{D} \right) \tag{5.24}$$

where $Re$ is Reynolds number of the flow, $Fr$ is Froude number of the flow, $d$ is the representative diameter of sediment and $D$ is depth of the flow. The results discussed in the current chapter does corroborate the above equation. Even though in the current study, the effect of Froude number on $\frac{S_{side}}{S}$ has not been analyzed, based on the findings a modified version of the above relationship has been put forth:

$$\frac{S_{side}}{S} = \left( \frac{Q_{side}}{Q}, Fr, \frac{V_s}{u_* \kappa} \right) \tag{5.25}$$

# CHAPTER 6

# THREE-DIMENSIONAL NUMERICAL MODELING OF THE BULLE-EFFECT USING A RANS BASED FREE-SURFACE HYDRODYNAMIC MODEL

## Authors

Som Dutta, Dongchen Wang, Pablo Tassi, Marcelo H. Garcia

under revision for Earth Surface Processes and Landform, Wiley.

## Abstract

Bulle-Effect is a phenomenon in which a disproportionately high ratio of near-bed sediment load at a fluvial diversion moves into the diverted channel, even for cases in which the proportion of water (with respect to the main flow) entering the diversion channel is relatively small. This phenomenon has wide ranging implications for both engineered and natural systems; from efficient design of channels to redirect water and sediment for reclaiming sinking deltas, designing navigational channels that do not need frequent dredging, to morphological evolution of river bifurcations. The first ever, and one of the most extensive set of experiments conducted to explore this phenomenon, were conducted by Bulle in 1926. In the current study the experiments conducted by Bulle have been simulated using an open-source, free-surface finite-element based hydrodynamic solver. Main objectives were to explore to what extent the complex phenomenon of Bulle-Effect at the scale of a laboratory experiment can be simulated accurately using Reynolds-Averaged Navier-Stokes (RANS) based hydrodynamic solver, and to understand the details of the hydrodynamics that Bulle could not analyze through his experiments. The hydrodynamics captured by the simulations were found to match the observations made by Bulle through his experiments, and the distributions of sediment at the diversion predicted by the numerical simulations were found to match the general trend observed in the laboratory experiments. The results from the numerical simulations were also compared with existing one-dimensional models for sediment distribution at bifurcations, and the three-dimensional numerical model was found to perform appreciably better. This is expected due to the complex flow features at the diversion, which can only be captured satisfactorily using a three-dimensional

hydrodynamic model.

## 6.1 Introduction

Channel bifurcations and confluences are fundamental units of fluvial systems, and have been extensively studied due to their importance to the long-term evolution of the fluvial-system [48]. Flow at bifurcations and diversions have been found to be complex, primarily due to the highly three-dimensional nature of the flow [43, 40]. Complexity of the flow results in a non-linear distribution of sediment between the bifurcating channels, thus making the prediction of sediment transport relatively difficult [106]. The term non-linear refers to the ratio of near-bed sediment discharge entering the two channels after bifurcation being not linearly proportional to the ratio of water discharge entering the two channels. The importance of fluvial bifurcations have been further underlined by the comprehensive review of the state of art in research on fluvial bifurcations by Kleinhans et al. [17].

Diversions are a subset of bifurcations, where one channel after the bifurcation continues along the direction of the original channel and the other one branches out laterally at an angle. Many of the bifurcations in nature have features similar to a diversion. That apart, diversions are a common feature of engineered fluvial systems, where a lateral channel has been traditionally used for diverting water for different purposes, like navigation, irrigation etc. In the last few years, efficient diversion of water and sediment has also gained importance for various engineering purposes; e.g. significant effort have gone into studying the viability of diverting water and sediment from the lower Mississippi River to mitigate potential loss of coastal land in Louisiana [20, 21]. Various possible designs and locations of flow diversion structures along the Mississippi River are being evaluated to ascertain the optimal case that would allow maximum amount of sediment to be diverted for a particular water discharge [25]. Moreover creation of artificial diversions to divert water and sediment have been suggested as a possible solution to counter the problem of maintenance of large deltas all over the world [26]. Finding the optimal location and layout for a diversion will be more efficient, provided the fundamental mechanism behind the partition of both water and sediment-load between the channels at a diversion is fully comprehended.

One of the first systematic studies that quantified the aforementioned process was conducted by Bulle in 1926 [1]. To further illustrate the phenomenon, a few results from Bulle's experiments are discussed in the current section. Figure 6.1 shows a schematic 30 degree diversion, along with flow-structures observed by Bulle during his experiments. The angle of diversion represents the angle between the main and the diversion channel. Bedload sediment discharge and liquid discharge in the original channel have been represented using $S$ and $Q$

respectively. The discharge of water and bedload sediment remaining in the main channel have been represented by $Q_{main}$ and $S_{main}$, and the discharge of water and sediment going into the diverted channel have been represented by $Q_{side}$ and $S_{side}$, respectively.

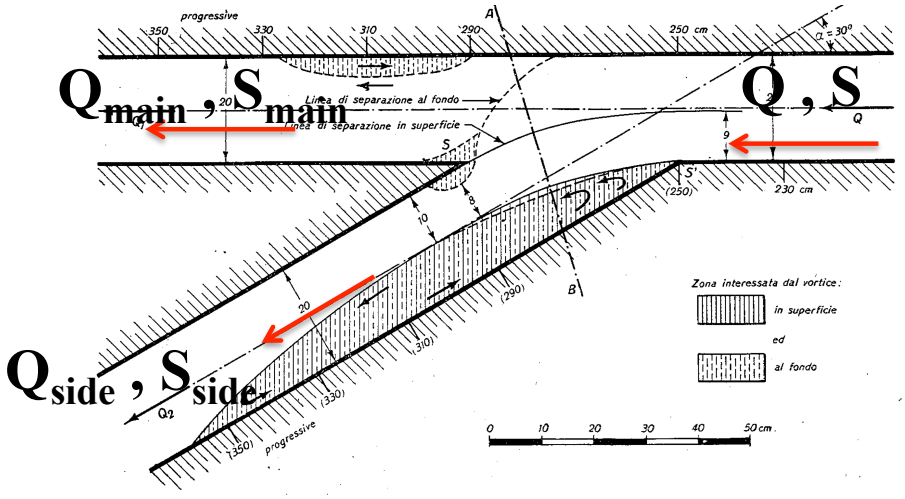


Figure 6.1: The figure shows a diversion with an angle of 30 degree. The figure has been reproduced from [1], and it shows the two recirculation zones observed by Bulle in his experiment. The arrows indicates the flow direction.

Bulle found that the amount of bedload sediment entering the diversion channel ($S_{side}$) was disproportionately higher with respect to the water discharge. This highly non-linear distribution of bedload sediment discharge, between the main and diverted channel at a diversion is often referred to as the *Bulle-Effect* [39]. The relationship between the ratio of bedload discharge moving into the two channels $S_{side}/S_{main}$, and the ratio of the corresponding water discharge $Q_{side}/Q_{main}$ can be defined using the equation :

$$\frac{S_{side}}{S_{main}} = a\left(\frac{Q_{side}}{Q_{main}}\right)^{b} \tag{6.1}$$

where $a$ and $b$ are constants. If the distribution of bedload sediment between the two channels were linear, then $b = 1$. From Bulle's experiments $b > 1$, thus making the sediment distribution *non-linear*.

Figure 6.2, plotted using data from Bulle's experiments, shows the division of water and bedload sediment at diversions with different angles for experiments conducted with $Q = 0.005\ m^3 s^{-1}$ (where $Q = Q_{main} + Q_{side}$). It is evident from the plot that sediment discharge ($S_{side}$) entering the diverted channel is disproportionately higher than that remaining in the main channel ($S_{main}$), even for cases where $Q_{main} > Q_{side}$. It can also be observed that the amount of bedload entering the lateral-channel varies with an increase in diversion-angle, with the maximum amount of sediment continuing in the main channel for a diversion angle of 120 degrees. Bulle also conducted experiments for different flow par-

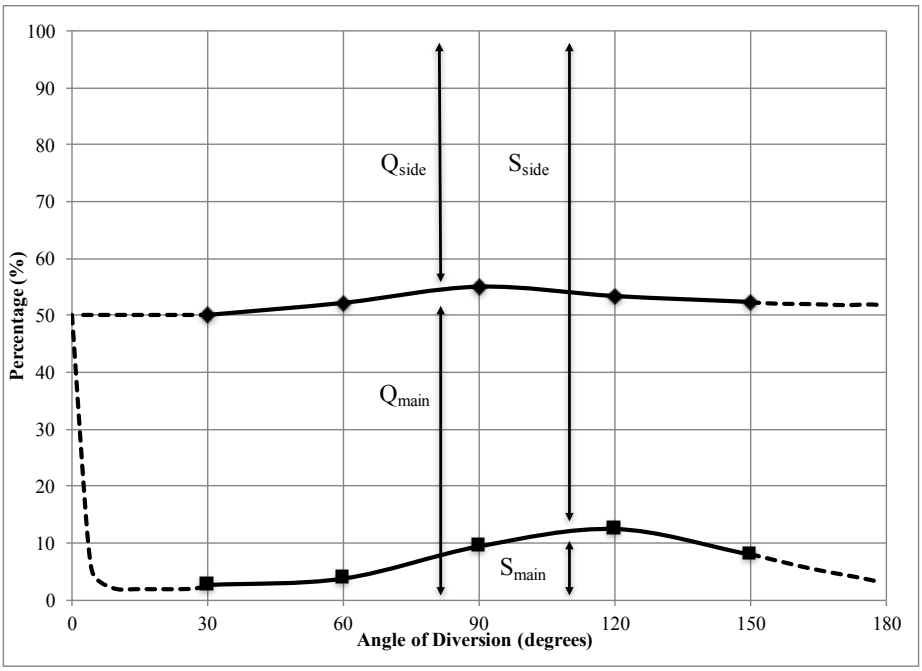


Figure 6.2: Variation of percentage of water discharge and percentage of the total bedload sediment moving into the main channel $(Q_{main}, S_{main})$, and the percentages of water and sediment moving into the lateral channel $(Q_{side}, S_{side})$ for $Q = 0.005\ m^3 s^{-1}$ (where $Q = Q_{main} + Q_{side}$ and $S = S_{main} + S_{side}$), with respect to different angles of diversion (represented on the $x$-axis). Bold lines with marker points represent the experiments conducted by Bulle, and the dashed line represent the extrapolation of the data suggested by Bulle. All the data have been reproduced from Bulle's study [1].

titioning and channel layouts, which are further discussed and compared with simulations results in the following sections. Even though the exact mechanism behind the Bulle-Effect is not fully understood, Bulle himself and some studies after his have hinted towards the presence of strong secondary currents that sweep the near-bed sediment into the diversion channel [84, 40].

In his experiments, Bulle also observed recirculation zones (see fig. 6.1); one in the diverted channel primarily caused due to separation of the flow going in the diverted-channel from the left-bank, and a smaller recirculation zone formed at the right-bank of the main-channel just after the diversion. The size of the recirculation zones were found to vary with depth [1], that is the width of the recirculation zone in the main-channel increases with an increase in depth, and the width of the recirculation zone in the lateral-channel decreases with an increase in depth. Variation of the recirculation zone width, with respect to the depth has also been observed in the results from Large Eddy Simulations (LES) of turbulent flow at an idealized 90-degree diversion that has dimensions similar to that of Bulle's experiments [40].

After Bulle's seminal work, there have been several experimental studies on the topic, and all of them have reaffirmed the observations made by Bulle.

Christani conducted experiments before World-War II for a diversion angle of 29 degrees, but with a water discharge higher than Bulle's [3]. His findings matched with those of Bulle, and were published after the War by Benini [3], as Christani had died during the War. At the same time, research and experiments on diversions were also being conducted in the USA, with the focus primarily on finding optimal locations to construct lateral channels on large alluvial streams for diverting water with least amount of sediment [6]. Dancy through his experiments on a 30-degree diversion showed dependence of Bulle-Effect on the ratio between sediment fall-velocity and bed shear velocity, which is also known as the Rouse number [37]. Riad conducted experiments at a scale larger than that of Bulle but his findings were similar, and he also performed dimensional analysis to come up with a set of parameters that may influence the distribution of sediment at a diversion [9]. Based on his experiments, Riad reduced the general parameter set from twelve to four parameters that he reasoned influenced near bed sediment distribution at all diversions (irrespective of angle of diversion). The parameters were, the ratio of specific flow discharge in the two channels after the diversion $q_{side}/q_{main}$, Froude number of the flow before the diversion $Fr$, Reynolds number of the flow before the diversion $Re$, and the ratio of sediment size ($d$) and depth of the flow ($D$) in the main channel before the diversion $d/D$. More recently, Herrero conducted experiments on a 90-degree diversion with a sand covered bed instead of the rigid bed used in majority of the previous experiments [39]. The experiments were run till the system reached a state of equilibrium, and the dimensions of the experimental layout was similar to that of Bulle's. The experiments were conducted to not only measure the sediment moving into the two branches, but to also observe the dynamics of the bed at the diversion. The experiments yielded non-linear distribution of sediment between the two channels, similar to the Bulle-Effect. It also put forth the formation of scour holes at the high-speed flow areas, and deposition of sediment below the flow recirculation zones. Recently, similar results have also been reported by Rezapour et al. [107].

Over the years few theoretical models have also been proposed to model the division of flow and sediment at diversions. Most of the formulations were based either on momentum balance between the branches of the channel [108, 109], or the energy balance between branches of the channel[18]. Riad proposed a formula to predict the division of sediment between the two-channels[9], which correlates the ratio of sediment moving into the two-channels with the ratios of flow moving into the two-channels. A similar expression was proposed by Wang et al. in 1995 [15]. While looking at braided channels, Bolla Pittaluga et al. in 2003 derived a one-dimensional sediment distribution model for symmetric bifurcations [16], and this model with some modifications is suitable for application on to diversions. Recently, van der Mark and Mosselman used irrotational flow theory to develop a conceptual model for division of sediment at diversions that can account for the strong secondary currents formed at diversions [110].

The model gave relatively reasonable results when compared against experimental data. In general, none of the proposed formulas have been able to accurately capture the phenomenon of Bulle-Effect, and that is understandable due to the highly complex nature of the flow-structure at the diversion.

The flow at the diversion have been observed to be relatively complex and highly three-dimensional, thus it is normal that the aforementioned 1-D models have been unable to capture the Bulle-Effect phenomenon. Over the years there have been two and three-dimensional numerical studies that have modeled the flow at diversions. However, almost none of the studies included sediment transport in their models. Three-dimensional numerical models were found to agree better with experimental observations than two-dimensional models [111, 112], and that is expected due to highly three-dimensional structure of the flow. Neary and Sotiropoulos [13] simulated laminar flow at a 90-degree diversion using a three-dimensional numerical model, and were able to capture some of the flow-structures observed in the experiments. Neary et al. [84] used a three-dimensional Reynolds Averaged Navier-Stokes (RANS) model to simulate flow at a 90-degree diversion, and it was able to capture the secondary currents that have been attributed for the movement of the near-bed sediment into the lateral channel. A RANS based three-dimensional flow model was also used by Ramamurthy et al. to model their experimental observations [113]. Heer and Mosselman numerically simulated Bulle's experiments, but without the sediment, using Delft-3D [114]. The numerical simulations were able to re-create some of the flow-structures observed by Bulle during his experiments, but in general the simulations suffered from numerical stability issues. Recently, Dutta et al. conducted Large Eddy Simulation (LES) of turbulent flow at a 90-degree diversion [40]. The Reynolds number of the simulation and dimensions of the computational domain were similar to experiments performed by Bulle. Sediment transport at the diversion was simulated by modeling the bedload transport using the Lagrangian Particle tracking formulation. Complex flow-features like strong secondary flow circulation in both the channels after bifurcation, flow-separation and recirculation were successfully captured. The simulation also predicted the division of bedload between the two channels satisfactorily, with the predicted ratio matching Bulle's observations. Conducting LES of field-scale (and even experimental-scale) diversions will require an impractical amount of computational resources, thus RANS based three-dimensional models might be more suited for studying field-scale diversions.

The current study was aimed at numerically reproducing the experimental observations of Bulle, using a free-surface three-dimensional hydrodynamic solver that solves the RANS equations using the finite-element method for the spatial discretization [115]. As such, the study addressed the issues faced by previous numerical studies, additionally it also simulated the near-bed sediment transport. Primary aim of the numerical experiments was to explore whether the RANS based solver could be used to capture the Bulle-Effect at the laboratory

scale, under different flow conditions. Furthermore, the simulation results were used to provide further insight and details about the hydrodynamics that Bulle could not analyze through his pioneering experiments, due to lack of sophisticated measuring instruments.

This paper has been divided into six major sections, including the forgoing introduction. The second section discusses details of the numerical model, the computational mesh, and the boundary conditions. The third section presents the results from all the simulations, divided into two major subsections, first featuring the characteristics of the flow at the diversion, and the second featuring the bedload distribution at the diversion. In the fourth section the bedload transport results from the simulations would be compared against existing theoretical models. The final two sections will discuss and conclude the findings of the study, and also propose potential research directions.

## 6.2 Hydrodynamic and Sediment Transport Model

Three-dimensional (3D) free-surface hydrodynamic simulations were conducted by solving the continuity and Reynolds Averaged Navier-Stokes (RANS) equations with the finite-element method. Bedload transport was computed from a sediment transport capacity equation, with an appropriate parameterisation for bed slope effects. To reproduce Bulle's experiments, the rigid-bed approximation was adopted, and the solution of the bed sediment mass balance equation was not considered. The numerical solver used herein was the open-source Telemac-Mascaret Modeling system [32]. This is an open-source, sequential and parallel free-surface solver based on the finite volume and finite element methods. Further details are given in [115]. Telemac has been previously used to successfully study different river hydrodynamic phenomena [116, 117]. Numerical simulations were conducted on the *GOLUB* high-performance computing cluster at University of Illinois at Urbana-Champaign. *GOLUB* has a total of 312 computational nodes. Each node has 20 processors (cores), 64-256 GB RAM, and it consumes 115 W of energy.

### 6.2.1 Governing Equations

The three-dimensional free surface hydrodynamics was simulated by solving the equation for conservation of fluid mass and the Reynolds Averaged Navier-Stokes (RANS) equations:

$$\frac{\partial u_i}{\partial x_i} = 0 \tag{6.2}$$

$$\frac{\partial u_i}{\partial t} + \frac{\partial u_i u_j}{\partial x_j} = F_i - \frac{1}{\rho}\frac{\partial p}{\partial x_i} + \frac{1}{\rho}\frac{\partial \tau_{ij}}{\partial x_j} \tag{6.3}$$

where the summation convention for repeated indices was used for $i, j = 1, 2, 3$. Above, $u_i = (u, v, w)$ correspond to the local time-averaged flow velocity components along the Cartesian coordinates $x_i = (x, y, z)$, $F_i$ is the external forcing term per unit mass, $p$ is the mean pressure, $\rho$ is the fluid density, and $\tau_{ij}$ corresponds to the components of the stress tensor calculated with the Boussinesq hypothesis, which is related to the mean velocity gradients and the turbulence eddy viscosity $\nu_t$:

$$-\frac{1}{\rho}\frac{\partial \tau_{ij}}{\partial x_j} = \frac{\partial}{\partial x_j}\left[(\nu + \nu_t)\left(\frac{\partial u_i}{\partial x_j} + \frac{\partial u_j}{\partial x_i}\right) - \frac{2}{3}k\delta_{ij}\right] \tag{6.4}$$

Above, $\nu$ correspond to molecular kinematic viscosity of water, $\nu_t$ is the turbulent eddy viscosity, $k$ is the turbulent kinetic energy and $\delta_{ij}$ is the Kronecker delta. For calculating the $k$ and $\nu_t$, a turbulence closure is required. In the current study the $k-\epsilon$ turbulence closure has been used, where the turbulent eddy viscosity is related to the turbulent kinetic energy and the rate of turbulence energy dissipation $\epsilon$. In equation 6.3, the pressure is split into a hydrostatic component $p_h$ and a dynamic component $p_d$:

$$p = p_h + p_d = \rho g\left(Z_s - z\right) + \rho_0 g \int_{Z_f}^{Z_s} \frac{\Delta\rho}{\rho_0} dz + p_d \tag{6.5}$$

with $Z_s = Z_s(x, y)$ the elevation of the free surface above datum, $Z_f = Z_f(x, y)$ the bottom elevation above datum, and $\Delta\rho = \rho - \rho_0$ is a deviation of the water density $\rho$ with respect to some reference value $\rho_0$. Further details can be found in [115].

The bedload transport model used for the current study has been coupled with the hydrodynamic model. In the resulting formulation, the bed shear stress is aligned with the near bed velocity in order to account for possible flow deviations, such as transport due to secondary currents and slope effects. The direction of the bed shear stress matches with the horizontal velocity at the first computational node above the bottom. The magnitude of the bed shear stress ($\tau_b$) is related to the classical quadratic relationship between the depth-averaged velocity and the total bed shear stress:

$$\tau_b = 0.5\rho C_f\left(U^2 + V^2\right), \tag{6.6}$$

where $U$ and $V$ are the depth-averaged velocity components in the $x$ and $y$ directions respectively, and $C_f$ is the dimensionless friction coefficient related to the bottom roughness.The shear stress is related to the bed shear velocity ($u_*$) through the relationship $u_* = \sqrt{\tau_b/\rho}$. For this study, the bottom friction is explicitly defined for the hydrodynamic simulations using a Chezy coefficient, which in turn is used as a calibration parameter. Details of the calibration process are discussed in the next section. The relationship between the Chezy coefficient $C$ and the friction coefficient is given by $C_f = 2g/C^2$.

For calculating the bedload discharge, a number of semi-empirical relationships are available in the literature [**?**]. Most of the bedload discharge formulas assume the existence of a threshold, beyond which the onset of bedload motion happens. These formulas relate the non-dimensional bed shear stress induced by the flow and the critical bed shear stress or critical Shields parameter to a non-dimensional bedload transport rate $\Phi_b$. The non-dimensional bedload transport rate is related to the bedload flux $Q_b$ by the relationship:

$$\Phi_b = \frac{Q_b}{\sqrt{g\,(R-1)\,D_{ch}^3}} \tag{6.7}$$

where $R$ is ratio of density of sediment and water, $D_{ch}$ is the characteristic sediment diameter. Herein the characteristic grain diameter has been chosen equal to $D_{50}$. From the plethora of relationships, the Meyer-Peter-Muller formula has been used to estimate the non-dimensional transport rate $\Phi_b$. The Meyer-Peter-Muller bedload formula has been previously validated for coarse sediments in the range ($0.4mm \leq D_{50} \leq 29mm$). The sediment diameter used in the current study falls within the aforementioned range. The Meyer-Peter-Muller formula is [**?**]:

$$\Phi_b = \begin{cases} 0 & \text{if } \theta' < \theta_c \\ \alpha_{mpm}\,(\theta' - \theta_c)^{3/2} & \text{if } \theta' \geq \theta_c \end{cases} \tag{6.8}$$

where $\alpha_{mpm}$ is a coefficient, $\theta'$ is the non-dimensional bottom shear stress, also known as the Shields parameter, $\theta_c$ is the critical Shields parameter. In this study, $\alpha_{mpm} = 8$ and $\theta_c = 0.0317$. The Shields parameter $\theta'$ is defined as

$$\theta' = \frac{\mu\tau_b}{(\rho_s - \rho)\,gD_{ch}} \tag{6.9}$$

where $\mu$ is the correction factor for skin-friction, and $\rho_s$ is the density of the sediment.

A sloping bottom results in increase of bedload flux in the downslope direction. The effect of the slope is accounted for by using a correction factor that can influence both the magnitude and direction of the bedload transport rate. The correction is based on the formula by Koch and Flokstra [118]. The relationship for the magnitude of solid transport rate with the correction factor is

$$Q_b = Q_{b0}\left(1 - \beta\frac{\partial Z_f}{\partial s}\right) \tag{6.10}$$

where $Q_{b0}$ is the bedload transport rate before correction, $\beta$ is an empirical factor equal to 1.3, and $s$ is the flow direction. The deviation of the bed load direction from the main flow direction is accounted by the expression:

$$\tan\alpha = \tan\delta - \frac{4}{6\theta'}\frac{\partial Z_f}{\partial n} \tag{6.11}$$

where $\alpha$ is the direction of the bedload transport with respect to the direction

of the flow, $\delta$ is the direction of the bottom shear stress with respect to the direction of the flow, and $n$ is the direction normal to the flow.

The following boundary conditions have been imposed in the model. For the hydrodynamic solver, a normal velocity was set to zero (impermeability condition) on the solid boundaries (bed and side-walls). A tangential stress was also imposed on the solid boundaries: an imposed shear stress was defined using Equation 6.6 at the channel bed and a slip condition (zero shear stress) was imposed at the side-walls. At the inlet boundary, the classical rough wall logarithmic profile was applied. At the outlet boundaries, the normal derivatives of the flow variables were set to zero. The position of the water surface elevation was determined from the solution of the depth-averaged shallow-water continuity equation (see [115]). At the inlet boundary, turbulence was assumed to be in equilibrium. At outlet boundaries, the gradients of turbulent energy and dissipation rate were assumed to be zero [119, 120]. At solid boudaries, the turbulent energy and its dissipation rate were specified by assuming that the local equilibrium of turbulence prevails near the wall. For the sediment transport solver, the value of the equilibrium bedload transport rate was specified at the inlet. At the outlets, boundary conditions were assumed to be free and bedload transport rate values were extrapolated from the values at adjacent internal points.

The governing equations have been discretized in space using the finite-element method, and integrated in time using a fractional step method. The domain is composed of prismatic elements that is built from an unstructured triangulation of the two-dimensional domain, then repeated along the vertical in superimposed layers from the bottom to the free surface. The time stepping algorithm can be divided into five computational steps as follows [115]:

*i*) The first step consists of calculating the advected velocity components by only solving the advection terms in the momentum equations,

*ii*) In the second step new velocity components are computed using the advected velocity components calculated in the previous step, and taking into account the diffusion terms and the source terms in the momentum equations,

*iii*) After the first two steps, an intermediate velocity field is obtained, which is then used as the starting point for the third step. In the third step, the new depth of the flow is computed by solving the depth averaged continuity and momentum balance equations. The updated water depth is then used to update the elevations of the all the mesh points of the three-dimensional mesh,

*iv*) In the fourth step the velocity field is updated again, taking into account the dynamic pressure gradient and satisfying the zero divergence condition

for the velocity field,

*v*) After one step of hydrodynamic calculations are completed, bedload fluxes are calculated and the procedure return to step one for the next time step until a specified time is reached.

### 6.2.2 Computational Domain, Boundary Conditions and Model Calibration

The computational domain was discretized with 577,650 triangular elements with typical edge lengths in the order of 0.01 $m$, which results in 302,420 computational nodes. The three-dimensional discretization was obtained by first dividing the two-dimensional domain with non-overlapping linear triangles and followed by extruding each triangle along the vertical direction into linear prismatic columns that exactly fitted the bottom and the free-surface. Then, each column was partitioned into non-overlapping layers, requiring that two adjacent layers comprised the same number of prisms. The simulation results using the refined mesh matched with the results from the original mesh. For the simulations presented herein, ten superimposed layers were used in the vertical direction. Simulations were also conducted for a more refined unstructured triangular mesh with typical edge lengths in the order of 0.0075 $m$. Solutions computed with an increasing number of layers have shown no perceptible differences in the results. The mesh used for the simulations has been reproduced in Fig. 6.3.

For initial condition, a constant water surface elevation and velocity components set to zero were specified. The boundary conditions used for the simulations have been illustrated in Fig. 6.3. A constant discharge $Q_{in}$ equal to 0.005 $m^3 s^{-1}$ has been imposed at the main channel inlet. A constant water surface elevation (WSE) was used to define the outflow boundary at the end of the main channel, and a constant discharge $Q_{out}$ was used as the outflow boundary condition at the end of the diverted channel. The value of $Q_{out}$ was based upon the outflow reported by Bulle in his experiments, hence it varied from experiment to experiment, depending on the diversion angle and width of the diversion channel. The ratios of the discharge between the two channels have been listed in Table 1. In most of his experiments Bulle kept the WSE at the outflow constant, by maintaining a constant depth of flow over the weirs placed at the outlet of the two channels. All the flows were subcritical, with Froude number less than one, with the control being exerted from downstream. Thus, the change in layout of the experiment results in change in water discharge entering the side-channel. For example, for the 30-degree case the flow is divided equally between the two channels, whereas for the 90-degree case 54.8 percent of the flow continues in the main channel.

The simulation was calibrated against the only case of Bulle's study for which

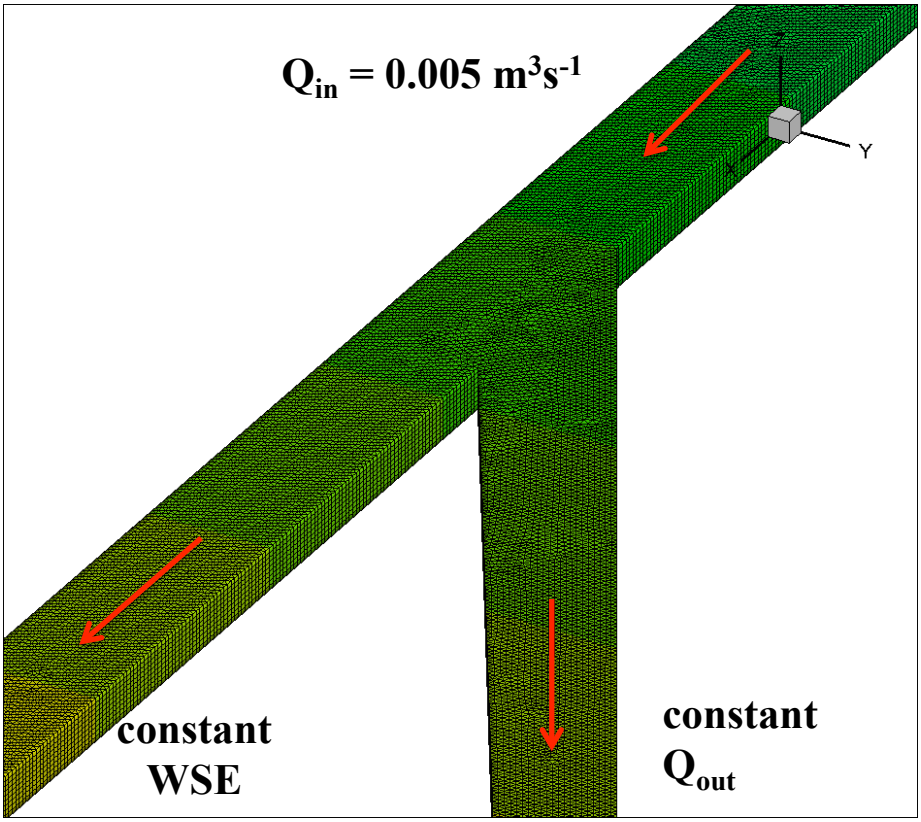


Figure 6.3: Detail of the computational mesh used for the simulations. The mesh has 577,000 triangular elements. The arrows indicate the flow directions.

the water depth at the center of the channel was reported; the case with diversion angle of 30 degree and total inflow of $0.005 m^3 s^{-1}$. Calibration was not straightforward, as the height of the weirs used to maintain constant WSE at the two outlets of the experiments was not explicitly mentioned in Bulle's report [1], thus making it necessary to perform an iterative process. For the calibration process, initially the WSE at outflow boundary of the main-channel was approximated based upon the extrapolation of center line water depths reported by Bulle, later this WSE was adjusted along with the bottom roughness to match the observed water depth. Water depth from the calibrated simulation has been plotted with the observed water depth in Fig. 6.4. Along with the calibrated case, water depths for the $60, 90, 120$ and 150 degree cases have also been plotted. The water depth from the calibrated simulation matches Bulle's observations satisfactorily, with the highest relative error less than 2 percent. The satisfactory match was found for the Chezy's friction coefficient of $100 m^{1/2} s^{-1}$. Water depth in the channel, especially before and at the diversion, was found to increase with increase in diversion angle. This can be attributed to the fact that, the flow requires a pressure head to move into a lateral channel, and the pressure head required increases with an increase in the diversion angle. Consequently, higher diversion-angles result in a lower amount of flow entering

the lateral-channel.

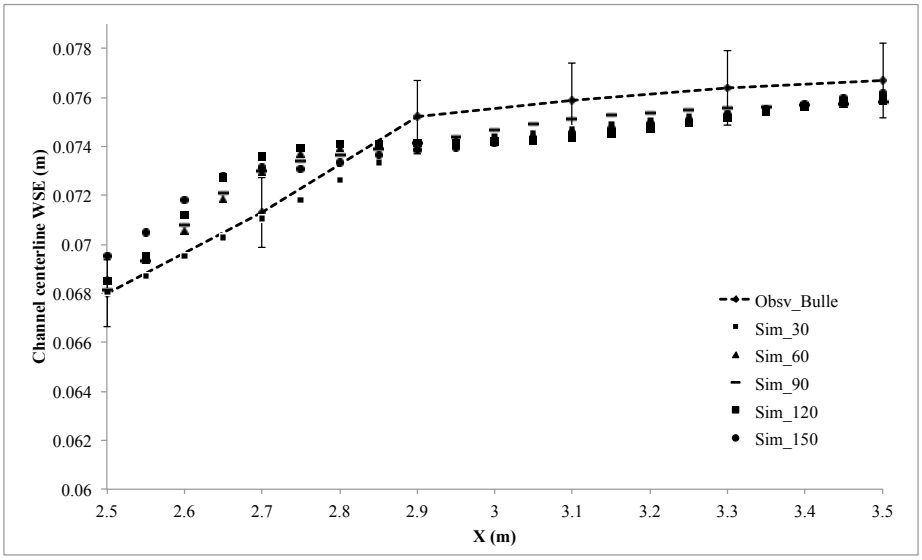


Figure 6.4: Comparison of channel center-line water depth observed for the 30 degree, 0.005 $m^3 s^{-1}$ experiment of Bulle, with the water depth from the simulation done with the roughness coefficient of 100 $m^{1/2} s^{-1}$ for the bottom. Error bars have been assigned to the experimental data, and they show that the difference between the measured and the simulated data never exceeds 2 %. Water depth for the 60, 90, 120 and 150 degree cases have also been plotted to illustrate the change in water depth with respect to angle of diversion.

## 6.3 Results

The results from the numerical simulations can be broadly divided into two parts, the first concerns the structure of the flow at the diversion, and second concerns the division of bedload sediment between the main and the diverted channel. Nine different simulations were conducted, for different diversion angles, ratio of lateral-channel to main-channel width, and water discharge distribution. A list of all the simulated cases is presented in Table. 1.

All the above listed cases were first simulated without sediment, and run long enough (3600 seconds of simulation time) to reach a steady state. On an average 3600 seconds of simulation took 500 cpu hours to complete on the *GOLUB* cluster. After that, the sediment was introduced in the system at the location of the hopper in Bulle's experiments, at a rate of 1.37 $gs^{-1}$, as specified by Bulle [1]. Properties of the sediment used in the simulations are similar to the sediment in Bulle's experiments. In his report, Bulle did not provide a specific mean diameter ($D_{50}$) for the sediment, but mentioned that none of the particles had diameter higher than 1.2 $mm$. Thus for the numerical simulations a $D_{50} = 0.6$ $mm$ was used. Interestingly, the density of the dry sediment reported in Bulle's report was 1500 $kgm^{-3}$, which is significantly lower the generally

Table 6.1: Numerical simulations with the corresponding configuration and boundary conditions. The first column lists the name given to each simulation. The second column lists the corresponding angle of diversion. The third column lists the ratio of the width between the main and the lateral channel, and the fourth column lists the ratio of the discharge between main-channel and the lateral-channel after the diversion.

| Simulation | Angle (in degrees) | Width-Ratio | $Q_{main}/Q_{side}$ |
|---|---|---|---|
| $sim1$ | 30 | 1 | 1.000 |
| $sim2$ | 60 | 1 | 1.075 |
| $sim3$ | 90 | 1 | 1.212 |
| $sim4$ | 120 | 1 | 1.128 |
| $sim5$ | 150 | 1 | 1.110 |
| $sim6$ | 90 | 2 | 2.226 |
| $sim7$ | 30 | 1 | 1.632 |
| $sim8$ | 30 | 1 | 2.448 |
| $sim9$ | 30 | 1 | 4.181 |

accepted value of 2650 $kgm^{-3}$ for sand. In order to remain consistent with the experiments performed by Bulle, the density of the sediment $\rho_s$ used in the simulations was 1500 $kgm^{-3}$. Based on the aforementioned properties of the sand used by Bulle, the critical Shields parameter $\theta_c$ used for the simulations was 0.0317.

### 6.3.1 Characteristics of the flow at the diversion

The characteristics of the flow at the diversion have been discussed in this subsection, which has been further divided into two parts, the first part describing the depth-averaged characteristics of the flow at the diversion, and the second part describing the three-dimensional characteristics of the flow.

#### Depth-averaged characteristics of the flow

The first case reported here corresponds to the 30-degree diversion experiment (case $sim1$). The scalar flow-rate at the diversion has been plotted in Fig. 6.5, along with the 2D velocity streamlines. In Fig. 6.5, the flow-separation zone at the left-bank of the diverted-channel can be observed. The position of the zone matches with Bulle's experiments (see Fig. 6.1). Bulle's experiment also mentions the presence of a relatively smaller separation zone on the right-wall in main-channel, just after the diversion. In the current simulation this separation zone is not completely captured, though the flow was found to get slower around this zone. The simulation has also been able to capture the relatively small low velocity zone around the acute-angle corner of intersection between the lateral and the main-channel, as observed in Bulle's experiments (see Fig. 6.1). The stream-lines show the primary structure of the flow, with most of the flow in the lateral channel hugging the right-wall. This results in a high-velocity zone at

entrance of the lateral channel, near the right-wall. The high flow velocity zone coincides with the high bed shear-stress zone, as evident from the plot of the bed shear velocity $u_*$ in Fig. 6.5. The plot of bed shear velocities at the diversion,

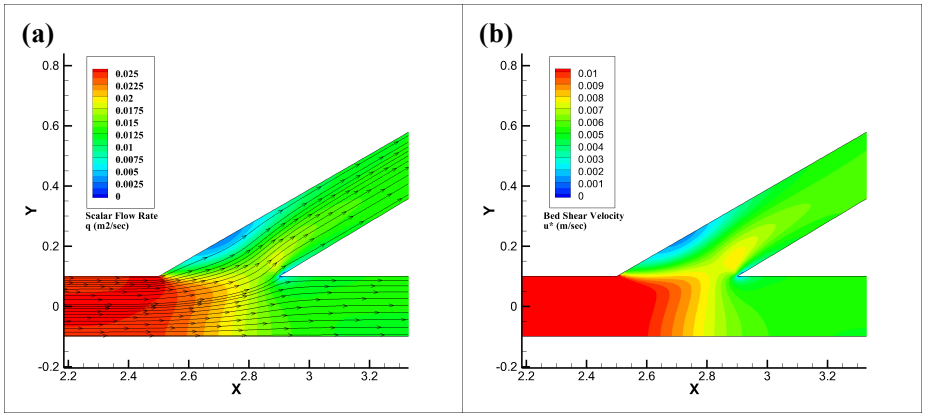


Figure 6.5: (a) Scalar flow-rate $m^2s^{-1}$ and the velocity streamlines at the bifurcation for the case $sim1$, that corresponds to the 30-degree diversion. (b) Shear velocity $u_*$ $(ms^{-1})$ at the bed for the case $sim1$.

allows the inference of the zones that will be prone to scouring or deposition of sediment. The region below the flow-separation zone have relatively low shear stress, thus bedload entering this zone will have a tendency to get deposited. On the contrary, the zone that has relatively high bed shear-stress will have a tendency to get scoured out. The formation of high and low shear-stress zones provide hints towards formation of possible morphological features, like bars and scour holes.

Next the cases with diversion angles of 60 ($sim2$), 90 ($sim3$), 120 ($sim4$) and 150 ($sim5$) degrees for the initial main-channel discharge of 0.005 $m^3s^{-1}$ have been analyzed. The scalar flow-rate for the aforementioned diversion-angles have been plotted along with the corresponding figures of the depth-averaged flow structures observed by Bulle (see Figs. 6.6 and 6.7). In accordance with Bulle's observations, the width of the flow separation zone can be seen to increase with an increase in diversion angle (see Fig. 6.6). Increase in width of the low-velocity zone in turn decreases the width for the high-velocity zone, thus the magnitude of the maximum velocity in the lateral channel increases with an increase in diversion-angle. With increase in diversion-angle the core of the high velocity-zone can be seen to move closer to the right wall of the lateral channel. The streamlines of the depth-averaged velocities show a division between the flow entering the lateral channel, and the flow continuing in the main channel; with the separation curve between the flows being similar to those observed by Bulle at the surface of the flow, but different from observations made at the bottom of the channel (see Fig. 6.6). This is not unexpected, because the depth-averaged streamlines will have a similar behavior to the flow at the surface, as it has relatively higher magnitude.

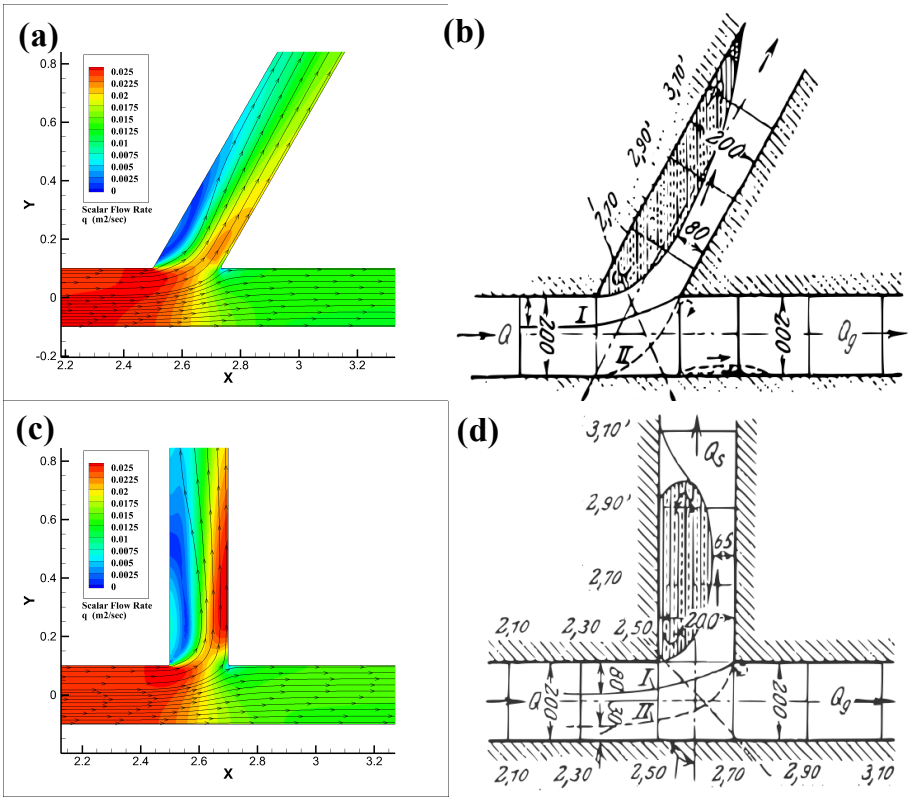


Figure 6.6: (a, c) Scalar/Specific flow-rate (units $m^2 s^{-1}$) and the velocity stream-lines at the bifurcation for the 60-degree and 90-degree cases ($sim2$ and $sim3$). (b, d) Bidimensional flow structure observed by Bulle for the 60-degree and 90-degree cases (reproduced from Bulle's report [1]).

Further increasing the diversion-angle to 120 and 150 degrees ($sim4$ and $sim5$ respectively), the structure of the flow changes even more drastically. For $sim4$, the simulation shows relative increase in length of the flow separation when compared to $sim3$, but a slight decrease in width of the zone (see fig. 6.7 a). The decrease in width of the flow-separation zone is akin to Bulle's observation, but the change in length is the opposite (see fig. 6.7 b). The point at which the curve separating the flows going into both the channel intersects the domain boundary, was observed by Bulle to have moved from the corner of the diversion into the lateral channel. This phenomenon has been correctly captured by the numerical simulations. This shift gets relatively more distinct for the diversion-angle of 150-degree (see fig. 6.7 c and d), where some of the streamlines can be seen to first enter the lateral channel and then move back into the main channel. The length of the separation zone decreases for the case $sim5$, when compared to $sim4$. This eventually has an effect on the maximum velocity in the lateral channel, with the 120-degree case having higher velocity compared with the 150-degree case. The above observation is also evident in the bed shear velocity plots for the cases $sim2$ to $sim5$ (see fig. 6.8).

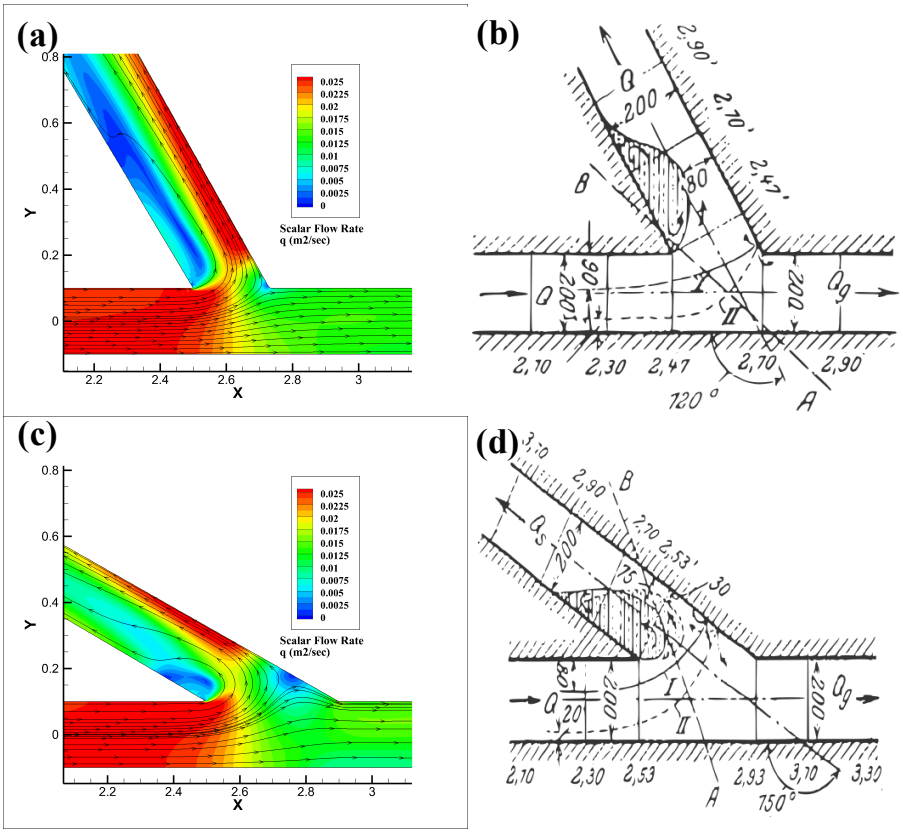


Figure 6.7: (a, c) Plot of the Scalar/Specific flow-rate ($m^2s^{-1}$) and velocity streamlines at the bifurcation for the 120-degree and 150-degree cases ($sim4$ and $sim5$). (b, d) Bidimensional flow structure observed by Bulle for the 120-degree and 150-degree cases (reproduced from Bulle's report [1]).

The core of the high bed shear stress zone in the lateral channel for case $sim2$ has higher magnitude compared to $sim1$, and the zone also shifts towards the right wall of the channel. This increase in magnitude and shift in position can be seen to get further accentuated in cases $sim3$ and $sim4$. This shift of the high bed shear stress zone towards the right wall of the channel can have multiple geomorphological consequences for real streams and rivers, e.g. formation of a scour hole, failure of side-wall and eventual shift of the lateral channel towards the right side due to the flow impinging into the right wall. Further increase of the diversion angle to 150 degrees ($sim5$) results in a decrease in maximum magnitude and size of the high bed shear zone in the lateral channel (see fig. 6.8 d). A small zone of relatively low bed shear stress can also be seen to have formed near the right wall of the main-channel and lateral channel, just after the diversion. Though one pattern that prevails across all the cases from $sim1$ to $sim5$ is that the core of the zone of high bed shear stress in the lateral channel shifts further downstream with increase in an diversion angle. This could be attributed to the shift of the curve that separates the two parts of the flow (one moving into the lateral and the other into the main channel) into the lateral

channel.

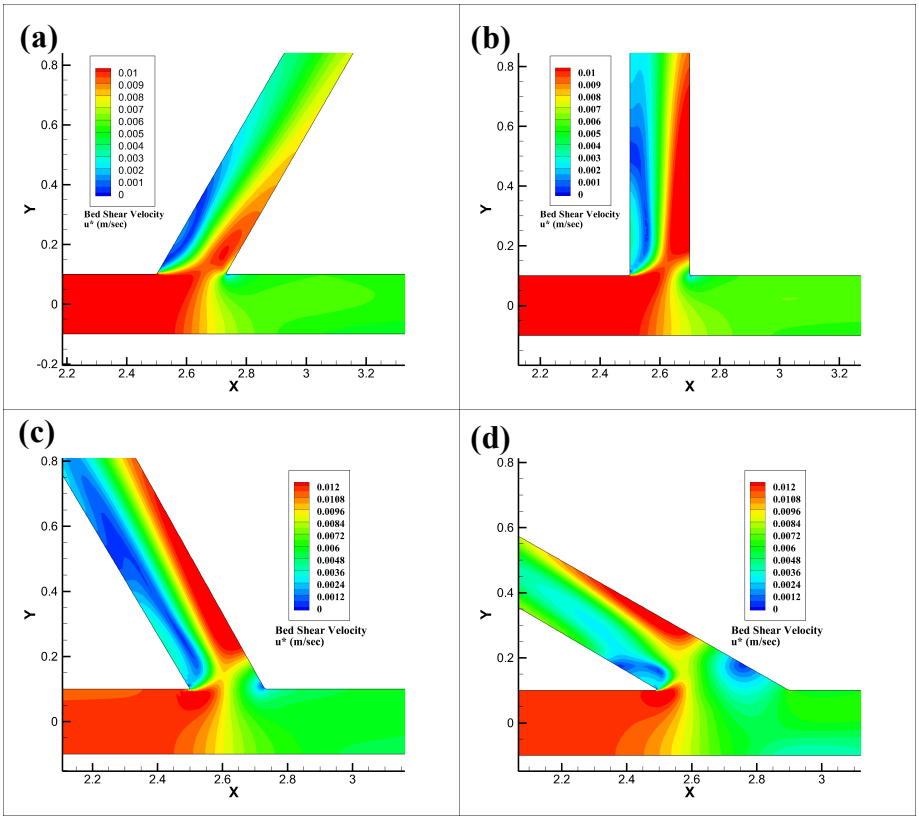


Figure 6.8: Bed shear velocity $u_*$ $ms^{-1}$ for different diversion angles, (a) 60-degree $sim2$, (b) 90-degree $sim3$, (c) 120-degree $sim4$, (d) 150-degree $sim5$. It should be noted that the range of the color scale for (c, d) is slightly larger than figures (a, b).

The case that has been analyzed next is $sim6$, where the diversion-angle is 90 degrees but the width of the lateral channel is half of the main-channel (see Fig. 6.9). As in the previous cases, the WSE at the outlets were kept constant resulting in only 31 percent of the flow getting into the lateral channel. This case is more akin to a real river, where the lateral channel usually has a width smaller than the main channel. The structure of the flow is somewhat similar to the 90-degree case with equal width of the lateral and main-channel ($sim3$). But there are a few significant differences, first the relative size of the flow separation zone (relative to lateral-channel width) is smaller. This might be attributed to the fact that, even though the width of the lateral channel is reduced by half, the discharge going into the lateral channel does not reduce proportionally. If observed carefully, the flow in the main-channel after the diversion for $sim6$ has a tendency to be on the right side of the channel, whereas for $sim3$ the tendency is towards the left side of the channel. This could be due to the general shift of the flow towards the lateral channel (left wall), required for passing almost 45 percent of the flow into the lateral channel for case $sim3$.

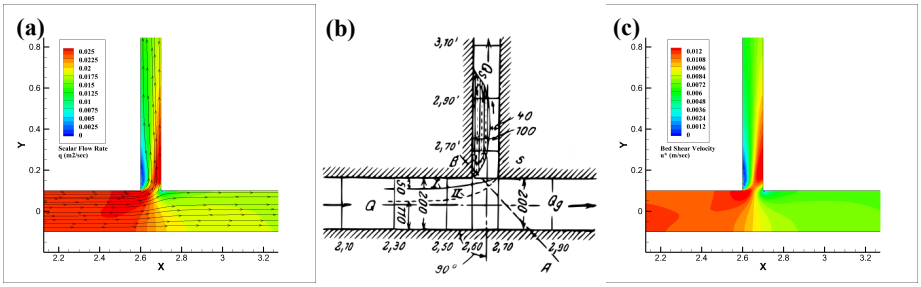


Figure 6.9: (a) Scalar/Specific flow-rate ($m^2 s^{-1}$) and velocity streamlines at the bifurcation for the case $sim6$. (b) Flow structure observed by Bulle (reproduced from [1]) (c) Shear velocity $u_*$ $ms^{-1}$ at the bed.

Finally a set of simulations were conducted for the experiments with a diversion angle of 30-degrees (cases $sim7$, $sim8$ and $sim9$), where the flow going into the lateral channel is monotonically decreased compared to case $sim1$. The decrease in flow into the lateral channel is brought about by decreasing the WSE at the outlet of the main-channel, which increases the flow in the main channel. Decreases in discharge going into the lateral channel results in an increase in size of the zone with relatively low velocities, with the high flow being confined to the right side of the lateral channel (see Fig. 6.10). In the main-channel the high-velocity zone at first is situated near the left wall, but once the discharge in the main-channel increases to $Q_{main}/Q_{side}$ equal to 4.181, the high-velocity core can be seen to have shifted towards the right side of the channel. This pattern can also be observed in the bed shear velocity at and just after the diversion (see Fig. 6.10 d, e, f). In a sense, $sim9$ correspond to regime change in the general flow structure and this may have a significant effect on the bed-load sediment transport. Next, the three dimensional features of the flow are analyzed and discussed.

### Three-Dimensional characteristics of the flow

In order to visualize the streamlines of the flow at different depths, Bulle injected dye into the flow. Bulle found that the dye injected near the bottom mostly entered the lateral channel, whereas the dye near the top continued into the main-channel. In order to visualize the flow at different depths, velocity magnitude and streamlines at two different levels (depths) in the domain were plotted. The plotted planes were taken near the bottom of the channel at a height of 0.004 m from the bottom, and near the top of the channel at a height of 0.04 m from the bottom. First the 30-degree ($sim1$) and the 90-degree case ($sim3$) have been plotted in fig. 6.11.

For the 30-degree case, most of the flow near the bottom can be seen to be moving into the lateral channel, compared to the flow near the top of the channel. This is obvious from the magnitude of velocity in the two channels,

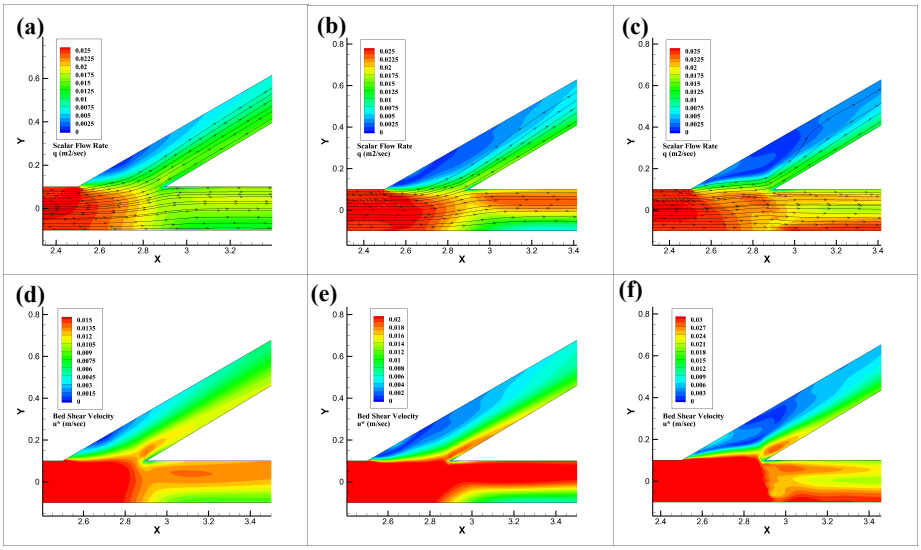


Figure 6.10: (a, b, c) Scalar/Specific flow-rate ($m^2s^{-1}$) and velocity streamlines at the bifurcation for cases $sim7$, $sim8$ and $sim9$. (d, e, f) Shear velocity $u_*$ $ms^{-1}$ at the bed for the three cases with different flow splits. Note the different scales used for plotting the bed shear velocities of each case.

which is substantially lower in the main-channel for the plane near the bottom (see fig. 6.11 a). This is also evident from the streamlines of the flow, and also by the position of the curve that separates the flow moving into the lateral channel and the flow continuing along the main-channel. Distance of the curve, that separates the flow moving into the lateral channel and the flow continuing in the main channel, from the left wall of the main channel (before the diversion) decreases with an increase in distance from the bottom of the channel. The aforementioned property of the curve separating the flows, is in agreement with the observations of Bulle. It also hints towards the mechanism behind non-linear distribution of near-bed sediment between the lateral and the main channel. At the diversion, the flow near the bed tends to go into the lateral channel, taking the near-bed sediment with it; thus causing relatively higher amount of near-bed sediment being transported into the lateral channel. Another observation of Bulle that is well represented by the model, is the increase in width of the flow separation zone, on the left hand side of the diversion channel, with increase in distance from bottom of the channel. It can also observed from Fig. 6.11 a-b, that the flow at the bottom in the main-channel after the diversion is mostly confined to the left side of the channel. This might consequently lead to the formation of a flow recirculation zone near the right wall of the main-channel, which has a relatively higher width near the bottom of the channel.

The characteristics of the flow discussed in the previous paragraph were also observed for other diversion angles. The 90-degree case also shows difference in the flow structure at different flow depths (see Fig. 6.11 c-d). The distance of the curve separating the two flows (henceforth would be referred to as the

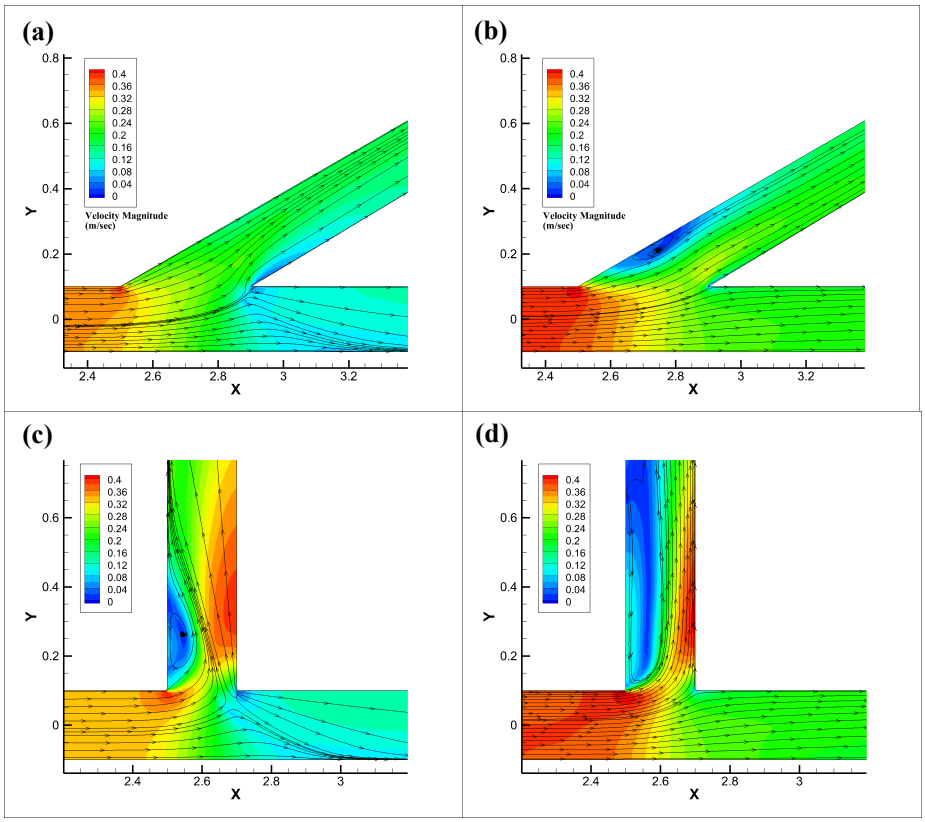


Figure 6.11: Velocity magnitude and streamlines at two different depths. (a, b) For diversion angle of 30 degree at a height (a) 0.004 m, and (b) 0.04 m from the bottom. (c, d) For diversion angle of 90 degree at a height (c) 0.004 m, and (d) 0.04 m from the bottom.

separation-curve) from the left wall of the main-channel is relatively smaller for the 90-degree case, compared to the 30-degree case. This might be attributed to the fact that only 45.2 percent of the total flow goes into the lateral channel in the 90-degree case compared with 50 percent in the 30-degree case. The 90-degree case also illustrates the variation in width (and length) of the separation-zone in the lateral channel with change in depth. Three other diversion angles, 60, 120 and 150 degree were analyzed; and the results have been plotted in Fig. 6.12. For these cases, the flow shows structure similar to those discussed above. The 60-degree case ($sim2$) has a relatively larger flow separation zone in the lateral channel, compared to the 30-degree case discussed in the previous paragraphs. The size of the separation-zone further increases for the 120-degree case ($sim4$). For the 150-degree case ($sim5$), the width of the separation zone near the top of the domain gets wider whereas near the bottom the width decreases substantially. The distance of the separation-curve from the left wall of the main-channel shows an interesting variation with diversion-angle (see Fig. 6.13), near the bottom of the channel the distance of the separation-curve was found to be around 0.125 m for the 30-degree and 150-degree cases, around

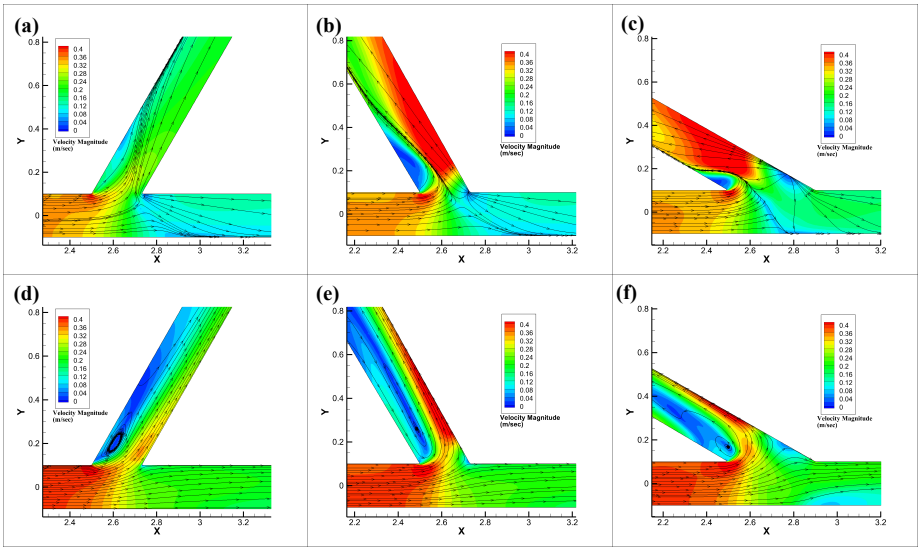


Figure 6.12: Velocity magnitude and streamlines at different flow depths. (a, d) For diversion angle of 60 degree, at a height (a) 0.004 m, and (d) 0.04 m from the bottom. (b, e) For diversion angle of 120 degree, at a height (b) 0.004 m, and (e) 0.04 m from the bottom. (c, f) Diversion angle of 150 degree, at a height (c) 0.004 m, and (f) 0.04 m from the bottom.

0.12 m for the 60 and 120 degree cases and 0.11 m for the 90-degree case. The distance of the separation-curve near the top is about 0.095 m for 30 and 60 degree cases, 0.09 m for the 90 and 120 degree cases, and 0.8 m for the 150 degree case. In order to find a trend in such variation, the distance of the separation-curve have been plotted against angle of diversion, along with the percentage of total flow moving into the lateral channel in Fig. 6.13.

The distance of the separation-curve from the left wall of the channel can be seen to have a direct correlation with the amount of flow going into the lateral channel, which first decreases with an increase in diversion-angle till 90-degree and then increases again. Interestingly, for the cases of 120 and 150 degree the distance of the separation-curve, from the left-wall of the main-channel, near top of the channel does not increase. Particularly for the 150-degree case it even decreases with increase in flow going into the lateral channel. On the contrary, the distance of the separation-curve (from the left wall of the channel) near the bottom of the channel increases with increase increase in flow going into the lateral channel. This may be attributed to the fact that for cases with diversion angles greater than 90 degree, the flow needs to go through a drastic change in direction thus requiring a substantial increase in pressure gradient, which results in a more extended separation zone. The shift of the separation-curve (near the water-surface) into the lateral channel reduces the distance between curve and the left wall of the main-channel resulting in reduction of the flow going into the lateral channel when compared with the 60-degree and the 30-degree cases. As the total amount of flow going into the lateral channel has to increase with

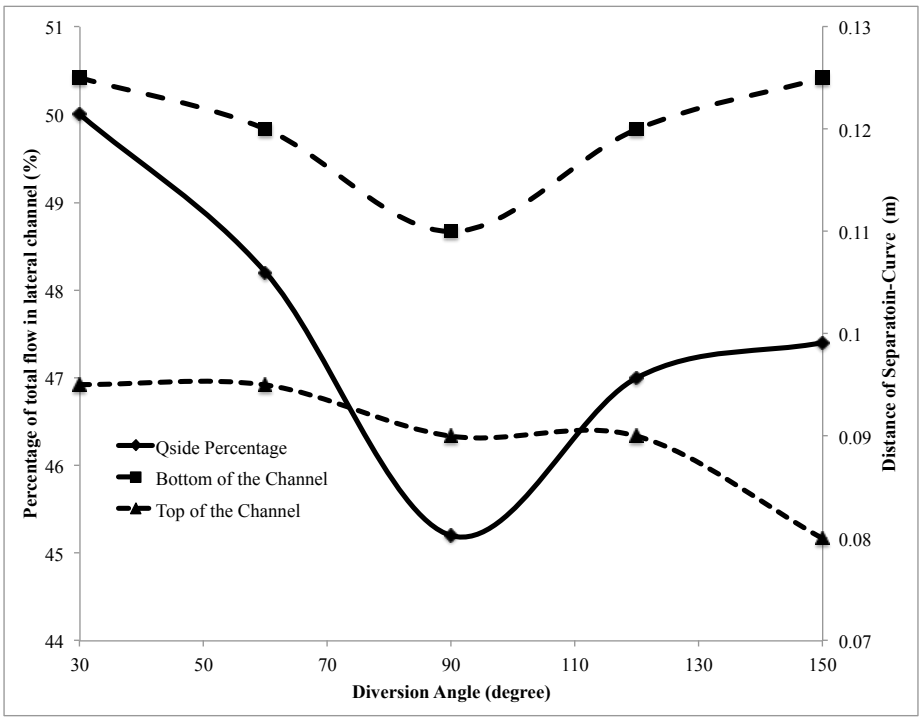


Figure 6.13: Percentage of total flow going into the lateral channel and distance of the separation-curve from the left wall of the main-channel at two different depths, has been plotted for different diversion angles on the secondary axis.

respect to the 90-degree case, this loss in flow into the lateral channel at the top is compensated by pulling in more flow from the bottom of the channel, thus resulting in an increase in distance of the separation-curve from the left wall of the main-channel. In the next section the importance of the distance between the separation-curve near the bed and the left wall of the channel would be further illustrated by its direct influence on the amount of bedload entering the lateral channel.

Important three-dimensional feature of the flow that have been observed in experiments [39], and also in high-resolution Large Eddy Simulation of the flow at a 90-degree diversion by Dutta et al. [40], is the presence of clock-wise rotating secondary current in the lateral channel, and the anti-clockwise rotating secondary current in the main channel. These secondary currents/circulations have also been referred to as rotating vortex in the literature [39, 40]. The numerical simulations in the current study were also analyzed to asses if the aforementioned secondary-currents were captured by the simulations. The vertical velocity at different cross-sections after the diversion have been plotted for the 90-degree case (see Fig. 6.14). The location of the plotted cross-sections have been listed in Fig. 6.15.

The 90-degree case was analyzed first because all the previous studies that have described the presence of secondary circulations in the flow were for the 90-

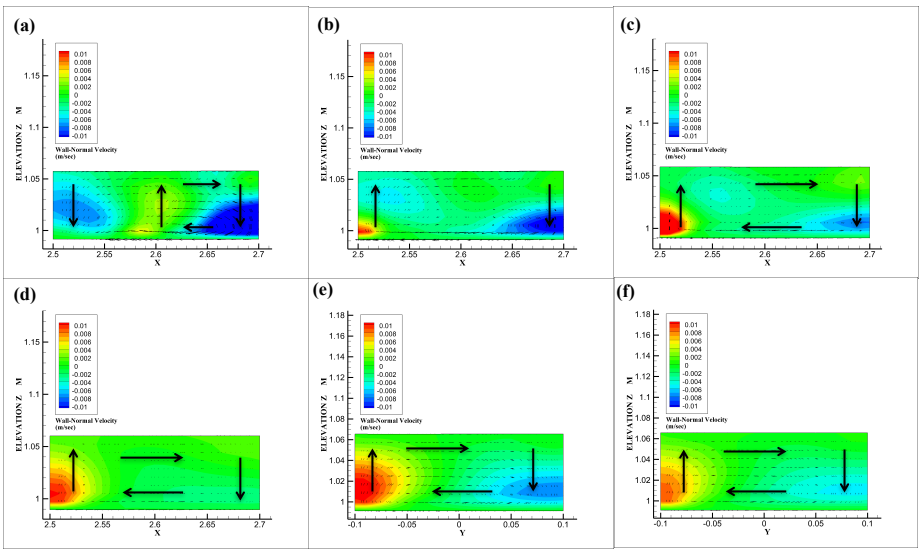


Figure 6.14: Contour plots of the velocity component along the z-axis ($w$) and 2D velocity vectors calculated using the vertical and transverse components of the velocity at the cross-sections, for different cross-sections after the diversion, for the 90-degree $sim3$ case. (a-d) The cross-sections in the lateral channel have been plotted at (a) $y = 0.3$ m, (b) $y = 0.4$ m, (c) $y = 0.5$ m, and (d) $y = 1.0$ m. (e-f) The cross-sections in the main-channel have been plotted at (e) $x = 2.9$ m and (f) $x = 3.0$ m. The primary flow direction in panels (a-d) is into the plane, and for panels (e-f) is is coming out of the plane. Figure 6.15 shows the locations of the visualized cross-sections.

degree diversion. The flow going into the lateral channel can be seen to rotate in the clock-wise direction (see Fig. 6.14 a), and the secondary-circulation can be seen to be confined to the right hand side of the channel. The strong rotation of the flow can also be seen to induce some motion in the left hand side of the flow, where the flow in general has separated from the left-wall resulting in formation of a recirculation-zone. As the flow moves further downstream (see Fig. 6.14 b-d) the influence of the recirculation-zone reduces, thus resulting in a clock-wise rotating vortex that covers the entire width channel. The secondary-circulation was found to loose its strength with an increase in distance from the the entrance of the lateral channel (see Fig. 6.14 d). In the main channel (see panels e-f) a counter-clockwise vortex is formed, with the flow near the left wall moving down and flow near the right wall moving up. Similar secondary-circulations have also been observed in channel bends [48].

The cases with diversion angles of 30, 60, 120 and 150 degrees were also analyzed to check the characteristics of the rotating flow in those cases. Vertical velocity and flow vectors in the main-channel have been plotted (see fig. 6.16). As for the 90-degree case, the flow in the main channel for all the different diversion angles rotate in the counter-clockwise direction. Though the intensity of rotation of the 30-degree case (see fig. 6.16 a) can be seen to be relatively less intense compared to the 90-degree case, whereas the 60 and 120 degree

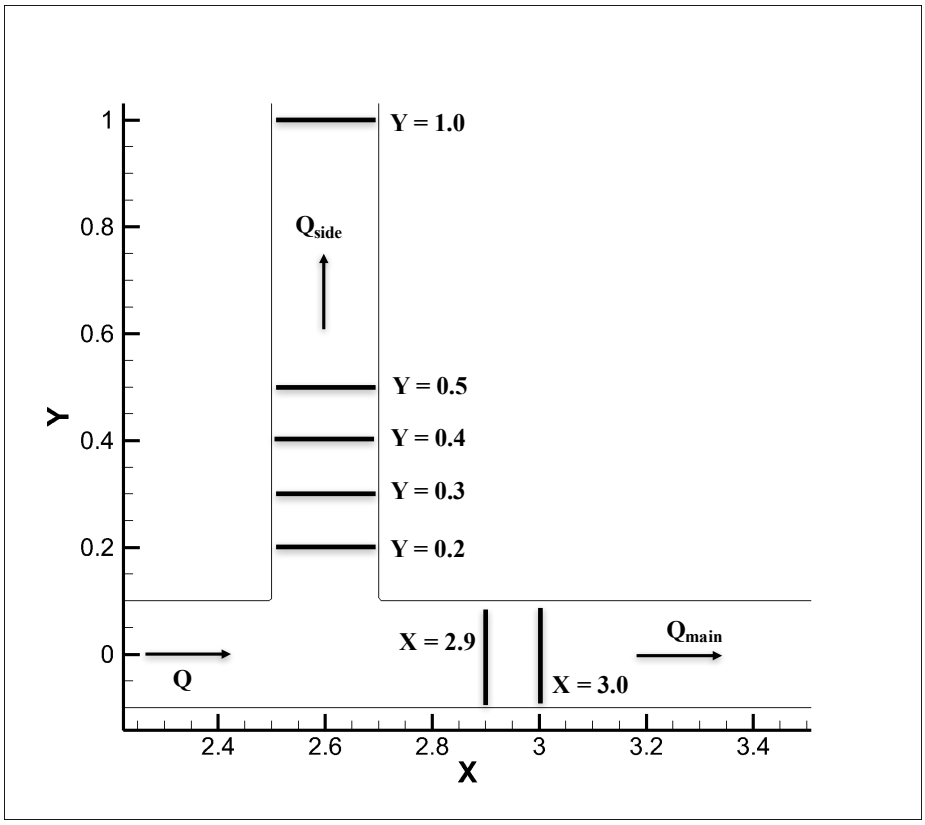


Figure 6.15: Locations of the cross-sections visualized in fig. 6.14, 6.16, and 6.17.

cases have an intensity similar to the 90-degree case. The intensity is usually quantified using vorticity ($\overrightarrow{\omega} = \overrightarrow{\nabla} \times \overrightarrow{u}$), but here it is also obvious from the difference in the vertical component of velocity ($w$) at the left and right hand sides of the cross-sections. The flow in the lateral channel for the 30, 60, 120 and 150 degree cases also show characteristics similar to the 90-degree case, with the secondary-circulation rotating in the clock-wise direction.

The 90-degree diversion angle case with lateral channel width half of the main channel (case *sim*6) has been analyzed (see fig. 6.17). As expected the distance of the separation-curve from the left wall of the main-channel, is relatively more for the plane near the bottom of the channel compared to the plan near the top of the channel. Though the distance of the separation-curve in general is less than all the previous cases discussed above. This can be attributed to the fact that the percentage of total discharge getting into the lateral channel in the case *sim*6 is substantially less than the other cases. As per the previous cases, the size of the separation zone in the lateral channel is relatively larger near the top of the channel, compared to bottom of the channel.

Similar to case *sim*3, the main channel after diversion has a counter-clockwise rotating secondary circulation and the lateral channel has a clock-wise rotating secondary circulation.

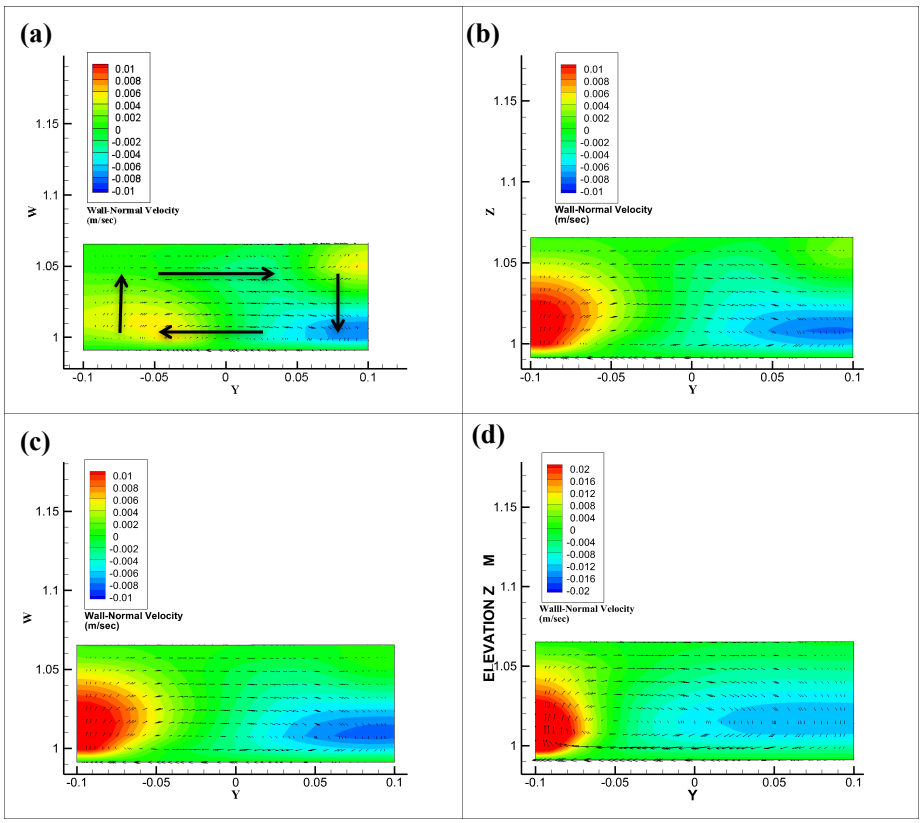


Figure 6.16: Contour plots of the velocity component along the z-axis ($w$) and 2D velocity vectors calculated using the vertical and transverse components of the velocity at the cross-sections, for the cross-section at $x = 3$ m in the main channel, for different diversion angles. (a) 30 degree, (b) 60 degree, (c) 120 degree, (d) 150 degree. The primary flow direction is into the plane. Figure 6.15 shows the locations of the different cross-sections.

Though the strength of the secondary circulation in the main-channel for case *sim*6 is relatively weaker than *sim*3. This might be due to relatively smaller percentage of the total discharge getting into the lateral channel, which reduces the pressure gradient required to force the water into the lateral channel. And since the as the same pressure gradient is also responsible for inducing the secondary circulations, reduction in strength of the pressure gradient reduces the intensity of the secondary circulations. Also for case *sim*6, in the lateral channel the secondary circulation covers the full width of the channel compared to the circulation being initially confined to the right hand side of the channel for *sim*3. This might be due to the width of the lateral channel being half of the main channel in *sim*6 (compared to *sim*3), which results in a smaller size of the flow-separation zone, thus allowing the secondary circulation to cover the full width of the lateral channel. In the next section the bedload transport distribution between the main and lateral channel is analyzed and compared with Bulle's observations.

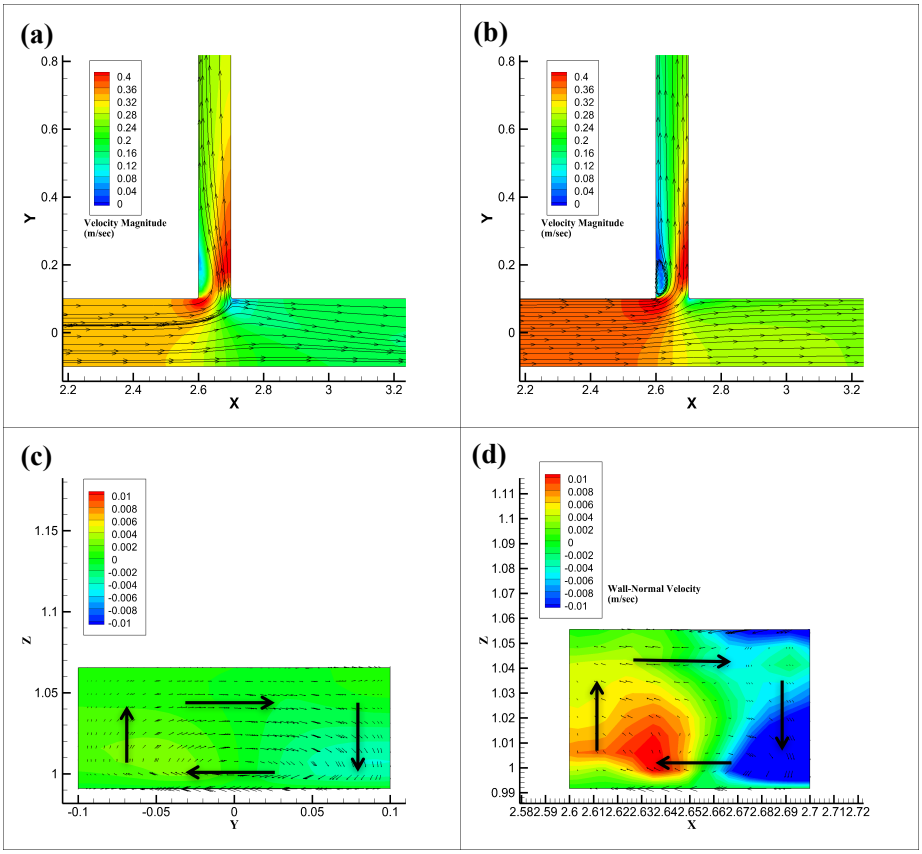


Figure 6.17: Velocity magnitude and vertical component of velocity ($w$) have been plotted for the 90-degree diversion, with width of the lateral channel being half of the main-channel ($sim6$). (a) Velocity magnitude at a depth near the bottom of the channel, (b) Velocity magnitude at a depth near the top of the channel, (c) Vertical velocity ($w$) at x = 3 m, (d)Vertical velocity ($w$) velocity at y = 0.2 m. Figure 6.15 shows the locations of the visualized cross-sections.

### 6.3.2 Characteristics of the bedload transport at the diversion

In this section, the effect of different diversion angles on the division of bedload discharge between the main and the lateral channel is analyzed. Total bedload transported into the lateral channel, and into the main channel after the diversion was evaluated from the numerical simulation results. Cases $sim1$ to $sim5$ were analyzed and plotted along with the observations made by Bulle through his experiments in Fig. 6.18.

Bulle's experiments show the trend that an increase in diversion angle results in increase in bedload entering the main channel after the diversion, till the diversion angle of 120-degree. Further increase in diversion angle results in decrease of bedload entering the lateral channel. The numerical simulations were found to capture the general trend well (see Fig. 6.18). However the position of the maxima of the curve for the simulated cases is at 90-degree

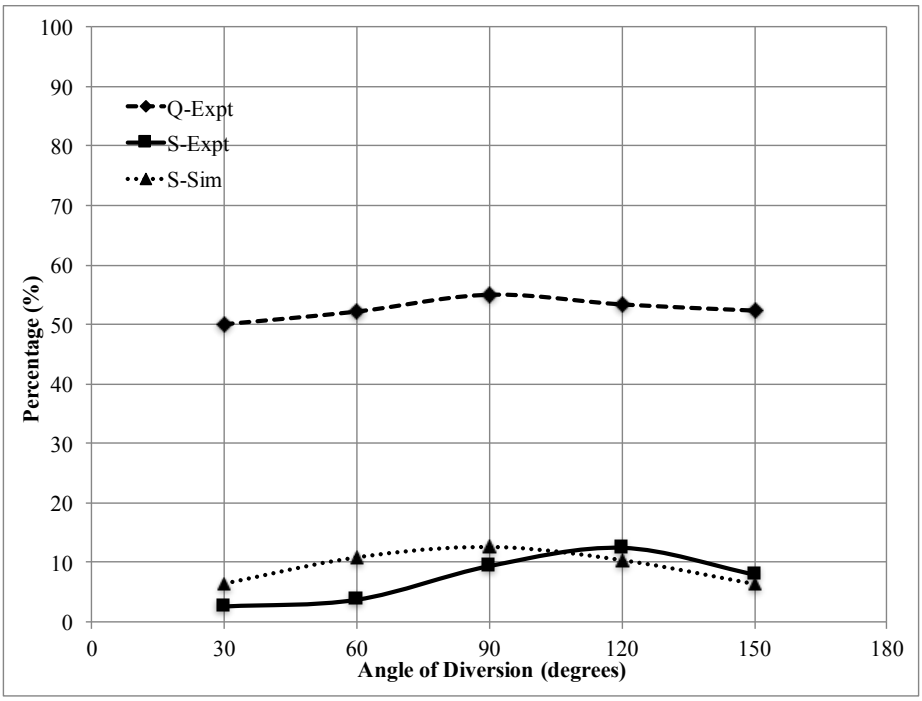


Figure 6.18: Comparison between the simulated and the observed sediment distributions for different angles of diversion. The figure plots the percentages of the total water discharge ($Q - Expt$) moving into the main channel. It also plots the percentage of total bedload sediment moving into the main-channel, observed in the experiment ($S - Expt$), and the predicted by the numerical simulations ($S - Sim$).

whereas Bulle observed the maxima at 120-degree. Also, the exact percentage of bedload moving in to the lateral channel have been slightly underestimated by the numerical simulations (within 8 percent) for the cases $sim1$, $sim2$ and $sim3$, and overestimated (within 2.5 percent) for the cases $sim4$ and $sim5$. Even though the percentages of bedload sediment entering the main and the lateral channel were not predicted by the numerical simulations perfectly, the general trend shown by the experiments was captured successfully. The sensitivity of the bedload transport results on the coefficient $\alpha_{mpm}$ of the Meyer-Peter-Muller formula (see Eqn. 6.8) was tested, and it was found that 20 percent change in the coefficient does not translate into more than 0.2 percent change in the bedload flux continuing into the main-channel.

Next the effect of four different splits of the total water discharge, induced by different boundary conditions (water surface elevation) at the outlet, on the Bulle-Effect has been analyzed for the diversion angle of 30 degree. The simulations $sim1$, $sim7$, $sim8$ and $sim9$ were analyzed. Percentage of the total water discharge, and percentage of the total bedload discharge continuing into the main-channel have been plotted in fig. 6.19. It can be seen that the simulations successfully capture the general trend , with the prediction getting better for the cases where 70 percent of more of the total water discharge continues in the

main channel. Moreover, The highly non-linear nature of Bulle-Effect can be observed in the data plotted in fig. 6.19. It can observed that even after increas-

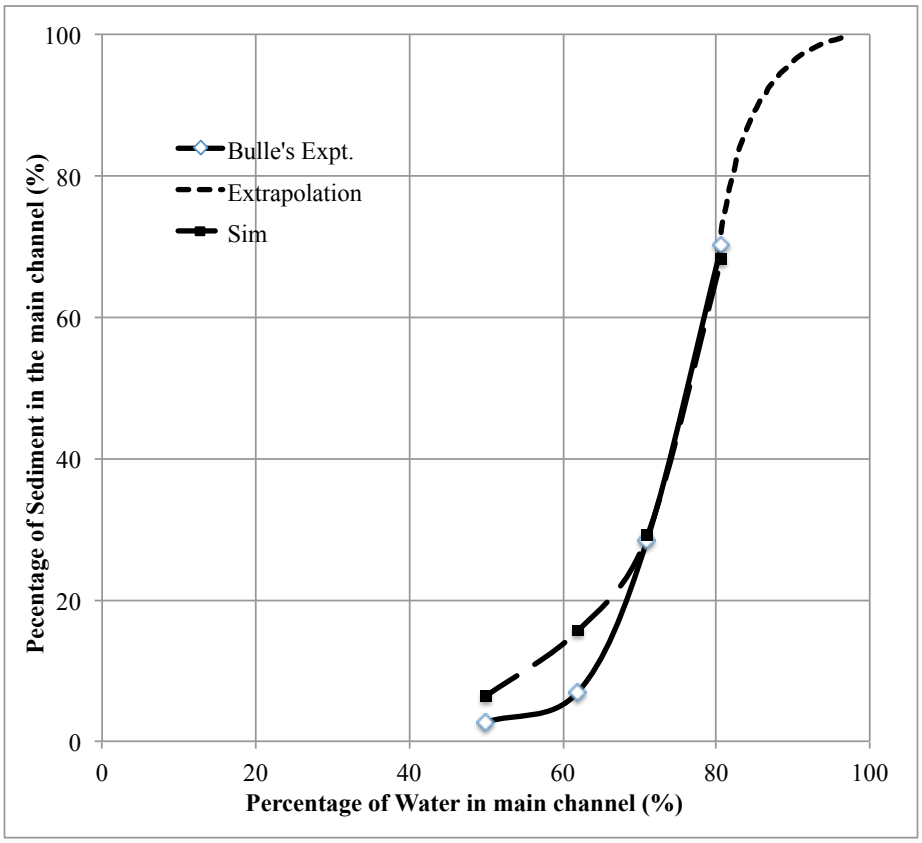


Figure 6.19: Comparison between the simulated and the observed sediment distributions for different flow splits at the diversion, with the diversion-angle of 30 degree. The experimental data against which the simulations have been compared, has been reproduced from Bulle's report [1].

ing the percentage of total water discharge continuing in the main-channel to upto 65 percent, the percentage of sediment continuing in the main channel does not increase substantially. This trend changes appreciably once the percentage of water continuing in the main channel gets more than 70 percent. From 70 to 80 percent, a transition occurs in the characteristics of the flow at the diversion, such that the percentage of bedload discharge continuing in the main channel jumps from about 30 percent (for the 70 percent case) to about 70 percent (for the 80 percent case). Based on these observations, Bulle estimated that further increase in water discharge continuing in the main-channel would result in a similar percentage of bedload discharge continuing in the main channel. This prediction was confirmed later by the experiments of Christani [3].

The numerical simulations were found to overestimate the bedload discharge continuing into the main-channel for the cases with relatively lower percentages of water discharge (cases $sim1$ and $sim7$). For $sim8$, the simulations slightly overestimates, and for $sim9$ the numerical simulation slightly underestimates,

but in general the predictions are substantially better than the previous two cases. This might be due to the fact that an increase in percentage of water continuing in the main channel after diversion makes the flow at the diversion relatively less complex, which makes the modeling of the hydrodynamics and bedload transport using RANS based 3D numerical model relatively more accurate. In the next section of the paper the results from the three-dimensional numerical simulations would be compared against some existing theoretical models to appreciate the usefulness of conducting 3D simulations for correctly capturing Bulle-Effect.

## 6.4 Comparison with one-dimensional models

One of the first models to analytically predict the distribution of sediment between two branches of a diversion (and bifurcation) was proposed by Wang et al. in 1995 [15]. The model relates the ratio of the water discharge going into the two channels $Q_{main}/Q_{side}$, and ratio of width of the channels $B_{main}/B_{side}$ with ratio of the sediment discharge $S_{main}/S_{side}$. The formula is given as:

$$\frac{S_{main}}{S_{side}} = \left(\frac{Q_{main}}{Q_{side}}\right)^{r} \left(\frac{B_{main}}{B_{side}}\right)^{1-r} \tag{6.12}$$

where $r$ is an empirical exponent, which is usually an unknown and is used as a calibration parameter. However the recommended value of $r$ is always greater than $b/3$. For stable bifurcations that have both the branches open, the recommended value of $b > 3$. A similar formulations was also proposed by Riad in 1961 [9]. The model proposed by Wang et al. (Eqn. 6.12) can be modified to relate the ratio of the discharge going into the lateral channel and the total discharge $Q_{side}/Q$, and the ratio of the width of the lateral channel to the main channel $B_{side}/B$, with the ratio of the sediment discharge going into the lateral channel to the total sediment discharge $S_{side}/S$ [110]:

$$\frac{S_{side}}{S} = \left[\left[\left(\frac{Q_{side}}{Q}\right)^{-1} - 1\right]^{r} \left(\frac{B_{side}}{B}\right)^{r-1} + 1\right]^{-1} \tag{6.13}$$

Recently, van der Mark and Mosselman derived a model to predict the fraction of total bedload moving into the lateral channel at a diversion [110]. The model accounts for the effect of the helical nature of the flow at the diversion on the bedload distribution. The derived formula for the fraction of total bedload going into the lateral channel $S_{side}/S$ is given by:

$$\frac{S_{side}}{S} = \frac{Q_{side}}{Q} + \left(\frac{c_o Q_{side} B}{Q B_{side}}\right)^{b_o/3} \frac{R\theta}{B} \left(\frac{1}{\cos\delta} - 1\right) \tag{6.14}$$

where $c_o$ is a constant that accounts for assumptions made during the derivation,

which includes the assumption that the streamwise velocity of the flow entering the lateral channel being uniform throughout the width of the channel, $b_o$ is related to the the sediment transport formula used while deriving the model, e.g. for Engelund and Hansen $b_o = 5$ [78], $R$ is the depth-averaged radius of curvature of the plane separating the flow going into the lateral channel and continuing into the main channel, $\delta$ is a coefficient that parameterizes the angle made between the direction of the bed shear stress and the primary flow direction, $\theta$ stands for the angle, the plane separating the flows going into the two channels, has to rotate in order to change its direction from the primary flow direction in the main channel to the point of intersection between between the left wall of the main channel and right wall of the side-channel (see Fig. 6.1). Both equations 6.13 and 6.14 have the limitation that they do not take into account the effect of different diversion angles explicitly.

Figure 6.20 presents the comparison between 3D numerical simulations and equations 6.13 and 6.14. As a reference, the line representing the linear relationship $S_{side}/S = Q_{side}/Q$ has also been plotted. The 3D numerical simulations perform better in predicting the bedload transport distribution at the diversion, when compared with both of the one-dimensional models. The discrepancy between the 3D numerical model and Bulle's observations are within 10 percent for almost all the cases. The model by Wang et al. (Eqn. 6.13) fails to predict the general trend found in the Bulle-effect. The parameter $r$ in Eqn. 6.13 is a calibration parameter for the model, so results from the model were plotted for different values of $r$ in order to asses the model's sensitivity to $r$. The model was unable to predict the bedload distribution, despite using a range of values for $r$. Equation 6.14 performs relatively better for the cases with higher $Q_{side}/Q$, and for the single case in which the width of the lateral channel is half of the width of the main channel. A better prediction capability of Eqn. 6.14 compared to Eqn. 6.13 is expected, as the model was derived based on assumptions that take into account the helical nature of the flow at a diversion.

## 6.5 Discussion

In previous sections, results from the 3D numerical simulation of Bulle's experiments were analyzed. The numerical simulations were found to fare well in capturing the non-linear distribution of bedload between the two channels after the diversion. Then the bedload distribution predictions made by the 3D numerical model were compared with existing one-dimensional models, and the predictions made by the 3D model was found to be relatively more accurate than 1D models. In this section, the major findings of the current study are summarized and discussed.

In general, the 3D numerical model was able to capture most of the flow characteristics observed in Bulle's experiments and related studies [40]. The water

surface elevation predicted by the model matched well with the measurement from Bulle's experiments. Regions of the domain where flow separation was observed by Bulle, were well captured in the simulations, e.g. the separation at the left wall of the lateral channel just after the diversion, though the exact size of the resulting recirculation zones were slightly over or under predicted by the 3D model. As can be seen in Figs. 6.5 to 6.7, the formation of the recirculation zone in the lateral channel results in formation of a high-velocity zone next to it, which results in an increase of the shear stress at the bottom in those regions. With an increase in diversion angle, the core of the high flow velocity region of the lateral channel was found to move towards the right wall and also further downstream. The distance of the separation curve, that is the plane separating the flow going into the lateral channel and the flow continuing in the main channel was found to vary with change in diversion angle, with the minimum at 90-degree. The position of the flow separation curve predicted by the simulations were found to match well with Bulle's observations. Further, the distance of separation curve from the left wall of the main channel was found to correlate with amount of flow going into the lateral channel, which in turn depends on the diversion angle as can be seen in Fig. 6.13. Thus, the minimum distance of the separation curve from the left wall of the main channel occurs for the 90-degree diversion case. Though one might point out that width of the entrance of the lateral channel (which is twice for the 30-degree case compared to the 90-degree case) also plays a role but has not been explored in the current study. The importance of the distance of the flow-separation curve from the left wall was further underlined by the observation that this distance is larger near the bottom compared to the top of the channel. This is important because it provides an insight into the mechanism behind the Bulle-Effect.

Bulle observed that the majority of the flow near the bottom moved into the lateral channel and majority of the flow near the top of the channel continue into the main-channel. This observation can explain the fact that as most of the flow near the bottom moves into the lateral channel, it takes with it most of the near bed sediment, thus resulting in a disproportionately higher amount of bedload getting into the lateral channel. Thus the distance of the separation curve from the left wall of the main channel being higher near the bottom is congruent with the aforementioned observation by Bulle. The phenomenon of relatively larger percentage of flow near the bottom moving into the lateral channel was also observed in the velocity magnitude plots of the flow, see Fig. 6.11 and 6.12. These plots also confirmed an observation made by Bulle about the size of the recirculation zone in the lateral channel, which can be seen to increase with increase in distance from the bottom. A characteristic of the flow that was not observed by Bulle, but was later seen in other studies was the presence of secondary flow circulation downstream from the diversion. A clockwise rotating secondary circulation was observed in the lateral channel, whereas a counter-clockwise rotating one was observed in the main channel, see Fig. 6.14

and 6.16.

Along with all the different cases with different diversion angles, a case of 90-degree diversion was simulated with lateral channel width being half of the main channel, and three cases with diversion-angle of 30-degree but different percentages of the total water discharge (lower than 50 percent) going into the lateral channel. The general characteristics of the flow for the 90-degree case with smaller lateral channel width is similar to the case with lateral channel width being equal to the main channel. From the analysis of Fig. 6.17 two differences were observed, first the strength of secondary circulation in the main channel was found to be relatively lower than the one in the lateral channel, and the secondary circulation in the lateral channel was found to occupy the whole channel. Second the high-velocity zone in the main channel after the diversion was near the right wall of the channel, instead of the left wall.

The 30-degree cases with increasing percentage of water discharge continuing into the main-channel was found to have two distinct regime (see fig. 6.10). Increase in water discharge continuing into the main channel results in increase in size of the recirculation zone in the lateral channel. The shift in regime was found to occur in the range of $Q_{main}/Q_{side}$ 2.448 and 4.181. The major difference between the two regimes is the location of the high-flow zone in the main channel after the diversion. Initially the high-flow zone can be seen to be located near the left wall of the main channel, but after the change in regime it shifts to the right wall of the main channel. The importance of this regime shift is underlined by the fact that it coincides with shift in regime of the bedload discharge distribution at the diversion (see fig.6.19). The percentage of bedload discharge continuing in the main channel jumps from about 30 percent (for $Q_{main}/Q_{side} = 2.448$) to about 70 percent (for the $Q_{main}/Qside = 2.448$). It can be concluded that depending on the percentage of the flow continuing in the main channel, the sediment distribution between the two channels goes from a highly non-linear regime to a linear regime.

Finally, the 3D model was able to predict the bedload distribution between the lateral and the main channel relatively well with the error being at most 10 percent. For the cases with different diversion angles, the numerical simulations were found to capture the trend satisfactorily (see fig. 6.18). Though, it was not able to predict the diversion angle for which the bedload continuing into the main-channel is maximum. For the cases with diversion angle of 30-degree but different water discharge ratios, the numerical simulation was able to capture the general trend satisfactorily, but overestimated the percentage of sediment continuing in the main channel for the cases with relatively lower $Q_{main}/Q$ (see fig. 6.19). The predictions by the 3D numerical model were also compared with two existing 1D models for sediment distribution at bifurcations, and the predictions made by the 3D numerical model were found to yield relatively more accurate results than the 1D models (see fig. 6.20).

## 6.6 Conclusions

In this work, a RANS based three-dimensional free-surface hydrodynamic model was used to simulate the flow and bedload transport at an experiment scale water-sediment diversion. A specific set of experiments from the extensive work of Bulle in 1926 [1] were used. Through laboratory experiments Bulle studied the non-linear distribution of bedload between the two channel after the diversion. Bulle discovered that the amount of bedload entering the lateral channel was disproportionately higher than the amount continuing in the main channel, even when a lower amount of water was flowing into the lateral channel. Hence this phenomenon is usually referred to as Bulle-Effect. The primary aim of the study was to numerically simulate Bulle's experiments in order to gain insight into the highly non-linear phenomenon, and to asses the applicability of a 3D RANS based model to predict the phenomenon. A better understanding of the phenomenon is crucial for practical applications such as efficient design of flow and sediment diversion structures, irrigation and navigation, as well as for better understanding of dynamics at fluvial bifurcations.

A 3D hydrodynamic model based on the RANS equations was successfully applied to model the phenomena of Bulle-Effect. The model is able to predict the bedload distribution at the diversion satisfactorily. The simulations capture most of the complex flow characteristics. One of the areas it did not perform satisfactorily was with the size of the flow separation zones. This is understandable, because the exact size and location of the recirculation zone depends on precise resolution of the boundary-layers of the flow, which is not possible for a RANS based model. The current study showed that RANS based models should be able to capture the main aspects of the highly non-linear phenomenon of Bulle-Effect satisfactorily. Our next step will be to extend the study to experiments with a movable bed, so that the consequence of Bulle-Effect on morphological evolution of diversions could be studied. Over the course of the current study it became obvious that different parameters, e.g. diversion angle, water discharge ratio. sediment size etc., can influence the distribution of sediment at a diversion. Further exploration of the parameter space will provide insights into the sensitivity of the phenomenon on different variables. Finally, the study needs to be extended to field-scale diversions in order to understand to what extent does the phenomenon of Bulle-Effect observed in the laboratory scales up in nature.

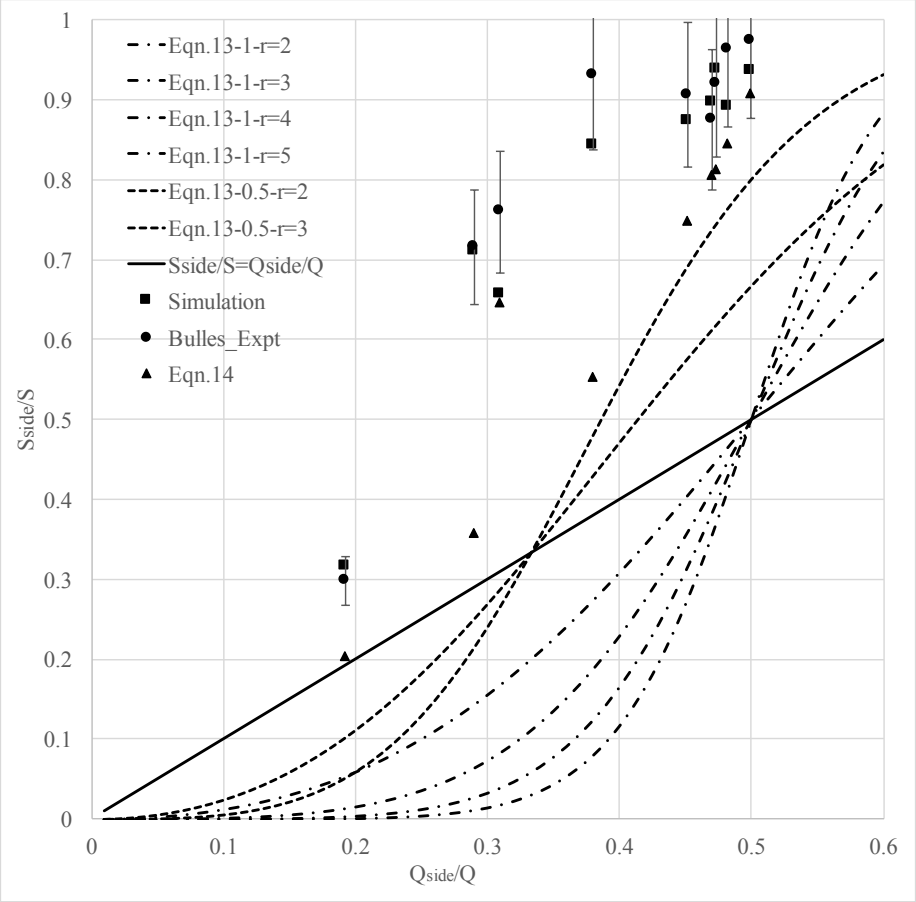


Figure 6.20: Comparision between simulated and observed sediment distributions for all the simulated cases. Also included are predictions made using the one-dimensional models by Wang et al. [49], and by van der Mark and Mosselman [110] (see Eqns. 6.13 and 6.14 respectively). For Eqn.6.13 the cases that have equal width of the lateral and the main channel, the legend is $Eqn.13 - 1 - r =$; and the cases for which the lateral channel is half the width of the main channel, it is $Eqn.13 - 0.5 - r =$. As a reference, the relationship $S_{side}/S = Q_{side}/Q$ has also been plotted. 10 percent error bars are provided to visualize the deviation of the model predictions from Bulle's observations.

# CHAPTER 7

# IMPLICATIONS OF BULLE-EFFECT ON MORPHODYNAMICS AT AN EXPERIMENTAL DIVERSION: A NUMERICAL INVESTIGATION

## 7.1 Introduction

In the previous chapter, a 3D RANS based hydrodynamic model was used to model the flow and bedload sediment transport at an experimental diversions, similar to Bulle's experiments. The simulations results were compared with Bulle's experiments. The numerical simulations were found to fare well in capturing the non-linear distribution of bedload between the two channels after the diversion, especially when compared with existing one-dimensional models. In general, the 3D numerical model was able to capture most of the flow characteristics observed in Bulle's experiments. The water surface elevation (WSE) predicted by the model matched well with the measurement from Bulle's experiments. The WSE at the diversion was found to increase substantially, with an $\approx 9$ percent increase of water-depth. The steepness of the increase in WSE was relatively higher for larger diversion-angle; which may be attributed to the need for a higher pressure-gradient to move part of the original flow into the lateral-channel with larger diversion-angle. The sudden increase in WSE at the diversion was also observed by Thomas et al. [42] in their experiments on symmetric bifurcations. Regions of the domain where flow separation was observed by Bulle, were well captured in the simulations, e.g. the separation at the left wall of the lateral channel just after the diversion; though the exact size of the recirculation zones, especially length, were under predicted by the 3D model. Width of the separation-zone was found to increase with increase in diversion-angle, this matches with observations made by Hardy et al. [121] through hydrodynamic simulations of flow at bifurcations.

The argument that larger diversion-angle results in larger flow-separation zone in the diverted channel, has been previously used by Constantine et al. [122] to propose a mechanism for filling up of oxbow lakes that result from chute cutoffs at sharp meander bends. In the proposed mechanism, the cutoff channel had been assumed to be equivalent to the main-channel of Bulle's experiment, and the abandoned channel equivalent to the lateral-channel. On the other hand, recent field measurements at chute cutoffs by Zinger et al. [123] showed formation of separation-zone at the left-bank of the cutoff channel and a high-velocity (and shear stress) zone at the right-bank; which is similar to the separation and

high-velocity zones observed in the lateral-channel through the 3D RANS simulations (and the LES simulations in Chapter 4 and 5) of Bulle's experiments. Irrespective of the layout of cutoffs, higher diversion angles will result in the high flow velocity core in the lateral to move towards the right wall and also further downstream, which may result in deposition of sediment under the separation-zone and erosion of the right-bank of the lateral-channel. The separation of the flow from the left-bank of the lateral-channel is similar to flow-separation observed at the inner-banks of the bends in the experiments conducted by [124], where they ascertained the detailed flow structure using 3D-PIV.

A characteristic of the flow that was not observed by Bulle, but was later seen in other studies was the presence of secondary flow circulation downstream from the diversion [84]. A clock-wise rotating secondary circulation was observed in the lateral channel, whereas a counter-clockwise rotating one was observed in the main channel. Similar secondary circulation pattern was also observed in high-resolution LES simulation [40], and laboratory experiments [39] conducted for a layout similar to Bulle's experiments. Zinger et al. [123] in their measurements at chute cutoffs also observed clock-wise rotating secondary flow circulation on the right-hand side of the cutoff channel. This secondary circulation would sweep incoming near-bed sediment from the high-velocity core of the flow towards the flow-separation, the sediment would eventually deposit there and contribute towards formation of a point bar.

Strong secondary flow circulation was also observed in the experiments on symmetric bifurcations by Thomas et al. [42] and Marra et al. [43]. The above mentioned authors detected the presence of counter-clock wise rotating secondary flow circulation in the channel on the right-hand side of the symmetric bifurcation, and a clock-wise rotating one in the channel on the left-hand side. This is similar to the pair of clock-wise and counter clock-wise rotating secondary circulation observed in the current study. Marra et al. [43] also found formation of secondary flow cells upstream of the bifurcation, though the orientation of the rotations were opposite to what they eventually become downstream from the bifurcation. Experiments done on symmetric bifurcations, but with unequal discharge split found a strong increase in the secondary flow circulation in the channel with the dominant discharge [43], which was found to influence a larger volume of the near-bed flow to enter the dominant flow channel. From the results of the previous chapter, similar increase in strength of the secondary flow can also observed in the main channel after the diversion.

Recently, there have been studies that analyzed the sediment capture efficiency of different potential diversion designs at the Lower Mississippi River (LMR). Gaweesh and Meselhe [23] used 3D free-surface hydrodynamic model to analyze the effect of diversion-angle, elevation of the bottom of the diversion, and the width of the diversion on the sediment capture efficiency (SCE) of a diversion. For the cases tested by Gaweesh and Meselhe [23], diversion-angle was not found to have a major effect on SCE, whereas decreasing the elevation

of the bottom of the diversion and increasing the width of the diversion was found to increase SCE. The positive effect of reduction of bottom elevation on SCE is because most of the flow going into a diversion comes from bottom of the channel, as observed in the results from the previous chapters, which brings along with it most of the sediment moving near the bottom. If the bottom elevation of the diversion is too far (say half channel depth) from the bottom of the river (main-channel), then it precludes the movement of sediment from near the bottom into the diversion. Proclivity of the flow near the bottom to enter the diversion was also observed by Gaweesh and Meselhe in their numerical simulations. Thus, future designs of diversions to capture sediment efficiently should be placed at an elevation that allows it to capture most of the flow from the bottom of the main channel.

In all the numerical studies discussed above, none of them considered the evolution of the bottom of the channel, which happens at a natural bifurcation or diversion. Bulle did conduct some experiments with a bed covered with sediment, but all the result he discussed were qualitative in nature, unlike his experiments done with a rigid channel bottom. Thus, as an extension of the analysis conducted in the previous chapter, simulations were conducted for different diversion-angles but with an erodible channel bottom. Rest of the boundary conditions were kept the same as those used in the previous chapter. The results from the analysis have been presented below presented int he following section.

## 7.2 Results and Discussion

The first case to be analyzed is the 90-degree diversion, with about 45.2 percent of the total flow going into the lateral-channel. The hydrodynamic initial condition used for the current case was the steady-state solution of the corresponding case with non-erodible channel bottom. This strategy was adopted for all the simulated cases, and was done to take into account the initial transient the flow goes through while reaching a steady-state solution. The morphological evolution of the bed at the diversion has been monitored and analyzed (see fig. 7.1,7.2 and 7.3). The parameter plotted in the in the figures is bed evolution, where positive evolution represent deposition of sediment and negative evolution represents erosion. The bedload sediment input from upstream is maintained same as the case with non-erodible bottom.

Just after the start of the numerical experiment, initially one can see scouring downstream of the entrance of the lateral-channel, near the right-wall (see fig. 7.1a). One can also see deposition at the entrance near the left-wall. In the next few minutes, the deposition at the diversion grows bigger and starts to move into the lateral and the main channel (fig. 7.1b,c). During this time, initially the scour in the lateral-channel gets filled up, whereas a small scour hole can

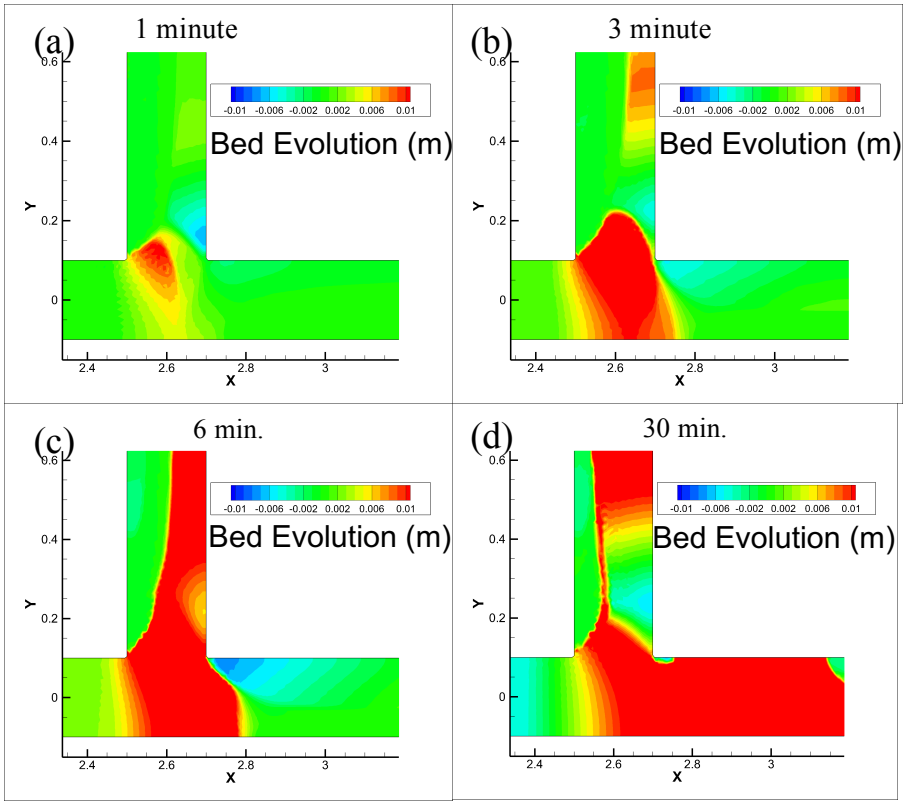


Figure 7.1: The bed evolution at a 90-degree, when 45.2 percent of the total flow is moving into the lateral-channel. The color-scale represents "bed-evolution" with the units m. (a) 1 minute after the start of the simulation (b) after 3 minutes (c) after 6 minutes (d) after 30 minutes.

be seen forming near the left-wall of the main channel. Within the next 30 minutes, the above mentioned scour hole in the main-channel gets filled up by the aggrading front, whereas the one in the lateral-channel starts to reappear (see fig. 7.1d). The sustained scouring in the lateral-channel is caused by the incoming bottom hugging flow, which impinges on right-wall at the position of the scouring. The above mentioned current and high-shear flow zone had been corroborated earlier by the visualization of the flow near the bottom for both the LES and the RANS simulations. The above mentioned aggradation at the diversion, which then travels downstream into the lateral and main channel, is due to the initial sediment transient caused by scouring upstream. After that initial transient of sediment, the only sediment flux from upstream is the imposed constant sediment load.

In the next 30 minutes, the size of the scour in the lateral channel can be seen to increase (see fig. 7.2a), while the aggradation continued to move further downstream. On the left side of the lateral channel, sediment can be seen to have deposited, resulting in formation of a point bar under the flow re-circulation zone formed due to separation of the flow from the left-wall of the lateral-channel. In the next hour, the aggradatoin has moved further away from the diversion, and the scour hole under the high-flow zone in the lateral-channel has increased in size (see fig. 7.2b). Unlike the scour hole in the lateral-channel, the scouring near the left-wall of the main-channel does not reappear after some time.

After the initial transient of sediment has moved away from the diversion, the amount of sediment coming from upstream is less than the sediment being scoured. Thus after running the numerical experiment for 9 hours, the main-channel upstream from the diversion has degraded by 2 cm (see fig. 7.3a). By the time the numerical experiment has run for 10 hours, it is evident that the bed morphology at the diversion has reached an equilibrium, as there is no discernible evolution in the last one hour (fig. 7.3b). Over the course of the last 420 minutes, the channel bottom under the high-flow zones in the lateral and main channel has eroded, leading to consolidation of the point-bar near the left-wall of the lateral channel. In the main-channel scouring has occurred almost everywhere, except for a small region just after the diversion and near the left-wall. The depth-averaged structure of the flow at the diversion with the evolved bathymetry is slightly different from the case with rigid bottom. The flow going through the lateral-channel is completely confined to the scoured right side of the channel, this results in slight increase in the flow re-circulation zone. Scouring under the high-flow zone was also observed by Eicke during his experiments [38]. In the current case, the change in morphology of the bed at the diversion did not to hinder the preferential movement of bed-load into the lateral-channel. Though one needs to point out that this depends on the boundary-condition in place. In the simulated cases, free-outflow was imposed for sediment at the outlet and a constant sediment inflow at the inlet. The outflow boundary condition allowed sediment to go out of the system unhindered

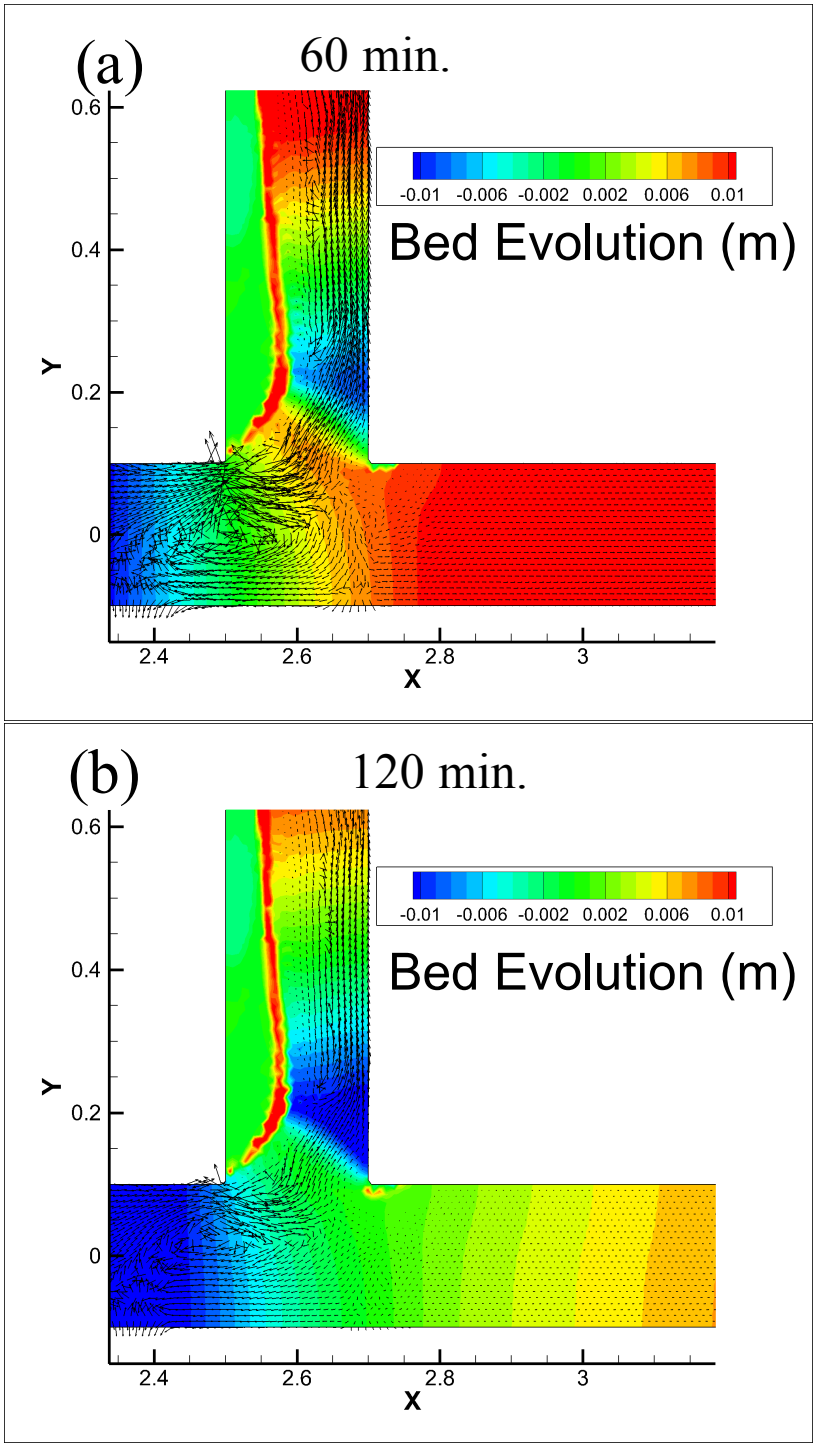


Figure 7.2: The bed evolution at a 90-degree, when 45.2 percent of the total flow is moving into the lateral-channel. The color-scale represents "bed-evolution" with the units m. (a) 60 minutes after the start of the simulation (b) after 120 minutes. The vectors show the direction of sediment flux.

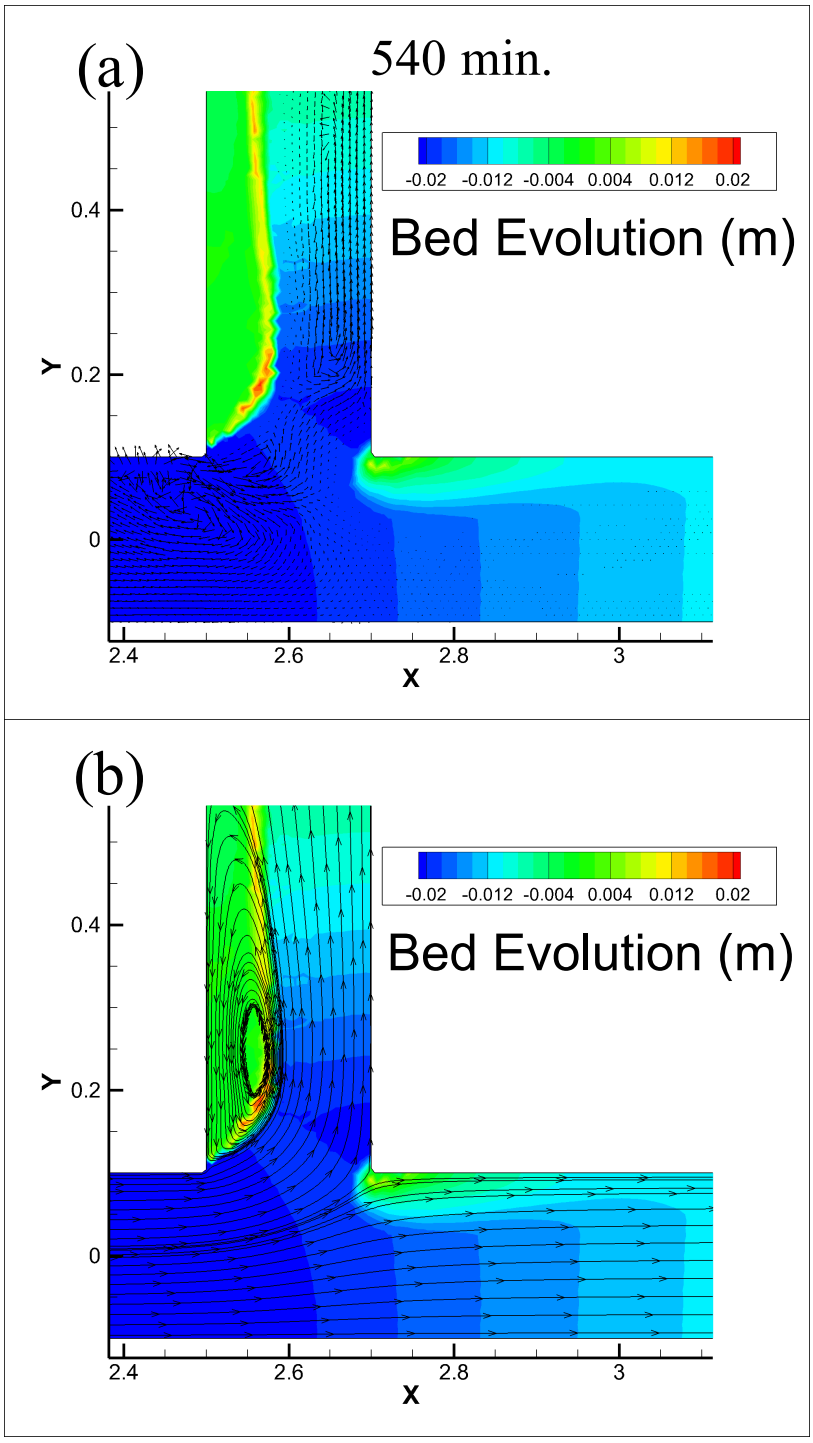


Figure 7.3: The bed evolution at a 90-degree, when 45.2 percent of the total flow is moving into the lateral-channel. The color-scale represents "bed-evolution" with the units m. (a) 540 minutes after the start of the simulation (b) after 600 minutes. Figure (b) also shows the depth-averaged flow streamlines.

and the sediment flux inputted in the system was not enough to cause permanent aggradation in the lateral-channel. If the imposed conditions would have been different, then reduction in transport capacity of the lateral-channel would have adversely affect the phenomenon of Bulle-Effect.

Next the cases with 60-degree, 120-degree and 150-degree has been analyzed. In all the cases, along with the evolution of the channel bottom, the shear stress at the bed has also been plotted (see fig. 7.5,7.6 and 7.7). For the 60-degree case (see fig. 7.4), relatively low shear stress zone is formed under the flow re-circulation in the lateral-channel. Additionally, a low shear stress zone is also formed at the left-wall of the lateral channel. Substantial sediment deposition can be seen to have occurred at the low shear stress zone in the lateral-channel. Unlike the previous case, the deposition is not just at the edge of the re-circulation zone, but under it too. One can also observe the incoming erosion front from upstream of the diversion. Like in the previous case, over time the front will travel further downstream and erode the channel bottom under the high flow zones.

Similar to the previous cases, in the 120-degree case a relatively low shear stress zone is formed under the re-circulation zone in the lateral-channel, which is also the region where deposition of bedload takes place (see fig. 7.5). Even though some bedload is deposited at the edge of the above mentioned zone, majority of it is moved downstream through the high flow zone. The high-flow region near the entrance of the lateral-channel is also the place where substantial erosion takes place. Eventually the erosion front coming from upstream will lower the general bathymmetry of the high-flow zone in lateral-channel (and also the main-channel). Finally, one can also observe the deposition at the right corner of the diversion, due to stagnation of the flow caused by the obtuseness of the diversion-angle.

In the 150-degree case, due to increase in size of the stagnation zone the size of the deposition also gets bigger (see fig. 7.6). Also, as the stagnation zone moves into the lateral-channel (this was also observed in the LES simulations), so does the zone of sediment deposition. Formation of sediment deposits near both the right and left wall of the lateral-channel further constricts the flow, leading to high shear stress point where the flow impinges the right-wall.

## 7.3 Conclusions

In the current chapter, the impact of Bulle-Effect on the morphological evolution of an idealized experimental scale diversion was evaluated. Numerical simulations were conducted for some of the cases of Bulle's, but with an erodible channel bottom. This allowed the bathymmetry of the system to evolve in time. In all the cases, sediment was deposited in the low shear stress zone formed due to separation of the flow from the left-wall of the lateral-channel.

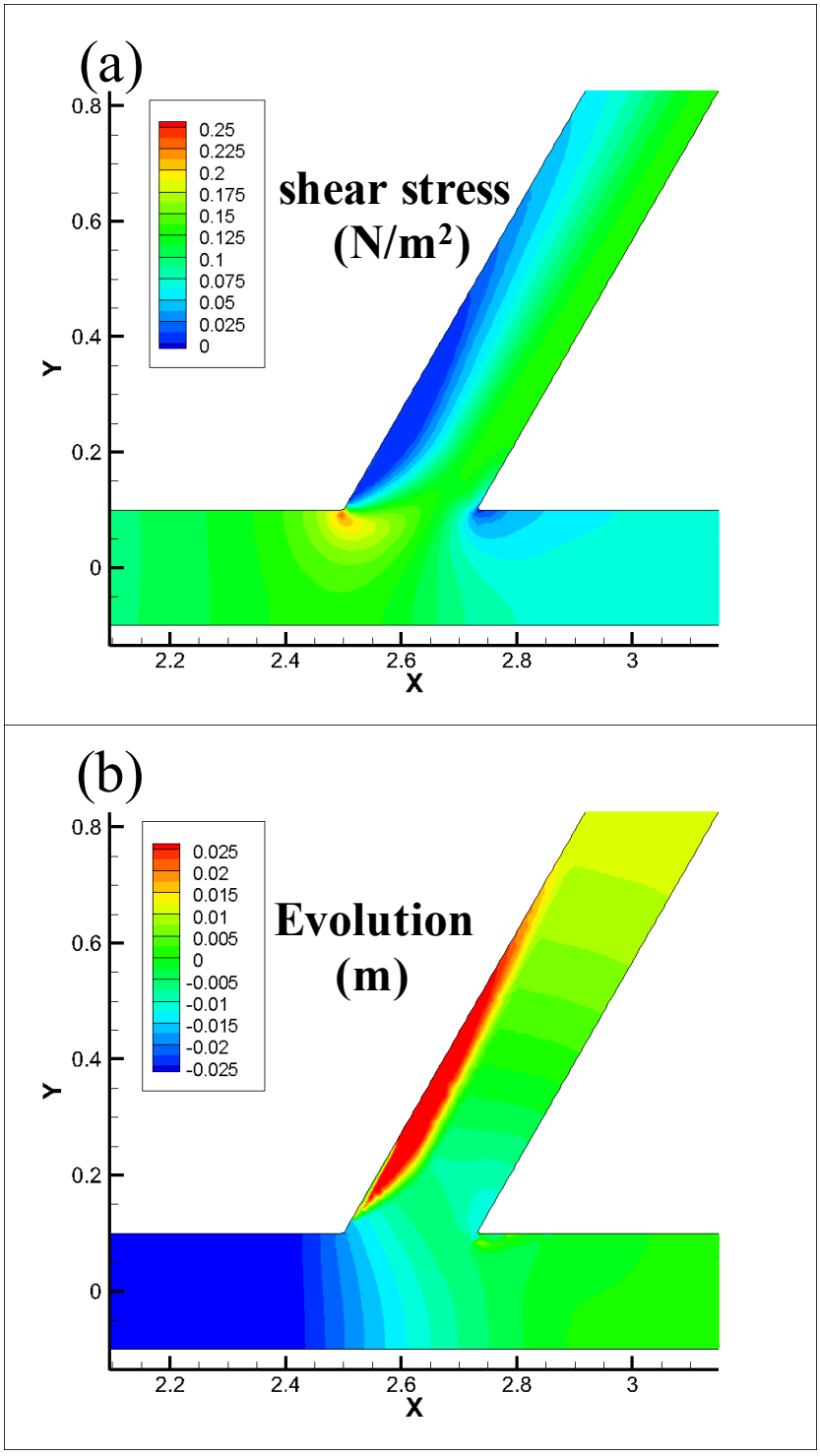


Figure 7.4: The bed evolution at a 60-degree, when about 48 percent of the total flow is moving into the lateral-channel. (a) shear stress at the bed (b) Bed evolution after about 2 hours of simulation time.

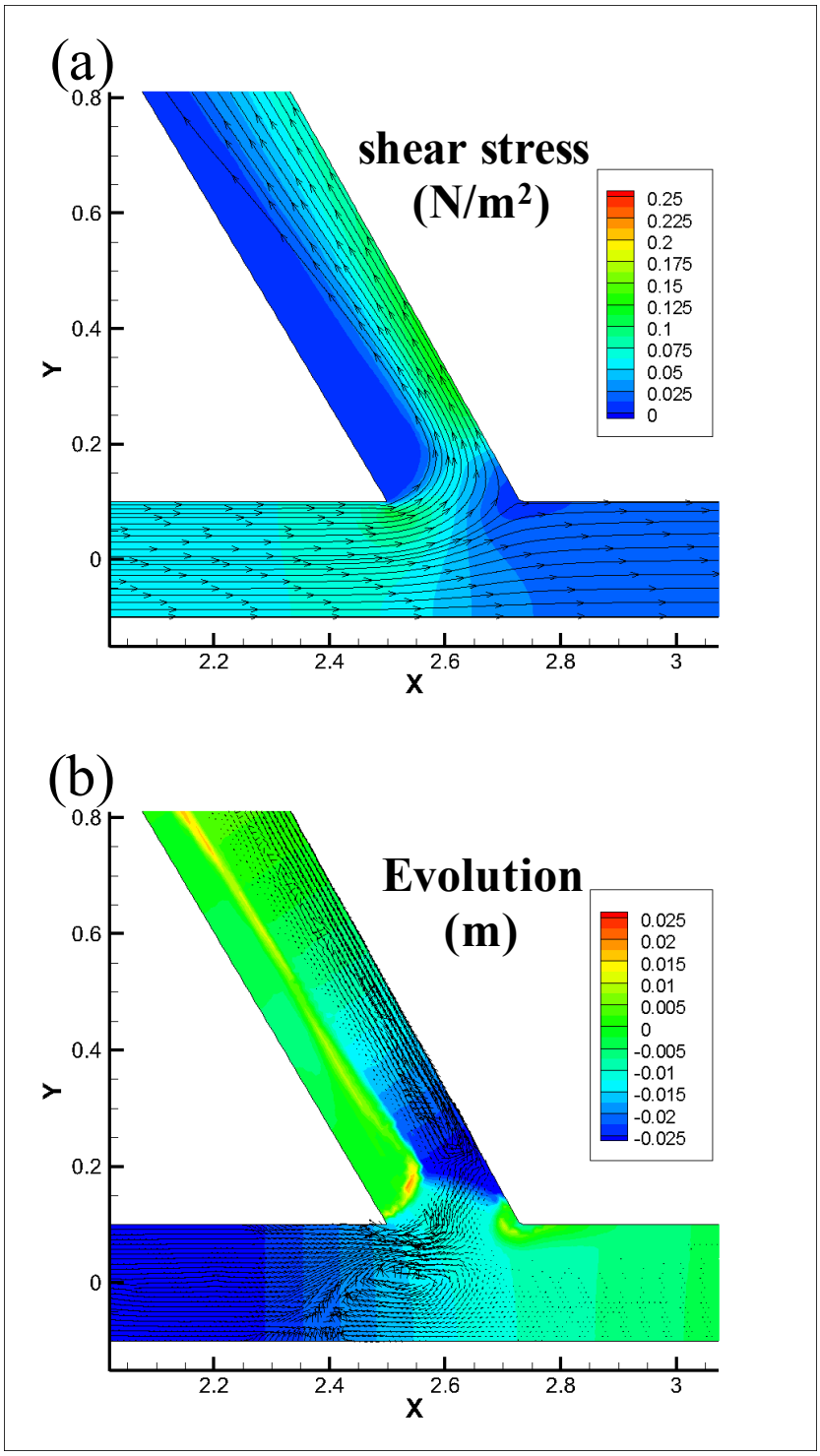


Figure 7.5: The bed evolution at a 120-degree, when about 47 percent of the total flow is moving into the lateral-channel. (a) Bed shear stress, along with streamlines of depth-averaged flow (b) Bed evolution after about 2 hours of simulation time. The vectors in (b) represent bedload flux.

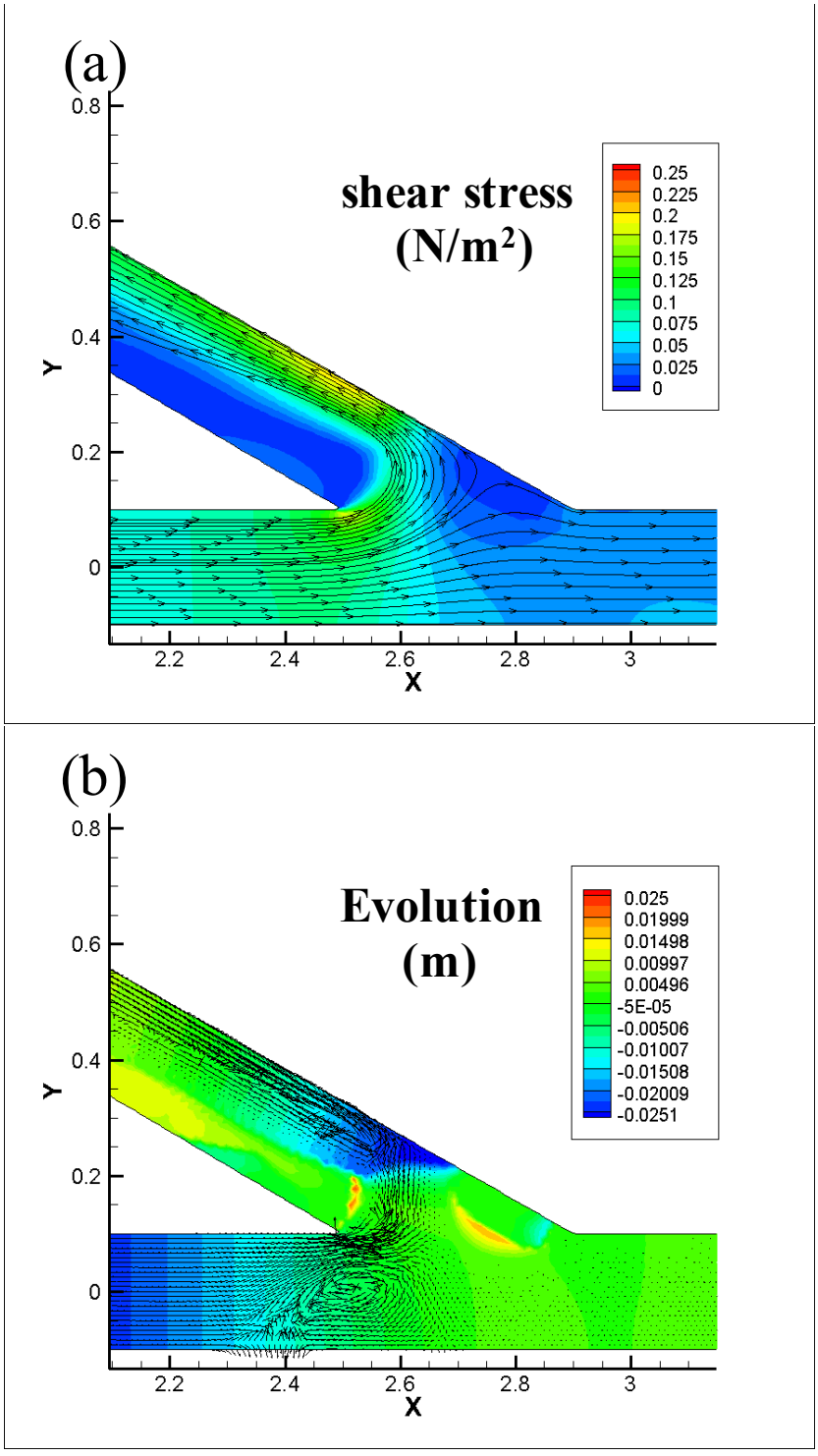


Figure 7.6: (a) Bed shear stress, along with streamlines of depth-averaged flow (b) Bed evolution after about 2 hours of simulation time. The vectors in (b) represent bedload flux.

Additionally, sediment also deposited around the area where the flow stagnates, especially in the cases with diversion angle greater than 90-degree. In general, change in channel bottom bathymmetry did not alter the preferential movement of bedload into the lateral-channel. On the other hand, even though most of the bedload sediment went into the lateral-channel, it was not deposited in the high-flow zone on the right side of the channel. Instead, most of it was moved further downstream, resulting in formation of scour hole at the point where the incoming flow impinges the right-wall.

It should be pointed out that the evolution pattern shown in the current simulations is specifically valid for the imposed boundary conditions and size of sediment. In the current study, the sediment only moved as bedload, this constrained the deposition of sediment in the flow re-circulation zones. In case the size of sediment in the system was fine enough to travel in suspension, the amount of deposition under the flow re-circulation zone would have been higher. Thus, in order to fully understand the morphdynamical reaction of the diversion, further sensitivity analysis is required through changing the boundary conditions like flow division and sediment input, and sediment property like the size of the sediment. Finally, in the current study the analysis was confined to evolution of the bathymmetry, but in a the real world a river not only erodes or aggrades, but can also change direction in the horizontal. For example, the high shear stress point in the lateral-channel where the flow impinges the wall, is a prime candidate for bank failure. Failure of the right-bank and sediment deposition near the left-wall can together result in an avulsion. This is one aspect of the morphodynamics which needs to be studied in the future, using improved numerical models developed to study river morphodynamics [125].

# CHAPTER 8

# CONCLUSIONS AND FUTURE WORK

In the final chapter the key contributions of this dissertation have been summarized, along with possible future research directions.

1) It has been almost hundred years since Bulle's seminal work on sediment distribution at fluvial diversions. Since then, there has been studies that have confirmed Bulle's findings that disproportionately higher amount of bedload sediment enters the lateral-channel at a diversion, compared to the percentage of total flow entering the lateral-channel. Recently, there has been a renewed interest in fluvial diversions, primarily due to their potential use for diverting water and sediment to reclaim endangered deltas around the world. Despite the interest, there has not been a study that brings together and analyzes the available literature and data from disparate sources. The current study is a step towards doing it, as various studies like Bulle's original report [1], the often overlooked but important work of Dancy [55], to the recent numerical study by Gaweesh and Meselhe [23], have been reviewed in some detail. In the future, the above mentioned literature survey would be extended further, in order to bring together all the available data from experiments on diversions.

Based on the data collected during the above mentioned literature review process, the current study also explored the potential implication of Bulle-Effect on the calculation of sediment capture efficiency (SCE) of a diversion channel. It was found that the current methodology employed for calculating SCE is based on an assumption that the amount of sediment entering the diversion channel is a linear function of water entering the diversion channel, that is $S_{side}/S_{main} = \alpha Q_{side}/Q_{main}$. Though experimental and field data on sediment (especially bedload) distribution at diversions belied the above assumption; and the alternative relationship that came out of the data was $S_{side}/S_{main} = \alpha(Q_{side}/Q_{main})^{\beta}$, where $\alpha > 1$ and $\beta > 1$. Additionally, the discrepancy between the actual SCE and the one calculated based on the linear assumption was demonstrated, and an improved methodology for calculating SCE suggested.

2) Part of the dissertation involved conducting high-resolution eddy-resolving numerical simulations of flow and sediment transport at idealized diversions,

where sediment transport has been modeled as Lagrangian particles. A novel semi-implicit algorithm was developed for time-stepping of the Lagrangian particles. A semi-implicit time-stepper is required for efficient time-stepping of poly-disperse sediment particles, and as there are none currently available for Lagrangian particles, the algorithm was developed as part of the current dissertation. The algorithm was then implemented in the open-source computational fluid dynamics solver Nek5000. Even though the new method was developed specifically for the thesis, its utility goes beyond the domain it was used in.

Currently the model is coupled one-way that is only the flow and properties of the particles influence the movement of the particles. In the future the model could be developed further to include two-way and four-way coupling of the particles, which will take into account the feedback of the particles onto the flow and particle-particle interactions.

3) One of the main objectives of the dissertation was to study in detail the mechanism behind the phenomenon of Bulle-Effect, and to ascertain the major controls on the phenomenon. For it, Direct Numerical Simulations (DNS) and Large Eddy Simulations (LES) of flow and sediment transport were conducted and analyzed for an idealized experimental-scale diversion. Simulations were conducted for different flow-divisions, Reynolds number ($Re_{bulk}$), diversion angles, and sediment with different diameters, in order to understand the sensitivity of the phenomenon to different factors. Some of the major findings from the simulations and their analysis have been listed below.

It was confirmed that the phenomenon occurs due to the majority of the flow near the bottom entering the lateral-channel, even when a relatively larger portion of the total flow continued along the main-channel, thus taking disproportionate amount of near-bed sediment with it. Also, the phenomenon was found to be stronger for laminar flows, when compared with the corresponding turbulent case. The flow at the diversion was found to result in strong secondary circulations in the lateral and main channel after the diversion. Similar clockwise rotating secondary-circulation in the lateral-channel has also been observed in the field during studies on chute-cutoff [123]. The strength of the secondary-circulation was found to increase with increase in diversion angle, with the secondary-circulation for the 150-degree case being appreciably stronger than the corresponding 30-degree case.

Simulations were conducted for a 90-degree diversion with 50 : 50 flow division and for different $Re_{bulk}$, and with fine buoyant particles initiated at different height from the bottom. The particles were tracked to check if they entered the lateral or the main-channel. In case of laminar flows, almost all the particles initiated in the lower 40 percent of the water-column ended up in the lateral-channel, even though the total flow is divided equally. For the turbulent cases, 60-70 percent of the particles in the lower 30 percent of the water-column ended up in the lateral-channel. It was concluded that Bulle-Effect should not only be

valid for bedload, as suggested by most experiments, they should also be valid for sediment primarily moving in the bottom 25-35 percent of the water-column.

In order to analyze the effect of sediment size on its proclivity to enter the lateral-channel, simulations were conducted with sediment of different sizes and flow-divisions, for turbulent flow at a 90-degree diversion. The results clearly showed that increase in size of sediment (for the same specific gravity of sediment) increases the chance of the sediment to enter the lateral-channel. The results matched the trend shown by experiments conducted by Bulle and Dancy [55]. This can be attributed to the fact that heavier sediment particles tend to move nearer to the channel-bottom, where majority of the flow enters the lateral-channel, even in a case when only 35 percent of the total flow enters the lateral-channel. Additionally, it was found that rather than size of sediment, the parameter that better represents if sediment is more likely to move into the lateral-channel is the Rouse number, or the ratio of the particle settling velocity ($V_s$) and bed shear velocity ($u_*$).

These fundamental insights also helped in recognizing the mechanism that causes the flow near the bottom to enter the lateral-channel. The fundamental reason the phenomenon occurs is due to relatively lower inertia/velocity of the flow near the bottom of the channel, compared to the top. When part of the flow starts to enter the lateral-channel, a favorable pressure-gradient is established between the diversion and the lateral-channel, whereas a corresponding negative pressure-gradient is established in the main-channel. With increase of the percentage of flow moving into the lateral-channel, the aforementioned pressure-gradient increases. This pressure-gradient causes to an extent acts uniformly throughout the water-column, but faster moving flow near the top is able to overcome it and continue into the main-channel, whereas slower moving flow near the bottom is driven into the lateral-channel. This transverse forcing causes a secondary flow-circulation in the flow, similar to flow through bends.

In the future the simulations with sediment would be extended to other diversion-angles, to gauge the effect of diversion-angle on Bulle-Effect. Simulations would also be conducted for cases with depth of the lateral-channel being smaller than the depth of the main-channel (often the case in real-world lateral off-takes), and higher width to depth ratio of the main-channel (for the cases discussed above it is 3). Finally, simulations and analysis similar to the present study, would be extended to other symmetric and asymmetric bifurcations, in order to ascertain the presence of Bulle-Effect like phenomenon in a generic asymmetric bifurcation.

4) As high-resolution numerical simulation of nature-scale fluvial diversions are not possible, it was important to check if a RANS based hydrodynamic model, like the ones usually used for simulation of fluvial dynamics, were capable to capture the complex phenomenon of Bulle-Effect. For that purpose a 3D hydrodynamics model for Bulle's experiment was developed. Almost the full set

of Bulle's experiments were simulated, and the model was able to capture the primary characteristics of the phenomenon. The model was able to capture the behavior of the water surface elevation shown in the experiments. The simulations were also able to capture the highly three-dimensional flow-structure, and predict the bedload sediment distribution at the diversion satisfactorily. It was also demonstrated that 1D models were unable to predict the sediment distribution at the diversion. This is primarily due to the highly three-dimensional nature of the phenomenon, the fact that lower part of the water-column at the diversion behaves differently from the upper part. So, not just 1D models, even the current 2D depth averaged models will not be able to capture the phenomenon accurately. Thus, in the future models that take into account the mechanism of Bulle-Effect are needed to be developed for 2D depth-averaged numerical solvers, similar to the ones developed to capture the secondary currents in a bend.

Finally, the extent to which the Bulle-Effect plays a role in real-world diversions has to be studied. Based on dissproportinately high sediment transported into the diversions of the Yellow River, China [53], Canal del Dique on the Magdalena River, Columbia etc., it can be conjectured that the Bulle-Effect plays a major role at the aforementioned diversions. In the future, numerical simulations of real-world diversions should be conducted ( in conjunction with field measurements) in order to study in detail the flow-structure and sediment distribution pattern at the diversion.

5) The 3D RANS model developed was then used to simulate Bulle's experiments with erodible channel bottom. This was done to ascertain the impact of Bulle-Effect on the morphodynamics of the bathymetry at a fluvial diversion. At the diversion, scouring occured below the high-flow zone in the lateral-channel, similar feature was also observed by Eicke during his experiments [38]. Sediment deposition was found to happen at the flow re-circulation zone in the lateral-channel, and around the flow-stagnation zone at the right corner of the diversion. The change in morphology of the bed at the diversion was found not to hinder the preferential movement of bedload into the lateral-channel. Also, due to relatively low influx of sediment from upstream of the diversion, apart from the initial transient due to scouring upstream, in general the bottom the whole system (including the channel upstream) erodes before reaching an equilibrium. The current simulations only considered the evolution of the channel bottom, though the region of the lateral-channel where appreciable scouring takes place could also have bank failure of the right-wall due the incoming flow impinging onto the wall of the channel. This is one aspect that should be modeled to get the full picture of possible morphodynamic changes at a diversion.

The morphodynamic patterns seen in the current simulations depend on the boundary-condition and the property/size of sediment in the system. Thus more simulations and analysis needs to be conducted with different sediment input

into the system and different sediment sizes. Finally, the studies should be extended to morphodynamics of field-scale diversions, in order to make assessment of Bulle-Effect's impact on morphodynamics of real-world diversions.

The findings of this dissertation will not only add to the fundamental understanding of an important phenomenon in nature, these also provide insights that will help in optimal design of engineered diversions and other facilities where vorticity and secondary-flow driven sediment/particle transport occurs.

# REFERENCES


[1] H. Bulle, "Untersuchungen ber die Geschiebeableitung bei der Spaltung von Wasserlufen (in German)," V.D.I Verlag, Berlin, Germany, Tech. Rep., 1926.

[2] D. Sokolow, "Untersuchengen uber den Entnahmewinkel (in German)," *wasserkraft und wasserwirtschaft*, p. pag. 145, 1936.

[3] G. Benini, "Sull'angolo Di Migliore Incidenza di una Derivazione (in Italian)," *L'ENERGIA ELETTRICA*, vol. XXIX, no. 6, pp. 1–11, 1952.

[4] G. Benini, "Sull'angolo di Una di una Derivazione (in Italian)," *L'ENERGIA ELETTRICA*, vol. XXXII, no. 9, 1955.

[5] H. D. Vogel, "Movement of Bed Load in a Forked Flume," *Civil Engineering*, vol. 4, pp. 73–77, 1934.

[6] C. P. Linder, "Diversions from Alluvial streams," *Trans. A.S.C.E.*, vol. 118, pp. 245–269, 1953.

[7] L. I. Tison, "Des dispositions a donner a la prise d'eau d'un canal pour reduire l'intro- duction des materrieaux solides dans ce canal (in French)," Report on the fourth meeting of I.A.H.R., Bombay, India, Tech. Rep., 1951.

[8] H. M. Ismail, "Diversion of canals," *A.S.C.E. Separate no. 461*, vol. no. 461, July 1954.

[9] K. Riad, "Analytical and experimental study of bed load distribution at alluvial diversions," Delft, Netherlands, pp. 1–112, 1961.

[10] A. Rocha, "Distributions De Material Solide Dans Les Bifurcations Des Lits Alluvionnaires (in French)," in *Vol. 3, 14th Congress IAHR, Paris*, 1971, pp. 153–160.

[11] J. L. Ordonez, "Sediment exclusion at river diversions," Hydraulics and Sanitary Engineering Laboratory, UC, Berkeley, Tech. Rep., 1974.

[12] A. Ramamurthy and M. Satish, "Division of Flow in Short Open Channel Branches," *J. Hydraul. Eng.*, vol. 114(4), pp. 428–438, 1988.

[13] V. S. Neary and F. Sotiropoulos, "Numerical investigation of laminar flows through 90-degree diversions of rectangular cross-section," *Comp. and Fluids*, vol. 25(2), pp. 95–118, 1996.

[14] A. S. Shettar and K. K. Murthy, "A Numerical study of division flow in open channels," *J. Hydrl. Res.*, vol. 34(5), pp. 651–675, 1996.

[15] B. Wang, R. Fokking, M. D. Vries, and A. Langerak, "Stability of river bifurcations in 1D morphodynamics models," *J. Hydrl. Res.*, vol. 33 (6), pp. 739–750, 1995.

[16] M. B. Pittaluga, R. Repetto, and M. Tubino, "Channel bifurcation in braided rivers: Equilibrium configurations and stability," *Water Resources Res.*, vol. 39 (3), p. 1046, 2003.

[17] M. G. Kleinhans, R. I. Ferguson, S. N. Lane, and R. J. Hardy, "Splitting rivers at their seams: bifurcations and avulsion," *Earth Surface Processes and Landforms*, vol. 38, no. 1, pp. 47–61, 2013.

[18] A. Herrero, "Experimental and Theoretical Analaysis of Flow and Sediment Transport in 90-Degree Fluvial Diversions," Barcelona, Spain, pp. 1–176, 2013.

[19] F. Etudes, "Restauracion del Canal del Dique - Informe final (in Spanish)," DI-EE 07 -262a, Lyon, France, Tech. Rep., 2007.

[20] M. Allison and E. Meselhe, "The use of large water and sediment diversions in the lower Mississippi River (Louisiana) for coastal restoration," *J. Hydrology*, vol. 387, pp. 346–360, 2010.

[21] M. A. Kenney, B. F. Hobbs, D. Mohrig, H. Huang, J. A. Nittrouer, W. Kim, and G. Parker, "Cost analysis of water and sediment diversions to optimize land building in the Mississippi River delta," *Water Resour. Res.*, vol. 49, pp. 3388–3405, 2013.

[22] G. Brown, C. Callegan, R. Heath, L. Hubbard, C. Little, P. Luong, K. Martin, P. McKinney, D. Perky, F. Pinkard, T. Pratt, J. Sharp, and M. Tubman, "West Bay Sediment Diversion Effects," ERDC Workplan Report - DRAFT, CHL U.S. Army ERDC, Vicksburg, Tech. Rep., 2009.

[23] A. Gaweesh and E. Meselhe, "Evaluation of sediment diversion design attributes and their impact on the capture efficiency," *Journal of Hydraulic Engineering*, vol. 142, no. 5, p. 04016002, 2016.

[24] J. A. Nittrouer, J. L. Best, C. Brantley, R. W. Cash, M. Czapiga, P. Kumar, and G. Parker, "Mitigating land loss in coastal Louisiana by controlled diversion of Mississippi River sand," *Nature Geoscience*, vol. 5, pp. 534–537, 2012.

[25] E. Meselhe, I. Georgiou, M. Allison, and J. McCorquodale, "Numerical modeling of hydrodynamics and sediment transport in Lower Mississippi at a proposed delta building diversion," *J. of Hydrology*, vol. 472-473, pp. 340–354, 2012.

[26] L. Giosan, S. Constantinescu, F. Filip, and B. Deng, "Maintenance of large deltas through channelization: Nature vs. humans in the Danube delta," *J. of Hydrology*, vol. 1, pp. 35–45, 2013.

[27] A. K. Misra, A. Saxena, M. Yaduvanshi, A. Mishra, Y. Bhadauriya, and A. Thakur, "Proposed river-linking project of India: a boon or bane to nature," *Environmental Geology*, vol. 51(8), pp. 1361–1376, 2007.

[28] S. Dutta, T. E. Tokyay, Y. A. Cataño-Lopera, S. Serafino, and M. H. Garcia, "Application of computational fluid dynamic modelling to improve flow and grit transport in Terrence J. O'Brien Water Reclamation Plant,

Chicago, Illinois," *Journal of Hydraulic Research*, vol. 52, no. 6, pp. 759–774, 2014.

[29] S. Dutta, Y. Catano, X. Liu, and M. H. Garcia, "Computational fluid dynamics (CFD) modeling of flow into the aerated grit chamber of the MWRD's North Side Water Reclamation Plant, Illinois," in *World Environmental and Water Resources Congress 2010: Challenges of Change*, 2010, pp. 1239–1249.

[30] M. K. Ghosh, S. Dutta, and D. Sen, "Sediment Flushout from Pond of River Diversion Barrages by Gate Operation," *Water resources management*, vol. 28, no. 15, pp. 5335–5356, 2014.

[31] P. F. Fischer, J. W. Lottes, and S. G. Kerkemeier, "Nek 5000 Webpage," 2008, http://nek5000.mcs.anl.gov.

[32] J.-M. Hervouet, A. Weisgerber, P. Tassi, and C. Coulet, "open TELEMAC-MASCARET Webpage," 2014, http://http://opentelemac.org/.

[33] L. Giosan, J. Syvitski, S. Constantinescu, and J. Day, "Climate change: protect the world's deltas," *Nature*, vol. 516, no. 7529, pp. 31–33, 2014.

[34] W. Kim, D. Mohrig, R. Twilley, C. Paola, and G. Parker, "Is it feasible to build new land in the Mississippi River Delta," *Eos*, vol. 90, no. 42, pp. 373–374, 2009.

[35] H. Rehbock, "modellversuche ber die zweckmigste gestaltung einzelner bauwerke (in German)," veroffentlichung der mittleren Isar A. G. Munchen Rom - Verlag, Charlottenburg, Tech. Rep., 1926.

[36] H. Thoma, "modellversuche ber die zweckmigste gestaltung einzelner bauwerke (in German)," veroffentlichung der mittleren Isar A. G. Munchen Rom - Verlag, Charlottenburg, Tech. Rep., 1923.

[37] G. Dancy, "Stream sedimentation in a divided channel," Ames, lowa, pp. 1–253, 1947.

[38] S. Eicke, *Geschiebebewegung bei Flussverzweigungen*. Versuchsanst. f. Wasserbau u. Schiffbau, 1958.

[39] A. Herrero, A. Bateman, and V. Medina, "Water flow and sediment transport in a 90 channel diversion: an experimental study," *Journal of Hydraulic Research*, vol. 53, no. 2, pp. 253–263, 2015.

[40] S. Dutta, P. Fischer, and M. H. Garcia, "Large Eddy Simulation (LES) of flow and bedload transport at an idealized 90-degree diversion: Insight into Bulle-Effect," in *River Flow 2016*. CRC Press, 2016, pp. 101–109.

[41] J. A. Zinger, B. L. Rhoads, and J. L. Best, "Extreme sediment pulses generated by bend cutoffs along a large meandering river," *Nature Geoscience*, vol. 4, no. 10, pp. 675–678, 2011.

[42] R. E. Thomas, D. R. Parsons, S. D. Sandbach, G. M. Keevil, W. A. Marra, R. J. Hardy, J. L. Best, S. N. Lane, and J. A. Ross, "An experimental study of discharge partitioning and flow structure at symmetrical bifurcations," *Earth Surface Processes and Landforms*, vol. 36, no. 15, pp. 2069–2082, 2011.

[43] W. A. Marra, D. R. Parsons, M. G. Kleinhans, G. M. Keevil, and R. E. Thomas, "Near-bed and surface flow division patterns in experimental river bifurcations," *Water Resources Research*, vol. 50, no. 2, pp. 1506–1530, 2014.

[44] D. Edmonds, "Stability of backwater-influenced river bifurcations: A study of the Mississippi-Atchafalaya system," *Geophysical Research Letters*, vol. 39, no. 8, 2012.

[45] D. Edmonds and R. Slingerland, "Stability of delta distributary networks and their bifurcations," *Water Resources Research*, vol. 44, no. 9, 2008.

[46] C. Brink, "Bend diversion to minimize sediment intake," Stellenbosch University, South Africa, pp. 1–253, 1947.

[47] J. A. Nittrouer, J. L. Best, C. Brantley, R. W. Cash, M. Czapiga, P. Kumar, and G. Parker, "Mitigating land loss in coastal Louisiana by controlled diversion of Mississippi River sand," *Nature Geoscience*, vol. 5, no. 8, pp. 534–537, 2012.

[48] M. H. Garcia, *Manual 110. Sediment Engineering: Process, Measurements, Modleing and Practice*. VA, USA: American Society of Civil Engineering, 2008.

[49] Z. Wang, M. De Vries, R. Fokkink, and A. Langerak, "Stability of river bifurcations in ID morphodynamic models," *Journal of Hydraulic Research*, vol. 33, no. 6, pp. 739–750, 1995.

[50] K. Riad, "Analytical and experimental study of bed load distribution at alluvial diversions," Ph.D. dissertation, TU Delft, Delft University of Technology, 1961.

[51] A. Schoklitsch, *Hydraulic structures: a text and handbook*. The American Society of Mechanical Engineers, 1937, vol. 1.

[52] J. I. Ordoñez, "Sediment control at large canal diversions," in *Proc., 35th IAHR World Congress*. Chengdu, China: IAHR, 2013, vol. 3. pp. 1826–1837.

[53] T. Erxun, "Sediment Problems in Diverting Water for Water Supply in the Lower Yellow River," in *Taming the Yellow River: Silt and Floods*. Springer, 1989, pp. 657–676.

[54] W. Ta, H. Wang, and X. Jia, "Downstream fining in contrasting reaches of the sand-bedded Yellow River," *Hydrological Processes*, vol. 25, no. 24, pp. 3693–3700, 2011.

[55] A. G. Dancy, "Stream sedimentation in a divided channel," M.S. thesis, Iowa State College Ames, 1947.

[56] V. E. Vanoni, *Manual of Practice 54, Sedimentation Engineering*, classic ed. American Society of Civil Engineers, 2008.

[57] G. Parker, M. Garcia, Y. Fukushima, and W. Yu, "Experiments on turbidity currents over an erodible bed," *Journal of Hydraulic Research*, vol. 25, no. 1, pp. 123–147, 1987.

[58] Y. Niño and M. García, "Gravel saltation: 2. Modeling," *Water resources research*, vol. 30, no. 6, pp. 1915–1924, 1994.

[59] C. T. Crowe, J. D. Schwarzkopf, M. Sommerfeld, and Y. Tsuji, *Multiphase flows with droplets and particles.* CRC press, 1998.

[60] J. Capecelatro and O. Desjardins, "An Euler–Lagrange strategy for simulating particle-laden flows," *Journal of Computational Physics*, vol. 238, pp. 1–31, 2013.

[61] S. Elghobashi, "Particle-laden turbulent flows: direct simulation and closure models," *Applied Scientific Research*, vol. 48, no. 3-4, pp. 301–314, 1991.

[62] M. Maxey, "The gravitational settling of aerosol particles in homogeneous turbulence and random flow fields," *Journal of Fluid Mechanics*, vol. 174, pp. 441–465, 1987.

[63] S. Balachandar and J. K. Eaton, "Turbulent dispersed multiphase flow," *Annual Review of Fluid Mechanics*, vol. 42, pp. 111–133, 2010.

[64] M. van Hinsberg, J. ten Thije Boonkkamp, F. Toschi, and H. Clercx, "Optimal interpolation schemes for particle tracking in turbulence," *Physical Review E*, vol. 87, no. 4, p. 043307, 2013.

[65] S. Elghobashi, "On predicting particle-laden turbulent flows," *Applied Scientific Research*, vol. 52, no. 4, pp. 309–329, 1994.

[66] S. Dutta, M. Cantero, and M. Garcia, "Effect of self-stratification on sediment diffusivity in channel flows and boundary layers: a study using direct numerical simulations," *Earth Surface Dynamics*, vol. 2, no. 2, p. 419, 2014.

[67] A. Ferrante and S. Elghobashi, "On the physical mechanisms of two-way coupling in particle-laden isotropic turbulence," *Physics of Fluids (1994-present)*, vol. 15, no. 2, pp. 315–329, 2003.

[68] M. W. Vance, K. D. Squires, and O. Simonin, "Properties of the particle velocity field in gas-solid turbulent channel flow," *Physics of Fluids (1994-present)*, vol. 18, no. 6, p. 063302, 2006.

[69] G. B. Jacobs, D. A. Kopriva, and F. Mashayek, "Towards efficient tracking of inertial particles with high-order multidomain methods," *Journal of computational and applied mathematics*, vol. 206, no. 1, pp. 392–408, 2007.

[70] P. P. Popov, R. McDermott, and S. B. Pope, "An accurate time advancement algorithm for particle tracking," *Journal of Computational Physics*, vol. 227, no. 20, pp. 8792–8806, 2008.

[71] J. Horwitz and A. Mani, "Accurate calculation of Stokes drag for point–particle tracking in two-way coupled flows," *Journal of Computational Physics*, vol. 318, pp. 85–109, 2016.

[72] K. Sengupta, B. Shotorban, G. Jacobs, and F. Mashayek, "Spectral-based simulations of particle-laden turbulent flows," *International Journal of Multiphase Flow*, vol. 35, no. 9, pp. 811–826, 2009.

[73] A. Noorani, G. Sardina, L. Brandt, and P. Schlatter, "Particle transport in turbulent curved pipe flow," *Journal of Fluid Mechanics*, vol. 793, pp. 248–279, 2016.

[74] B. Fornberg, "A practical Guide to pseudospectral Methods, vol. 1 of Cambridge Monographs on Applied and Computational Mathematics," 1996.

[75] T. Auton, J. Hunt, and M. Prud'Homme, "The force exerted on a body in inviscid unsteady non-uniform rotational flow," *Journal of Fluid Mechanics*, vol. 197, pp. 241–257, 1988.

[76] M. R. Maxey and J. J. Riley, "Equation of motion for a small rigid sphere in a nonuniform flow," *Physics of Fluids (1958-1988)*, vol. 26, no. 4, pp. 883–889, 1983.

[77] C. Escauriaza and F. Sotiropoulos, "Lagrangian model of bed-load transport in turbulent junction flows," *J. Fluid Mech.*, vol. 666, pp. 36–76, 2011.

[78] F. Engelund and E. Hansen, *A Monograph on Sediment Transport to Alluvial Streams.* Teknik, 1967.

[79] R. Mei, "An approximate expression for the shear lift force on a spherical particle at finite Reynolds number," *International Journal of Multiphase Flow*, vol. 18, no. 1, pp. 145–147, 1992.

[80] P. Saffman, "The lift on a small sphere in a slow shear flow," *Journal of fluid mechanics*, vol. 22, no. 02, pp. 385–400, 1965.

[81] E. Loth and A. Dorgan, "An equation of motion for particles of finite Reynolds number and size," *Environmental fluid mechanics*, vol. 9, no. 2, pp. 187–206, 2009.

[82] M. Deville, P. Fischer, and E. Mund, *High-Order Methods for Incompressible Fluid Flow.* Cambridge, England: Cambridge University Press, 2002.

[83] V. Neary and F. Sotiropoulos, "Numerical investigation of laminar flows through 90-degree diversions of rectangular cross-section," *Computers & fluids*, vol. 25, no. 2, pp. 95–118, 1996.

[84] V. Neary, F. Sotiropoulos, and A. Odgaard, "Three-dimensional numerical model of lateral-intake inflows," *Journal of Hydraulic Engineering*, vol. 125, no. 2, pp. 126–140, 1999.

[85] P. Sagaut, *Large Eddy Simulation for Incompressible Flows.* Germany: Springer-Verlag, 2010.

[86] S. Dutta, C. Pantano-Rubino, M. I. Cantaero, M. H. Garcia, and G. Parker, "Effects of self-stratification on turbidity currents: A large eddy simulation approach," in *Proceedings of the XIX International Conference on Water Resources*, 2012, pp. 1–10.

[87] Y. Niño and M. García, "Using Lagrangian particle saltation observations for bedload sediment transport modelling," *Hydrological Processes*, vol. 12, no. 8, pp. 1197–1218, 1998.

[88] M. O. Deville, P. F. Fischer, and E. H. Mund, *High-order methods for incompressible fluid flow.* Cambridge University Press, 2002, vol. 9.

[89] P. Fischer and J. Mullen, "Filter-Based Stabilization of Spectral Element Methods," *Ser. IAnal. Numer., C. R. Acad. Sci., Paris*, vol. 332, pp. 265–270, 2001.

[90] P. F. Fischer, F. Loth, S. E. Lee, S.-W. Lee, D. S. Smith, and H. S. Bassiouny, "Simulation of high-Reynolds number vascular flows," *Computer methods in applied mechanics and engineering*, vol. 196, no. 31, pp. 3049–3060, 2007.

[91] C. Escauriaza and F. Sotiropoulos, "Lagrangian model of bed-load transport in turbulent junction flows," *Journal of Fluid Mechanics*, vol. 666, pp. 36–76, 2011.

[92] P. F. Fischer, G. W. Kruse, and F. Loth, "Spectral element methods for transitional flows in complex geometries," *Journal of Scientific Computing*, vol. 17, no. 1, pp. 81–98, 2002.

[93] H.-O. Kreiss and J. Oliger, "Comparison of accurate methods for the integration of hyperbolic equations," *Tellus*, vol. 24, no. 3, pp. 199–215, 1972.

[94] S. A. Orszag, "Spectral methods for problems in complex geometries," *Journal of Computational Physics*, vol. 37, no. 1, pp. 70–92, 1980.

[95] Y. Maday, A. T. Patera, and E. M. Rønquist, "An operator-integration-factor splitting method for time-dependent problems: application to incompressible fluid flow," *Journal of Scientific Computing*, vol. 5, no. 4, pp. 263–292, 1990.

[96] P. F. Fischer, "An overlapping Schwarz method for spectral element solution of the incompressible Navier–Stokes equations," *Journal of Computational Physics*, vol. 133, no. 1, pp. 84–101, 1997.

[97] J. W. Lottes and P. F. Fischer, "Hybrid multigrid/Schwarz algorithms for the spectral element method," *Journal of Scientific Computing*, vol. 24, no. 1, pp. 45–78, 2005.

[98] K. Mittal, "Spectral element mesh generation and improvement methods," M.S. thesis, 2016.

[99] J. Ohlsson, P. Schlatter, P. F. Fischer, and D. S. Henningson, "Direct numerical simulation of separated flow in a three-dimensional diffuser," *Journal of Fluid Mechanics*, vol. 650, pp. 307–318, 2010.

[100] F. Loth, P. F. Fischer, and H. S. Bassiouny, "Blood flow in end-to-side anastomoses," *Annu. Rev. Fluid Mech.*, vol. 40, pp. 367–393, 2008.

[101] S. Dutta, "Effect of self-stratification on channel flows and boundary layers: a study using direct numerical simulations," M.S. thesis, University of Illinois at Urbana-Champaign, 2013.

[102] K. K. Chen, C. W. Rowley, and H. A. Stone, "Vortex dynamics in a pipe T-junction: Recirculation and sensitivity," *Physics of Fluids*, vol. 27, no. 3, p. 034107, 2015.

[103] S. E. Lee, S.-W. Lee, P. F. Fischer, H. S. Bassiouny, and F. Loth, "Direct numerical simulation of transitional flow in a stenosed carotid bifurcation," *Journal of biomechanics*, vol. 41, no. 11, pp. 2551–2561, 2008.

[104] J. T. Ault, A. Fani, K. K. Chen, S. Shin, F. Gallaire, and H. A. Stone, "Vortex-Breakdown-Induced Particle Capture in Branching Junctions," *Physical review letters*, vol. 117, no. 8, p. 084501, 2016.

[105] K. K. Chen, C. W. Rowley, and H. A. Stone, "Vortex breakdown, linear global instability and sensitivity of pipe bifurcation flows," *Journal of Fluid Mechanics*, vol. 815, pp. 257–294, 2017.

[106] K. Sloff and E. Mosselman, "Bifurcation modelling in a meandering gravel–sand bed river," *Earth Surface Processes and Landforms*, vol. 37, no. 14, pp. 1556–1566, 2012.

[107] K. F. M. S. Rezapour and S. T. O. Naeeni, "Experimental study of flow and sedimentation at $90^o$ open-channel diversion." Proceedings of the 33rd IAHR Congress, 2009, pp. 2979–2986.

[108] A. S. Ramamurthy, D. Minh Tran, and L. B. Carballada, "Dividing flow in open channels," *Journal of Hydraulic Engineering*, vol. 116, no. 3, pp. 449–455, 1990.

[109] S. K. Lama, M. Kuroki, and K. Hasegawa, "Study of flow bifurcation at tic 30 open channel junction when the width ratio of branch channel to main channel is large," *Proceedings of Hydraulic Engineering*, vol. 46, pp. 583–588, 2002.

[110] C. F. vander Mark and E. Mosselman, "Effects of helical flow in one-dimensional modelling of sediment distribution at river bifurcations," *Earth Surface Processes and Landforms*, vol. 38, no. 5, pp. 502–511, 2013.

[111] H. Shamloo and B. Pirzadeh, "Numerical investigation of velocity field in dividing open-channel flow," in *Proceedings of the 12 th WSEAS International Conference on APPLIED MATHEMATICS*, 2007, pp. 194–198.

[112] A. Khan, R. Cadavid, and S. Wang, "Simulation of channel confluence and bifurcation using the CCHE2D model," *Proc. Instn. Civ. Engrs Water and Mar. Engng*, vol. 142(June), pp. 97–102, 2000.

[113] A. Ramamurthy, J. Qu, and D. Vo, "Numerical and experimental study of dividing open-channel flows," *J. of Hydraulic Engineering*, vol. 133(10), pp. 1135–1144, 2007.

[114] A. de Heer and E. Mosselman, "Flow structure and bedload distribution at alluvial diversions," in *River Flow*, 2004, pp. 801–806.

[115] J. Hervouet, *Hydrodynamics of free surface flows-Modelling with the finite element method*. France: John Wiley Sons, 2007.

[116] P. R. Jackson, S. Sinha, S. Dutta, K. K. Johnson, J. J. Duncker, and M. H. Garcia, "Evaluation of the potential for hysteresis in index-velocity ratings for the Chicago Sanitary and Ship Canal near Lemont, Illinois," US Geological Survey, Tech. Rep., 2013.

[117] D. Wang, S. Dutta, M. H. Garcia, and P. R. Jackson, "Three-dimensional numerical modeling of mixing at the junction of the Calumet-Sag Channel and the Chicago Sanitary and Ship Canal: A comparison between density-driven and advection-driven mixing," in *River Flow 2016*. CRC Press, 2016, pp. 1587–1595.

[118] C. Flokstra and F. Koch, "Bed level Computations for Curved alluvial Channels." IAHR Congress, 1980.

[119] W. Rodi, *Turbulence models and their application in hydraulics*. CRC Press, 1993.

[120] F. Lopez and M. Garcia, "Open-Channel Flow Through Simulated Vegetation: Turbulence Modeling and Sediment Transport," DTIC Document, Tech. Rep., 1997.

[121] R. Hardy, S. Lane, and D. Yu, "Flow structures at an idealized bifurcation: a numerical experiment," *Earth Surface Processes and Landforms*, vol. 36, no. 15, pp. 2083–2096, 2011.

[122] J. A. Constantine, T. Dunne, H. Piégay, and G. Mathias Kondolf, "Controls on the alluviation of oxbow lakes by bed-material load along the Sacramento River, California," *Sedimentology*, vol. 57, no. 2, pp. 389–407, 2010.

[123] J. A. Zinger, B. L. Rhoads, J. L. Best, and K. K. Johnson, "Flow structure and channel morphodynamics of meander bend chute cutoffs: A case study of the Wabash River, USA," *Journal of Geophysical Research: Earth Surface*, vol. 118, no. 4, pp. 2468–2487, 2013.

[124] K. Blanckaert, M. G. Kleinhans, S. J. McLelland, W. S. Uijttewaal, B. J. Murphy, A. Kruijs, D. R. Parsons, and Q. Chen, "Flow separation at the inner (convex) and outer (concave) banks of constant-width and widening open-channel bends," *Earth Surface Processes and Landforms*, vol. 38, no. 7, pp. 696–716, 2013.

[125] E. J. Langendoen, A. Mendoza, J. D. Abad, P. Tassi, D. Wang, R. Ata, K. El kadi Abderrezzak, and J.-M. Hervouet, "Improved numerical modeling of morphodynamics of rivers with steep banks," *Advances in Water Resources*, vol. 93, pp. 4–14, 2016.